



**BRNO UNIVERSITY OF TECHNOLOGY**

VYSOKÉ UČENÍ TECHNICKÉ V BRNĚ

**FACULTY OF MECHANICAL ENGINEERING**

FAKULTA STROJNÍHO INŽENÝRSTVÍ

**INSTITUTE OF MATERIALS SCIENCE AND  
ENGINEERING**

ÚSTAV MATERIÁLOVÝCH VĚD A INŽENÝRSTVÍ

**SHORT CRACK GROWTH IN MATERIALS  
FOR HIGH TEMPERATURE APPLICATIONS**

ŠÍŘENÍ KRÁTKÝCH TRHLIN V MATERIÁLECH PRO VYSOKÉ TEPLoty

**DOCTORAL THESIS**

DIZERTAČNÍ PRÁCE

**AUTHOR**  
AUTOR PRÁCE

Ing. Veronika Mazánová

**SUPERVISOR**  
ŠKOLITEL

prof. RNDr. Jaroslav Polák, DrSc. dr.h.c.

BRNO 2019



**Abstract:** Advanced highly-alloyed austenitic stainless steel Sanicro 25 based on Fe-Ni-Cr matrix was studied under the conditions of low cycle fatigue at room temperature and at elevated temperature of 700 °C. Several state-of-the-art experimental techniques were used to investigate the mutual effects of alloy composition, microstructural changes and deformation mechanisms, which determine the overall damage resistance of the material. The main effort has been focused on the fatigue crack initiation and the short crack growth, two stages which play an essential role in the resulting fatigue life of the material in the service.

- The internal deformation mechanisms were correlated with the evolution of the surface relief in the form of persistent slip markings. It was found that the high planar character of the dislocation slip causes the high cyclic plastic strain localization into the persistent slip bands and thus the early Stage I crack nucleation associated with the presence of the persistent slip markings in all studied samples. The twin boundary cracking was found to be related to the presence of the persistent slip marking along the surface trace of twin boundary as well.
- The intergranular crack initiation was observed only rarely at high strain amplitude loading. It was found to be related to the presence of the persistent slip markings at the grain boundary. Owing to high number of local incompatibilities at the grain boundary caused by the shape of the persistent slip markings the grain boundary cracks under the external tensile loading.
- The crack growth mechanisms of natural short cracks were studied on the samples subjected both to low and high strain amplitude cycling. The role of microstructure was analysed using experimental techniques and discussed.
- The crack growth rates of the longest cracks were measured on the samples with a shallow notch. The results were analysed using the fracture mechanics approaches based both on amplitude of  $K_I$  and of  $J$ -integral as well as on the plastic strain amplitude. All approaches were discussed in the relation to the Manson-Coffin fatigue life curve. The simple power law of the short crack growth based on the plastic strain amplitude shows very good correlation to the fatigue life law.
- In the case of cycling at elevated temperature the role of oxidation was studied. The brittle cracking of the oxidized grain boundaries was found to play a major role in the early stages of crack nucleation. Later the crack growth path changes to be preferentially transgranular. The crack growth path is very similar to that studied in room temperature cycling.

**Key words:** low cycle fatigue, austenitic stainless steel, damage mechanisms, fatigue crack initiation, PSBs, PSMs, natural short crack growth, fracture mechanics, short crack growth law, fatigue life, high temperature oxidation, SEM, EBSD, STEM

**Abstrakt:** Pokročilá vysoce legovaná austenitická nerezová ocel Sanicro 25 s Fe-Ni-Cr matricí byla studována za podmínek nízkocyklové únavy za pokojové a vysoké teploty 700 °C. Široká škála moderních experimentálních technik byla použita ke studiu vzájemně souvisejících efektů chemického složení slitiny, mikrostrukturních změn a deformačních mechanismů, které určují odolnost materiálu vůči poškození. Hlavní úsilí bylo zaměřeno na studium iniciace únavových trhlin a růstu krátkých trhlin, tedy dvě stádia, která hrají zásadní roli ve výsledné celkové délce únavového života materiálu v provozu.

- Vnitřní deformační mechanismy byly korelovány s vývojem povrchového reliéfu, který je pozorován ve formě persistentních skluzových stop na povrchu. Bylo zjištěno, že vysoce planární charakter dislokačního skluzu způsobuje vysokou lokalizaci cyklické plastické deformace do persistentních skluzových pásů, což v důsledku vede k nukleaci “Stage I” trhlin, která je spojena s přítomností persistentních skluzových stop na povrchu ve všech studovaných vzorcích. Bylo zjištěno, že praskání dvojčatových hranic je taktéž spojeno s přítomností persistentních skluzových stop podél povrchové stopy dvojčatové roviny.
- Interkrystalická iniciace únavové trhliny byla pozorována pouze zřídka, a to za podmínek zatěžování amplitudami vysoké deformace. Bylo zjištěno že interkrystalická iniciace je spojena s přítomností persistentních skluzových stop na hranicích zrn. Hranice zrn praskají za podmínek externího tahového zatížení zejména z důvodu vysokého počtu nekompatibilit na hranicích zrn, které jsou způsobené tvarem persistentních skluzových stop.
- Mechanismy růstu přirozených krátkých trhlin byly studovány na vzorcích vystavených nízkocyklove únavy s nízkou i vysokou deformací. Role mikrostruktury byla analyzována pomocí experimentálních technik a diskutována.
- Rychlosti šíření nejdělsích trhlin byly měřeny na vzorcích s mělkým vrubem. Výsledky byly analyzovány použitím přístupů lomové mechaniky založených na amplitudě  $K_I$  a  $J$ -integrálu stejně jako na amplitudě plastické deformace. Všechny přístupy byly diskutovány v souvislosti s Mansonovými-Coffinovými křivkami únavové životnosti. Jednoduchý mocninový zákon růstu krátkých trhlin založený na amplitudě plastické deformace ukazuje velice dobrou korelaci se zákonem únavové životnosti.
- Byla studována role oxidace v podmínkách cyklického zatěžování za vysokých teplot. Bylo zjištěno, že křehké praskání zoxidovaných hranic zrn hraje hlavní roli v počátečních stádiích nukleace trhlin. Později po iniciaci se dráha růstu trhliny mění preferenčně na transkrystalickou. Dráha šíření trhlin je velmi podobná dráze zjištěné při cyklování za pokojové teploty.

**Klíčová slova:** nízkocyklová únavy, austenitická nerezová ocel, mechanismy poškození, iniciace únavové trhliny, persistentní skluzové pásy (PSBs), persistentní skluzové stopy (PSMs), růst přirozených krátkých trhlin, lomová mechanika, zákon růstu krátkých trhlin, únavový život, oxidace za vysokých teplot, rastrovací elektronová mikroskopie (SEM), EBSD, rastrovací transmisní elektronová mikroskopie (STEM)

## **Bibliography of the Thesis**

MAZÁNOVÁ, V. Short Crack Growth in Materials for High Temperature Applications. Brno: Brno University of Technology, Faculty of Mechanical Engineering, 2019. 147 p. Supervisor: Prof. RNDr. Jaroslav Polák, DrSc. dr.h.c.

### **Declaration**

I declare that my doctoral thesis “Short Crack Growth in Materials for High Temperature Applications” was written by my own under the supervision of Prof. RNDr. Jaroslav Polák, DrSc. dr.h.c. All information sources are given in the References section at the end of the thesis.

Brno, 23.10.2019

.....  
signature



## Acknowledgement

Throughout my study and writing of the dissertation I have received a great deal of support and assistance.

I would first like to thank my supervisor, Prof. RNDr. Jaroslav Polák, DrSc. dr.h.c., who gave me the opportunity to come to the Institute of Physics of Materials and to collaborate on several interesting research projects here. I would also like to thank for his support and professional guidance during whole of my doctoral study.

Further thank belong to my colleagues from the Institute of Physics of Materials for their help and many interesting advices related not only to my study but also to my personal life. Especially I would like to thank to Jiří Tobiáš and Robin Mádle, and other technicians for their help with experiments. Further thanks belong to Prof. Mgr. Tomáš Kruml, CSc for many valuable discussions during solving the issues related not only to my dissertation. I would like thank him for his patient leadership and support in my academic career.

I would like to acknowledge my colleagues from my internship at Paul Scherrer Institut. The thanks belong also to Prof. Philippe Spätig who gave me an opportunity to be part of their research group in PSI, Switzerland, within the frame of the project Mobility of young researchers. I would like to thank everyone for advice associated with my work and stay there.

In addition, my family deserves special thanks; Milan, not only my live partner but also colleague in work, due to the discussions and help with the transmission electron microscopy and my parents, Jozef and Daniela, and siblings for their patience and support which helped me to overcome through tough times during my study. You are always there for me.

Thank you all.





# Contents

<b>I. INTRODUCTION</b> .....	<b>- 13 -</b>
<b>II. AIMS OF THE WORK</b> .....	<b>- 14 -</b>
<b>III. CURRENT STATE OF THE KNOWLEDGE</b> .....	<b>- 16 -</b>
<b>1. Austenitic stainless steel - Sanicro 25</b> .....	<b>- 16 -</b>
<b>2. Low cycle fatigue of ductile materials</b> .....	<b>- 18 -</b>
2.1. Cyclic stress-strain response and fatigue life .....	- 19 -
2.2. Cyclic plasticity and microstructural changes .....	- 21 -
2.3. Effect of high temperature .....	- 23 -
<b>3. Initiation of natural fatigue cracks in ductile polycrystalline metals</b> .....	<b>- 23 -</b>
3.1. Sites of natural crack initiation at room temperature .....	- 24 -
3.2. Surface relief evolution in form of persistent slip markings .....	- 27 -
3.2.1. Theoretical models of surface relief formation .....	- 28 -
3.3. Stage I fatigue crack growth .....	- 37 -
3.4. Effect of high temperature .....	- 39 -
<b>4. Growth of short fatigue cracks in ductile metals</b> .....	<b>- 40 -</b>
4.1. Crack growth mechanisms .....	- 42 -
4.1.1. Effects influencing the crack growth .....	- 42 -
4.1.2. Crack growth path .....	- 44 -
4.2. Crack growth kinetics .....	- 45 -
4.2.1. Small scale yielding approach ( <i>AK</i> ) .....	- 47 -
4.2.2. Large scale yielding approach ( <i>J-integral</i> ) .....	- 48 -
4.2.3. Plastic-strain dependence crack growth rate approach ( $\epsilon_{ap}$ ) .....	- 49 -
4.3. Effect of high temperature .....	- 50 -
<b>IV. EXPERIMENTS</b> .....	<b>- 51 -</b>
<b>5. Material</b> .....	<b>- 51 -</b>
5.1. Sanicro 25 .....	- 51 -
<b>6. Mechanical testing</b> .....	<b>- 51 -</b>
6.1. Specimens .....	- 51 -
6.2. Cyclic loading .....	- 52 -
<b>7. Microscopic observation</b> .....	<b>- 53 -</b>
7.1. Light microscopy .....	- 53 -
7.2. Scanning electron microscopy .....	- 55 -
7.3. Transmission electron microscopy .....	- 57 -

<b>V. RESULTS .....</b>	<b>- 59 -</b>
<b>8. Initial state of the material .....</b>	<b>- 59 -</b>
<b>9. Fatigue damage at room temperature .....</b>	<b>- 61 -</b>
9.1. Natural fatigue crack initiation sites .....	- 61 -
9.1.1. Crack initiation along persistent slip markings .....	- 61 -
9.1.2. Crack initiation at large angle grain boundaries .....	- 66 -
9.1.3. Crack initiation from inclusions .....	- 70 -
9.1.4. Crack initiation statistics .....	- 71 -
9.2. Surface relief evolution in the form of PSMs .....	- 72 -
9.2.1. STEM characterization of PSM profile and corresponding dislocation structure .....	- 72 -
<b>10. Crack growth of natural short cracks at room temperature .....</b>	<b>- 80 -</b>
10.1. Crack growth path of natural cracks .....	- 80 -
10.1.1. Stage I fatigue crack growth along PSM/PSB .....	- 80 -
10.1.2. Crack growth at the surface .....	- 80 -
10.1.3. Crack growth in the bulk of the material .....	- 84 -
10.2. Crack growth rates of short cracks .....	- 88 -
<b>11. Fatigue at a temperature of 700 °C .....</b>	<b>- 90 -</b>
11.1. Grain boundary oxidation and crack initiation .....	- 90 -
11.1.1. Environmentally assisted crack initiation .....	- 90 -
11.1.2. STEM characterization of the oxides at GB .....	- 94 -
11.1.3. Analysis of $M_{23}C_6$ Cr-rich carbides nucleated at the grain boundaries .....	- 95 -
11.2. Crack growth under environmental conditions .....	- 97 -
11.2.1. Crack growth at the surface .....	- 97 -
11.2.2. Crack growth in the bulk of the material .....	- 99 -
11.2.3. Crack growth path statistics .....	- 102 -
<b>VI. DISCUSSION .....</b>	<b>- 103 -</b>
<b>12. PSM assisted crack initiation at room temperature .....</b>	<b>- 103 -</b>
12.1. Cyclic plastic strain localization and PSM formation .....	- 103 -
12.2. PSM profile/Crack initiation in relation to the theoretical models .....	- 106 -
12.3. PSM assisted TB and GB cracking .....	- 108 -
<b>13. Crack growth of short natural cracks .....</b>	<b>- 110 -</b>
13.1. Crack growth mechanisms .....	- 110 -
13.2. Crack growth kinetics .....	- 112 -
13.2.1. Equivalent crack length concept .....	- 112 -
13.2.2. Fracture mechanics approaches .....	- 114 -
13.2.3. Crack growth under plastic strain amplitude .....	- 117 -
13.2.4. Fatigue life .....	- 120 -

<b>14. The role of oxidation in damage mechanisms during high temperature loading</b> .....	<b>- 122 -</b>
14.1. Oxidation assisted grain boundary cracking .....	- 122 -
14.2. Crack growth under the environmental conditions .....	- 125 -
<b>VII. CONCLUSIONS</b> .....	<b>- 128 -</b>
<b>VIII. REFERENCES</b> .....	<b>- 130 -</b>
<b>IX. LIST OF ABBREVIATIONS AND SYMBOLS</b> .....	<b>- 142 -</b>
<b>X. Curriculum Vitae</b> .....	<b>- 145 -</b>
<b>XI. Veronika Mazánová – List of publications</b> .....	<b>- 146 -</b>



# I. INTRODUCTION

The demands on the increase of the material properties from the site of the industry force the materials research highly forward. In the case of new generation of coal-fired power plants the increase of the material properties such as creep strength, high-temperature strength and high-temperature corrosion resistance are essential material features leading to the increase of the power plant heat efficiency higher than 50 %. Moreover, the environmental impact in the form of carbon dioxide generated by combustion processes can be decrease by more than 15 % compared with modern power plants [1]. Such a material can be newly developed austenitic stainless Sanicro 25 steel. It is advanced high strength heat-resistant material primarily designed for service in high temperature corrosive environments [1]. However, based on its excellent properties, there is an expectation for its wider utilization also in other industrial applications.

During the service conditions variable forces or rapidly changing temperatures lead to the production of alternating stresses and strains, preferably in critical locations. Repeated alternating stresses introduce fatigue damage and lead to initiation of fatigue cracks, their propagation, and fracture. Due to service conditions, both high and room temperature fatigue can result in failure of structural components. Therefore, not only the deformation mechanisms taking place during the cyclic loading but also the detailed knowledge of the damage evolution leading to final fracture is useful in preventing catastrophic failures. The knowledge of the weaknesses of the material can help to its future improvement.

Numerous studies of the fatigue process in materials revealed [2] principal stages in the fatigue life, initiation of fatigue cracks and their propagation. In elastoplastic cyclic loading resulting in low cycle fatigue failure, the highest importance represents the initiation of fatigue cracks and growth of short cracks because they determine the fatigue life. The early study of fatigue crack initiation started in the beginning of the last century (see the pioneering work of Ewing and Humfrey [3]), but the intensive study of both crack initiation and short crack growth in a number of polycrystalline materials with the aim to document the advancement of fatigue damage and damaging mechanisms started much later (see the review [4; 5]).

Complex conditions in real service need thorough studies of deformation and damage mechanisms during both unidirectional and cyclic loading. The microstructural features that lead to the cyclic strain localization and the initiation of fatigue cracks at room temperature and at elevated service temperature differ significantly [6]. At high temperatures, the early fatigue damage is not only affected by the type of loading [7; 8], but also by the environmental effects causing grain boundary oxidation and cracking [9; 10].

The purpose of this work is to reveal the details of the low-cycle fatigue crack initiation and natural short crack growth both at room temperature and at a temperature of 700°C in Sanicro 25 and to provide the insights into the mechanisms determining the fatigue life of this austenitic steel. Advanced experimental tools are used to investigate the microstructural changes leading to the early stages of fatigue crack initiation and growth. The results are discussed in relation to the proposed models of fatigue crack initiation and estimation of residual fatigue life. The role of high temperature is discussed in relation to the overall fatigue life of the alloy.

## II. AIMS OF THE WORK

This thesis is focused on the fatigue damage mechanisms taking place during the low cycle fatigue of recently developed austenitic stainless Sanicro 25 steel used in power generation industry. The damage mechanisms are studied during cyclic straining at both room and elevated temperatures. Special emphasis is put on the investigation of the fatigue crack initiation since in the low cycle fatigue regime the fatigue crack initiation period represents the important stage of the fatigue life. The parameters describing the short crack growth were evaluated for the samples cycled at room temperature. Several minor goals were specified to be accomplished within the study as listed below:

- Characterization of the initial state of the material.
- The analysis of the fatigue crack initiation taking place at both ambient and elevated temperatures. Discuss the role of the environment in the crack nucleation mechanism.
- The investigation of the crack initiation sites leading to the growth of the major cracks. Discuss the microstructural changes of the material due to the cyclic loading in relation to the early stages of the crack nucleation.
- Study of the short crack growth mechanisms in the material subjected to loading at room temperature as well as at elevated temperature. The study of short cracks growth was performed under the tension-compression loading.
- Measurement of the crack growth rates on the samples subjected to cycling with constant total strain amplitudes at room temperature.
- The evaluation of the characteristic parameters, which determine the rate of fatigue crack growth. The prediction of the fatigue life and the estimation of the residual fatigue life.



### III. CURRENT STATE OF KNOWLEDGE

#### 1. Austenitic stainless steel - Sanicro 25

Materials resisting high stresses and temperatures are the necessary prerequisite to achieve higher efficiency of coal-fired power plants and consequential reduction of CO<sub>2</sub> emissions. The next generation of power plants is designed to operate at notably elevated temperature. By increasing the steam temperature to 700 °C and steam pressure from 30 MPa to 35 MPa the maximum heat efficiency can increase from 45 % to more than 50 % and the emission can be reduced by about 45 %. This led to a need for development of new heat-resistant materials with improved high-temperature strength, enhanced creep properties, and high-temperature corrosion resistance. In order to minimize the use of expensive materials such as Ni-based superalloys, highly-alloyed austenitic heat-resistant steels have been designed [11]. One of the alloys developed principally for use in advanced ultra-supercritical (A-USC) coal-fired boilers is the austenitic stainless steel Sanicro 25 (UNS S31035).

Compared to other steels in this class (e.g. NF709, Super304H, H3RC, etc. [2]), this alloy has relatively unique composition in terms of type and amount of chemical elements used together. It is based on the Fe-Ni-Cr alloy system with a high amount of Ni and Cr combined with variety of other alloying elements. While 22.5 wt% Cr should secure good steam oxidation resistance and hot corrosion resistance, a high Ni content of approximately 25.0 wt% and high amount of N are used for the stabilization of the FCC austenitic phase. For solid solution and precipitation strengthening, a combination of a high content of W, Co, Nb, Cu and other elements have been added [12]. The observed precipitates of type M<sub>23</sub>C<sub>6</sub>, MX, Laves phase, Z-phase and Cu-rich particles that can play an important role in creep resistance of the material [11].

As reported recently [11; 13; 14], Sanicro 25 has achieved the highest creep strength at a temperature of 700°C among all austenitic stainless steels commercially available today. Other significant properties exhibited are the extraordinary high temperature cyclic strength [15-17] and excellent corrosion and oxidation resistance observed also in high-pressure steam environment [18; 19].

Recently the studies have been focused on the low cycle fatigue properties [15; 16; 20-22]. The fatigue life curves and cyclic stress-strain curves show that Sanicro 25 steel has promising not only creep and oxidation resistant properties but also the fatigue properties compared to the other used materials [16; 17].

Based on the excellent high-temperature properties of Sanicro 25 steel, there is an expectation for its wider utilization in industrial applications.

The thorough studies of the tensile properties (see Table 1.1.) and of the cyclic stress-strain response of Sanicro 25 steel were already reported [15; 17; 21; 23]. The cyclic hardening/softening curves of specimens cycled with constant total strain amplitude in the range from  $2 \times 10^{-3}$  to  $1 \times 10^{-2}$  at room and at elevated temperature are shown in Figs. 1.1a and 1.1b respectively. In the case of room temperature cycling with strain amplitudes higher



than  $5 \times 10^{-3}$  initial cyclic hardening is present followed by softening whereas the lower strain amplitude cycling exhibits cyclic softening followed by saturation until failure. Essentially different behaviour was observed in the case of cycling at elevated temperature. The cyclic hardening with a tendency to reach saturation was observed for all strain amplitudes.

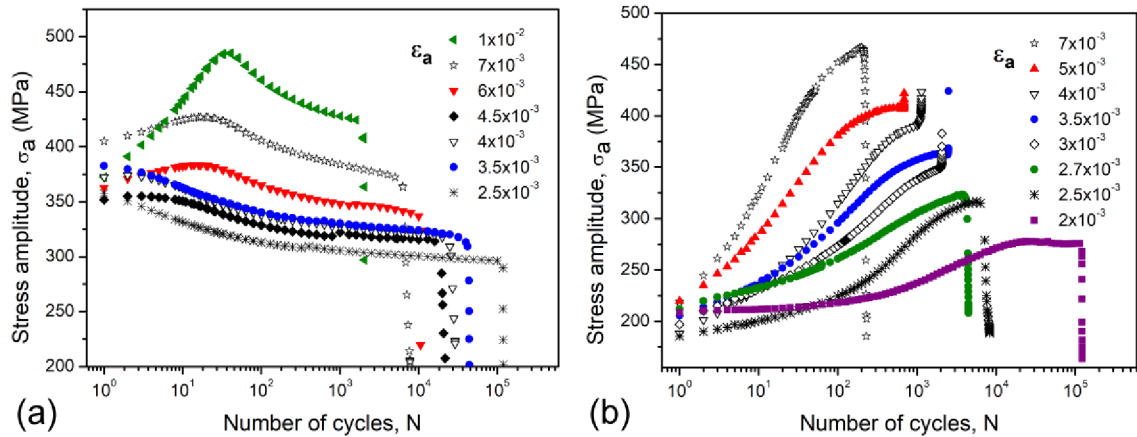


Figure 1.1: Cyclic hardening/softening curves in loading at two temperature (a) room temperature, (b) 700°C. (Taken from [15])

Heczko et al. [21] discussed the initial room temperature hardening as the consequence of the activation of multiple slip systems. Later the cyclic plastic strain is localized into the persistent slip bands leading to the cyclic softening or saturation. The cyclic high temperature hardening was found [16; 17] to be related to the high temperature nucleation and growth of NbC nanoparticles. Their diffusion-controlled nucleation and growth is enhanced by preferential nucleation at dislocations. These nanoparticles present the effective obstacles for dislocation motion.

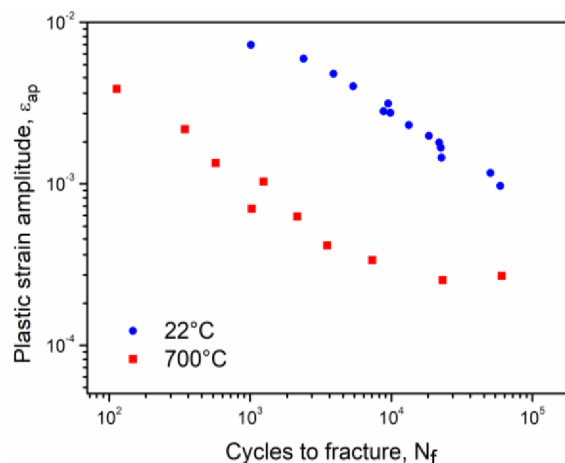


Figure 1.2: Manson-Coffin fatigue life curves at two temperatures. (Taken from [15])

The fatigue life curves at room and high temperature (Fig. 1.2) show significant shift of the number of cycles to fracture for all plastic strain amplitudes. The samples cycled at room temperature have longer fatigue lives than those cycled at elevated temperature. The parameters of the cyclic stress-strain curves and of the Manson-Coffin and Basquin relations are listed in Tab. 1.1.

$T$ (°C)	$E$ (GPa)	$R_{p0,2}$ (MPa)	$R_m$ (MPa)	$A$ (%)	$K'$ (MPa)	$n'$	$\epsilon_f'$	$c$	$\sigma_f'$ (MPa)	$b$ (MPa)
22	200	320	740	59	1006	0.186	0.700	-0.526	962	-0.100
700	130	190	487	51	1243	0.181	0.090	-0.539	797	-0.090

Table 1.1: Tensile and low cycle fatigue parameters of Sanicro 25 at two temperatures. (Taken from [15])

## 2. Low cycle fatigue of ductile materials

Fatigue of materials is a term which applies to changes in their properties due to the repeated application of external stresses or strains. As loading continues, these changes can lead to cracking or final failure of the components [24; 25]. The first systematic investigation of fatigue failure was performed by A. Wöhler during the period 1852-1869. Based on his observations (repeated loading by constant stress) he characterized the fatigue behaviour in terms of stress amplitude-fatigue life (S-N) curves [26]. Later Bauschinger observed that elastic limit of metals under cyclic loading can differ from that in monotonic loading [27]. He identified cyclic strain softening and cyclic strain hardening. The importance of the plastic strain in cyclic damage of materials was for the first time established by Coffin [28] and Manson [29]. They proposed the empirical relationship between number of cycles to failure and the amplitude of plastic strain called Coffin-Manson relationship.

The low cycle fatigue (LCF) processes are controlled by elasto-plastic cyclic behaviour of the material as introduced by Coffin and Manson. Since high number of components in variety of branches of industry are subjected to the cyclic loading with high stress or strain amplitudes the importance of the LCF characterization of the materials increases. The cyclic damage has a cumulative character and leads to the irreversible complex microstructural changes on both macroscopic and atomic-scale levels. Consequently, fatigue cracks initiate and grow through the material leading to the final fatigue fracture. [2; 30]

On the basis of the type of irreversible changes caused by cyclic plastic deformation, it is possible to divide the whole fatigue process into three consecutive and partly overlapping stages: (a) fatigue hardening/softening, (b) microcrack nucleation and (c) crack propagation ending in final failure.

From the engineering point of view, fatigue life can be divided into two important stages: (a) initiation of an engineering crack and (b) the long crack propagation until it reaches the critical length. The individual stages of fatigue life are shown in Fig. 2.1. The first period of fatigue life is represented by the microstructural changes due to dislocation movements taking place during the fatigue life. The microstructure of the metal subjected to cyclic

loading during the fatigue life differs substantially from the original microstructure. This is connected with the alternating character of the cyclic plastic response (hardening/softening of the material). Microstructural changes lead to the formation of surface relief and to the initiation of shallow fatigue cracks. Their mutual interactions anticipate the growth of natural short fatigue cracks. The short fatigue cracks grow and interact until one dominant crack develops. Later, the fatigue life period is represented by the growth of one long crack (macrocrack growth) till the final fatigue fracture. [31]

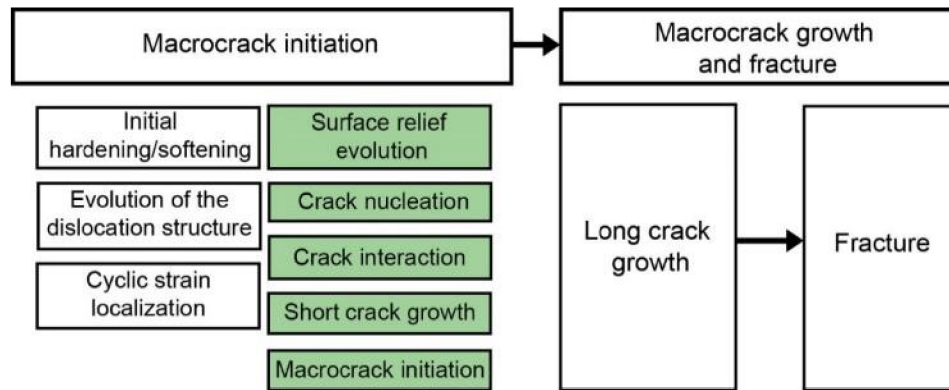


Figure 2.1: Evolution of fatigue damage leading to failure of materials.

## 2.1. Cyclic stress-strain response

Cycling loading of metals leads to changes in their structure. The evolution of internal defect density and corresponding changes of dislocation structure as well as the effects of precipitation or phase transformation are in mutual correlation with the overall stress-strain response of the material.

Standardized smooth specimens are typically used to study the behaviour of the material during symmetrical uniaxial cyclic loading test with controlled constant amplitude. The asymmetry of the cycling is characterized by the parameter  $R$ . It is the proportion of the upper and to the lower limit of applied cyclic loading. For symmetrical cycling  $R$  is equal to  $-1$ . Depending on the amplitude, which is kept constant, three regimes are adopted: constant plastic strain amplitude ( $\varepsilon_{ap}$ ), constant total strain amplitude ( $\varepsilon_a$ ) and constant total stress amplitude ( $\sigma_a$ ) loading. Other parameters change during cycling and can be measured directly in each cycle from the hysteresis loop (Fig. 2.1.1). In the linear, elastic component of the hysteresis loop the relation between the stress and elastic strain is given by Hook's law as follows

$$\sigma = E \varepsilon_{a,el} \quad (2.1.1)$$

where  $E$  is Young's modulus. The plastic strain amplitude can be evaluated also as the difference between the total and elastic strain amplitudes. [2]

The other useful characteristic of hysteresis loop shape describing the plastic deformation behaviour of the material is loop shape parameter  $V_H$  [2] defined as

$$V_H = \frac{W}{4\varepsilon_{ap}\sigma_a} \quad (2.1.2)$$

where the hysteresis loop area  $W$  represents the specific energy dissipated in a material within one cycle,  $\varepsilon_{ap}$  is plastic strain amplitude and  $\sigma_a$  is stress amplitude. In the early stages of cyclic hardening, the loop shape parameter decreases with the number of cycles. As soon as the plastic strain starts to be localized, the loop shape parameter starts to increase.

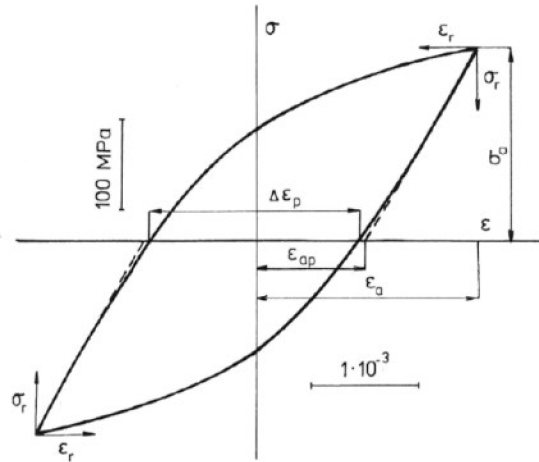


Figure 2.1.1: The saturated hysteresis loop corresponding to one cycle. (Taken from [2])

The appropriate plots showing the changes in the behaviour of the material during loading are called cyclic hardening/softening curves. In cycling with constant total strain amplitude, these curves are represented by the dependence of the stress and plastic strain amplitude on the number of cycles. In cyclic hardening/softening curves of f.c.c. materials it is usually possible to find three basic stages: rapid initial hardening (for annealed initial state of the material), the saturation and a slow long-term hardening or softening stage. At the beginning of cycling the changes are very marked, their intensity decreases with increasing number of cycles. In total strain controlled cycling the increase of the stress amplitude and the drop of the plastic strain amplitude represents cyclic hardening. Cyclic softening is the opposite effect, i.e. the stress amplitude decreases and the plastic strain amplitude increases with increasing number of cycles. After a relatively small number of cycles the measured quantity usually reaches its saturated values. It means that the hysteresis loop is closed and does not change significantly with the number of cycles. [2]

Many ductile metals subjected to strain controlled cyclic loading have a tendency to stabilize their stress-strain response. Therefore, the dependence between cyclic stress and strain which is independent of number of cycles and characterises this stabilised stress-strain response is introduced. The cyclic stress-strain curve (CSSC) is the dependence of the stress amplitude ( $\sigma_a$ ) on the strain or plastic strain amplitude ( $\varepsilon_{ap}$ ) in the stabilised state and can be expressed as

$$\sigma_a = K'(\varepsilon_{ap})^{n'} \quad (2.1.3)$$

where  $K'$  is the fatigue hardening coefficient and  $n'$  is the fatigue hardening exponent. [2]

In the case of LCF (constant strain amplitude cyclic loading) the number of cycles to fatigue fracture ( $N_f$ ) of the specimen is usually plotted vs. strain or plastic strain amplitude. As most materials reveal the saturated behaviour it is possible to plot the plastic strain amplitude

( $\varepsilon_{ap}$ ) representing the damage of the material in saturated state in bilogarithmic plot with the number of cycles ( $2N_f$ ). The plot can be described by the Coffin-Manson law as mentioned earlier

$$\varepsilon_{ap} = \varepsilon_f' (2N_f)^c \quad (2.1.4)$$

where  $\varepsilon_f'$  is the fatigue ductility coefficient and  $c$  is the fatigue ductility exponent.

## 2.2. Cyclic plasticity and microstructural changes

The original microstructures of the metals subjected to cyclic loading can differ substantially and depends on the composition, thermal and mechanical treatment, previous history, environment, etc. However, the changes in the initial structure or formation of a new microstructure in cyclically loaded metals have some features common to various metals. These are closely connected with the alternating character of cyclic plastic straining and other specific features characteristic for the lattice structure and the properties of dislocations and other lattice defects in the particular metal. Most relevant in the characterization of the metallic materials is the dislocation arrangement and point defects distribution in cyclic plastic straining. Additional structural parameters, such as the size and the distribution of strengthening particles, inclusions, etc., are necessary to be accounted to in multiphase materials and structural alloys. [2]

Cyclic plasticity and its relation to the dislocation structure have been studied most intensively in f.c.c. polycrystalline metals and single phase alloys, namely in copper and its alloys [32], aluminium and its alloys [33], nickel and its alloys [34], and stainless steels [35-38].

The dislocation arrangement evolves substantially during the external loading. In the initial state of the material (usually after the annealing), the dislocation density is remarkably low. Under cyclic loading the dislocation density increases significantly. The evolution of the internal dislocation structure in relation to the saturated shear plastic strain amplitude in copper single crystal [39] is shown in Fig. 2.2.1. Region A represents homogeneous cyclic straining of the single crystal. The existing dislocation network serves as Frank-Read sources and new dislocation loops are produced under shear stress. As the dislocation density is increased, the frequency of mutual dislocation interactions increases and new substructures are created. These tangled or vein-like dislocation structures consist of dislocation dipoles. Increase in dislocation density and the formation of tangled or vein-like structures is usually connected with the initial cyclic hardening of cyclically loaded material. In region B of the CSSC, the saturated stress amplitude is fairly constant, independent of applied plastic strain amplitude. This behaviour was found to be connected with strain inhomogeneity on a macroscale. Cyclic plastic strain is localized into the regions of intensive plastic strain, so-called persistent slip bands (PSBs). The PSBs are usually observed in the form of ladder-like dislocation structure consisting of walls with high dislocation density separated by regions with low dislocation density i.e. dislocation channels. As a result, the shape of the hysteresis loop changes what can be characterized by the loop shape parameter. At minimum of the  $V_H$  parameter the localization of the plastic deformation was observed as well as the first fatigue induced slip markings at the surface [40; 41]. According to Winter [42] the shear plastic strain ( $\gamma_{pl}$ ) in region B is proportional to the fraction  $f$  of persistent slip bands in agreement with the two-phase model

$$\gamma_{pl} = f\gamma_{PSB} + (1 - f)\gamma_M \quad (2.2.1)$$

where  $\gamma_{PSB}$  and  $\gamma_M$  are constant plastic shear strain amplitudes in PSB and in the matrix, respectively. By increasing the applied shear strain amplitude close to the region C the secondary slip systems becomes active and additional hardening appears. Dislocations from secondary slip systems can interact with the structures formed in the region A and B leading to rearrangement of the overall dislocation microstructure. As a consequence, labyrinth and cellular dislocation structures are usually observed. In region C the applied plastic strain amplitude is higher than the average plastic strain amplitude in PSB. As a result, secondary slip systems are activated and walls and cells structures arise in the whole volume. The corresponding dislocation structures may differ depending on the value of the resolved shear stress on the secondary slip systems. [2]

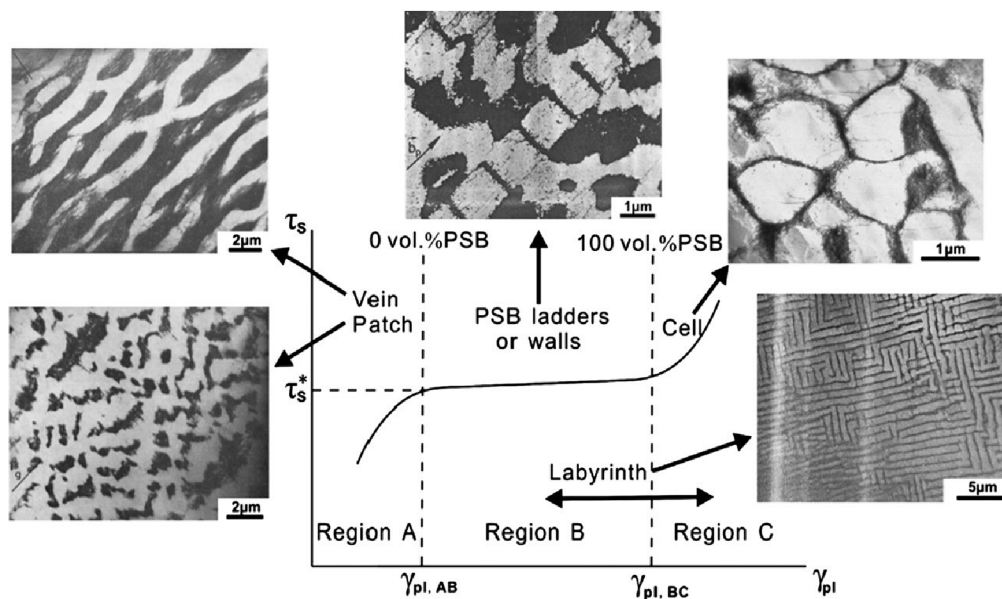


Figure 2.2.1: The schematic diagram of the cyclic stress-strain curve of copper single crystal oriented for single slip. The corresponding dislocation structures observed in individual regions are shown. (Taken from [43])

The similar cyclic behaviour is expected also in the case of polycrystalline metals. The observations on 316L steel cycled with constant plastic strain amplitudes at room temperature were reviewed by Polák [44]. The early cyclic hardening period is followed by softening with a tendency to reach saturation [45-47]. More detailed study [48] documents that the saturation develops only for medium plastic strain amplitudes while for high amplitudes secondary hardening is observed and for the lowest plastic strain amplitudes fatigue softening continues until fracture. Moreover, the  $V_H$  parameter can be correlated with the localization of the cyclic plastic strain into the PSBs. Transmission electron microscopy observations [38; 45; 47; 49; 50] revealed that the planar slip is characteristic for low and medium plastic strain amplitudes resulting in dislocation tangle- and vein-like arrangements. In addition, at medium plastic strain amplitudes the dislocation structure similar to that found in PSB structure was observed. For the highest plastic strain amplitudes, labyrinth-like and cellular dislocation structures are the most typical. It is worthy to note, that the addition of nitrogen to 316L type of steels can lead to decrease of SFE thus further promoting planar slip as reported by Vogt et al. [51; 52].

### **2.3. Effect of high temperature**

At high temperatures, the mechanical behavior of materials can differ significantly since the role of the thermally activated processes increases. In the case of many austenitic stainless steels, e.g. 316L types, the stacking fault energy was found to be relatively low, in particular lower than  $20 \text{ mJ m}^{-2}$  [38; 53; 54]. This implies large dissociation distance between Shockley partial dislocations thus preventing easy recombination and cross-slipping. However, since both the cross-slip and the climb of the dislocations are thermally dependent, dislocation motion at high temperatures is not necessarily fixed to the particular type of planes what subsequently leads to easier recovery processes.

It has been reported previously for both simple metals (e.g. copper [35]) and complex structural alloys (e.g. 316 L [37; 55]) that after a rapid initial increase the total dislocation density has a tendency to reach saturated equilibrium values in the very early stage of cyclic loading. After that, dislocations tend to form arrangements with lower stored internal energy. Sufficiently high temperature and external loads enhance diffusion of point defects and facilitate dislocation climb and cross-slip. Mutual interaction of dislocation stress fields leads to dislocation annihilation or dipole formation, which are important to the recovery processes. Initially tangled dislocations rearrange to cellular structures bordered by the walls with a high density of dislocations with alternating signs. Upon further recovery, dislocations in the cell interiors are annihilated. The internal stored strain energy is significantly decreased usually leading to so called softening of the material response to external load [17].

At high temperatures, the diffusion rates of interstitial and substitutional solute atoms are much higher. Therefore, the segregation events can occur. The mobility of dislocations can be directly affected by the formation of solute atom atmospheres (Cottrell, Suzuki, etc.). Interstitial atoms whose diffusion rate at high temperature is high enough to follow moving dislocations can segregate to their cores and immobilize them by pinning. As a consequence, the cyclic stress-strain response of the material can be significantly modified.

The segregation can be eventually followed by rapid precipitation of secondary phases. While dense dispersion of nanoscale precipitates can in general increase the strength of the alloy, secondary phases formed at the grain boundaries can decrease corrosion and oxidation resistance of the material.

## **3. Initiation of natural fatigue cracks in polycrystalline metals**

The initiation of the fatigue cracks is considered being one of the most important stages of the fatigue life. The initiation period corresponds to the number of cycles required to nucleate small crack (incompatibility or decohesion) in the material. During cycling with low cycle fatigue conditions this period may take several percent of fatigue life in cycling at room temperature. The importance of the fatigue crack initiation period increases with decreasing applied strain amplitude.

This issue has been studied in numerous materials for more than hundred years. The first observations of surface fatigue crack initiation at room temperature were performed by Ewing and Humfrey [3] using the light microscope. They studied polished polycrystals of Swedish iron. Based on their observations they found that cracks prefer initiating from the surface markings produced during cyclic loading. The surface was considered being the

prominent site of fatigue crack nucleation, nevertheless, the crack nucleation was observed in the bulk of the material as well. Subsurface crack nucleation is significant mainly in the case of materials containing internal defects or inclusions. The mechanism of fatigue crack nucleation can be affected by several factors such as surface finish and thermal and mechanical treatment, environment, type of cyclic loading, character of cyclic slip and secondary phases present in the matrix.

In following sections, the early fatigue damage mechanisms are discussed in detail based on recent monographs on fatigue [2; 25; 56].

### **3.1. Sites of natural crack initiation at room temperature**

It is well experimentally established that the fatigue failure is very sensitive to surface state and stress concentrators in the form of different types of notch-like defects or secondary hard phases. In the case of ductile materials the nucleation and whole fatigue process is controlled by the cyclic-plastic deformation. Therefore, it can be expected that fatigue cracks initiate at positions where the cyclic deformation is higher than average, in places of plastic-strain concentration. The plastic-strain concentration is associated with the local increase in stresses due to stress concentration. [56]

Number of experimental observations indicate the free surface as the preferential site where microcracks initiate in homogeneous materials. However, in engineering materials the cracks may originate at the interface between hard secondary phases and ductile matrix or from the internal defects. Three basic types of nucleation site are observed:

#### **1) Sharp fatigue-induced surface relief**

In metals without any internal defects and inclusions, the preferred and most studied type of natural crack initiation is found to be along the bands of cyclic slip under cyclic loading. The impact of crack initiation along the surface slip bands was subjected to intensive study in the past. The surface relief formation and crack initiation along the surface slip bands during fatigue life was thoroughly studied. The experiments of Thompson, Wadsworth and Louat [57] showed that removal of cyclically induced surface roughness, i.e. by electropolishing can increase fatigue life. More demonstrative evidence was later done by Basinski, Pascual and Basinski [58]. They studied the influence of surface roughness on fatigue life in copper single crystals. Based on their studies, the elimination of surface roughness by electropolishing drastically enhances total fatigue life not only in low plastic strain amplitude loading but also in high plastic strain amplitude loading. The mechanisms of surface relief formation and models of crack nucleation along the slip markings will be discussed later in this Chapter.

#### **2) Grain and twin boundaries**

The presence of the grain boundary fatigue crack initiation in ductile polycrystalline metals is relatively less common. Incompatible shape changes induced by asymmetric slip in neighbouring grains at the surface contribute to crack initiation at grain boundaries [2]. The occurrence of grain or twin boundary cracking depends on loading conditions such as temperature, strain amplitude and strain rate, and material characteristics such as crystalline structure and grain size. The effect is particularly enhanced at low temperatures, high strain



rates and high plastic strain amplitudes. In generally, grain boundary cracking is more typical for low cycle fatigue carried out under high strain amplitudes [59-61].

These early results point to two mechanisms of grain boundary cracking during cyclic loading. In Cu subjected to cyclic loading with several plastic strain amplitudes two mechanisms were found: (i) at low to intermediate plastic strain amplitude, the impingement of PSBs at grain boundary causes cracking. Crack initiation occur at sites where primary slip bands intersect a grain boundary. This causes local plastic incompatibilities and stress concentrations, and as a result decohesion of the grain boundary. (ii) At high plastic strain amplitudes, grain boundary cracking occurs as consequence of surface steps formed at the boundary. [25]

Kim and Laird [61] studied the mutual misorientation of cracked grains and relative orientation of their slip systems in polycrystalline copper subjected to high strain amplitude cycling. They identified several qualitative requirements for crack nucleation at grain boundary: (i) the crystallographic misorientation of surrounding grains is high, (ii) high angle grain boundaries contain a large angle ( $30\text{-}90^\circ$ ) with tensile stress axis at the surface, and (iii) at least one active slip system of the surrounding grains is oriented perpendicular to the projection of the grain boundary at the surface.

Mughrabi and Christ [62; 63] observed intergranular cracking in fatigued Cu polycrystal. Based on their observations intergranular fatigue cracking strongly depends on the interactions of PSBs with GBs and their mutual orientation (see Fig. 3.1.1). PSBs promote the initiation of GB cracking by interfacial dislocations in the form of pile-up. GB cracking can be later facilitated by environmental interaction (oxidation).

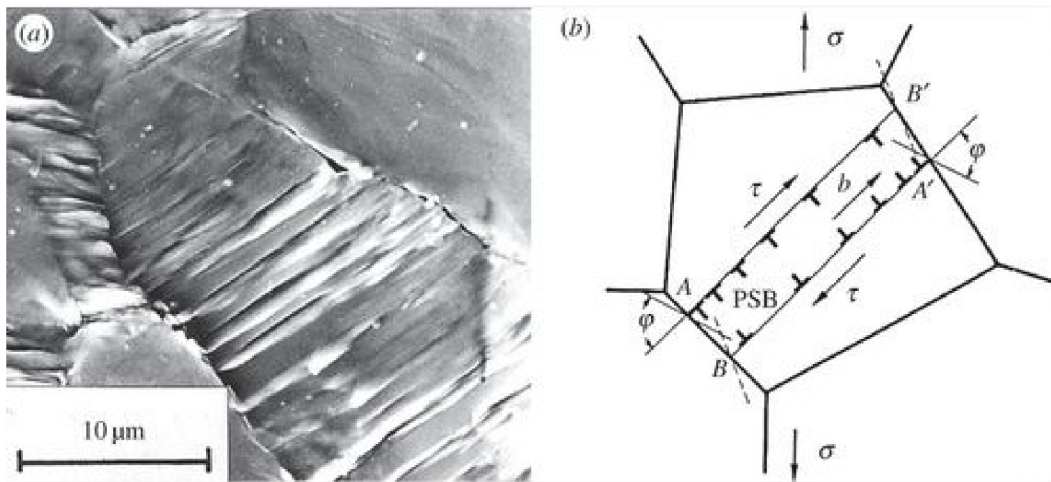
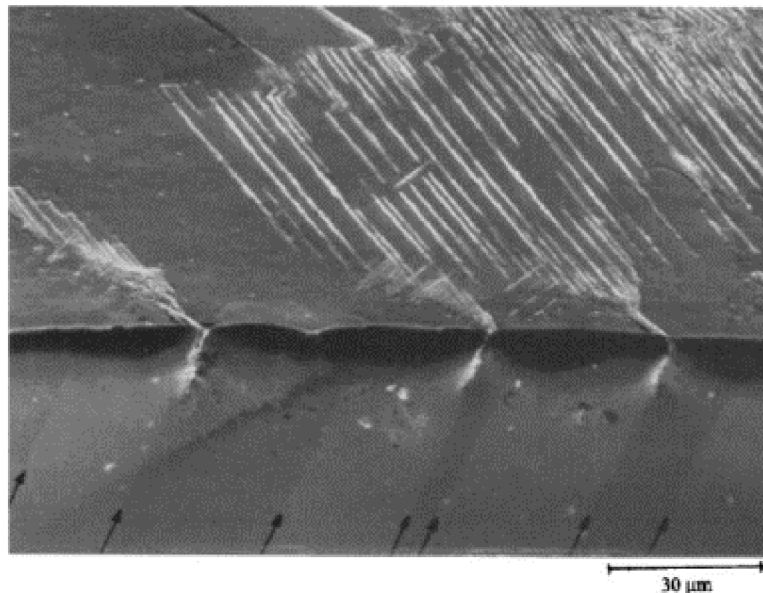


Figure 3.1.1: Intercrystalline PSB-GB cracks induced by PSBs impinging against grain boundaries. (a) SEM micrograph of PSB-GB cracking in fatigued copper polycrystal. (b) Dislocation model of action of PSBs against grain boundaries. (Taken from [64])

The role of twin boundaries in the crack nucleation has long been known [57; 65; 66]. In FCC metals, twin boundaries are parallel to the slip planes of type  $\{111\}$  so that the persistent slip bands can fit into the region of high local stresses at the boundary. Therefore, the geometric relationship between the boundary and the slip plane may provide possible clues to the role of twins in fatigue crack nucleation [25]. Boettner et al. [65] found

interesting aspect that there is inclination for slip bands formation and crack nucleation only at every other twin boundary. Later, more detailed studies were done by Neuman and Tönnensen [66] on annealing twin boundaries in FCC metals. In Cu fatigued with low stress amplitude at room temperature the formation of PSBs within the grains was suppressed. Against that, PSBs were found parallel to and coincident with twin interfaces (see Fig. 3.1.2). Local stress concentrations due to elastic anisotropy were considered being origin of the twin boundary cracking. In order to ensure strain compatibility at twin boundaries in the elastically anisotropic material, internal stresses must be generated in the vicinity of the twin boundaries. Consider a stack of lamellar twins, where the crystallographic orientation of the lamellae changes back and forth from that of the matrix to the twin to the matrix as one traverses across the boundaries. With the change in orientation there is also a change in the direction of internal stresses. The internal stresses act in concert with the resolved stresses from the applied loads at every other twin boundary. When the resultant stress is of sufficient high magnitude, a PSB is formed near the twin-matrix interface and eventually develops into a fatigue crack in each second twin boundary. [25]



*Figure 3.1.2: Nucleation of fatigue cracks along every other twin boundary (indicated by arrows) in polycrystalline Cu fatigued at room temperature. (Taken from [67])*

### 3) Inclusions and internal defects

Many commercial materials are not single-phase structural alloys. Some non-metallic phases can be present in the material in the form of inclusions. Other possible sites of heterogeneous crack nucleation can be voids, slag or gas entrapments, inclusions, dents, scratches, forging laps and folds, macroscopic stress concentrations, as well as regions of microstructural and chemical nonuniformity [25]. The effect of inclusions is specific to the alloy systems, preferentially in high strength steels [68] aluminium alloys [69] and titanium alloys [70]. Internal defect of such character significantly influence total fatigue life in markedly decreased number of cycles to fracture. In numerous cases, pores have been considered as initiated cracks already present within the material. In reality cracks start growing from these pores in a few cycles and almost no crack initiation at the surface can be found.

Models of fatigue crack initiation at inclusions depend on the matrix material, type of inclusion and properties of the interface between the inclusion and the matrix. The relative importance of the inclusions in fatigue crack initiation depends, on the size of inclusion. Very small inclusions (less than 1  $\mu\text{m}$ ) can suppress crack initiation through slip homogenisation. Large inclusions are the primary sources of crack initiation. The larger inclusion the higher probability for fatigue crack initiation. [2]

Several mechanisms of crack initiation from inclusions were observed experimentally. In high strength steels and in aluminium alloys the fatigue damage was observed in the early stages of loading by debonding of inclusion from the matrix. After debonding the crack initiates from the newly created notch or void. Another type of crack initiation due to the presence of inclusion in the matrix involves cracking along persistent slip bands. These persistent slip bands are formed as a result of locally increased stress concentration in the inclusion vicinity giving rise to strain concentration or they are terminating at the inclusion.

### **3.2. Surface relief evolution in form of persistent slip markings**

As discussed in previous sections, the most common fatigue crack initiation in cyclically deformed metals is due to roughening of the surface. Therefore, this section will discuss the historical progress in experimental and theoretical studies focused on the surface relief evolution anticipating fatigue crack nucleation.

The surface relief evolution and fatigue crack initiation has been studied for more than hundred years. As mentioned before, the pioneering work of Ewing and Humfrey in year 1903 [3] showed the role of cyclic slip in surface grains in the formation of surface relief. Their most important observation was the identification of fatigue cracks within the rough surface relief. Since their finding, many other investigations were performed on fatigued single- and polycrystalline metals. The studies up to 1972 were reviewed by Thompson and Watsworth [57] and Laird and Duquette [59]. One of the conclusions was that more thorough studies are needed to develop relevant model of fatigue crack initiation. Progress in experimental techniques, mainly in electron microscopy, allowed to present new models of surface relief evolution and fatigue crack initiation. These models are based on the bulk and surface changes of metals during cycling. The most important breakthrough in the identification of the mechanisms in surface relief formation was the discovery of extrusions [71], intrusions [40; 72], persistent slip bands [57], dislocation structure of persistent slip bands [73; 74] and its relation to surface slip markings [75]. Current state and historical progress in experimental and theoretical studies of surface relief leading to fatigue crack initiation is critically reviewed by Man et.al [5]. Based on this study, the cyclic plastic strain localization and slip irreversibility in persistent slip PSBs is generally accepted as the first sign of fatigue damage of cyclically strained crystalline materials.

Experimental studies on fatigued copper, nickel, aluminium single crystals and polycrystalline fcc metals reviewed by Man et. al. [5] reveal some common characteristics:

- (i) The morphology of persistent slip markings in single and polycrystals differs. The single PSMs are typical for both single and polycrystals, whereas macro-PSMs are observed only in single crystals. The individual PSMs consist of tongue-like or ribbon-like extrusions accompanied by intrusions.

- (ii) Vast protrusions roughed by superimposed extrusions and intrusions (macro-PSMs) are found on opposite sides of single crystals. They grow in the direction of primary Burgers vector from the interior to the specimen surface.
- (iii) The height of extrusion in polycrystalline FCC metals is proportional to the corresponding PSB thickness and to the grain size below the surface. Extrusions grow mostly in the direction of the active Burgers vector.
- (iv) The growth rate of extrusions is high at the beginning of the cycling at room temperature and later the rate is stabilized. The growth rate and the profiles of PSMs are temperature dependent.
- (v) In grains which contain no initiated cracks, the extrusions can develop during the whole fatigue life.
- (vi) The inert environment such as vacuum can delay crack nucleation stage, decrease crack growth rate and subsequently significantly increase the fatigue life.

### ***3.2.1. Theoretical models of surface relief formation***

Models of surface relief formation and crack initiation can be divided into 3 groups based on the considered various physical relations: surface-stress-assisted models, vacancy models and micromechanical models. In following, only the most discussed models from each of group will be discussed.

#### (1) Surface-stress-assisted models

##### *Brown and co-workers:*

The first model considering the real dislocation microstructure of PSBs in fatigue crack initiation have been proposed by Antonopoulos and co-workers in 1976 [76]. Taking into account the experimental findings, they concluded that fatigue straining produces dislocation dipoles predominantly of vacancy type . The practical consequence of this statement is that the persistent slip bands into which cyclic deformation concentrates are gradually “fiber-loaded” in tension during later stages of cycling.

Based on their experimental findings they considered that after saturation, cyclic straining produces a steadily increasing density of vacancy dipoles within the area of cumulative plastic deformation. As a consequence, there is a growing difference in vacancy dipole density between the cyclically deformed PSB and undeformed matrix. Later, this difference produces a characteristic set of internal stresses which does not reverse sign during the cycling [76]. They concluded that the elastic misfit might have an effect on crack nucleation in the form of completely relaxed tensile stress/strain by crack initiated at the edge of PSB and growing along the primary slip plane. The growth was driven by the elastic strain energy released.

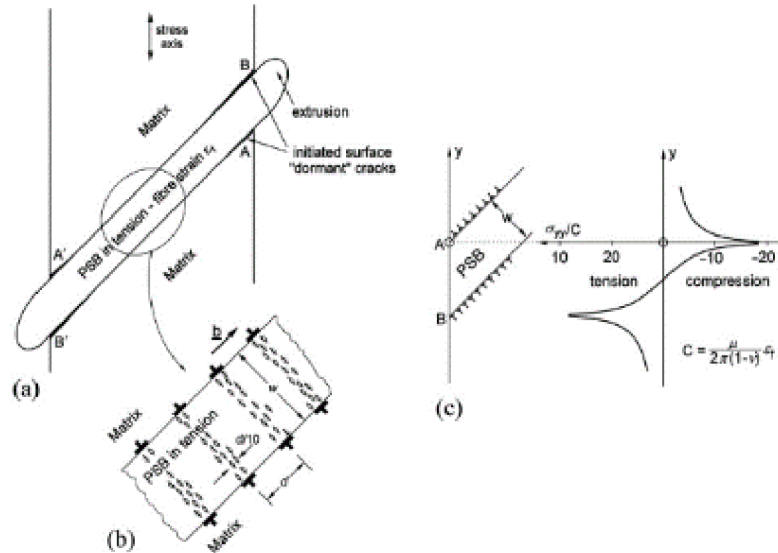


Figure 3.2.1: (a) Schematic of PSB with extrusion. Surface cracks initiated along the PSB-matrix interface as the result of stress singularities at the intersection of PSB with the free surface. (b) Detail of PSB. (c) Surface stresses at the intersection of PSB with the free surface. (Taken from [5])

Later Brown and Ogin [77] slightly modified the previous model. They considered that the sign of the internal stresses changes every half cycle and the crack nucleates as a consequence of the reversing macroscopic internal strains. The highest stresses are close to the surface where the interface between the PSB and matrix meets. Locations A is in compression (crack closing) and location B is in tension (crack opening). These near surface stresses fields with opposite signs give rise to the Stage I fatigue crack initiation by decohesion at point B and B' (see Fig. 3.2.1).

## (2) Vacancy models

### *EGM (Essmann-Gösele-Mughrabi) model:*

The first model considering the role of point defects in terms of producing surface relief during the cyclic loading was EGM (Essmann-Gösele-Mughrabi) model [78]. This model is based on their previous studies [39; 79; 80] of dislocation structure within the PSBs and discuss the irreversibility of dislocation glide within PSBs in f.c.c. metals. It considers two earlier physical processes, which act during the cycling: (i) the production of point defects in fatigued metals in concentrations of  $\sim 10^{-4}$  inferred from changes in microstructure and the recovery of electrical resistivity [81-83] (ii) vacancies (or their agglomerates) produced by repeated glide processes which are responsible for extrusion of the material [57; 65].

The walls of the PSBs are composed of the edge dislocations. Under external loading edge dislocation segments bow out of the walls and traverse the channels producing screw dislocation whose glide along the channels generate edge dislocations along the walls. Thus a continuous flux of screw dislocations along the channels and of edge dislocations across

the walls is maintained, ensuring compatible accommodation of the imposed cyclic strain in the whole volume of the PSBs. [78]

Essmann et. al [80] considered in their model the annihilation of both edge and screw dislocations moving on the primary slip plane. In steady state cyclic deformation conditions the dislocation density within the channels and walls is kept constant by dynamic equilibrium between the multiplication and annihilation of both screw and edge dislocations. Based on the annihilation of dislocations they presented two assumptions for irreversibility and for the randomness of the glide processes [78]:

- (1) The annihilation of narrow edge dislocation dipoles in the walls of the PSBs is associated with the formation of point defects.
- (2) The random of the glide processes leads to a statistical roughening of the surface at a site of emerging PSBs.

Since the dipoles appear to be predominantly of vacancy type, they considered the production and annihilation of vacancies mainly within the walls where the measured edge dislocation density is of two orders of magnitude higher ( $\rho_w = 6 \times 10^{15} \text{ m}^{-2}$ ) compared to that in channels ( $\rho_{ch} = 5 \times 10^{13} \text{ m}^{-2}$ ) [78]. Moreover, Polák's measurements of electrical resistivity [82; 83] shows the increase of point defects concentration and simultaneously the increase in resolved shear stress amplitude. They deduced that the concentration of point defect in the matrix is also negligible since the plastic shear strain amplitude within the PSB is two order of magnitude larger compared to that in the matrix. Therefore, assuming only point defects within the walls, they are repeatedly produced by annihilation of two opposite edge dislocations to reach in the walls saturated concentration,  $C^{sat}$ , previously reported by Polák [83] based on the electrical resistivity measurements.

They estimated the local decrease of edge dislocation density responsible for vacancy concentration,  $\rho_e$ , under conditions of steady state when the density is constant as:

$$\Delta\rho_e = 2\rho_e y_e \frac{\Delta\gamma}{b} \quad (3.2.1)$$

where  $\Delta\gamma$  is shear strain range,  $b$  is modulus of Burgers vector and  $y_e$  is annihilation distance of two edge dislocations with opposite sign.

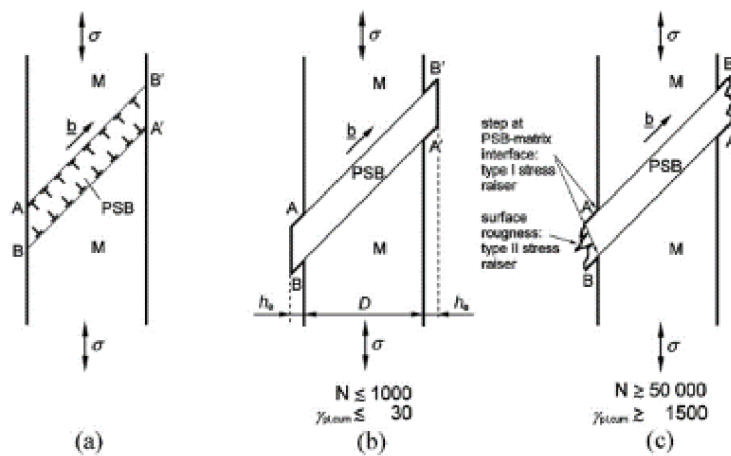


Figure 3.2.2: EGM model of PSB emerging at the surface. (a) Accumulation of PSB-matrix interface dislocations. (b) Growth of static extrusion by emerging of edge dislocations at free surface. (c) Roughening of the static extrusion by random slip. Two types of the stress raisers are marked. (Taken from [5])

The fundamental microscopic model of surface formation based on steady-state cyclic deformation is shown in Fig. 3.2.2.

The specific sequence of slip processes within the PSBs leads to the deposition of so-called ‘interface’ edge dislocations at PSB-matrix interfaces or to the emerging of edge dislocations at the free surface. The arriving edge dislocations disappear at the free surface of PSB and create slip steps. Due to the extra half-plane of interface dislocations directed into the PSB, the PSB is in the state of compression and surrounding matrix is in tension. The applied stress acts additively to the stress arising from the interface dislocations. As the result, the interface dislocations emerge at the surface and PSB lamella becomes elongated in the direction of the active slip vector by

$$e = C_v^{sat} d / \cos\beta \quad (3.2.2)$$

where  $d$  denotes the structural diameter and  $\beta$  the angle between specimen axis and the normal to the active slip plane. Under the action of applied stress the interface dislocations arrive at the free surface at A and A’ during the tensile phase and B and B’ during the compression phase of the loading. [78]

With increasing temperature the vacancies become mobile and diffuse from region of high vacancy concentration in the wall into the matrix (see Fig. 3.2.3). If their diffusivity is sufficiently high, these vacancies will reach sinks in the matrix, such as dislocations, before a high supersaturation of vacancies can be built up. This leads to the mass transfer between matrix and PSB during cycling and to the continual growth of the extrusion. According to their model, most of the mobile point defects will anneal out within the PSB walls. Only those created within a narrow layer of the walls given by the average diffusion length (typically 5-10 nm) will manage to escape into the matrix. [78]

In addition to the rather rapid formation of static extrusions, the slow roughening of static extrusions by random glide processes later in the fatigue life results in the final profile of the extrusions.

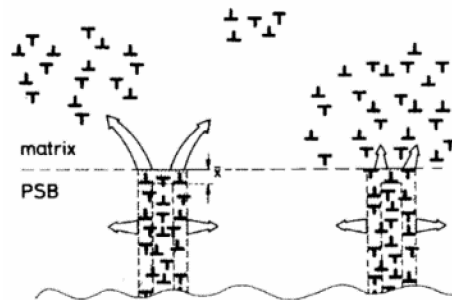


Figure 3.2.3: Flow of vacancies out of dislocation walls. Open arrows denote direction of flux. Vacancies produce in hatched layer of width  $x$  can escape. (Taken from [78])

As the result of extrusion formation two types of stress raisers develop at the surface where PSBs emerge and act as possible nucleation sites for Stage-I shear cracks. (1) the surface steps that form at the PSB-matrix interfaces as a consequence of the elongation of the PSB parallel to the slip vector and (2) the notch-like valleys of the rough surface profile within the PSBs. [78]

*Polák's model:*

In this section the mechanisms leading to the production of surface relief along the PSBs is discussed based on the papers by Polák et al. [84-86].

Thorough review of several observations of fatigue surface relief, the knowledge of dislocation arrangement within the PSB and in the matrix after the fatigue, and knowledge of properties of point defects lead Polák to modify EGM model of generation, migration and annihilation of point defects [84]. Polák modified the EGM model and predicted the formation of both extrusions and intrusions along the PSB, extrusions within the PSB width and intrusion at the interface PSB and matrix. Contrary to EGM model, Polák's model considers the mechanism for point defect generation consisting of mutual annihilation of two opposite edge dislocations moving on adjacent slip planes in the channels. These point defects can be swept by other dislocations or can annihilate in both PSB walls/channels and in the matrix. Other important point was, that intrusions are not the early stage of fatigue cracks, but Stage I fatigue cracks initiate from intrusion tips as the result of stress and strain concentration.

Based on measurements of electrical resistivity [82; 87] he considered the generation and annihilation rate of point defects due to cyclic plastic slip within the PSBs. He concluded that non-equilibrium point defects are steadily generated in PSBs and can migrate out of the PSBs. By considering the flow of atoms in different directions Polák proposed the evolution model of both tongue-like and ribbon-like extrusions [84]:

- (i) In the case of tongue-like extrusion continuous production of vacancies within one region, i.e. in the channel, and their net flow under concentration gradient in the other regions, i.e. in the walls and the matrix, result in the net flow of atoms in the opposite direction. The flow of atoms from the wall into the channels within the PSB results in the accumulation of mass in two directions perpendicular to the direction of flow. In the direction perpendicular to the primary plane the whole PSB can freely expand. Internal stress field is added to the alternating stress field and periodically relaxed. As a result, material is extruded from the crystal along the channels and intruded into the crystal along the walls. Polák observed that the extrusions and intrusions within one PSB vary with some period. He derived that this shift is dependent on the distance  $d$  between the lamellae and the angle  $\alpha$  between the Burgers vector and the intersection of the primary slip plane with the surface. [84]

$$s = \frac{d}{\cos \alpha} \quad (3.2.3)$$

- (ii) In the case of ribbon-like extrusion the flow of atoms is in a direction perpendicular to the primary plane. The extrusions rise along the whole PSB and possibly intrusions develop at the PSB/matrix interface. The height of extrusions can be considerably greater than the depth of intrusions, as vacancies can migrate along the channels into the matrix, annihilating at the edge dislocations at some distance from the PSB/matrix interface. [84]



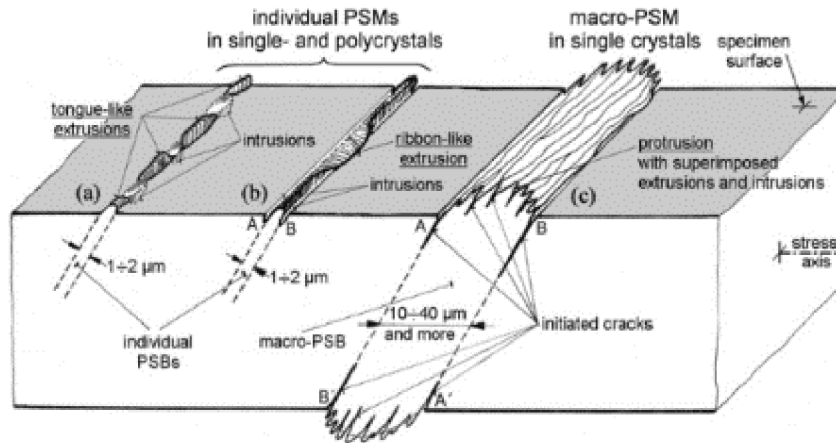


Figure 3.2.4: Schematic diagram of three characteristic forms of PSM morphology in fatigued fcc metals. (a) Tongue-like extrusions alternating with intrusions. (b) Ribbon-like extrusion accompanied by two intrusions. (c) Macro-PSM in single crystal composed of protrusion with superimposed extrusions and intrusions. (Taken from [5])

Both predicted shapes of extrusions and intrusions are shown schematically in Fig 3.2.4 as well as a comparison with macro-PSM emerging at the free surface of single crystal.

Polák and Sauzay [88] calculated the extrusion shape and the growth kinetics provided all vacancies are annihilated at PSB/matrix interface.

Later, Polák extended his model [85; 86] by considering the generation and migration of vacancies and interstitials. Using the knowledge of dislocation arrangement within PSB and motion of dislocation he analytically predicted the production and annihilation rates of point defects leading to surface relief formation called persistent slip markings (PSMs).

The distribution of dislocations within PSB and their mutual annihilation is schematically shown in Fig 3.2.5. The lamella of PSB is composed of alternating dislocation rich areas (walls) and dislocation poor areas (channels). Walls consist of immobile edge dipoles and multipoles. He considers that the edge dipoles act as the Frank-Read sources and under the external loading the resulting plastic strain is carried by formation of dislocation loops from the edge dipoles in the walls and their expansion into the channels. These dislocation loops consist of edge and screw segments. The edge segments of two dislocation loops with opposite Burgers vectors,  $\mathbf{b}$ , can annihilate within the channel by producing row of point defects composed of vacancies or interstitials. [85]

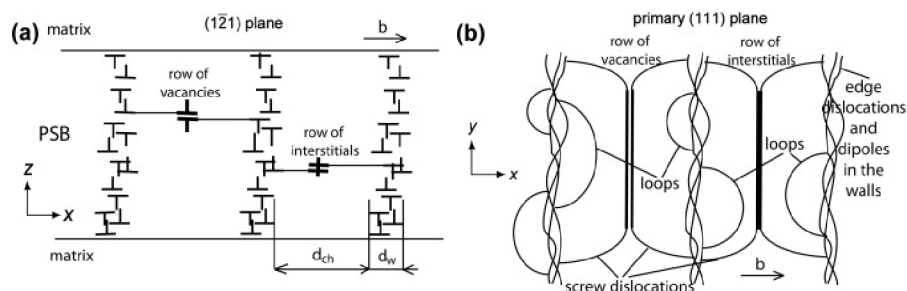


Figure 3.2.5: Schematics of dislocation interactions and formation of point defects in a PSB, (a) projection in  $(\bar{1}21)$  plane and (b) projection in primary  $(111)$  slip plane. (Taken from [85])

According to Polák's model these rows of point defects have the major impact on the mass redistribution between the PSB lamella and the matrix. Later only the generation and annihilation of vacancy-type point defects have been considered as the main mechanism of mass transfer. In Fig. 3.2.6 the point defects within the PSB are shown along with the direction of vacancy transfer leading to growth of ribbon-like extrusion accompanied by the intrusions.

As was mentioned before, the relaxation of internal stresses induced within PSB and at the PSB-matrix interface by mass redistribution can proceed only in the direction of active Burgers vector where it represents mean stress. Since the internal stress is compressive it is equivalent to external tensile mean stress. Multiple repetitions of the cycle with the internal compressive mean stress result in cyclic creep in the PSB lamella and in the growth of an extrusion within the whole width of the PSB. Contrary to that at the PSB/matrix interface internal tensile mean stress induces depression of the material layer and growth of an intrusion. To reach critical value of the mean stress  $\Delta\sigma_{M/PSM}$  necessary for the activation of the first layer, Polák considers several cycles have to be applied before cyclic creep in PSB lamella starts. By increasing number of cycles the layers situated far from the interface reach the critical value and can be activated. As a result, intrusion has a specific conical shape and its growth starts with some delay compared to growth of extrusion. [86]

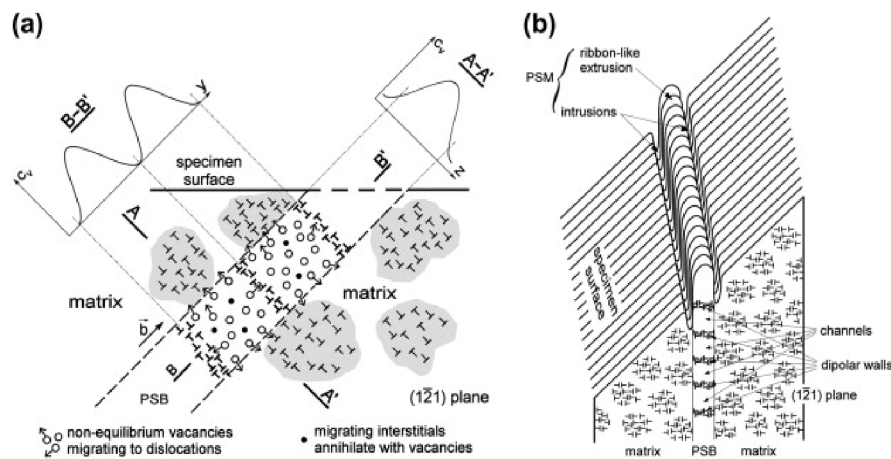


Figure 3.2.6: Formation of surface relief in the temperature interval in which both interstitials and vacancies are mobile: (a) schematics of ladder-like dislocation arrangement in a PSB and vacancy migration and annihilation at dislocations and (b) the shape of predicted surface relief at emerging PSB. (Taken from [85])

Polák and Man [85] extended the model by quantitative predictions of the point defects concentration, annihilation and diffusion rates. The probability of production of a dipole of vacancies of unit height responsible for internal mean stresses in a channel within a half-cycle  $P_{pj}$  is equal to the probability that two edge dislocations on neighbor slip planes are simultaneously emitted from the opposite walls and meet in the channel. The production rate of point defect of vacancy type in a cycle,  $p_v$ , depends on the local plastic strain amplitude. Vacancies are steadily produced in the whole volume of the PSB with the production rate  $p_v$  and simultaneously are annihilated by sweeping dislocations.

By considering that average plastic shear strain amplitude within the PSB is  $\gamma_p$  the production rate of vacancies in one cycle can be expressed as follows [85]

$$p_v = \left( \frac{dc_j}{dN} \right) = 2P_{pv} \frac{b}{d_{ch}} = 2s_v \frac{b}{d_{ch}} \gamma_p^2. \quad (3.2.4)$$

where  $b$  is the modulus of the Burgers vector and  $d_{ch}$  is the average distance between the PSB walls.

Considering production, annihilation and migration of vacancies from the channels to the matrix the steady vacancy concentration  $c_j$  is a function of the distance  $x$  (distance from the center of PSB). It can be obtained by solving appropriate diffusion equation

$$\frac{d^2 c_v}{dx^2} - \frac{A}{\tau D_v} c_v + \frac{p_v}{\tau D_v} = 0 \quad \text{for } x \leq w/2, \quad (3.2.5)$$

where  $D_v$  is the diffusion coefficient of vacancies,  $A$  is the annihilation coefficient expressed as the fraction of vacancies swept by mobile dislocations during one cycle and  $\tau$  is the cycle period.

Knowing the steady profile of vacancies in the PSB and the adjoining matrix the growth rate of the extrusion and intrusion can be evaluated. The rate of volume change due to migration and annihilation of vacancies is equal to the difference of the vacancy flux in the volume and out of the volume. Vacancy flux,  $J_v$ , is expressed as

$$J_v = -D_v \frac{\partial c_v}{\partial x}. \quad (3.2.6)$$

Since absorption of each vacancy correspond to arrival or removal of one atom from the lattice, the additional internal compression stress or the internal tensile stress is produced during one cycle in each sheet of the thickness  $dx$ . Complete plastic relaxation of this mean stress results in the adding or removal of atoms on the surface of the grain. The change of the height  $h$  on the surface in the direction of the Burgers vector during one cycle at a distance  $x$  from the center of the PSB is expressed as

$$\frac{dh}{dN} = \tau l \frac{dJ_v}{dx}, \quad (3.2.7)$$

where  $l$  is the PSB length below the surface.

Polák and Man [85] predicted the shape of the PSM considering the annihilation of the point defects at the PSB/matrix interface. One half of the symmetrical PSM profile is shown in Fig. 3.2.7.

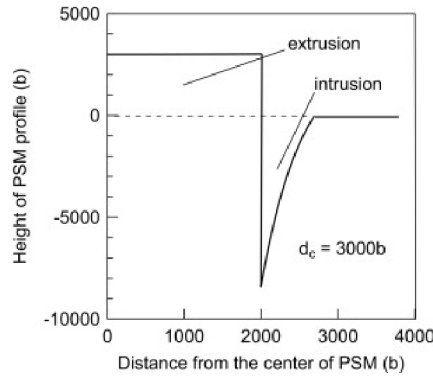


Figure 3.2.7: Height of the half of the symmetric PSM profile consisting of the extrusion and intrusion in fatigued copper. All dimensions are in units of the Burgers vector modulus  $b$ . (Taken from [85])

### (3) Micromechanical models

#### *Tanaka and Mura model:*

In Tanaka and Mura model [89], they considered the polycrystalline material loaded by uniaxial stress. This type of loading implies the maximum shear stress on the plane under  $45^\circ$  inclination with the stress axis. Fig. 3.2.8a shows the section through the surface grain perpendicular to the specimen surface. The slip plane is perpendicular to the cross section and the slip direction is in it. During the loading the dislocations are generated at the surface and move deeper into the grain. In their model, the dislocations formed by previous forward loading are irreversible and the reverse plastic flow is taken by the motion of dislocation with opposite sign on the other slip plane which is located very close to the previous one [89].

The dislocation pileups made under reverse loading are on layer II. The pileups of negative dislocations on layer II causes a positive back stress on layer I. This back stress enhances the pileup of positive dislocations during the next stage of forward loading. In this way, the accumulation of dislocation dipoles is amplified with the number of cycles and extrusion, intrusion or their combination is monotonically built up. [89]

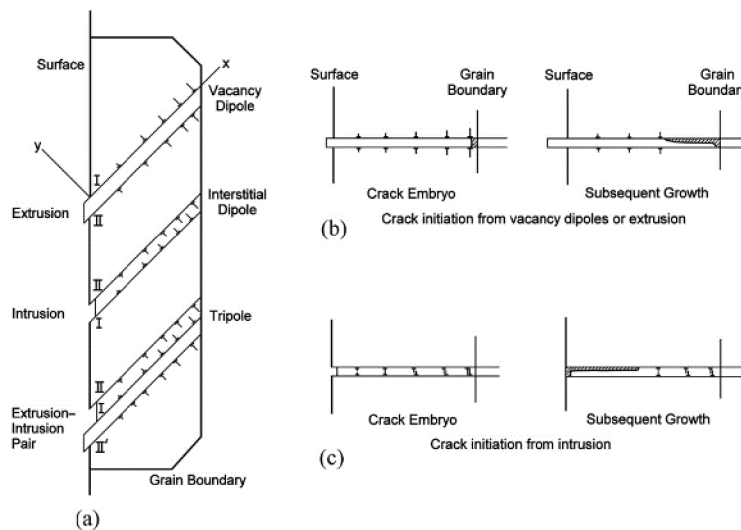


*Figure 3.2.8: Schema of plane-like layer with accumulated dislocation pile-ups at the GB. The dislocation pile-ups on layer I and II are under tension and compression, respectively. (b) Crack initiation from vacancy dipoles or extrusion. (c) crack initiation from intrusion. (Taken from [5])*

Fig. 3.2.8b illustrates two types of initiation and growth of fatigue cracks. Growing tensile stress built up with the number of cycles between two layers at the top of piled-up of vacancy dipoles becomes large enough to suddenly create the nucleus of a crack when the fracture criterion is satisfied. In the case of extrusions, embryonic cracks are formed inside the material at the grain boundary of the surface grain where the vacancy dipoles are piled-up. The formation of an intrusion causes stress concentration under the applied stress and

it can be also regarded as the crack embryo. The following growth of a crack embryo is expected to take place along the slip band. [5]

### 3.3. Stage I fatigue crack growth

The nucleation, as well as the whole fatigue process, is controlled by the cyclic-plastic deformation. Therefore, it can be expected that cracks nucleate at positions where the cyclic-plastic deformation is higher than the average, in other words, in places of plastic-strain concentration. [30]

Many observations of Stage I fatigue crack initiation and growth are related to the fatigue induced surface roughening. As discussed earlier it is connected with the evolution of internal dislocation structure, e.g. ladder-like structure, within the PSBs. One of the first direct observations of crack initiation and its early growth along PSB was performed in polycrystalline Cu by Katagiri et al. [90] as shown in Fig. 3.3.1.

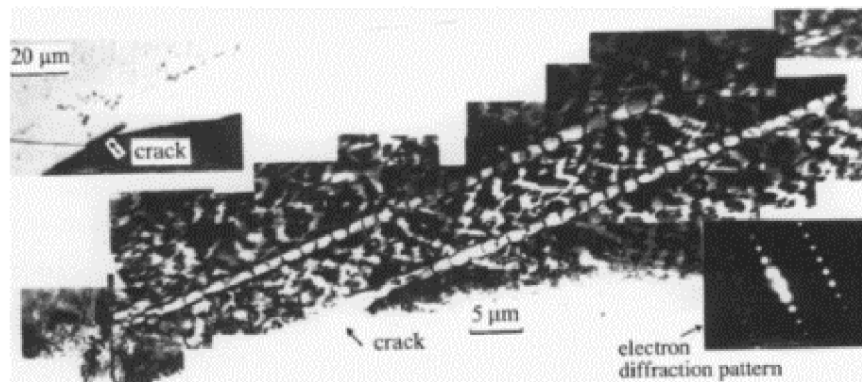


*Figure 3.3.1: Fatigue crack along the ladder structure of a PSB in a fatigued polycrystalline copper. (Taken from [90])*

Experimental studies performed in vacuum show that the slip-unslip mechanism can be reversible and new surface can be rewelded. The slipping-unslipping mechanism is enhanced by the environment which leads to the formation of new surface, i.e. primary crack. In the case of a row of semielliptic intrusions along the PSM subjected to cyclic shear strain the material between intrusions shears first, the intrusions are connected, and a shallow surface crack is initiated. Both Mode II and III straining in the immediate vicinity of the intrusion contribute to gradual decohesion and crack initiation (see Fig. 3.3.2). As soon as the rate of new surface formation due to the stress concentration becomes higher than that due to intrusion growth the surface defect can be considered as a surface crack.

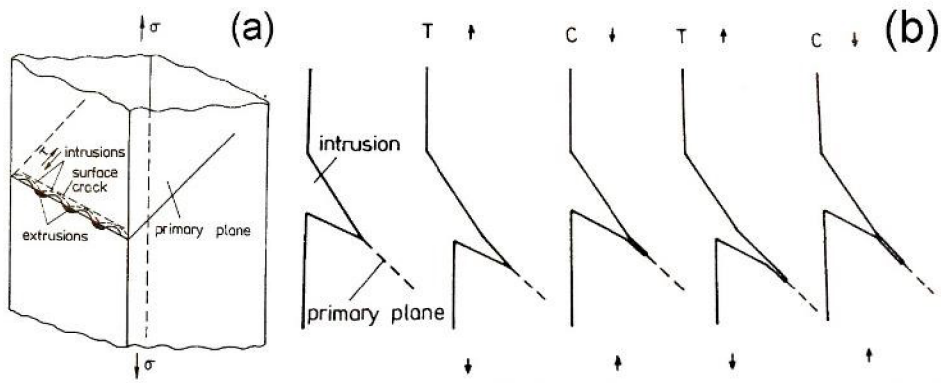


Figure 3.3.2: Schematics of environment assisted crack initiation. (a) Initiation of shallow surface crack from the intrusions. (b) Crack initiation and early growth by irreversible slip-unslip at the tip of the intrusion. (Taken from [2])

The environment plays an important role in crack initiation rates due to slip irreversibility. Fig. 3.3.3 shows schematically the influence of environment in a metal cycled in air and in vacuum. Single slip during the tensile/compressive loading cycle produces slip steps at the surface. Additionally, the slip steps forming during the tensile portion of a fatigue cycle in laboratory air or in a chemically aggressive medium suffer to chemisorption of the embrittling species (oxygen, hydrogen) and formation of an oxide layer on the freshly formed slip step. It makes the reverse slip difficult on the same slip plane upon a load reversal. [25]

As documented many times, the fatigue crack initiation is related to the basic properties of the material like chemical composition, crystalline structure, degree of strain localization and others but also to grain size and straining amplitude. Numerous experimental studies focused on the structural materials without internal defects reported earlier show that primary cracks initiate in the PSMs. Sharp intrusions represent an effective stress concentration as the radius at the tip of the intrusion is very small. In the case of structural materials, the annealing twins [4; 66; 91] and grain misorientation can increase the stress state in the vicinity of the grain and twin boundaries and PSMs, from which the fatigue crack can initiate. The number of initiated Stage I cracks increases with number of cycles and stress or plastic strain amplitude as documented earlier by Polák [92].

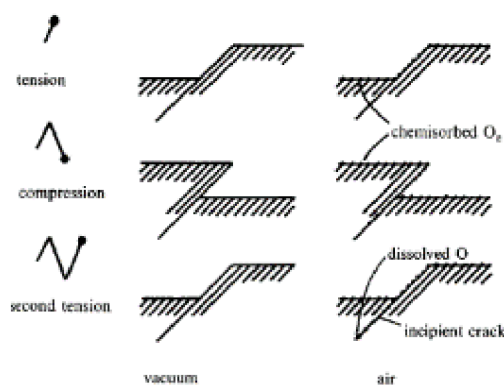


Figure 3.3.3: Model of fatigue crack nucleation near a free surface by the synergistic effect of single slip and environmental interactions. (Taken from [25])

The issue of the crack initiation due to the PSM formation at the specimen surface is studied using various modern techniques since the mechanism is still not clear. As discussed earlier the basic mechanisms describing the PSM formation and crack initiation was investigated mainly on the simple materials such as the copper. Recently the thorough study of Man and coworkers performed on 316L austenitic steel [93; 94] showed the growth rate of a PSM during the cycling and the evolution of its shape in the form of extrusions and intrusions. They studied the surface evolution and crack initiation using AFM and the results have been verified by FIB cutting, since AFM does not provide the correct information about the profile due to the shape of the AFM tip. The internal microstructure studied using the electron channeling contrast imaging (ECCI) revealed the localization of the cyclic plastic strain into the PSBs with the irregular ladder-like dislocation structure along the primary slip planes documented by the EBSD. Their analysis supports the point-defect model of fatigue profile evolution and the crack initiation in the tip of the intrusion. Similar observations were done also on the martensitic steel [95].

Roach et al. [91] found on fatigued 316L steel also the preferential localization of the crack initiation in twin boundary (TB) along which the PSB has been developed. Moreover, according to study of Vogt and Mu et al. [36; 96] the crack initiation along the PSMs can be promoted by the enhanced nitrogen content in the material. Considering all results about the PSM formation and the crack initiation, some authors [97] started modelling dislocation motion with the aim to simulate the formation of PSMs.

### 3.4. Effect of high temperature

Fatigue crack initiation in the materials used at elevated temperatures is highly affected by the factors dependent on service temperature, stress amplitude and environmental effects. Mechanisms contributing to the formation of microscopic damage can be outlined as follows:

- a) Crack nucleation due to cyclic slip
- b) Cavity formation at the grain boundaries
- c) Nucleation and evolution of defects as a result of inclusions and precipitates
- d) Oxidation and corrosion

The oxidation is one of the most important damaging mechanisms taking place during the high temperature loading of the metals in the environment. The oxidation rate in the case of metals where the surface oxide layer represents the protective surface layer against further diffusion of oxygen ions into the metal can be evaluated using the parabolic equation

$$m^2 = k t , \quad (3.4.1)$$

where  $m$  is the oxide scale thickness,  $k$  is the parabolic constant and  $t$  is the exposure time.

The intermediate steps between the “initial state” in the form of pure metal and “final state” in the form of oxide require external energy input represented by the free energy of activation  $\Delta G_{activ}$ . As the temperature of the system is increased, more thermal energy is available to overcome the barrier, and therefore the oxidation rate increases. The rate of the oxidation is given by the exponential dependence known as Arrhenius equation

$$k = k_1 \exp(-\Delta G_{activ}/RT) , \quad (3.4.2)$$

where  $k$  is the rate constant,  $k_1$  is constant,  $T$  is temperature and  $R$  is gas constant. The oxidation rate depends also on the partial pressure of oxygen. [98]

Based on the mentioned effects influencing the oxidation the neutral or slightly corrosive environment such as air is with increasing temperature converted into highly aggressive environment. The degree of aggressiveness depends considerably on the material structure and chemistry.

In simple metals, oxidation is appreciable at temperature above 300 °C. Low alloy heat resistant steels oxidize above 350 °C, but since oxidation is not selective, the effect on crack initiation is small in most cases. The actual mechanisms can be very complex, such as the depletion of one type of atoms due to oxidation, internal oxidation or depletion of the protective oxide scale. [2]

The oxygen molecules are absorbed preferentially on the metal surface, since the forces between the individual atoms at the surface can differ from those in the bulk of the material due to the failed symmetry of the crystal structure. The diffusivity of oxygen atoms increases in the low-energy sites on the metal surface. It means that during high temperature fatigue in harsh environment near surface effect is important. Oxidation has a high impact on the crack initiation and growth of fatigue cracks. The affinity of the O<sub>2</sub> with Fe and Cr is higher than of the other elements. They preferably create surface oxide layers of an approximately uniform thickness [18]. Therefore, the environment effect in the form of oxidation and the increased element diffusion at a high temperature can significantly influence the tensile and fatigue properties of austenitic stainless steels. The high temperature leads to the higher diffusion rates of elements such as Cr, Ni, N, C... [99]. High diffusion rate of carbon at elevated temperatures causes carbide formation. Mainly M<sub>23</sub>C<sub>6</sub> type carbides are present in structure of the 300 series austenitic stainless steels [12]. These carbides are composed mostly of Cr. The precipitation occurs very rapidly during the early stages of loading (about half an hour at 750 °C) along the grain boundaries and consequently reduces the resistance to intergranular corrosion [12] due to the diminishing of the Cr<sub>2</sub>O<sub>3</sub> protective oxide layer formation. The Cr-depleted zone arises in the vicinity of chromium carbides. According to Marshal [99] the minimum Cr content to guarantee the corrosion resistance is 12% in solid solution of the alloy matrix. Moreover, the GBs consist of a high density of dislocations which under the external stress can increase the inner oxidation rate along the GB [100; 101] without any notable crack.

The most plausible crack nucleation mechanism during the interaction of environment and cyclic straining is the repeated oxide layer rupture model proposed by Coffin [102]. Further oxidation of the freshly exposed metal can be accelerated by the oxidation of carbides, formation of corrosion pits [103] or oxide intrusions along the grain boundaries and within the grains [99]. The early cracks propagate preferentially in the intergranular manner.

#### **4. Growth of short fatigue cracks in ductile metals**

Since the initiation of cracks appears in the early stages of fatigue life the growth of cracks represents in most cases the period determining the fatigue life of the structures. The important breakthrough in the study of fatigue crack growth was done by Forsyth [104; 105] who recognized two stages of fatigue crack growth denoted as Stage I and Stage II. Simultaneously, there was a great effort to predict the kinetics of the Stage II crack growth closely connected with the fail-safe design philosophy. By introducing the fracture mechanics the crack growth kinetics was analysed in several materials using the linear



elastic fracture mechanics. Nevertheless, linear fracture mechanics does not work for all cracks and all loading conditions [2; 25; 106; 107]. The crack growth rates significantly dependent on the nature of fatigue cracks and their length, mainly in the case of natural short cracks. This led Suresh and Ritchie to classify short cracks according to their character and “smallness”.

According to Suresh and Ritchie [108] short cracks can be classified into four groups based on their size scale:

- (a) *Microstructurally small cracks* - fatigue cracks for which the crack size is comparable to the scale of the characteristic microstructural dimension such as the grain size.
- (b) *Mechanically small cracks* - small fatigue cracks in smooth specimens for which the near-tip plasticity is comparable to the crack size, or cracks which are engulfed by the plastic strain field of a notch.
- (c) *Physically small cracks* - fatigue cracks which are significantly larger than the characteristic microstructural dimension and the scale of local plasticity. Their length is typically smaller than a millimeter or two.
- (d) *Chemically small cracks* - fatigue cracks which are nominally amenable to linear elastic fracture mechanic analyses but exhibit apparent anomalies in propagation rates below a certain crack size as a consequence of the dependence of environmental stress corrosion fatigue effects on crack dimensions.

Later the elasto-plastic fracture mechanics [109] was introduced to describe the crack growth rates under elasto-plastic straining. It was implemented also to the description of the short cracks growth [110].

Since the evaluation of the actual crack growth rate in the bulk of the material is difficult using conventional methods some approximations are considered in calculations. Based on the observations of Polák and Obrtlík [111] using heat-tinting method that the extension of the crack front in the bulk is approximately equal to the half of the surface crack extension it was concluded that crack has approximately semi-circular shape (see Fig. 4.1).

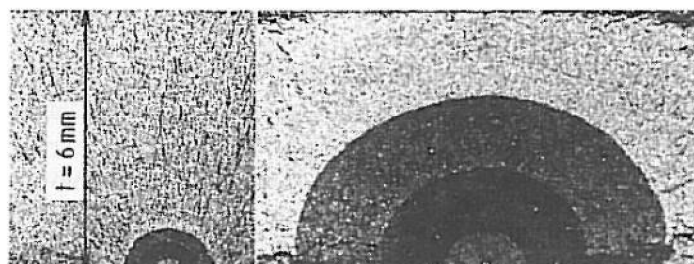


Figure 4.1: Crack fronts of several crack lengths in low carbon steel. (Taken from [2])

Irwin studied the influence of loading path on the behaviour of cracks [112]. Based on his observations he introduced three different loading modes: Mode I (opening mode under tensile loading), Mode II (sliding mode under shear loading in the crack growth direction) and Mode III (shearing mode under shear loading perpendicular to the crack growth

direction). The modes are divided according to the relative position of the vector of loading force and the crack plane in Fig 4.2.

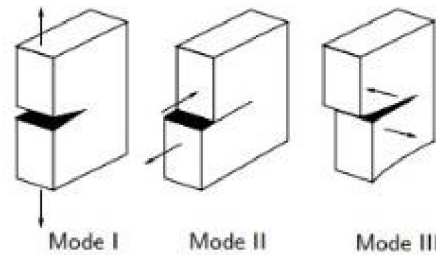


Figure 4.2: Three standard loading modes of cracks. (Taken from [2])

In following sections, the early fatigue damage mechanisms are discussed in detail based on recent monographs on fatigue [2; 25].

## 4.1. Crack growth mechanisms

### 4.1.1. Effects influencing the crack growth

The initiation period is supposed to be completed when microcrack growth no longer depends on the material surface conditions. As long as the microcrack is within one grain, the microcrack is obviously present in an elastically anisotropic material with a crystalline structure and number of different slip systems. The microcracks grow under the cyclic shear. The microcrack contributes to an inhomogeneous stress distribution on a microlevel, with a stress concentration at the tip of the microcrack. As a result, more than one slip systems may be activated. Moreover, if the crack is growing in some adjacent grains, the constraint on slip displacements will increase due to the presence of the neighbouring grains. Similarly, it will become increasingly difficult to accommodate the slip displacement by slip on one slip plane only. It should occur on more slip planes. The microcrack growth direction will then deviate from the initial slip band orientation. In general, there is a tendency to grow perpendicular to the loading direction (see Fig. 4.1.1). [25]

Because microcracks grow close to the surface under the cyclic shear and depend on cyclic plasticity, some structural barriers can imply a threshold for their growth. Such a threshold can be grain boundaries. Two grains with a significant mutual misorientation may decrease or stop the crack growth rate [113]. Later when the crack reaches the sufficient length and grows under the plane strain conditions its growth rate is steady or increasing. By increasing its length the crack front have a tendency to extend like in as a continuum and become approximately semi-elliptic.

In general, the aspects influencing the growth of cracks can be divided into several groups as follows:

- Crystallographic nature of the material
- Surface effects
- Crack growth barriers

- Number of crack nuclei
- Macrocrack growth and striations
- Environmental effects

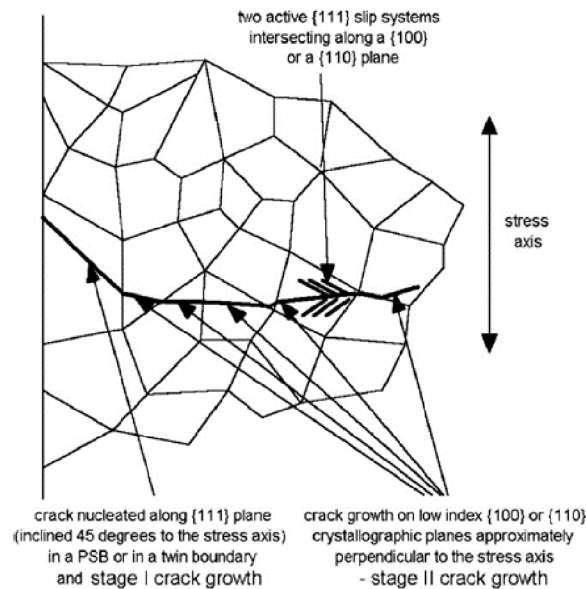


Figure 4.1.1: Schematics of the short crack growth in a polycrystal. (Taken from [31])

Based on the nature of the initial cracks growing along the preferential slip planes there is a crystallographic dependence on their mechanistic behaviour. These aspects can be divided as follows:

- Type of crystal lattice, elastic anisotropy
- Slip systems
- Grain size and shape
- Texture of the material structure - grain orientation

These material characteristics are closely related to the fatigue crack initiation and Stage I crack growth. As a result of the elastic anisotropy, the stress distribution from grain to grain is not homogeneous. The inhomogeneity was found to be larger for steels revealing the elastic anisotropy changes by factor 2.15 compare to Al revealing the elastic anisotropy changes by factor 1.20 [25]. It means that the stress level ahead of the crack tip in each grain in the case of steels can significantly vary.

The number of activated slip systems can affect the growth path as well. If the number of easily activated slip systems is limited, microcracks persist much longer in growing along crystallographic directions. [106]

Another type of fatigue crack growth barrier in the form of inclusions or precipitates could be considered. Nevertheless, if their size is small compared to the size of microcracks they can imply a local effect on cyclic slip and crack growth. As a result, they do not represent a permanent threshold for crack growth and crack can grow around the inclusion.

It is known that the increasing stress level applied to the specimen increases the number of crack nuclei. This period of crack initiation takes appreciable part of the fatigue life. Schijve

[114] studied the average number of crack nuclei in relation to the S-N curve. Based on his results the single macrocrack grows as the consequence of growth of individual small cracks linked into one. The number of visible crack nuclei on the fracture surface decreases with decreasing stress level or elasto-plastic strain amplitude. The length of individual microcracks depends less on the microstructural threshold as the stress levels increases. As a result, more microcracks can develop successfully to a large size crack. [106]

It was pointed out also by Stolarz [115] that the growth of Stage I cracks is influenced by their mutual coalescence. Their growth into the neighbour grains is difficult without the linkage with other shallow crack.

#### 4.1.2. Crack growth path

Fatigue cracks in almost all ductile materials are growing in the trans-granular manner, i.e. through the grains. They follow the grain boundaries only occasionally, contrary to the stress corrosion cracks and creep failure during high temperature fatigue.

The early shallow cracks grow under the plastic deformation and the growth occurs predominantly by single slip in the slip system with the highest Schmid factor. The deviation of the crack path from Stage I to Stage II was studied on copper single crystals [116]. Crystallographic orientation has an impact on the change of the crack growth path. The higher ratio  $Q$  of the Schmid factor of the second highly stress slip system to that of the primary system the shorter is the crack length corresponding to the Stage I crack path. In the crack growth with high stress intensity range, the plastic zone at the crack tip encompasses many grains. The crack growth process involves simultaneous or alternating growth along two slip systems (see Fig. 4.1.2). This duplex slip mechanism, termed as Stage II by Forsyth [117], results in a planar (mode I) crack path normal to the loading axis. [25]

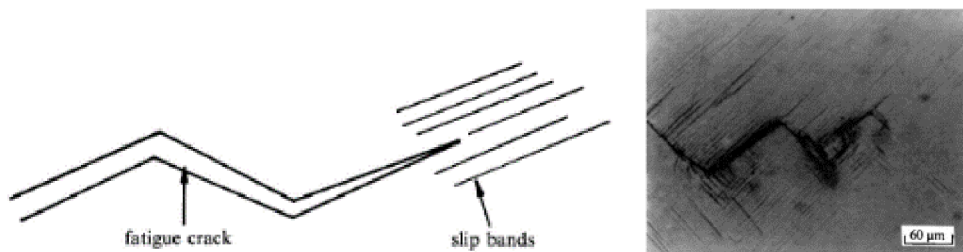


Figure 4.1.2: Schematic of stage II fatigue crack growth and an example in a single crystal of Ni-based superalloy. (Taken from [25])

Similar observations were made by Blochwitz et al. [118-120] who found that short cracks studied in 316L steel followed on the surface mostly transcrystalline path (60%).

Later during the Stage II growth the crack is opened by crack tip plastic strain inducing the blunting of the crack root. The radius of the crack tip was found to be about  $0.4 \mu\text{m}$ . Several mechanisms are introduced to predict the blunting of the crack tip (see Fig. 4.1.3). During cyclic loading the plastic strain will cause crack extension implying decohesion of the material. Typical surface features in the form of ridges are created on the fatigue fracture surface and are called striations. It is considered that each pair of striations corresponds to

one fatigue cycle in Paris regime of fatigue crack growth [121]. The striations are typical for pure and ductile metals. The research of Blochwitz et al. [118-120] done on 316L steel shows the highest crack growth rates for segments following  $\{100\}$  and  $\{110\}$  paths. Their findings support the model of striation formation proposed by Neumann [122; 123].

The formation of the striations was found to be dependent on the environmental effects. It was first published by Meyn [124] that no striations were apparent on the fracture surface of samples cycled in vacuum. Later Pelloux [125] discussed that alternating shear process is reversible unless an oxide film is formed on the slip steps created at the crack tip. The oxidation of the crack surface increases the crack growth rates by several orders of magnitude compared to that measured in vacuum. The rewelding processes at the crack tip [126] cannot be realized. In addition to that the cycling in vacuum promotes crack branching and causes the longer and poorly organised crack front [127].

The final fracture of the samples (long cracks) is of a quasi-static manner. It means that the sample is not anymore able to carry the maximum load of the cycle and the sample finally breaks by ductile fracture represented by dimples at the fracture surface.

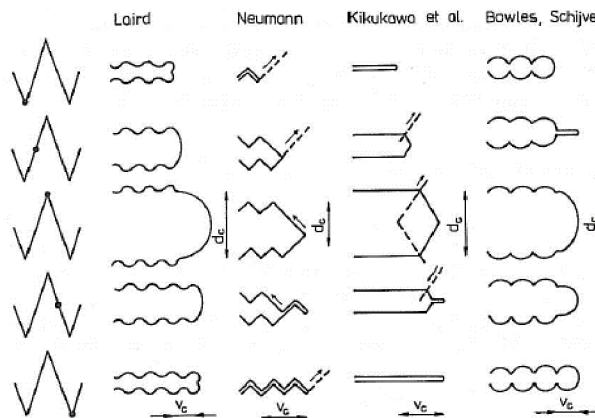


Figure 4.1.3: Proposed mechanisms of Stage II crack advance. (Taken from [2])

## 4.2. Crack growth kinetics

As discussed earlier in Chapter 2 the growth of fatigue cracks represents the major part of the total fatigue life of cyclically loaded components. The characterization of long fatigue cracks is usually based on the fracture mechanics. The propagation of small fatigue cracks is significant since it can represent appreciable fraction of the fatigue life. It is important for designing of engineering components such as turbine discs or blades. It is known that crack growth rates of small cracks and long cracks under the same driving force can differ significantly (see Fig. 4.2.1). It is due to the large scale yielding ahead of the crack tip in the case of small cracks. This can lead to the dangerous overestimation of safety life of components.

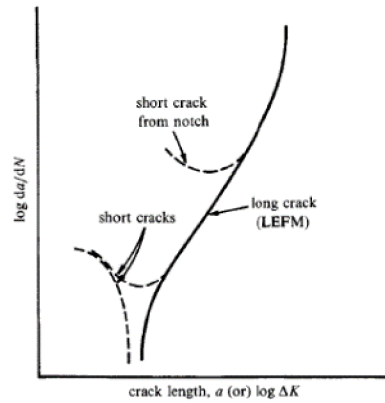


Figure 4.2.1: A schematics of the typical fatigue crack growth behaviour of long and short cracks at constant values of imposed cyclic range and load ratio. (Taken from [25])

It was shown also by Hudak et al. [128] on nickel-based superalloy that the estimation of fatigue life based on linear elastic fracture mechanics can significantly differ from that directly measured. The results in Fig. 4.2.2 shows that the LEFM approach is usable only for the cracks with the initial crack size larger than 0.3 mm even if the small-scale yielding conditions prevail in the case of smaller initial crack sizes (material defects). It is due to the different growth character i.e. zig-zag crack path and crack closure in the case of small cracks compared to long cracks.

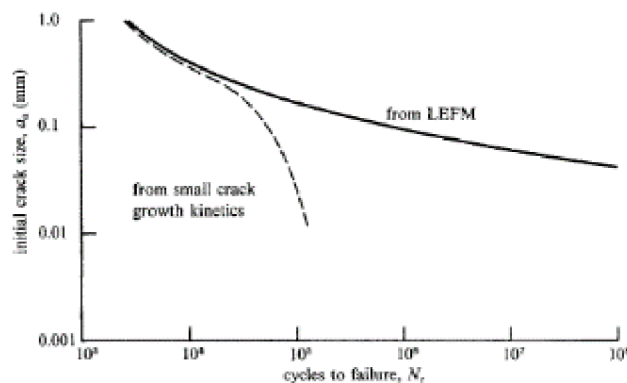


Figure 4.2.2: The plot shows the number of fatigue cycles to failure estimated by LEFM and small crack growth kinetics as the function of the initial crack size. (Taken from [128])

The highest attention to the growth of short fatigue cracks under the low cycle fatigue conditions was paid in the 1990s. It was observed by Gao et al. [129] that the important role in crack growth under high strain amplitude loading plays the crack coalescence. According to Vašek et al. [130] the increasing applied plastic strain amplitude increases the number of crack nuclei. The density of the initiated cracks (the size less than the grain size) increases almost up to the half of the fatigue life. Their density was observed to be stable up to the fracture for low plastic strain amplitudes. In the case of high plastic strain amplitude their density slightly decreases after reaching the maximum occurrence implying their mutual coalescence.

Based on the experiments showing the short crack behaviour under different levels of elasto-plastic loading the kinetics of short cracks growth was studied more intensively [130-134]. Using fractographic observations it was found that the final fracture of the samples or components is due to the propagation of one dominant crack. It means that the fatigue life is dependent on the growth of the actual longest crack in the material. This crack is called “*equivalent crack*”. It is the longest measured crack at a given number of cycles.

Based on the previous observations the crack growth rate and the analysis of the residual fatigue life can be estimated in terms of two approaches. The first one is the growth under the small scale yielding (LEFM -  $\Delta K$ ) and the second one is based on large scale yielding (EPFM -  $J$  integral,  $\varepsilon_{ap}$ ). Local inelastic yielding ahead of the crack produces the plastic zone. The size and the shape of the plastic zone depend on the mode of applied loading, the geometry of the body, and whether plane stress or plane strain is applicable. The early calculations of Rice [109] and Irwin [135] indicated that the size of the plastic zone is proportional to  $(K_I/\sigma_y)^2$ . Calculations using analytical estimates or finite element method shows that in plain strain condition the maximum extend of the plastic zone is inclined at an angle about  $70^\circ$  with the plane of the crack path. The individual approaches are discussed below.

#### 4.2.1. Small scale yielding approach ( $\Delta K$ )

In the case that the crack tip is small compared with the specimen dimensions and the crack-tip plastic zone is small compared with the length of the crack the linear elasticity theory can be used. Therefore, the linear elastic fracture mechanics approach is widely used mainly for the characterization of the long cracks. Irwin [136] quantified the near-tip fields for crack in terms of the stress intensity factor  $K_I$  (I represents the stress intensity factor for Mode I crack growth) as follows:

$$\sigma_{ij} = \frac{K_I}{\sqrt{2\pi r}} f_{ij,I}(\Theta) , \quad (4.2.1)$$

where  $r$  and  $\Theta$  are polar coordinates, and  $f_{ij,I}(\Theta)$  are trigonometric functions which depend on the  $ij$  components of stress tensor. The stress intensity factor  $K_I$  is a configuration independent parameter, which uniquely characterises the intensity of the local elastic stress field ahead of the crack. For a crack having the length  $a$  growing under the tensile mode with tensile stress  $\sigma$  the stress intensity factor can be described using function

$$K_I = \sigma\sqrt{\pi a} F(a, w) , \quad (4.2.2)$$

where the function  $F(a, w)$  depends on the crack length  $a$  and characteristic dimension  $w$  of a body in the direction of the crack. [2]

For the case of small scale yielding the size of the plastic zone ahead of the crack tip is defined by the area in which the stress is larger than the cyclic yield stress. Then the  $K_I$  is a parameter characterising the stress field around the crack if the extend of local plasticity is small compared with the extent of the elastic stress field which is itself small compared to the overall dimensions of the body. Several experiments done on the estimation of the crack growth rate as a function of the driving force led Paris and Erdogan [137] to correlate the crack growth rate of long cracks with the stress intensity range (see Fig. 4.2.3),  $\Delta K$ , as follows:

$$\frac{da}{dN} = C \left( \frac{\Delta K}{\Delta K_0} \right)^m \quad (\Delta K_{th} < \Delta K < K_{Ic}), \quad (4.2.3)$$

where  $C$  and  $m$  are experimentally determined material constants.  $\Delta K_0$  is a constant equal to 1 MPa/m<sup>2</sup> in order to simplify the units of  $C$  and  $m$  constants.

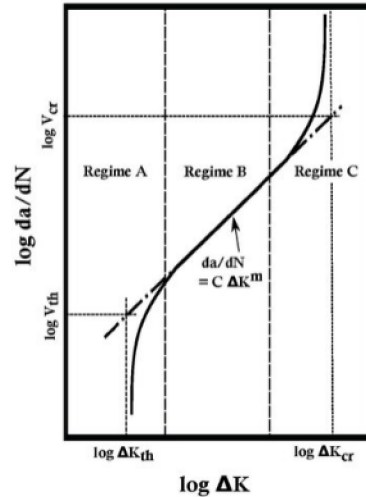


Figure 4.2.3: Crack growth rate of a long crack as a function of the stress intensity range. (Taken from [25])

As mentioned earlier, the growth of short cracks in the case of ductile materials takes place under the large cyclic plastic strain. Therefore, the correlation of crack growth rate with  $\Delta K$  parameter, representing mainly the elastic driving force ahead of the crack tip, is not sufficient.

#### 4.2.2. Large scale yielding approach ( $J$ -integral)

In the case of elasto-plastic cyclic loading a more general parameter is needed for the description of the crack growth rate. Such a parameter is path-independent  $J$ -integral.  $J$  is two dimensional line integral introduced by Rice [109]. For nonlinear elastic materials the  $J$ -integral has a character of a potential energy available for crack extension. For linear elastic materials, the  $J$  represents the strain energy release rate and is proportional to the square of the stress intensity parameter  $K$  divided by Young's modulus  $E$  [138]. For elastic-plastic materials  $J$ -integral is a measure of the intensity of the crack-tip strain field.  $J$ -integral has been employed successfully for many materials as the parameter describing the driving force at the crack tip [110; 139; 140] under plastic deformation conditions.

To use the  $J$ -integral in practical situations it must be evaluated. Dowling [140] estimated the  $J$  from the hysteresis loop as the sum of the elastic and the plastic strain energy densities multiplied by the crack length  $a$  (half of the semi-circular crack). Recently the implementation of the finite element analysis simplified the characterization of the  $J$ -integral at the crack tip assuming the true shape of the crack front [139].

Based on the work of Sih and Hutchinson [138] who estimated the  $J$  for extremal cases (fully linear, fully plastic) the  $J$  amplitude  $J_a$  can be evaluated as the summation of its elastic and plastic component as follows



$$J_a = J_{a,el} + J_{a,pl} . \quad (4.2.4)$$

Recently Náhlik and Hutař [110] introduced numerical model for characterization of short fatigue crack growth using  $J$ -integral. They rewrite the Paris-Erdogan law (Eq. 4.2.3) in terms of  $J$  amplitude  $J_a$ . They found that the plastic part of the  $J$ -integral plays dominant role in the short crack growth propagation during high strain cycling. Therefore, they described the small fatigue crack propagation rates using the non-linear component of the  $J$ -integral as follows

$$\frac{da}{dN} = C_{Jp} \left( \frac{J_{a,pl}}{J_{a,pl,0}} \right)^{m_{Jp}} , \quad (4.2.5)$$

$J_{a,pl,0}$  is a constant equal to 1 J/m<sup>2</sup> in order to simplify the units of  $C_{Jp}$  and  $m_{Jp}$  constants. They found very good correlations in many structural materials such as austenitic steel [139] and ODS steels [141].

#### 4.2.3. Plastic-strain dependence crack growth rate approach ( $\varepsilon_{ap}$ )

Polák and Liškutín [92] studied the short crack growth in polycrystalline copper subjected to constant plastic strain amplitude. They have found that the same fatigue life is reached if the aggregate of growing short cracks in the specimen subjected to constant plastic strain amplitude loading is replaced by the growth of the instantaneously longest crack, so-called equivalent crack [133; 134]. During the fatigue life, the growth of the smaller cracks slows down under the shielding effect of the dominant crack. Similar approach has been used in the studies of short crack growth in 316L steel, [118; 130; 142], duplex stainless steel, [143], Eurofer 97 steel, [142] and in ferritic stainless steel [144].

Other approach to analyse the crack growth rates is the comparison of the prediction of the fatigue life using the plastic-strain-dependent crack growth rates [144; 145]. Polák proposed the crack growth rate dependence on the plastic strain amplitude [144]. According to that the short crack growth in most materials can be described by the exponential dependence using equation

$$a = a_i \exp(k_g N) , \quad (4.2.6)$$

where  $a$  is the crack length,  $a_i$  is the crack length extrapolated back to zero number of cycles and  $k_g$  is crack growth coefficient and  $N$  is the number of cycles. The increment of the crack length per one cycle can be obtained by differentiation of equation (4.2.6):

$$\frac{da}{dN} = k_g a . \quad (4.2.7)$$

It is assumed that the crack growth coefficient  $k_g$  depends only on plastic strain amplitude  $\varepsilon_{ap}$  as follows

$$k_g = k_{g0} \varepsilon_{ap}^d , \quad (4.2.8)$$

where  $k_{g0}$  is constant and  $d$  is crack growth exponent.

### 4.3. Effect of high temperature

High impact on fatigue crack propagation at a high temperature has the corrosion effect of the environment. Stress corrosion cracking starts when the brittle oxide layer at the tip of the crack breaks under the tensile stress. It contributes significantly to the growth rate. Moreover, during the period when the crack is open the oxygen can penetrate into the metal and new oxides can rise [99]. Contrary to the cycling at a room temperature The most obvious change in the crack growth path in high temperature cycling is that from trans- to intergranular. Intergranular crack propagation at high temperature is faster than transgranular propagation and thus shortens the fatigue life of strain-controlled specimens. Formation of creep cavities, oxides, and precipitates at grain boundaries also leads to the reduction of the fatigue life. Transition from trans- to intergranular crack propagation is enhanced by the presence of oxidation environment as observed many times in Ni-based superalloys [146; 147].

The impact of the environment during high temperature loading on the fatigue crack growth path was well demonstrated in experiments performed in the vacuum and in the air [148]. In vacuum, the crack propagation at high temperature remains transgranular, while in air the crack propagation is almost exclusively intergranular. [2]

The effect of the oxidizing atmosphere on crack growth of iron-based superalloy 800H at 800 °C was found by Bressers et al. [149]. The crack density and crack length of the dominant crack increases more quickly in air than in vacuum resulting in three to four times higher fatigue life in vacuum. Crack nucleation enhancement and acceleration of microcrack growth in the air are apparent. The enhancement of crack nucleation rate in the air was ascribed to oxide scale cracking. The higher number of microcracks in the air contributes to the frequent crack coalescence and to the earlier fracture. [2]

Direct detailed experimental evidence on the mechanisms of environmentally assisted crack extension and fatigue crack propagation is rare. Skelton [150] shows that oxidation during high plastic strain cycling contributes directly to the cyclic growth either by the strain enhanced oxidation and the subsequent metal loss at the crack tip, or by the diffusion of the oxygen ahead of the crack tip.

Another effect typical for high-temperature tests is the strong influence of frequency. Krupp [147] and Carpenter [146] proposed mechanisms describing the grain boundary oxidation and embrittlement of the GBs during high temperature loading at low loading rates. The corrosion damage increases linearly with the time of exposure to corrosive environment [151]. Yamaguchi and Kanazawa [8] studied the impact of increasing temperature on crack growth rate for several loading rates. They found that the fatigue life of the specimens tested with low strain rate  $10^{-5}\text{s}^{-1}$  decreases more rapidly with increasing testing temperature compared to that measured for higher applied strain rate  $10^{-3}\text{s}^{-1}$ . The decrease in the fatigue life has been ascribed to the increase of the intergranular character of the fatigue crack path.

## IV. EXPERIMENTS

### 5. Material

#### 5.1. Sanicro 25

Austenitic stainless steel of the grade UNS S31035, and with the trade name Sanicro 25, was produced by Sandvik, Sweden. The chemical composition of the material in the as-received condition (in wt%) is listed in Table 5.1. The material was delivered in the form of hot rolled cylindrical rods of 150 mm in diameter. The specimens for the mechanical testing were machined parallel to the rod axis. After the production of their crude shape, the specimens were annealed at 1200 °C for one hour and cooled in the air.

	Fe	Ni	Cr	W	Cu	Co	Nb	Mn	N	Si	C
This work	42.9	25.0	22.5	3.6	3.0	1.5	0.5	0.5	0.23	0.2	0.1
Producer Min/Max	Bal.	23.5 – 26.6	21.5 – 23.5	2.0 – 4.0	2.0 – 3.5	1.0 – 2.0	0.3 – 0.6	0.6 Max	0.15 – 0.30	0.4 Max	0.04 – 0.1

Table 5.1: The nominal composition of studied Sanicro 25 highly alloyed austenitic stainless steel (in wt%). Composition of steel studied in this work is compared with the composition guaranteed by the producer [11].

### 6. Mechanical testing

#### 6.1. Specimens

Solid cylindrical specimens with the diameter of 8 mm and gauge length of 12 mm were used for cyclic straining at room temperature (see Fig.6.1.1a). The axis of the specimen is parallel to the axis of the cylindrical rod. Shallow notch of depth 0.4 mm was ground in the middle of the gauge length to facilitate the observation of the surface evolution and cracks. The theoretical stress concentration factor of the notch  $K_t$  was determined by finite element method (FEM) using numerical program ANSYS. Fig. 6.1.2. shows the detail of the notch and the result of elastic strain distribution. The theoretical stress concentrator factor  $K_t = 1.185$  is small enough to have only minor impact on the crack nucleation in other parts of the specimen but high enough to initiate the major crack in the observed area of the shallow notch. The effect of the shallow notch decreases as the strain amplitude or plastic strain amplitude increases. Specimens were mechanically and electrolytically polished. The area of the shallow notch was polished by soft 8" SiC grinding paper (European FEPA Grit Rating 1200). The chemical composition of the electrolyte was 500 ml of ethanol, 7.5 ml of nitric acid, and 25 ml of perchloric acid.

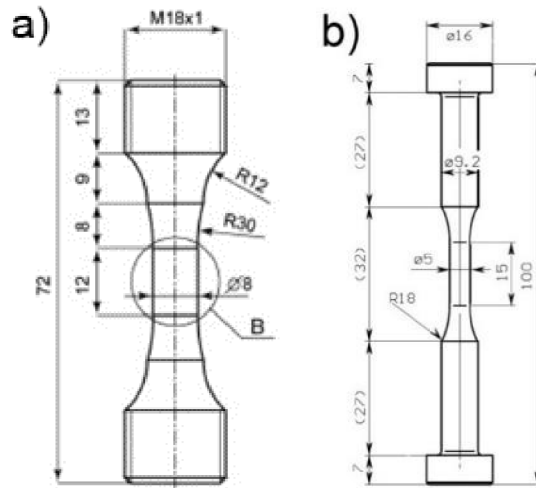


Figure 6.1.1: Geometry of the specimens: a) specimen for cyclic loading at room temperature and b) specimen for cyclic loading at high temperature

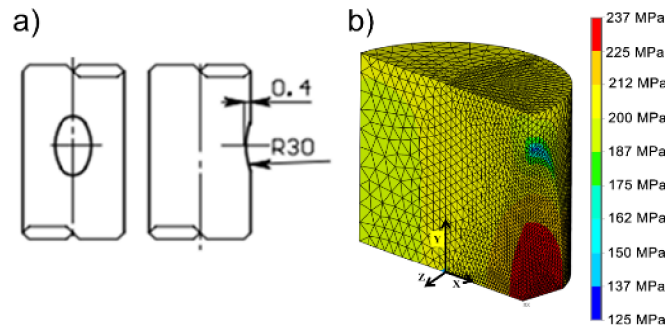


Figure 6.1.2: (a) Geometry of the shallow notch and (b) the stress analysis of the notch effect under static uniaxial loading using ANSYS in the specimen axis direction Y (loading direction).

In the case of high temperature loading the solid cylindrical specimens with the diameter of 6 mm and the gage length of 15 mm were used (see Fig.6.1.1b). To eliminate the effect of the surface roughness on the fatigue and to facilitate the observation of the surface relief evolution, the area corresponding to the gage length was mechanically grinded and electrolytically polished in the same manner as samples used for testing at room temperature.

## 6.2. Cyclic loading

All tests were carried out using servo-hydraulic tension-compression computer-controlled MTS testing machines MTS 810. The tests were performed under fully reversed ( $R_e = -1$ ) strain controlled cycling with constant strain rate. Temperature of the samples was controlled by thermocouples in the range  $\pm 2^\circ\text{C}$ . Stress and strain were recorded in regular intervals. During one hysteresis loop 400 data-points containing information about the stress and the strain were taken. Stress and strain amplitudes were derived from the

hysteresis loops acquired during the cycling. Plastic strain amplitude was determined as the half-width of the hysteresis loop at mean stress.

Cycling straining at room temperature was conducted under strain control with constant strain rate of  $5 \times 10^{-3} \text{ s}^{-1}$  and constant total strain amplitudes  $\varepsilon_a$  in the range of  $(2.5\text{--}7.0) \times 10^{-3}$ . The samples were tested in air. Mechanical grips held at constant temperature by water cooling system were used. Force was measured by a load cell. The displacement and the strain during loading were controlled and determined by uniaxial extensometer having the 8 mm base between the knife-edges. To measure the crack growth the area of the notch was regularly observed and photographed. In order to analyze the crack increment, the fatigue test was interrupted at a chosen number of cycles. The specimen was kept in tension (at zero strain) to ensure open cracks during the image acquisition.

Continuous isothermal tests were carried out at the temperature of 700 °C. High temperature hydraulic grips and a split three-zone resistance furnace were used to keep the desired temperature with minimum temperature gradient across the gage length. Specimen temperature was monitored by three thermocouples (two located on both heads of the sample and one monitoring the temperature in the middle of the gage length). Fully reversed cyclic loading with constant total strain amplitude of  $5.0 \times 10^{-3}$  and constant strain rate of  $2 \times 10^{-3} \text{ s}^{-1}$  was applied. Strain was measured and controlled using high temperature axial extensometer having long ceramic rods and 12 mm base. Specimen was heated to the high temperature (in around 30 minutes) and after a full stabilization (around 1 hour) the cyclic straining was started to minimize the high-temperature exposure of the specimen before cycling.

## 7. Microscopic observation

### 7.1. Light microscopy

Fatigue crack initiation and growth was studied on specimens with polished gage section using long focal distance light microscope (LM) Navitar equipped with Olympus DP 70 high resolution camera shown in Fig. 7.1.1. The images were acquired with the resolution of 0.15  $\mu\text{m}$  corresponding to 1 pixel.



*Figure 7.1.1: Long focal distance light microscope Navitar equipped with Olympus DP 70 high resolution camera.*

Surface cracks up to 2 mm of surface length were studied during cyclic loading. Images of the studied area were acquired regularly and the crack length was evaluated. To facilitate the observation of the notch area the periodic net of straight shallow lines was ground on the surface by the razor. The spacing of 0.5 mm between the lines was used. The test was stopped after the one of the cracks achieved the surface length higher than 2 mm within the observed area. The growth of particular selected cracks has been analyzed backwards from the previously stored images. Since the crack shapes in austenitic steel are assumed to be approximately semicircular [111; 118], the crack length  $a$  in the bulk was characterized by the half of its surface length (i.e. the distance between the crack tips on the specimen surface) projected on a plane perpendicular to the loading axis as marked by red line in Fig. 7.1.2. The crack growth rate was then defined as the increment of the crack length,  $\Delta a$ , in the number  $\Delta N$  of the cycles. Figure 7.1.3 shows the area of the shallow notch after the test. The lengths of five largest cracks within the observed area are marked.

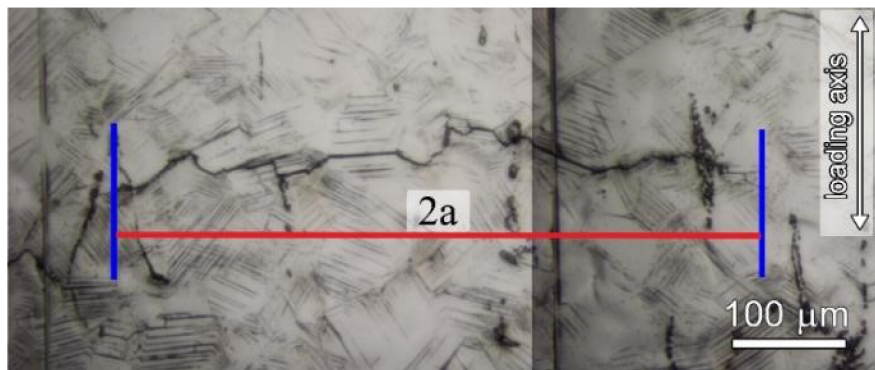


*Figure 7.1.2: Surface crack length  $2a$  (red line) of a semicircular crack in the direction perpendicular to the loading axis.*

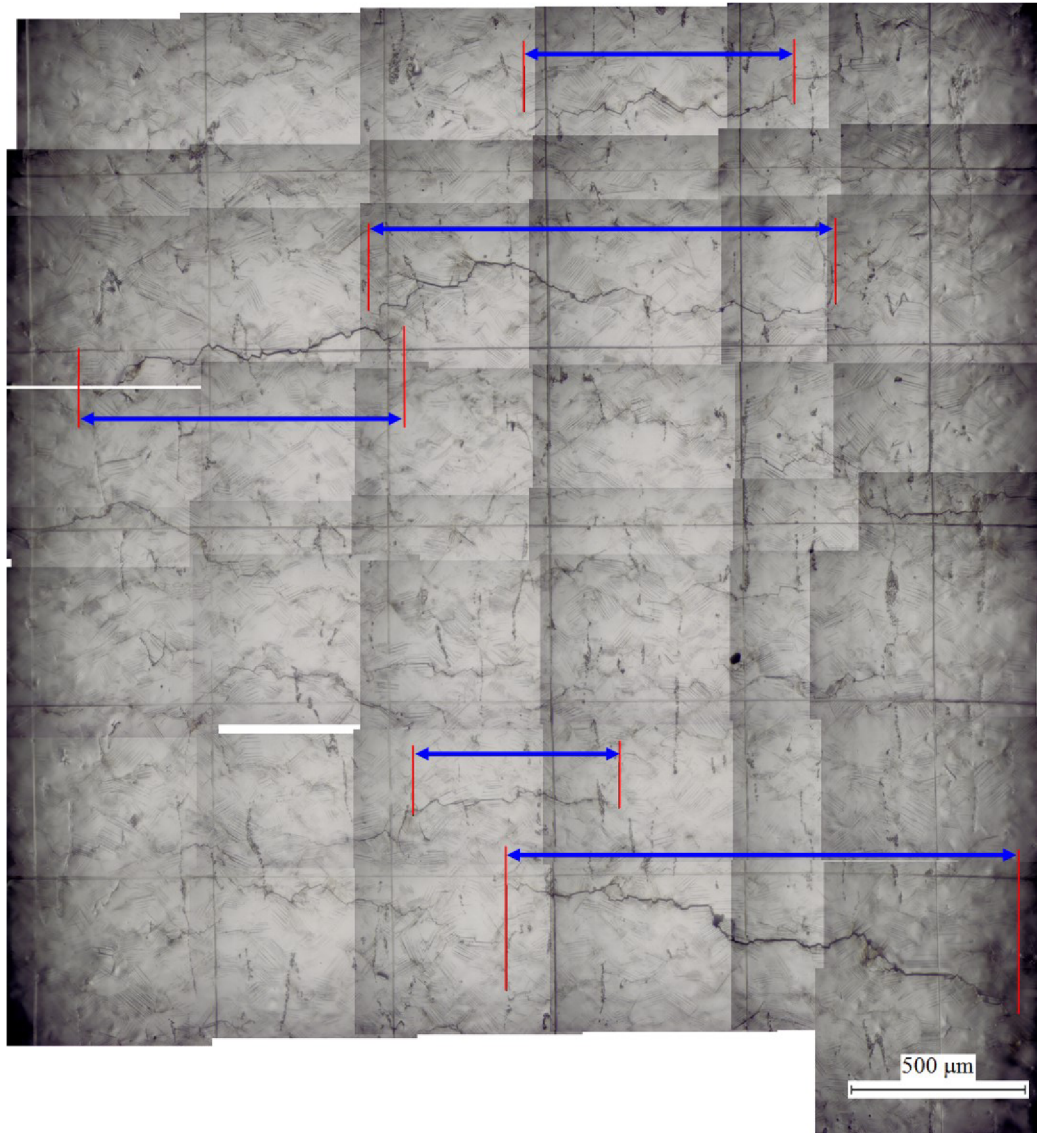


*Figure 7.1.3: Micrograph of the notch area imaged after the cycling. Five longest fatigue cracks are found and highlighted. The surface lengths of the individual observed longest cracks are marked by arrows. The specimen was subjected to cyclic loading with  $\varepsilon_a = 2.5\%$ . The picture is taken at the end of cycling.*

## **7.2. Scanning electron microscopy**

The surface of the selected specimen was inspected in detail using dual-beam Lyra 3 XMU FEG-SEM (Tescan) equipped with the focused ion beam (FIB), backscattered electron (BSE), electron backscatter diffraction (EBSD) and X-Max80 energy dispersive X-ray spectroscopy (EDS) detectors all produced by the Oxford Instruments and operated with the Aztec control system shown in Fig. 7.2.1.

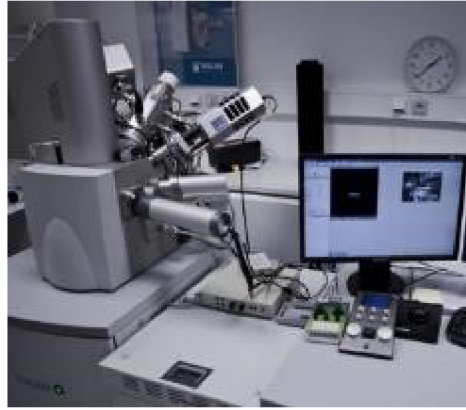


*Figure 7.2.1: Dual-beam scanning electron microscope TESCAN Lyra 3 XMU FEG-SEM.*

The mechanism of the initiation of the cracks was studied using technique of coupled FIB nanofabrication and EBSD analysis. In the case of loading at high temperatures the EDS analysis was also used to study the changes in the composition and to characterize the oxidation behaviour of the material. Specimens in selected stages of the fatigue life or at the fracture were investigated. In order to reveal the shape of the surface relief and the shape of the initiated crack in the third dimension, the grains with PSMs running perpendicular to the specimen axis were chosen. Lamellae perpendicular to the direction of PSMs were produced using FIB. Fig. 7.2.2 schematically shows the position of the lamella situated approximately in the center of the grain. The area of the interest was documented using FESEM, and later selected area of the grain with several PSMs was covered with platinum. Very thin platinum layer was first deposited using electron bombardment and later a layer of about 1.5 - 2  $\mu\text{m}$  in thickness was deposited using ion bombardment. FIB was used to produce rectangular craters from one side and later from both sides of the future lamella. However, only one lamella could be prepared using FIB from the grain containing PSMs and subsequently observed in transmission electron microscope (TEM). Lamella was further completely separated from the grain, mounted to the supporting copper grid, and subjected to further thinning. Selected steps from the procedure of the lamella lift-out are demonstrated in Fig. 7.2.3. Both surfaces of the lamella were finally thinned with ions using low acceleration voltage of 5 kV and current of 300 pA in order to remove or minimize the damage caused by previous steps.

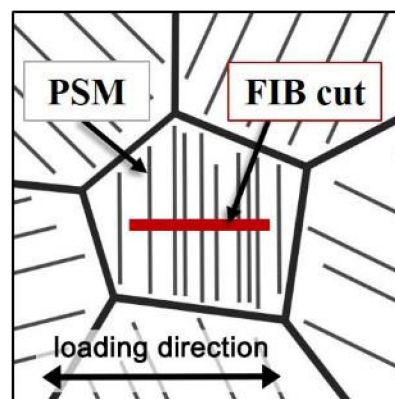


*Figure 7.2.2: Schematic position of the FIB cut in the grain perpendicular to the persistent slip markings.*



Thin TEM lamellae prepared by FIB were also used to study the oxidation of grain boundaries during the cycling at high temperature. The lamellae were extracted at the position where the grain boundary was roughly oxidized. The grain boundary was oriented approximately perpendicular to the loading axis. The procedure of the preparation of lamella extracted at oxidized grain boundary is shown in Fig. 7.2.3.

After the cycling, the relation between the structure of the material and the crack growth path was studied using the EBSD. The EBSD was performed using acceleration voltage of 20 kV and the average spot spacing up to 1  $\mu\text{m}$ . The crystallographic orientation of the grains along the crack was analysed. The obtained Euler rotation angles of individual grains were used to define the orientation of primary slip planes  $\{111\}$ . Subsequently their projection to the planes described in the basic cartesian coordinate system (XYZ) was analysed by software developed in Matlab at the IPM CAS by Roman Gröger.

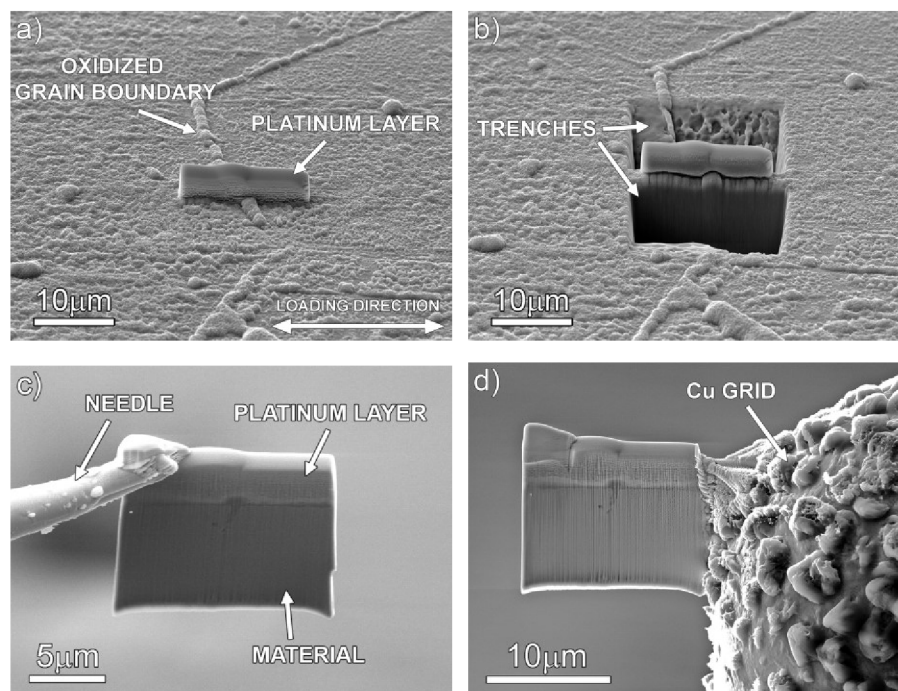


*Figure 7.2.3: Secondary electron images showing selected steps of the thin TEM lamella preparation procedure. The lamella is extracted in such a way that the plane of the lamella is parallel with the loading direction. (a) Deposition of the protective platinum layer. (b) Milling of the rectangular trenches on both sides of the lamella. (c) Lamella mounted to the needle and extracted from the material. (d) Rough shape of the lamella mounted to the Cu grid and later polished to the sufficient thickness.*

### 7.3. Transmission electron microscopy

Thin foils suitable for TEM observations could be inspected either in FESEM to document surface relief or directly in JEOL JEM-2100 F TEM (Jeol Ltd., Tokyo, Japan) equipped with FEG (Field Emission Gun) electron source (shown in Fig. 7.3.1). To visualize crystal defects such as dislocations the diffraction contrast imaging in STEM (scanning transmission electron microscopy) was used. Both the bright and dark field detectors were

utilized to inspect the crystal either along low index zone axes or in several different two-beam diffraction conditions. When inspecting arrangement of dislocation structures, the images were taken in at least four diffraction conditions to get all possible geometrical information about the crystal, slip planes and slip directions. The zero contrast invisibility rule known also as “*g.b*” rule was used to determine the Burgers vectors and the type and character of dislocations. To image different phases, electrons inelastically scattered to high angles were collected to annular dark field detector to obtain Z-contrast which is sensitive and proportional to atomic number ( $\sim Z^2$ ) of elements.

The TEM lamellae were fixed in the TEM holder with the loading direction aligned with the respect to the holder axis. The goal was to know the orientation of investigated crystal relative to the macroscopic loading axis during the observations. Diffraction patterns and Kikuchi lines were used to determine the crystallographic orientation of the stress axis in individual grains. If not stated otherwise, the Miller’s indexes were permuted so that the strain axis vector lay in or on the border of the basic stereographic triangle defined by the apexes [001], [011], [ $\bar{1}11$ ].



*Figure 7.3.1: Transmission electron microscope JEOL JEM-2100F equipped with STEM, HAADF and EDS detectors.*

## V. RESULTS

### 8. Initial state of the material

Microstructure characterization of initial state of the material before the loading was performed by SEM equipped with EBSD detector and STEM equipped with EDS detector. The area of  $0.8 \text{ mm}^2$  was analyzed to determine the average grain size. It was estimated to be about  $60 \text{ }\mu\text{m}$  using the intercept method from about 200 grains without consideration of annealing twin boundaries. Nevertheless, grains of the size up to  $500 \text{ }\mu\text{m}$  were also found. Closer characterization of microstructure was performed by EBSD (see Fig. 8.1). No preferred microstructural orientation was found (see Fig. 8.1a). The orientation of individual grains is random. Grain orientation analysis using EBSD shows the presence of multiple annealing twin boundaries in the structure. Phase analysis in Fig. 8.1b shows that the matrix is composed only from austenitic grains. The primary particles of other phase are present in the material as well (shown as black color in Fig. 8.1b)

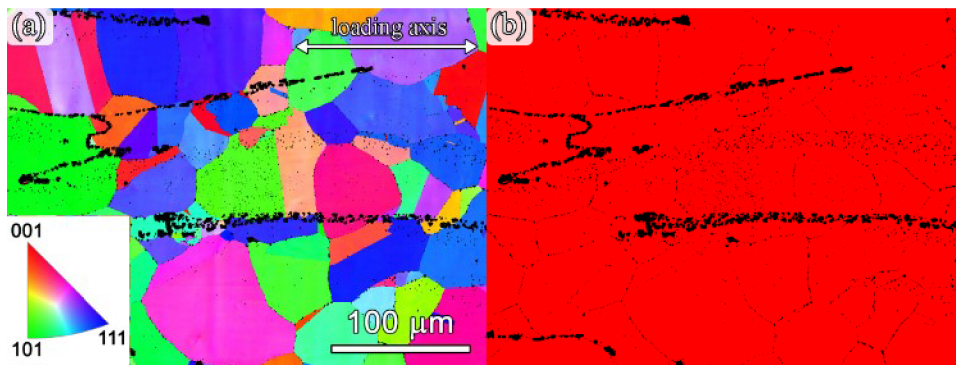


Figure 8.1: Structure of the Sanicro 25 after annealing; a) grain orientation relative to the loading axis obtained by EBSD; b) EBSD micrograph of phases (austenite — red, primary precipitates — black).

From the total number of analyzed grain boundaries the fraction of observed grain boundaries with particular misorientation angle at the interface was determined by EBSD. Results are shown in Fig. 8.2. It is evident, that the high angle grain boundaries (HAGB) significantly predominate when compared to low angle grain boundaries (LAGB).  $\Sigma 3$  twin boundaries with misorientation angle of about  $60^\circ$  with respect to the  $\{111\}$ -type of planes represent fraction of about 41% of all detected boundaries. Statistically, this means that approx. 80% of grains contain one twin boundary at maximum what is in a good agreement with the initial structure shown in Fig. 8.1a. Other special CSL type interfaces except for the twin boundaries represent only about 5%, what means that randomly oriented HAGB interfaces predominate.

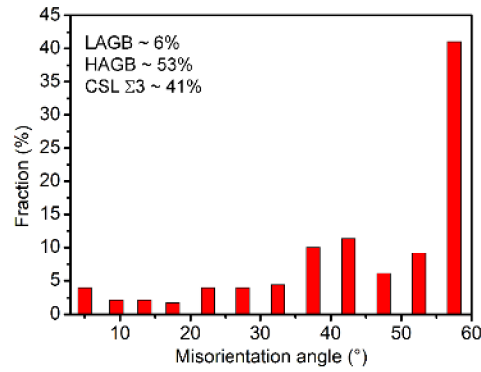


Figure 8.2: Statistics of the fraction of grain boundaries with particular misorientation angle in the initial state observed by EBSD. Low angle grain boundaries (LAGB) represent approx. 6%, high angle grain boundaries (HAGB) approx. 53% and twin boundaries ( $\Sigma 3$ ) approx. 41% of the total number of investigated grain boundaries.

The overall micrograph of the initial state is shown in Fig. 8.3. Back-scattered electron images show electrolytically polished surface of the specimen. Individual equiaxed grains can be recognized as well as annealing twin boundaries. At the grain boundaries but also inside the grains, large primary particles with size varying from 100 to 400 nm were observed (shown in Fig. 8.1b). Large precipitates were found also in groups elongated in the direction of the bar (rolling direction and specimen axis direction) [21].

Initial state of the material was thoroughly characterized using TEM. In Fig. 8.4a high-angle annular dark-field (HAADF) STEM image of initial state is shown. It contains very low density of dislocations as expected after the annealing. Dislocation structure can be characterized by planar slip presented by multiple individual loop segments attached to the primary particles.

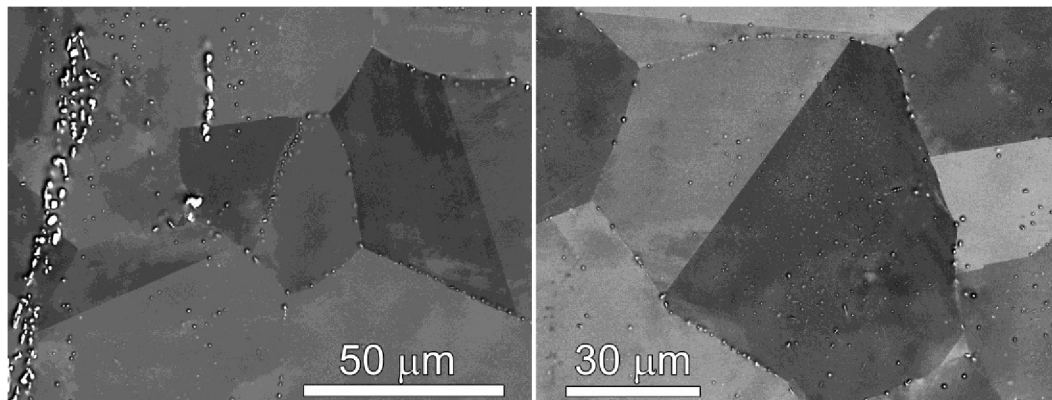
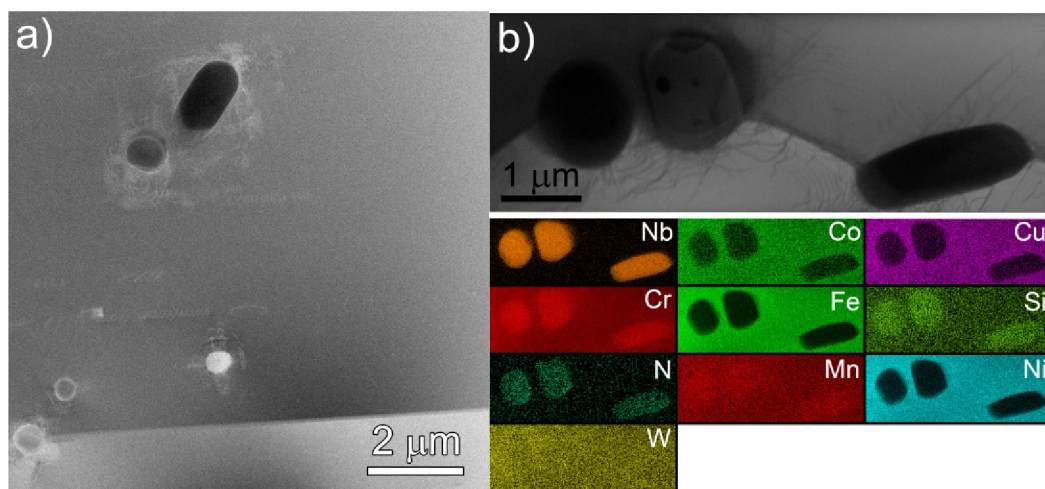


Figure 8.3: Back-scattered electron (BSE) images showing equiaxed austenitic grains along with the annealing twin boundaries. Three sizes of the precipitates are evident in the structure: large precipitates elongated in the rolling direction, middle-size precipitates arranging the grain boundaries, and small-size precipitates found within the grains.

In STEM mode, EDS was used for the analysis of the particles located at the grain boundaries (see Fig. 8.4b). The composition of the precipitates is similar to that previously

reported for a complex nitride designated as Z-phase [12; 14]. Nb-rich Z-phase particles are the only type of a precipitate observed in the initial state after the solution annealing at temperature of 1200 °C. Sometimes, also a very small amount of  $M_{23}C_6$  Cr-rich carbides can be present in the initial state of Sanicro 25. However, according to Sourmail [12], their dissolution temperature should be below 1100 °C suggesting their presence after annealing is arguable. In the present study, no carbides were observed in the initial state. Changes in the chemical composition inside the grains and along the grain boundaries were studied both by SEM-EDS and high-resolution STEM-EDS. No significant chemical inhomogeneity between the individual grains after the solution treatment was found (not shown here). This has been confirmed also by STEM-EDS. Colored chemical composition maps in Fig. 8.4b document that there are no significant differences in the chemical composition along the grain boundaries.



*Figure 8.4: (a) Bright field STEM image of the initial state of the material after final thermal treatment. Primary Z-phase particles are found along with very low dislocation density, characteristic by dislocation pile-ups. (b) Bright field STEM image of the Z-phase particles located at the grain boundary. The corresponding STEM-EDS map analysis documents the chemical composition of the primary precipitates.*

## 9. Fatigue damage at room temperature

### 9.1. Natural fatigue crack initiation sites

#### 9.1.1. Crack initiation along persistent slip markings

In all specimens cycled to less than 5% of the fatigue life, OM observations revealed significant density of fatigue cracks, which initiated on the specimen surface.

One of the typical site where cracks initiated is shown in Fig. 9.1.1. SE micrograph shows the surface of the specimen fatigued with  $\varepsilon_a = 4 \times 10^{-3}$ . It is notable that grain is oriented for multiple slip relative to the loading direction. However, the primary slip system is markedly evident to be the major slip system with well-developed PSMs. These PSMs do not extend across the all grain. Nevertheless, they represent the effective site for the crack initiation.

PSM along which the crack initiated is oriented approximately 45° in respect to the loading direction. The detail of the crack initiated and growing along the PSM is shown in Fig. 9.1.1 on the right. The extrusion is passing through the center of the micrograph Fig. 9.1.1. Two parallel fatigue cracks probably initiated on opposite sides of the extrusion started to grow as shown in micrograph. Later, during further cycling the cracks continued propagating and linked while cracking the central extrusion.

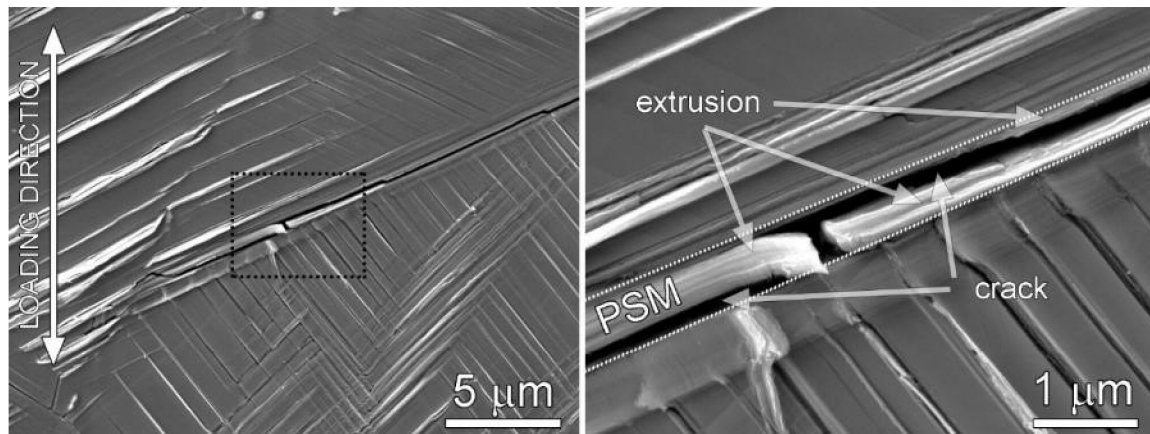


*Figure 9.1.1: SE micrograph shows the specimen surface with initiated fatigue crack along the persistent slip marking (PSM). Crack initiated along the extrusion and was parallel with the PSM. Detail (on the right) shows the initiated crack growing on both sides of the extrusion and crossing the extrusion.*

Surface relief evolution in the form of PSMs anticipates the crack initiation. Micrograph in Fig. 9.1.2a shows typical relief of surface grain after fatigue where two well-developed parallel PSMs A and B are present. PSMs consist of one or more extrusions and parallel intrusions. In some positions it seems that crack has already initiated along the PSM. Nevertheless, it is very difficult to recognize between the intrusions and initiated Stage I fatigue cracks based on the observation of the surface. Nanofabricated FIB trench perpendicular to the PSM A (see Fig. 9.1.2b) in the location marked by a shadow line in Fig. 9.1.2a reveals the relief of the PSM A. The presence of two extruded hills (extrusions) and depressed material (intrusion) in between them is evident. Here, from the tip of the intrusion, Stage I fatigue crack was found to initiate. Figure 9.1.2b shows that the relief of extrusions and intrusion is not smooth; some alternating small extrusions/intrusions can be found even within individual large extrusions.

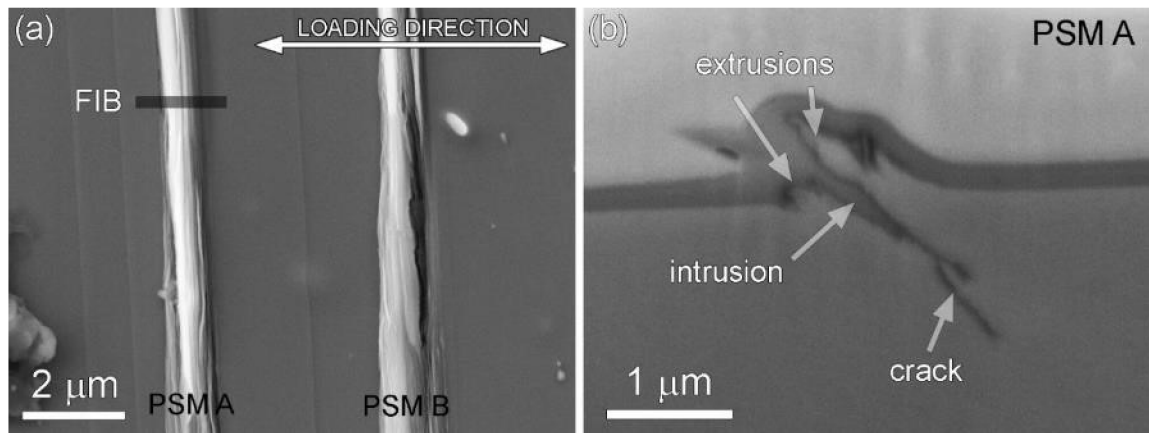


Figure 9.1.2: SE micrograph of the specimen cycled with total strain amplitude  $\epsilon_a = 0.35\%$ ; (a) specimen surface with 5 parallel PSMs; (b) the profile of the PSM a in the location marked in (a) as “FIB cut” showing extrusions, intrusion, and cracks starting from the tip of the intrusion.

Both the evolution of surface profile in form of two PSMs denoted as A and B, and Stage I crack initiation during cycling are shown in Fig. 9.1.3. The specimen was cycled with total strain amplitude of 0.25 % until first cracks had initiated. The area of interest was covered by platinum deposition. Then FIB cut was done perpendicular to the specimen surface.

The early stage of evolution of PSMs at 0.8 % of fatigue life is shown Fig. 9.1.3a. The PSM A consists of small extrusion and shallow intrusion on the left side. The height of the extrusion is only about 80 nm and the deepest point of the intrusion is about 100 nm. It is apparent that the intrusion is composed of several small extrusions growing within the intrusion. These small extrusions create intrusion-like defects increasing the stress concentrator effect in the intrusion and then probability of fatigue crack initiation. PSM B consists preferentially of several parallel extrusions of 110 nm in height. Intrusions are present only in the form of very shallow depressed material.

Further activity of the PSB in the bulk of the material is apparent from the roughening of the FIB-cut surface in Fig. 9.1.3b. Based on its morphology it is possible to say that the active Burgers vector is almost parallel with the FIB-cut plane. By applying of additional 1000 cycles the extrusion height increased in both cases by about 100 nm. The height of the extrusion in the case of PSM A is about 180 nm and in the case of PSM B it is about 200 nm. After cycling small intrusion appeared on the right side of the extrusion in PSM A and Stage I fatigue crack (white arrow in Fig. 9.1.3b) initiated from the intrusion on the left side. In the case of PSM B intrusion developed close to the left side of the PSM.

Figure 9.1.3c shows early stages of the growth of fatigue cracks initiated from both PSMs. In both cases the cracks initiated from the intrusions. The height of the extrusions increased only slightly of about 30 nm after additional 2000 cycles. Initially, the cracks were growing parallel with the PSBs and later they had tendency to deviate and the growth plane became nearly perpendicular to the loading direction (see crack initiated from PSM B). Slightly different situation was in the case of crack initiated from PSM A. The crack deflected from its original plane but continued growing on a parallel plane probably along the twin boundary.

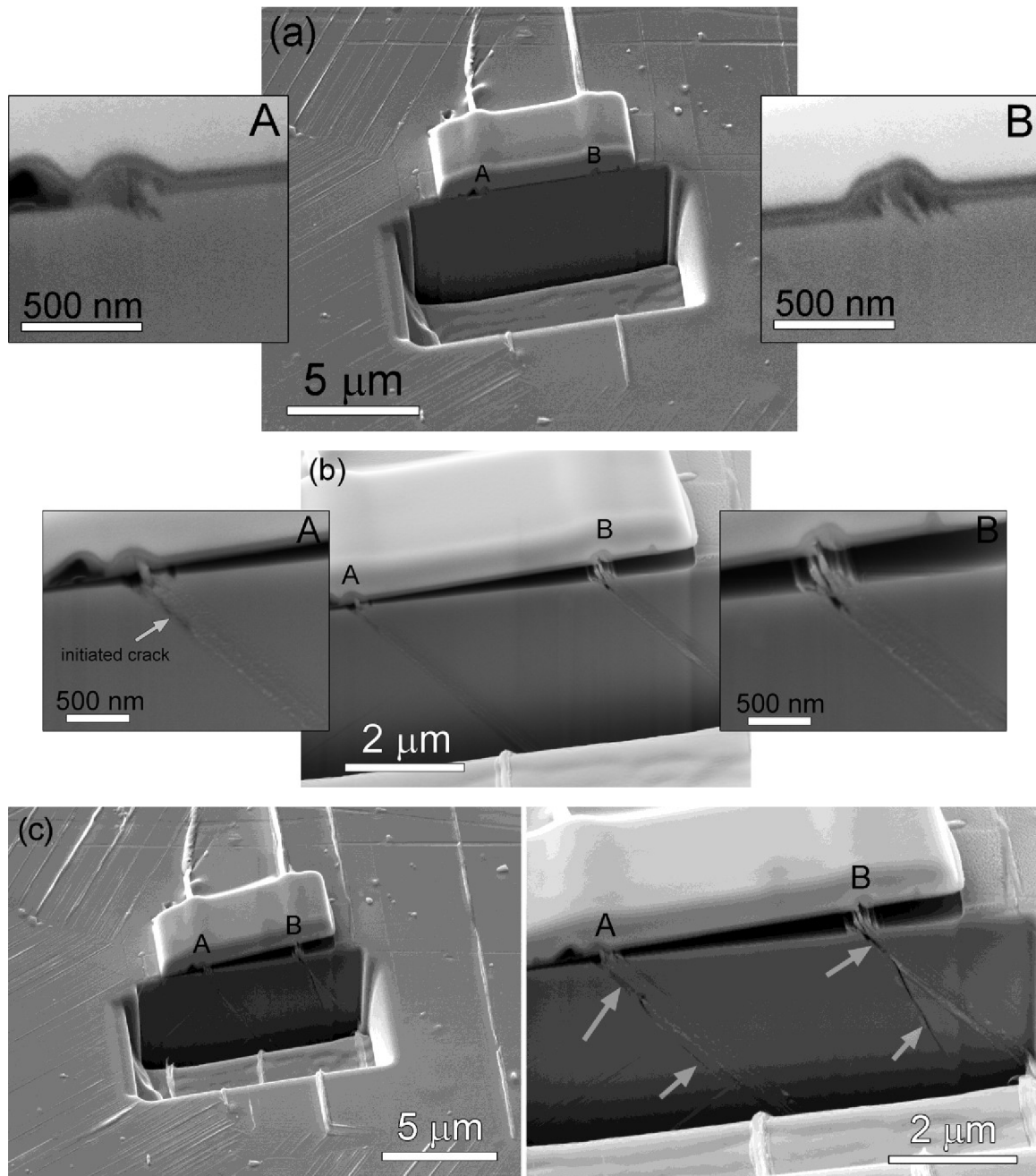


Figure 9.1.3: The evolution of PSMs at the specimen surface and Stage I crack initiation from PSMs A and B in the specimen cycled by  $\epsilon_a = 0.25\%$ . The PSMs are documented in different stages of fatigue life; (a) 900 cycles =  $0.8\% N_f$ ; (b) 1900 cycles =  $1.6\% N_f$ ; (c) 3900 cycles =  $3.3\% N_f$ . Number of cycles to fracture is 118400. Loading direction is horizontal. Note also decohesion of the Pt layer from the surface due to growth of the extrusions (Fig. b and c).



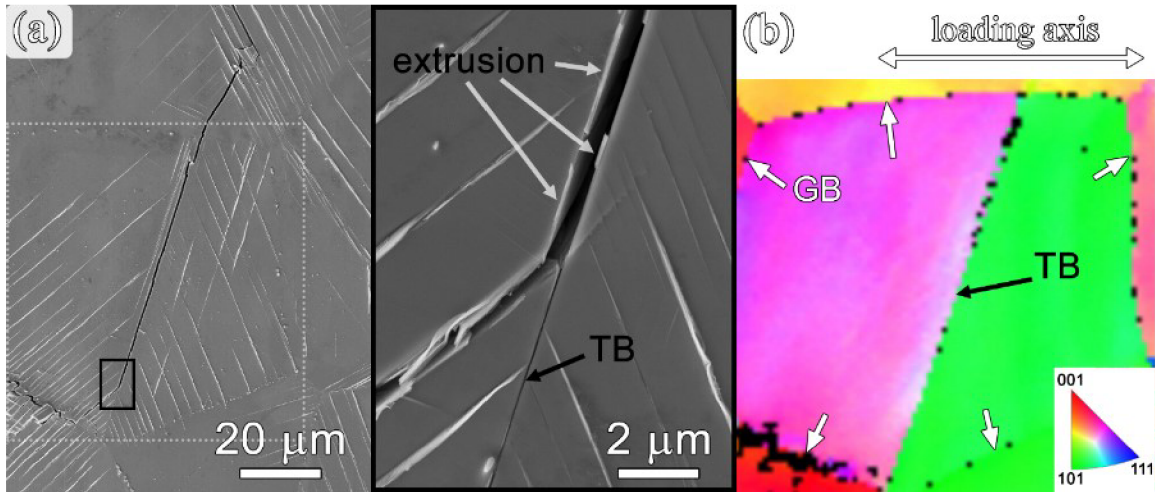


Figure 9.1.4: Crack initiation along the twin boundary: (A) SE micrograph of the specimen surface with a crack initiated in the TB along the PSM (see the detail highlighted by black inset); (B) EBSD image in the loading direction of the area selected by dashed rectangle in Fig. 9.1.4a.

The same approach was also applied to study the crack initiation “in” TB. Micrographs in Fig. 9.1.4 show fatigue crack initiation along the TB. Secondary electron micrograph in Fig. 9.1.4a shows the specimen surface after fatigue testing with developed PSMs and an initiated crack. In Fig. 9.1.4b, EBSD analysis of the area marked by the dotted rectangle in Fig. 9.1.4a detected both the grain boundaries and the TB (marked by the arrows). It is apparent that the crack initiated in or very close to the TB. Closer inspection of the fracture surface inside the crack along the twin boundary (see the inset in Fig. 9.1.4a) indicates the presence of the PSB in the bulk which emerges on the surface as PSM.

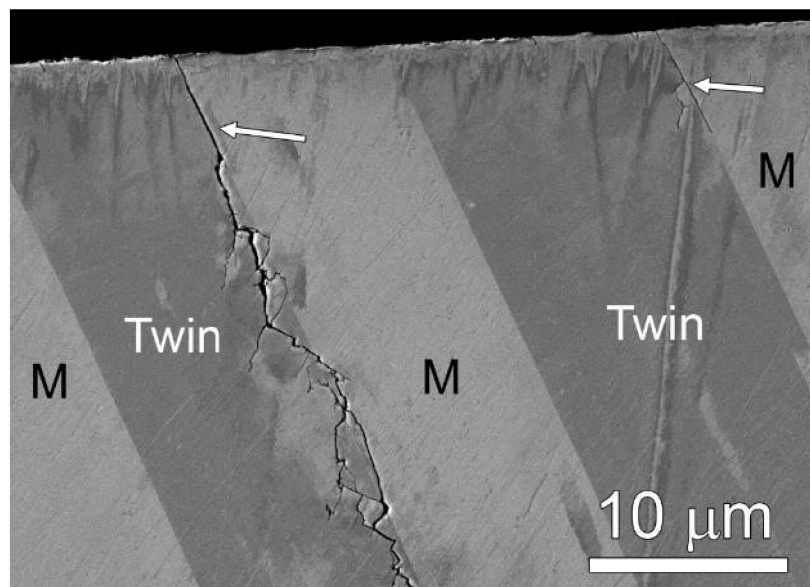


Figure 9.1.5: BSE micrograph showing the presence of initiated cracks along every other twin boundary. Loading direction is horizontal.

The growth of the Stage I fatigue crack initiated along the TB in the bulk of the material is shown in Fig. 9.1.5. The specimen was cyclically loaded by total strain amplitude 0.25%. BSE micrograph showing longitudinal section reveals the part of the surface grain containing several annealing twin boundaries. It is apparent that the fatigue cracks initiated from the surface at every other twin-matrix interface (marked by white arrows). The cracks continued growing along the twin boundaries only for a short distance. After a few micrometres, the cracks started to bifurcate and deviated from their original growth direction.

### 9.1.2. Crack initiation at large angle grain boundaries

Crack initiation at large angle grain boundaries caused by decohesion of the boundary in between two structural units was observed only rarely. Therefore, the cracks initiated at grain boundaries as shown in Fig. 9.1.6 (marked by the arrows) did not have high impact on the fatigue life of the material. These cracks continued propagating only for a short distance in the direction perpendicular to the loading axis. In the majority of cases the crack which initiated at the grain boundary stopped growing as a direct result of shielding effect of longer cracks which initiated previously.

The detail of the grain boundary decohesion marked by dashed rectangle in Fig. 9.1.6 is shown in Fig. 9.1.7. It allows to reveal the details of the mechanism leading to the grain boundary cracking. The neighbouring grains are denoted as G1 and G2. The projected slip traces of both grains at the specimen surface are perpendicular to each other. As shown in Fig. 9.1.7 the PSMs arise not only on the specimen surface but also at the grain boundary. Since the slip activity of one grain cannot continue to the other grain due to the high grain misorientation the PSBs of G1 emerge at the grain boundary in the form of PSMs. They consist preferentially of extrusions (white arrows). However, a few shallow intrusions (dark arrows) can be found as well.

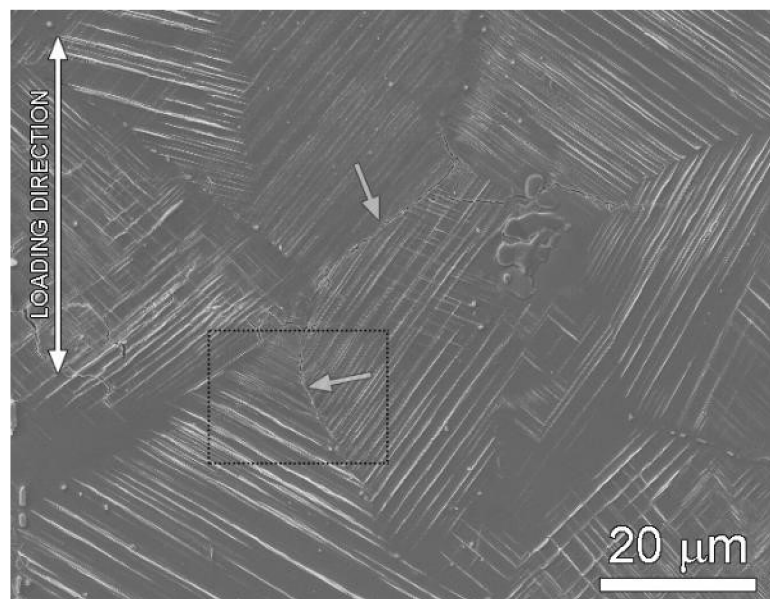


Figure 9.1.6: Surface of the fatigued specimen with total strain amplitude  $\varepsilon_a = 6 \times 10^{-3}$ . Individual surface grains are covered by multiple PSMs corresponding to several activated slip systems. The positions of the crack initiations at GB are marked by the arrows.

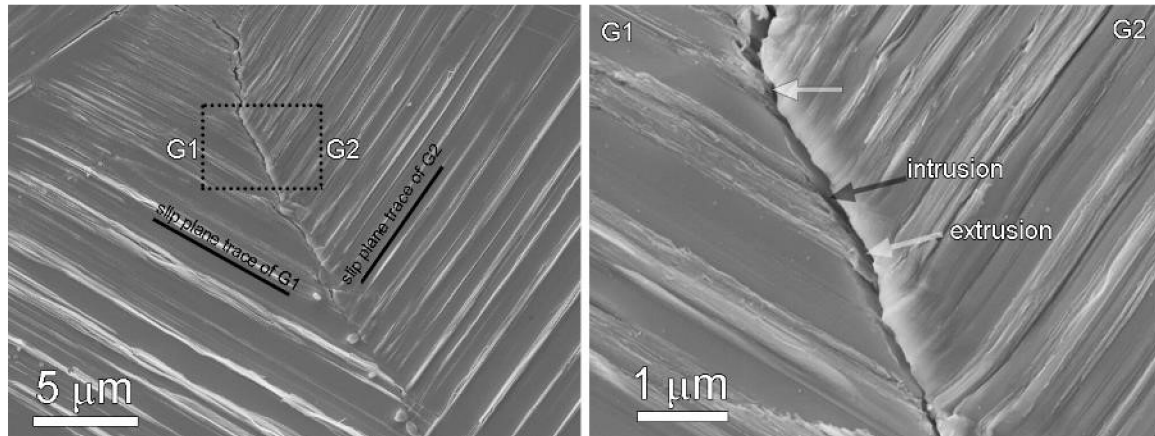


Figure 9.1.7: Details from Fig. 9.1.6 shows the GB in between two grains marked as G1 and G2. Well-developed PSMs and fatigue crack initiation at the grain boundary accompanied by the activation of slip systems are notable. Detail shows the emerging PSBs (extrusions marked by white arrows and intrusion marked by dark arrow) at the grain boundary leading to decohesion of the GB.

Figure 9.1.8 documents the opened crack initiated at the GB oriented perpendicular to the loading axis. Using EBSD analysis three differently oriented areas in terms of crystallography denoted by numbers 1, 2 and 3 are recognized (see the colour inset in the image). The corresponding electron backscattered diffraction patterns (EBSPs) of each area are present in the image as well. It is notable that there is no crystallographic relation of twin type or other types between each of the grains.

The mutual misorientation between the neighbouring areas 2 and 3 found by EBSD analysis is slightly above  $20^\circ$ . The angle between the surface traces of activated slip planes close to crack was evaluated to be about  $80^\circ$ . According to EBSD analysis and the crystallographic orientation of G3 the PSMs belong to  $(111)[\bar{1}01]$  slip system having the highest Schmid factor of 0.477. The dot product of vectors  $\mathbf{n}$  (normal vector to the specimen surface) and  $\mathbf{b}$  (Burgers vector) specifying the effectivity of the slip system at the surface and thus the visibility of the PSM at the specimen surface is only 0.07. PSMs in G2 correspond to the one of two possible slip systems. The first one  $(\bar{1}11)[101]$  has the highest Schmid factor of 0.460 and its dot product  $\mathbf{n}\cdot\mathbf{b}$  is equal to 0.31 and the second one  $(\bar{1}11)[\bar{1}10]$  has the Schmid factor of 0.395 and the dot product  $\mathbf{n}\cdot\mathbf{b}$  is equal to 0.78.

It is evident from the image that G2 is covered by dense parallel PSMs of significantly higher height than G3. These surface marks are composed of extruded material growing out of the specimen surface. The inset showing the detail of the cracked GB marked in Fig. 9.1.8 by dashed rectangle reveals the impingement of PSMs belonging to both areas 3 and 2 at GB.

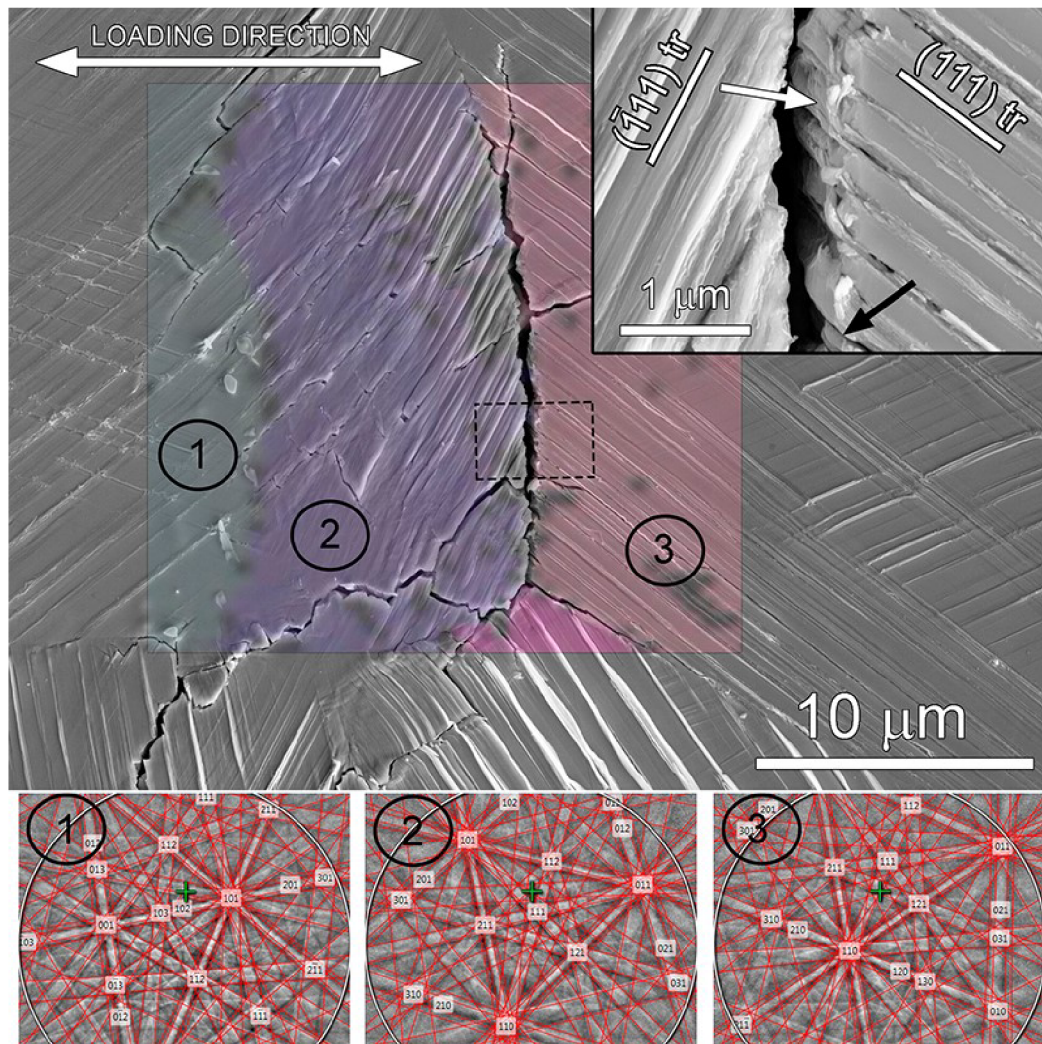


Figure 9.1.8: Surface of the specimen cyclically with  $\epsilon_a = 6 \times 10^{-3}$  ( $\epsilon_{ap}(N_f/2) = 4 \times 10^{-3}$ ). Crack in the central part of the image initiated at the GB as the result of decohesion of two neighbour grains. GB is oriented perpendicular to the loading axis. The inset shows the detail marked by the dashed rectangle. PSBs were found to emerge at GB and PSMs arise here in the form of bent extrusions (white arrow) accompanied by intrusions (black arrow). EBSD map reveals three different orientations of lattice in the neighbourhood of the crack. Corresponding EBSPs are below the image.

Fig. 9.1.8 indicates that PSMs in grain 2 arise predominantly at the specimen surface and no significant features of PSBs are formed at the GB. However, while grain 2 shows well-developed surface relief grain 3 exhibits only very thin and shallow fatigue-induced surface features. The profile of PSMs is very flat consisting of long shallow intrusions and low extrusions along the surface traces of PSBs. In the majority of grains extrusions alternate with intrusions along the PSM and create ribbon-like profile. The inset reveals that large extrusions emerge from the G3 at the interface of the grains (white arrow). These extrusions are accompanied by intrusions (black arrow). Unfortunately, it is very difficult to distinguish them due to the significant plastic deformation at the grain boundary and bending of already grown extrusions. This location and the profile of the surface relief indicates that the Burgers vector is oriented close to be parallel to the specimen surface, as can be seen also from  $\mathbf{g} \cdot \mathbf{b} = 0.07$ .

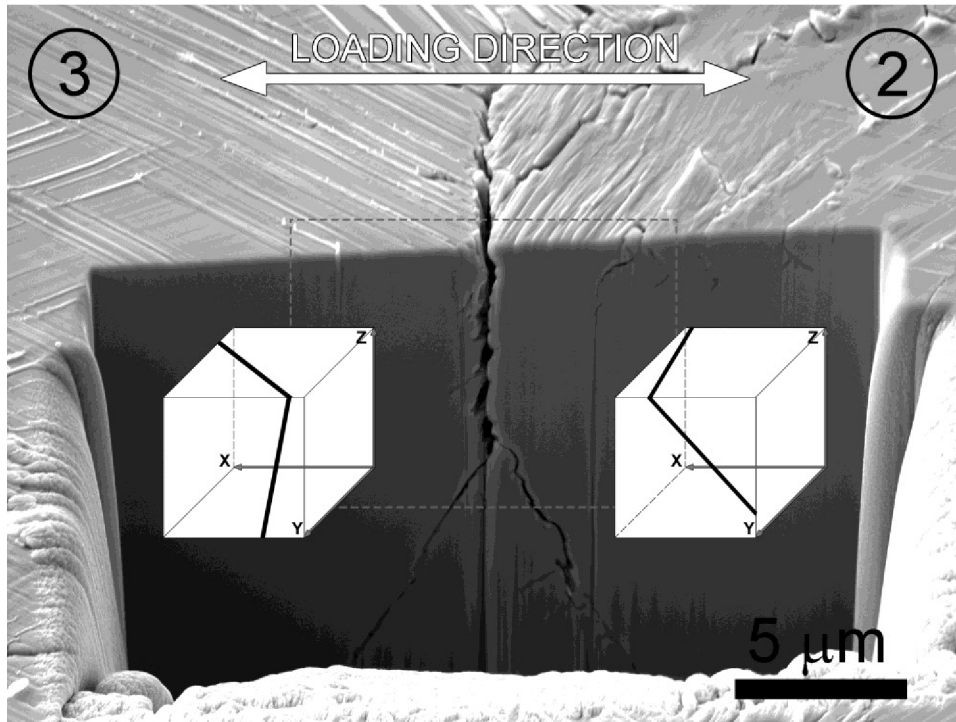


Figure 9.1.9: SE image of the area containing FIB cross section plane oriented perpendicular to the GB. The image was taken with the 35° tilt correction. The insets show the orientation of the primary slip planes (see Fig. 9.1.8) in individual grains.

The FIB cross section in Fig. 9.1.9 oriented perpendicular to the cracked GB shows slightly opened GB in the depth of the material. It is apparent that crack was growing perpendicular to the loading direction, i.e. its trace was perpendicular to the loading direction on both surfaces, specimen surface and FIB-cross section. Cracking of the GB does not occur along the whole length of the GB but only in a few micrometers beneath the specimen surface. Further, as can be clearly seen, the crack branches and two cracks have a tendency to grow along the slip planes. The inserted cubes show the traces of primary slip planes at the specimen surface and in the plane of the FIB-cut in both grains. The traces of the planes on each of the cube side are almost perpendicular.

Figure 9.1.10 shows closer view of the cracked GB. The traces of the individual slip planes are inserted in the image for each of the grains. It is apparent, that the two branched cracks deviate almost 45° in respect to the specimen surface. Moreover, the crack in G3 does not continue growing along the active slip plane marked in Fig. 9.1.9 but follows the plane  $(11\bar{1})$  oriented about 45° to the loading direction (direction of the highest shear stresses). It is also important to mention that grain boundary is highly deformed probably by high plastic deformation caused by the impingement of the PSMs at the GB and in some locations short secondary cracks started to growth from the notch-like defects.

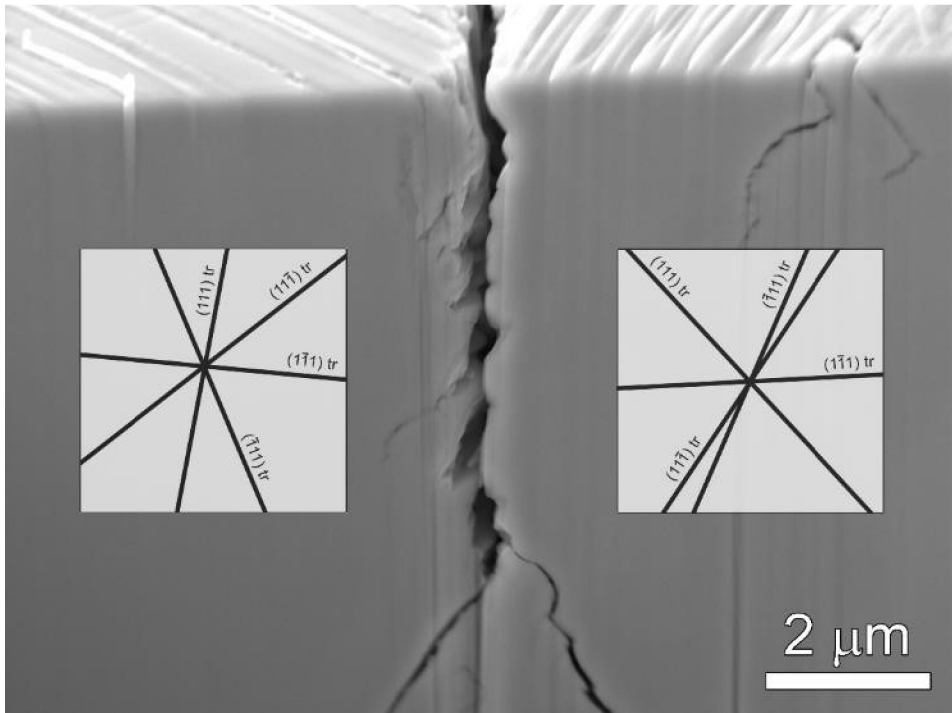


Figure 9.1.10: Detail of cracked grain boundary marked by dashed rectangle in Fig. 9.1.9.

### 9.1.3. Crack initiation from inclusions

Fatigue crack initiation from inclusions has been observed only rarely. Figure 9.1.11 shows the surface of the fatigued specimen with spherical inclusion of about 2 μm in diameter. Four cracks were observed to initiate from this inclusion as shown in detail in Fig. 9.1.11. The inclusion was probably debonded from the matrix early in cyclic straining. Later it was acting as the stress concentrator in terms of notch effect around the inclusion and fatigue cracks initiated from the inclusion. Within the neighboring grains well developed PSMs are apparent. The initiated cracks continued their growth along the PSMs as is clearly seen in Fig. 9.1.11.

Crack initiation mechanism is similar to the initiation in PSMs, but the stress concentration is limited to the short distance from the inclusion. Direction of the early very short cracks is in accord with the features typical for PSMs in a distance from the inclusion. With further cycling, the crack continues to grow along the well-developed PSMs. However, the direction of the crack growth has a tendency to grow on average perpendicular to the loading direction. The early growth of the crack is strongly affected by the PSMs direction.

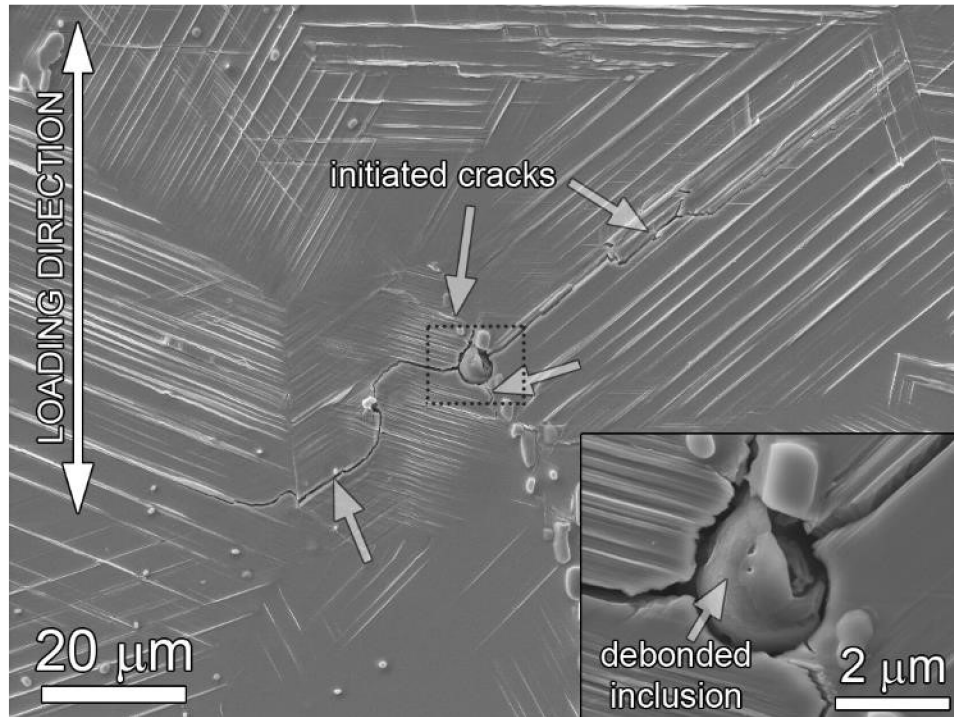


Figure 9.1.11: Crack initiation from the inclusion marked by white arrows and its further growth along PSMs in a specimen cyclically strained with total strain amplitude  $\epsilon_a = 6 \times 10^{-3}$ . Debonded inclusion with initiated cracks is shown in the inset.

#### 9.1.4. Crack initiation statistics

Preferential mechanisms and sites of the fatigue crack initiation were closely studied in specimens cyclically loaded with different total strain amplitudes. The fractions of all studied possible sites, where the crack initiation could be identified, i.e., in PSMs, PSMs along the TBs, GBs and close to inclusions were evaluated. Graphs in Fig. 9.1.12 show the percentage of the cracks initiated in 4 locations during cycling with small ( $2.5 \times 10^{-3}$ ) and high ( $6 \times 10^{-3}$ ) strain amplitudes. As can be seen, no crack initiation at the GB as the result of the slip band impingement on the GB was documented in the case of small strain amplitude cycling. All initiated cracks observed close to grain boundaries were initiated as the result of enhanced slip activity and development of PSMs. Unlike that, small fraction of cracks initiated at GBs was observed in the case of high strain amplitude loading. The inclusions played only a minor role in crack initiation in cycling with both low and high strain amplitude. Only approximately 1% of all studied cracks initiated from or was passing through inclusions. Twin boundaries were found to be often associated with the appearance of PSMs as reported in previous section. By comparing statistics in Fig. 9.1.12, it is apparent that the effect of TBs on the formation of PSMs and subsequently on the crack initiation along the TBs increases with increasing applied strain amplitude from 10% to 30%. Nevertheless, crack initiation along the PSMs developed within the grains plays a predominant role in both low and high strain amplitude loading. Because the initiation along the TB is associated with the production of PSM adjacent to TB, we can conclude that PSMs are the principal sites where the fatigue crack initiation was observed in both low and high strain amplitude cyclic loading.

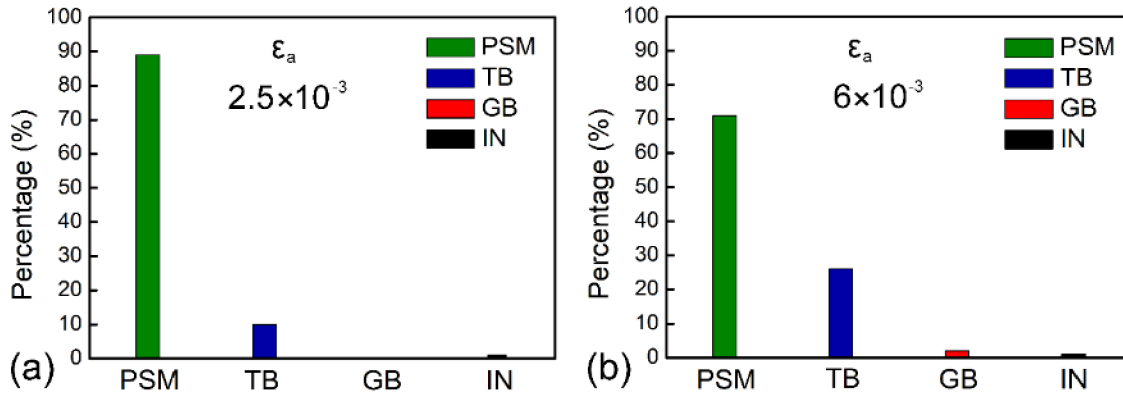


Figure 9.1.12: Fatigue crack initiation type for low ( $2.5 \times 10^{-3}$ ) and high ( $6 \times 10^{-3}$ ) total strain amplitude. PSM—persistent slip marking (PSB in the grain), TB—twin boundary (PSB along the TB plane), GB—grain boundary, IN—inclusion

## 9.2. Surface relief evolution in the form of PSMs

The main mechanism of the fatigue crack initiation observed during low cycle fatigue at room temperature was subjected to further thorough investigations using SEM and STEM. Since the major part of initiated and growing cracks is related to the fatigue-induced surface relief the following section is focused on the evolution of PSMs and corresponding internal dislocation structure.

### 9.2.1. STEM characterization of PSM profiles and corresponding dislocation structures

Symmetrical cycle (zero mean strain) with constant strain amplitude  $5 \times 10^{-3}$  was applied to the specimen. The saturated plastic strain amplitude at a number of cycles corresponding to the half of the fatigue life was  $\epsilon_{ap,s} = 3.14 \times 10^{-3}$  and the number of loading cycles to fracture was  $N_f = 9\,250$ . It corresponds to the elastoplastic cyclic loading still in the domain of low cycle fatigue.

Grain with several parallel PSMs oriented approximately perpendicular to the loading axis was chosen for further inspection (see the description of the method in Chapter 7.2). Specimen surface was documented using SEM as shown in Fig. 9.2.1. Micrograph reveals PSMs consisting of system of extrusions and parallel intrusions and possibly Stage I cracks. The true shape of some PSMs and their variability can be judged from the high-resolution SEM picture of some PSMs from this grain shown in the inset in Fig. 9.2.1a. Nevertheless, the information about the profile of PSMs in the direction perpendicular to the specimen surface and about intrusions and shallow initiated cracks is missing.

In order to see the exact profile of the PSMs in three dimensions, the rectangular area on the surface marked by the white rectangle shown in Fig. 9.2.1a was covered with platinum. Later FIB cutting was used to produce thin lamella which could be observed both in SEM and TEM. The shapes of five PSMs imaged in SEM using back-scattered electrons on the lamella and denoted as A, B, C, D and E are examined in Fig. 9.2.1b. It is evident that PSM C consists of two separate PSMs. Central extrusion, two parallel intrusions on both sides of the large extrusion and Stage I crack starting from the intrusion on the right side of the large extrusion are visible.



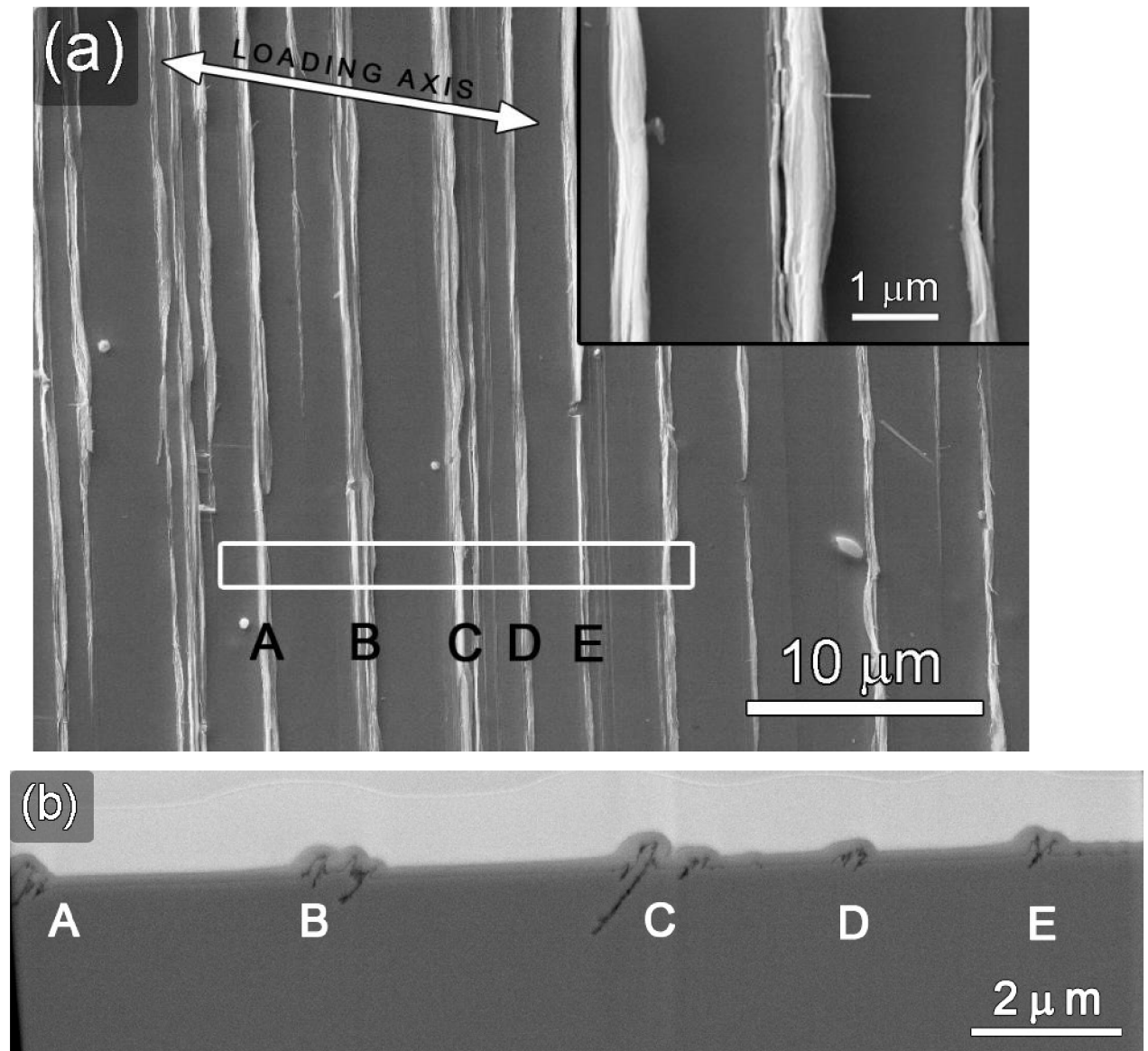


Figure 9.2.1: Shape of the persistent slip markings. Specimen was cycled with  $\epsilon_a = 5 \times 10^{-3}$ . (a) Secondary electron image of specimen surface after fatigue. The position of future lamella containing five PSMs is marked by triangle. (b) BSE image of FIB cut showing shape of five developed PSMs with several initiated cracks.

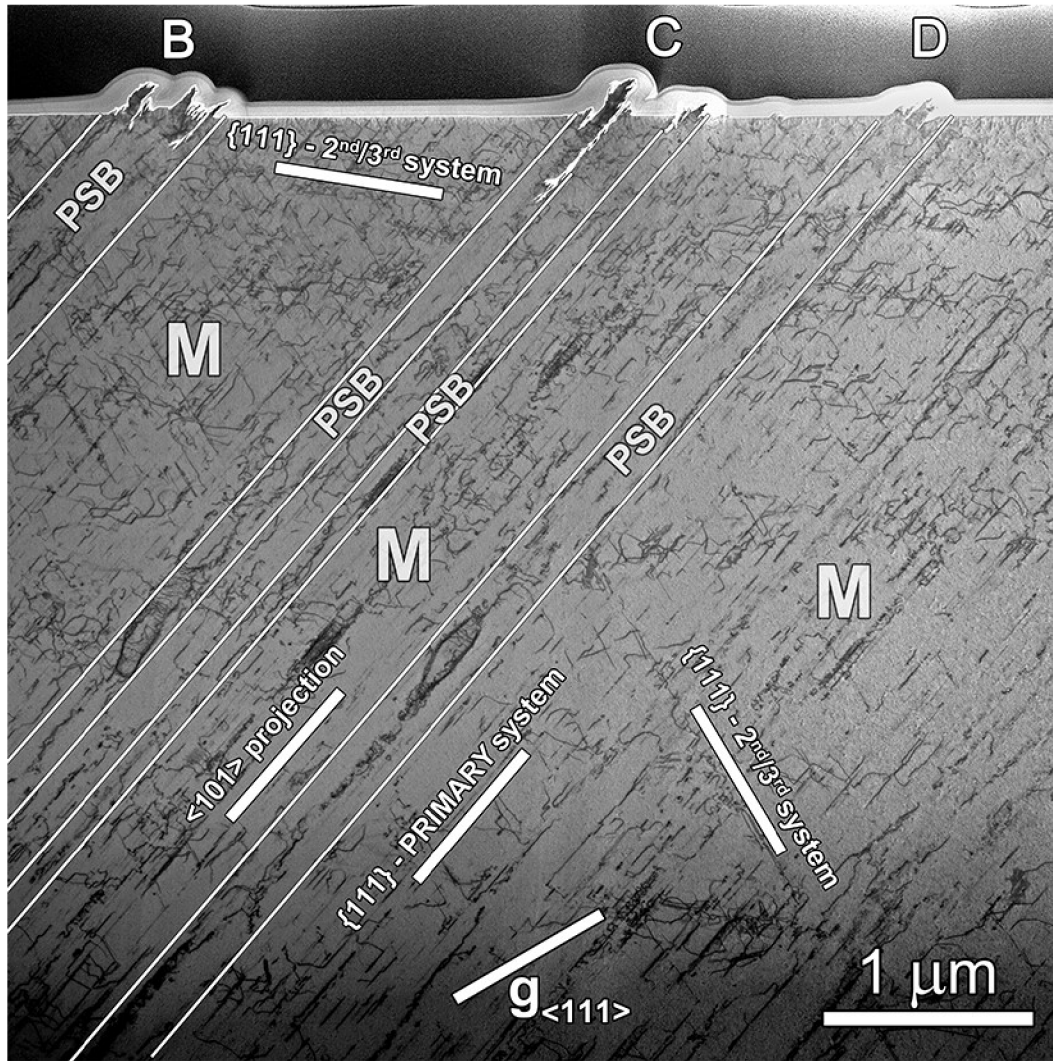


Figure 9.2.2: Large area of the surface lamella showing the surface relief (PSMs B, C and D) and underlying dislocation structure as obtained by STEM in bright field.

The shape of PSMs B, C, and D along with the dislocation structure below the surface as imaged in STEM bright field as shown in Fig. 9.2.2. Dislocation bands produced by the activity of three slip systems can be traced in the image. Dislocation structure has been analyzed using different diffraction vectors. Three activated slip systems were clearly identified and are marked by corresponding labels in the image. Dislocations from the primary system are most pronounced and we have marked the bands corresponding to areas of the intensive slip i.e., PSBs that participate in the formation of PSMs. PSBs are oriented parallel to the trace of the primary slip plane. Primary Burgers vector  $\langle 101 \rangle$  was projected into the micrograph. The remaining areas are denoted as M, i.e., matrix. Using zero contrast condition it was proved that only dislocations from the primary system and no dislocations from the secondary and tertiary systems are present in PSBs. This yields evidence that intensive cyclic slip in PSBs was able to eliminate all secondary dislocations that were produced presumably in the early stages of cyclic loading. No distinctive ladder-like dislocation structure was found. The dislocation arrangement in PSBs does not differ notably from the dislocation arrangement of the neighbor matrix. Nevertheless, within the marked bands some patches having high dislocation density and inclined at an angle to the trace of primary slip plane irregularly alternate with areas of low dislocation density. This

arrangement allows not only the production of point defects by dislocation interactions but also their migration from dislocation-poor areas to the dislocation-rich areas serving as sinks for point defects.

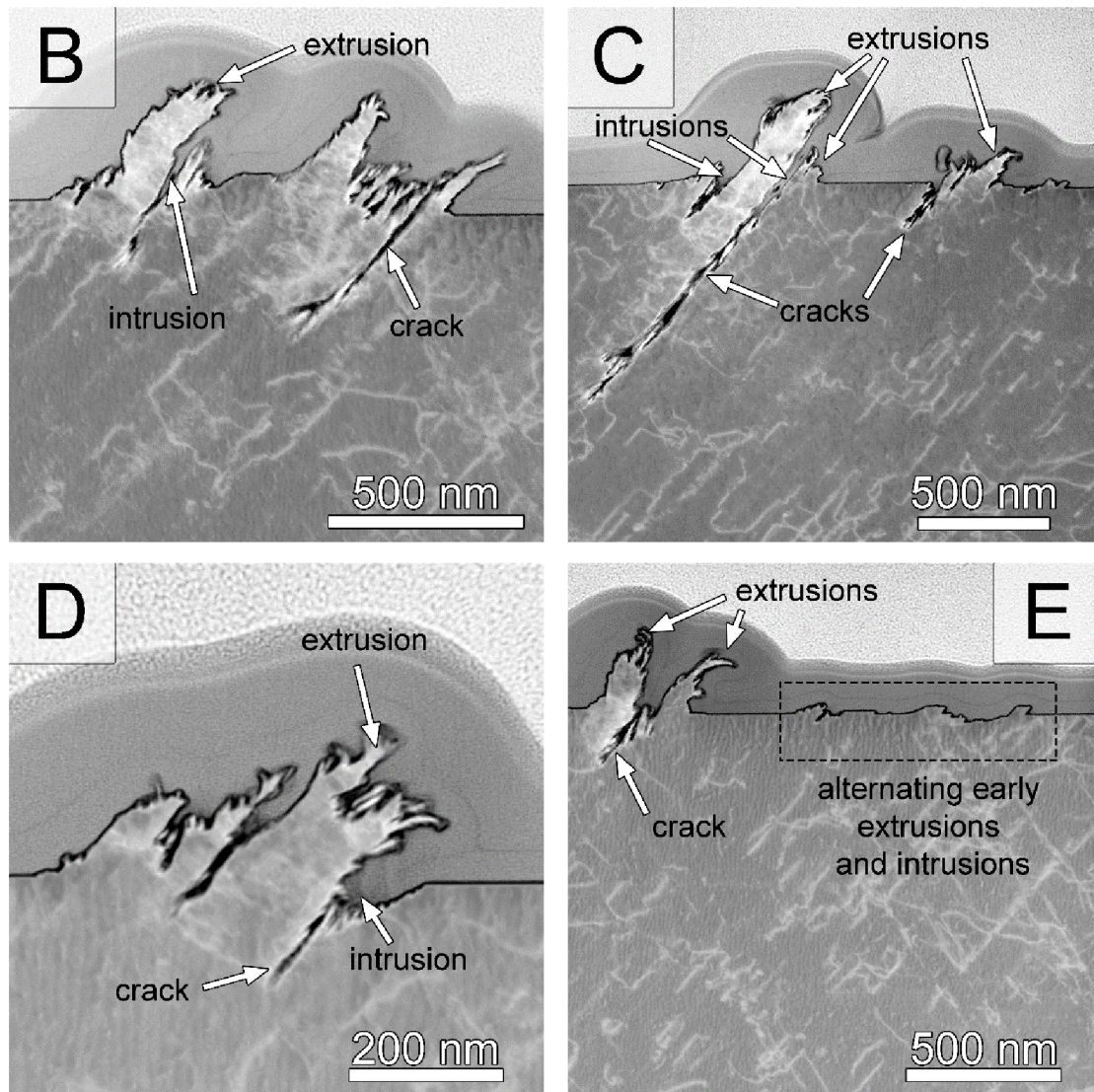
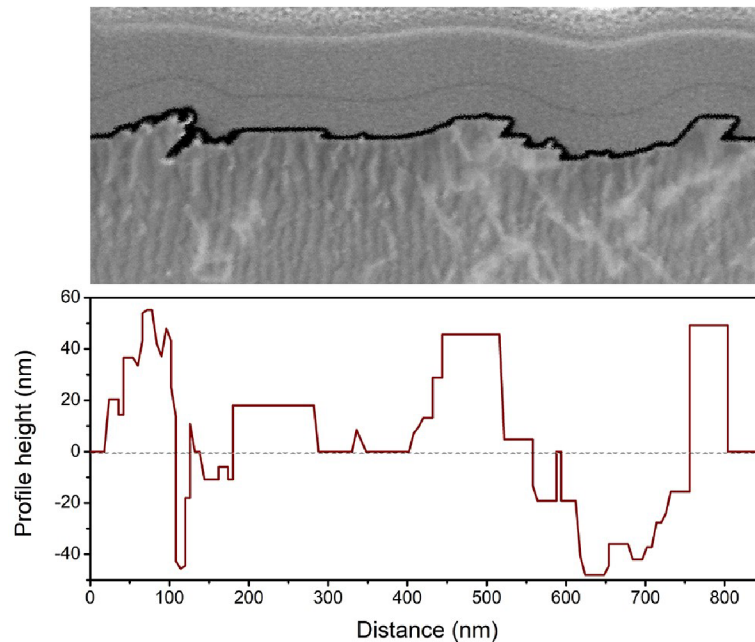


Figure 9.2.3: STEM dark field images show profiles of four PSMs B, C, D and E. PSMs consist of extrusions and intrusions. Stage I cracks initiated from the intrusion-like defects.

Figure 9.2.3 shows the dark-field STEM images of the areas of foil with detailed profiles of PSMs B, C, D and E, and only a small area of the dislocation structure below each of them. Mostly elevations of the surface (extrusions) are typical for all PSMs. Nevertheless, intrusions are easily distinguished. PSM B consists of three large extrusions and multiple smaller extrusions and intrusions. Its surface width is  $1.4 \mu\text{m}$ . Both wide extrusions have tiny extrusions and intrusions at the top. The extrusions occupy substantially higher volume than intrusions. Very thin extrusions and intrusions (10 nm in width) are also detected. A distinct intrusion partly cutting the extrusion to the right of the first extrusion is denoted by an arrow. The platinum was able to infiltrate into the intrusion though its width is only 20 nm. No deep intrusion accompanies the central extrusion but alternating extrusion/intrusion

geometry is present between the central and the right extrusion. A thin intrusion which extends as Stage I crack (denoted by an arrow) adjoins the third extrusion. Platinum did not penetrate into the crack and this allows us to distinguish between intrusions and cracks. Neither intrusion nor the crack is present on the right side of the third extrusion though high stress concentration at this location is expected.



*Figure 9.2.4: STEM dark field image of steps next to PSM E from Fig. 9.2.3 in the form of extruded and intruded material. Analysis of surface relief in the direction of primary slip plane trace.*

In PSM C, instead of one PSM two separate PSMs are present. The larger PSM to the left consists of central extrusion accompanied by intrusions on both sides of the extrusion. Again, platinum was able infiltrate deep into intrusions but not any further into the cracks. In this way, the end of intrusion and the start of the Stage I crack can be distinguished. The extrusion height above the surface is around 360 nm. The width of the intrusion to the left of the central extrusion from which no crack developed is 60 nm. From the intrusion developed to the right of the extrusion, a short crack has already arisen. It runs parallel to the primary slip plane and its depth (in the direction parallel to the trace of the slip plane) is around 1.1  $\mu\text{m}$ . The fine structure of the large extrusion consisting of tiny sharp intrusions and extrusions is visible. The smaller PSM to the right of the principal PSM consists again of an extrusion and parallel intrusion to the left of the extrusion from which a small crack started to develop. Within the extrusion, another thin intrusion or even a starting crack has arisen. Very similar features, i.e., alternating large extrusions and thinner intrusions could be seen in the images of PSMs D and E whose details are shown in Fig. 9.2.3 as well. A disposition of fatigue crack initiation in the tip of deeper intrusions is apparent in many more cases.

Steps of cyclic slip irreversibility arising at the surface marked in Fig. 9.2.3 on the right side of PSM E were analyzed in the direction of the primary slip plane trace. Their height and depth was measured as the difference from the electrolytically polished specimen

surface and the results are shown in Fig. 9.2.4. At the upper part of the image the DF-STEM shows the profiles of early stage growth of secondary PSMs. Under the PSMs no specific dislocation structure as in the case of PSMs B, C and D (see Fig. 9.2.2) is observed. Below that, the corresponding profile steps are measured in the direction of the primary slip plane trace highlighted in Fig. 9.2.2. The average height of three highest extrusions shown in Fig. 9.2.4 was found to be about 50 nm. The height of the highest extrusion was 56 nm. The average depth of the deepest intrusions was found to be about 42 nm, which is lower than the height of the extrusions. It is evident that from the measured profile that the volume of extrusions is bigger than that of the intrusions. The shape of most of the extrusions is the rectangle. The alternating protruded and depressed parts within one PSM are notable mainly in the case of PSM on the left side (see Fig. 9.2.4). The flat shape of the PSMs is apparently due to the early stage of the PSB evolution.

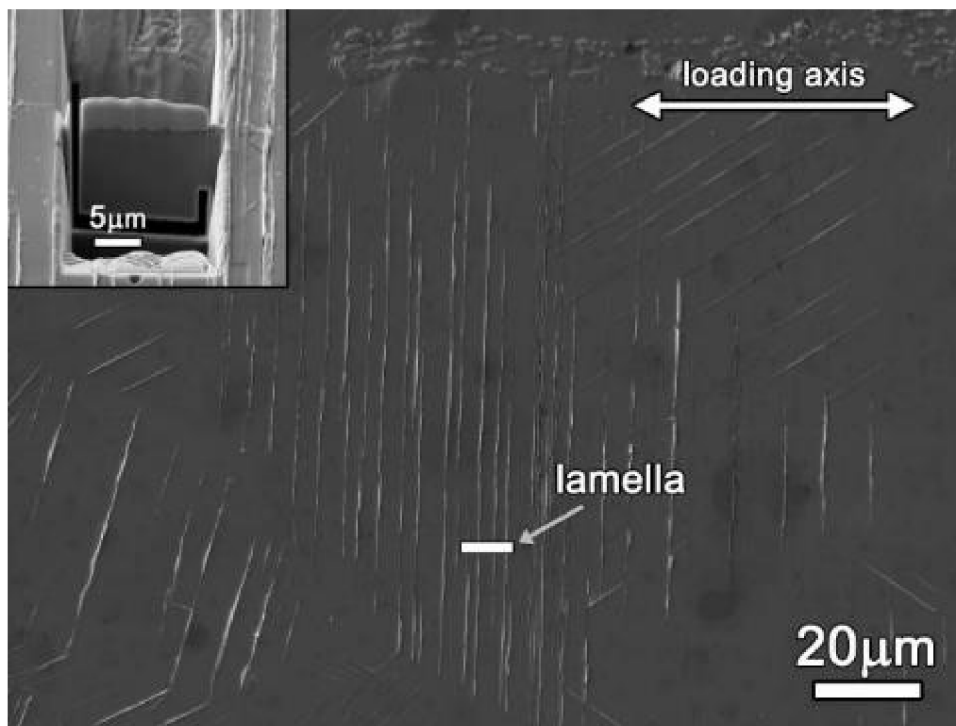


Figure 9.2.5: Grain of fatigued Sanicro 25 steel cycled with total strain amplitude  $2.5 \times 10^{-3}$ . Persistent slip markings and the position of the lamella within the grain.

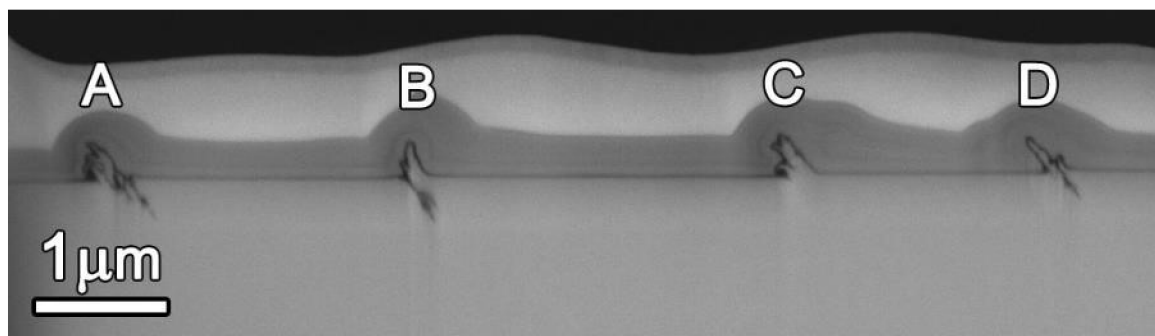


Figure 9.2.6: BSE micrograph of the profile of persistent slip markings on the focused ion beam cut of the lamella.

The surface area of the specimen cycled with constant total strain amplitude  $2.5 \times 10^{-3}$  to 10 000 cycles ( $\sim 1/10 N_f$ ) is shown in Fig. 9.2.5. The grains with PSMs approximately perpendicular to the stress axis were inspected using SEM. After FIB cutting and foil preparation, they were observed in TEM. Figure 9.2.5 shows parallel PSMs in one grain, all perpendicular to the loading axis. It also shows the position of the lamella. Covering the surface with platinum and using FIB cutting, we were able to see the profile of four PSMs on the perpendicular cut (see Fig. 9.2.6). Preferably extrusions, possibly intrusions and small starting cracks are recognized using the resolution of FESEM. Higher resolution of the profile and also the image of the dislocation structure below the surface are obtained by thinning the lamella and its observation in STEM.

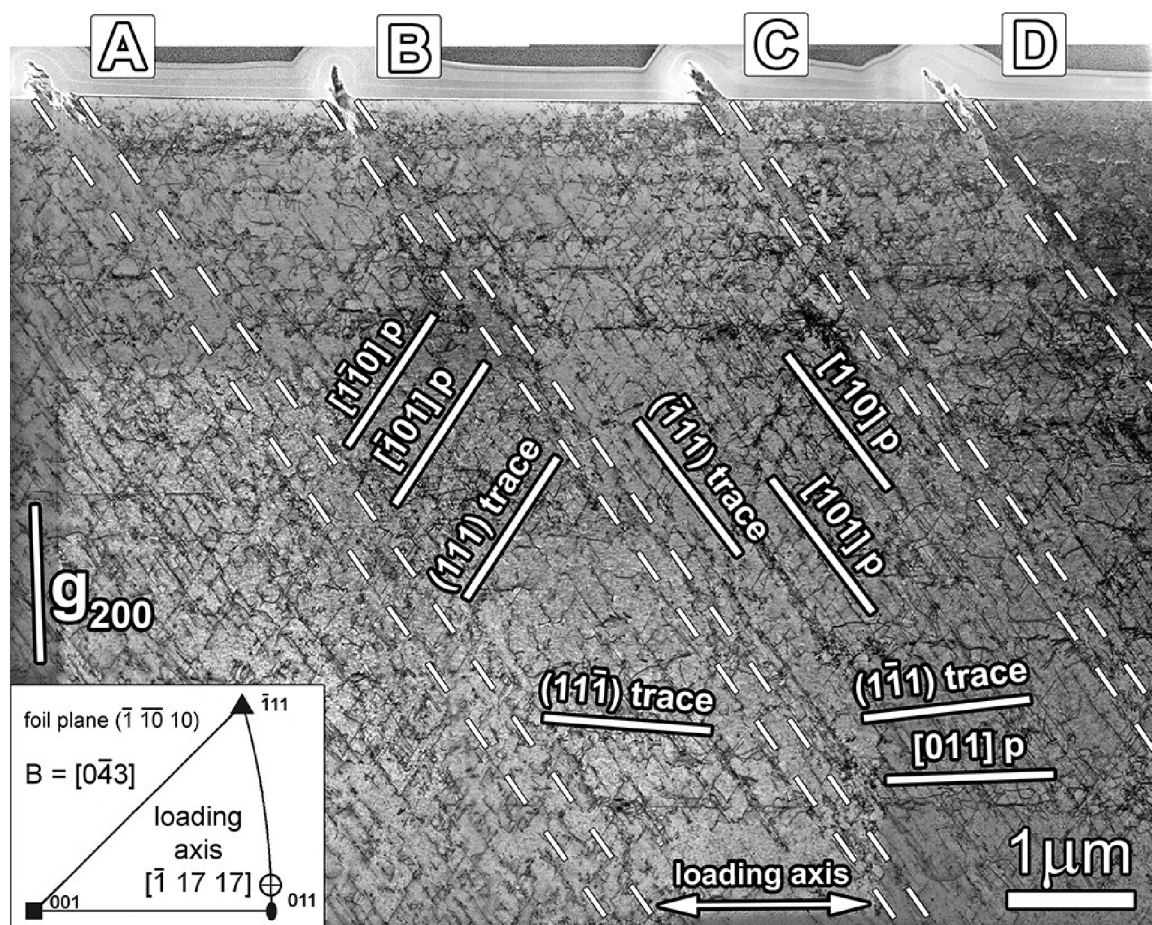
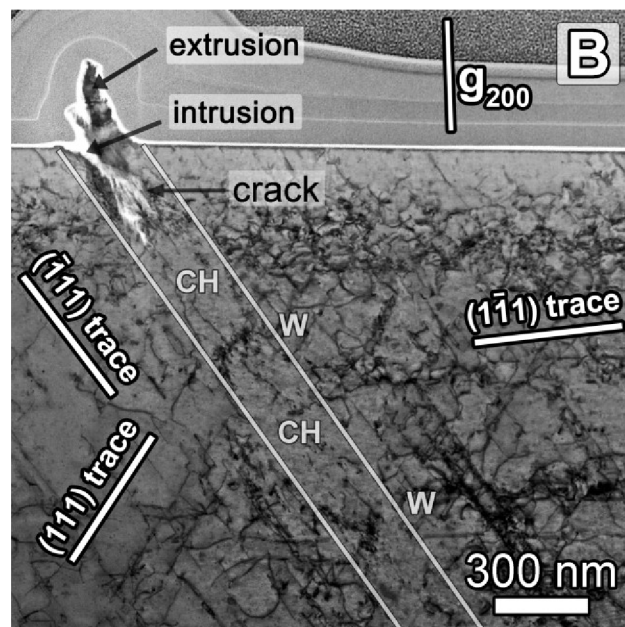


Figure 9.2.7: Scanning transmission electron microscopy image of the surface lamella from fatigued Sanicro 25 steel showing profiles of persistent slip markings and underlying dislocation structure. Persistent slip bands are marked using dashed lines. Inclination of both primary slip plane ( $\bar{1}11$ ) and secondary slip plane (111) with respect to the electron beam direction was  $7^\circ$ .

Figure 9.2.7 shows that the grain orientation is close to [011]. Using the diffraction condition, we can distinguish dislocations belonging to three slip systems which are activated in the grain. Primary slip plane corresponding to the PSBs was ( $\bar{1}11$ ) plane although Schmid factors on the (111) plane are slightly higher. We have inspected the foil using four different diffraction conditions to analyze the types of dislocations both in the

matrix and in PSBs. By tilting the specimen in such a way that we can observe deformation microstructure from different crystallographic directions and angles, we get information on spatial arrangement of dislocations and other crystallographic features. Using this analysis, all  $\{111\}$  planes and all  $\langle 110 \rangle$  slip directions could be thus identified. The inspection of dislocation structure using the invisibility criterion revealed that in the matrix, not only dislocations corresponding to  $(111)[101]$  primary slip system (mostly screw dislocation segments) are present but also dislocations from secondary slip systems  $(111)[101]$  and  $(111)[011]$  are active. Four PSBs in Fig. 9.2.7 running from the PSMs parallel to the primary slip plane are marked. The position of the line is based on the detailed analysis of the spatial arrangement of dislocations in the foil. Dislocation density in PSBs is generally lower than in the neighbor matrix. Closer inspection reveals that dislocation rich bands corresponding to the secondary slip systems are interrupted in locations where they intersect PSBs, that is dislocations of secondary slip systems are absent in PSBs. Apparently, the high slip activity of primary dislocations helps to annihilate the dislocations of secondary slip systems in PSBs (see Discussion section). Thus, the detailed analysis of the type of dislocations using different diffraction conditions allowed delineating the areas corresponding to PSBs.

Figure 9.2.8 shows the profile of PSM B at high magnification simultaneously with the neighbor dislocation structure below the surface. The profile of PSM consists of pronounced extrusion and a small parallel intrusion from which a crack started to develop. Appreciable dislocation density is found in the matrix consisting of dislocations of both primary and secondary slip systems. The width of the PSB running parallel to the primary slip plane is only 210 nm. PSB B has ladder-like dislocation structure of alternating rungs and channels although only two irregular rungs with high dislocation density are present in the area of PSB B in Fig. 9.2.8. Low dislocation density is present in all three channels.



*Figure 9.2.8: Detailed image of the persistent slip marking B showing the persistent slip markings consisting of extrusion and intrusion and a crack starting from the tip of the intrusion. Dislocation arrangement in the persistent slip band is ladder-like.*

## 10. Crack growth of natural short cracks at room temperature

### 10.1. Crack growth path of natural cracks

#### 10.1.1. Stage I fatigue crack growth along PSM/PSB

Figure 10.1.1 shows initiated Stage I fatigue cracks in the early stage of fatigue life as well as in the later stage of fatigue life. The area of the interest with several developed PSMs was covered by the platinum layer. FIB cut cross section revealing parallel initiated Stage I fatigue cracks is shown in Fig. 10.1.1a. FIB cut was milled perpendicularly to the specimen surface and to the direction of PSMs denoted as A to F. Strong localization of the plastic strain into the PSBs and subsequently the formation of surface relief in the form of PSMs lead to the multiple crack initiation in 1 grain. The cracks initiated in PSMs C, D, and E continue to grow along the parallel planes corresponding to the primary  $\{111\}$  slip plane. They are inclined at around  $45^\circ$  to the specimen surface. Figure 10.1.1b shows the specimen surface at a later stage of the fatigue life. In addition to primary cracks initiated along the well-developed PSMs, also secondary cracks initiate in secondary PSMs. These short secondary cracks link parallel primary cracks.

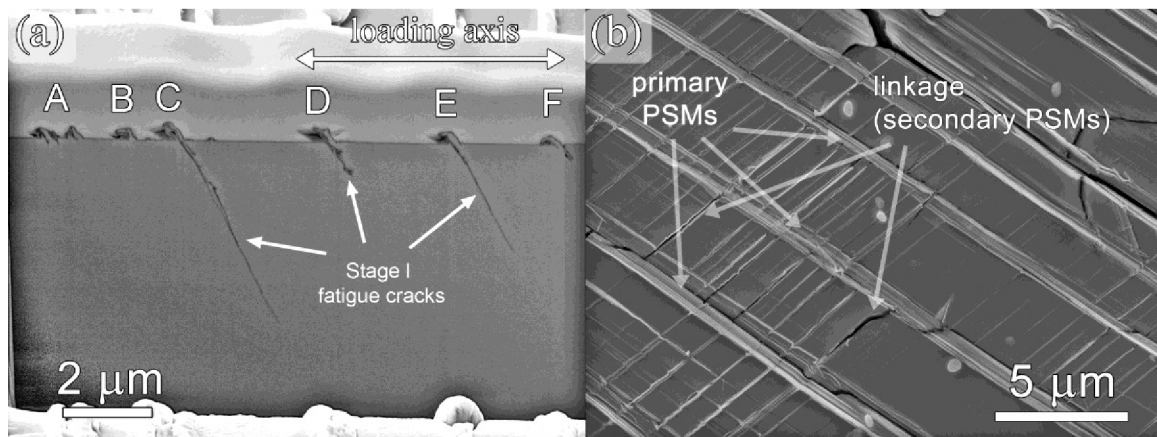


Figure 10.1.1: FIB section of a grain showing multiple crack initiations inside the grain and early growth in crystallographic direction (a); linking of 2 cracks, which initiated in parallel PSMs by secondary cracks after further cycling (b).

#### 10.1.2. Crack growth at the surface

The evolution of the internal dislocation arrangement plays an important role in the fatigue crack initiation as well as in the short crack growth. It was shown above that the natural cracks prefer to initiate along the PSMs from the intrusions. In order to see the details of the short crack growth, several SE micrographs of the different locations on the specimen surface were taken during cyclic loading. Multiple crack initiations in 1 grain have been found frequently (see Fig. 10.1.1). During further cycling, PSMs corresponding to the slip systems having low Schmid factors were also produced on the specimen surface. The cracks in these PSMs act as the bridges between the cracks which initiated along the primary slip systems. The linkage of cracks contributes to the early growth of natural fatigue cracks in the general direction perpendicular to the loading axis. This mechanism is typical for the



early growth of fatigue cracks within the grains. The central part of the grain of a size approximately  $500\ \mu\text{m}$  with long PSMs is shown in Fig. 10.1.2. The area was large enough to accommodate the initiation and growth of several individual cracks (cracks C1, C2, and C3) having the surface length of approximately 100 to  $150\ \mu\text{m}$ . Shallow initiated cracks running parallel with PSMs are mutually linked by activation of secondary slip systems (see the detail in Fig. 10.1.2). In spite of the fact that no other distinctive marks which correspond to the secondary slip systems are present on the specimen surface, the cracks coalesce along these systems.

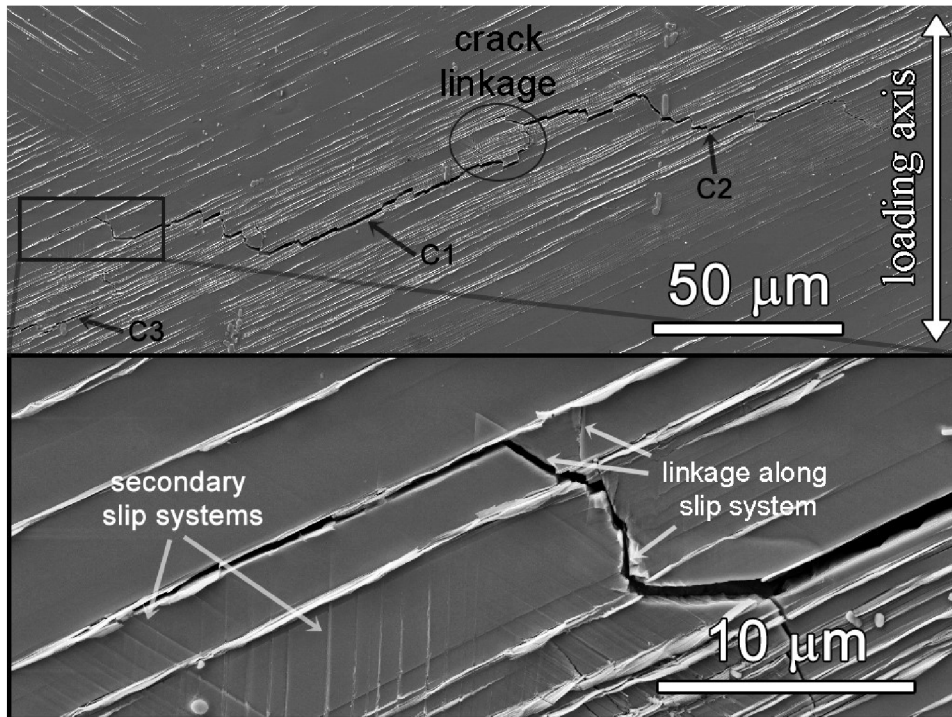


*Figure 10.1.2: Multiple crack initiation along PSMs in 1 surface grain. The upper image shows the central part of the grain with 3 cracks C1, C2, and C3. The detail shows how the cracks initiated along PSMs corresponding to primary system are linked by the cracks along the secondary slip systems.*

The growth of one of the largest cracks observed in the notch area of sample fatigued by strain amplitude  $3.2 \times 10^{-3}$  shows Fig. 10.1.3. At the beginning of cycling only individual PSMs developed at the free surface of grains. Later, after about 3000 cycles, small cracks initiated along these PSMs as marked by white arrows. Their length was less than grain size. By further cycling the longer cracks developed (see image corresponding to 9000 cycles). Individual initiated cracks along the PSMs appearing in close vicinity connected into one crack. Two cracks close to each other were grown as marked by white arrows. Later in the fatigue life they merged together creating one crack of the length  $2a$ .

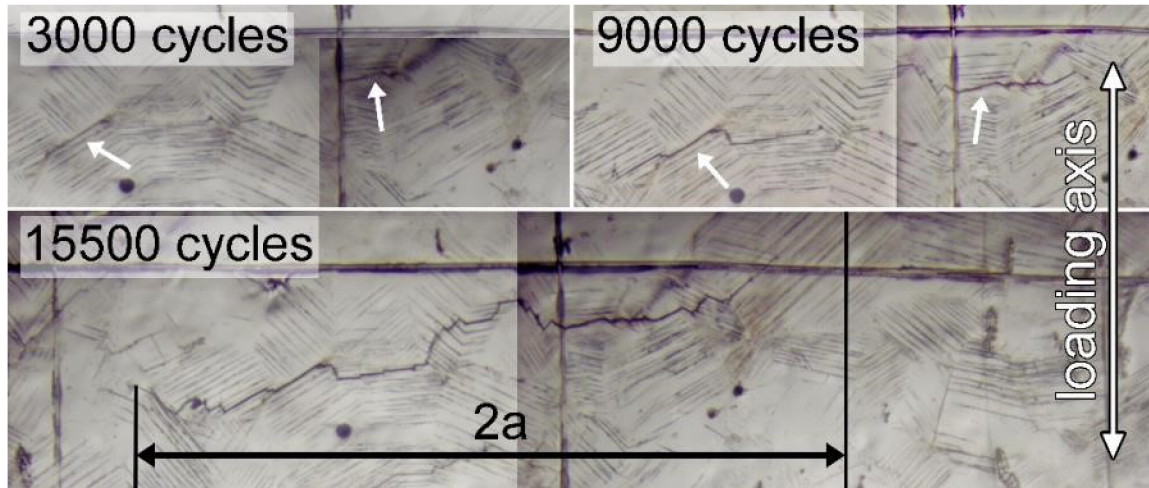


Figure 10.1.3: Micrograph obtained by optical microscope shows the growth of the surface crack by mutual linkage of previously initiated fatigue cracks. The specimen was cyclically loaded by  $\varepsilon_a = 0.32\%$ .

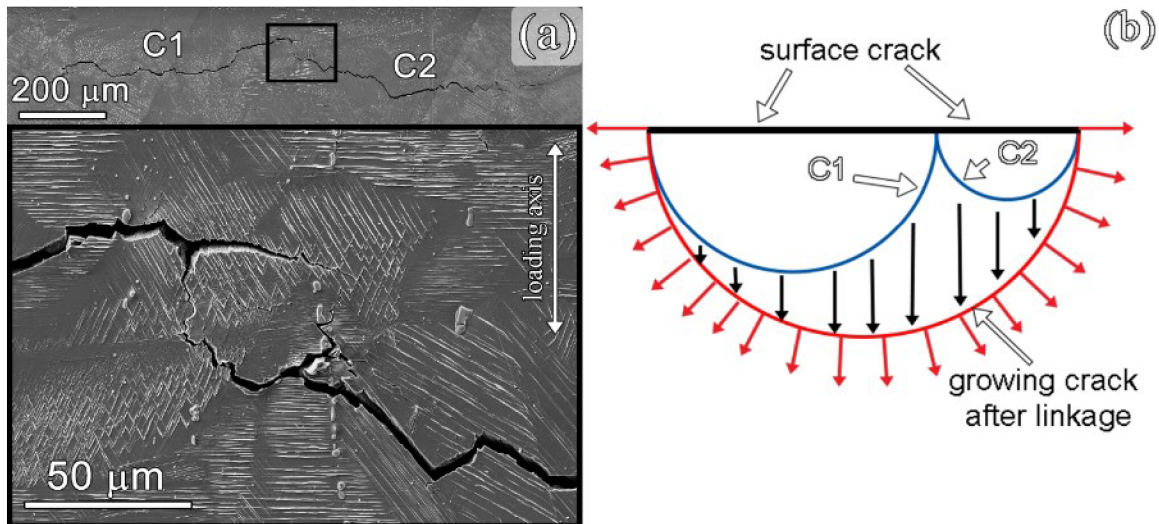


Figure 10.1.4: Linkage of 2 cracks C1 and C2; (a) SEM image in cycling with  $\varepsilon_a = 0.7\%$ . Detailed image below shows the area where both cracks interlinked; (b) schematic image of linking cracks in the bulk of the material. Growing crack at the surface and in the bulk after the mutual linkage is shown in red, and the growth is marked by arrows.

The coalescence of two cracks is often accompanied by crack branching. Two cracks C1 and C2 are shown in Fig. 10.1.4a. Due to the linking, the surface length of a crack increases suddenly but stops increasing further until the crack shape in the bulk achieves approximately semicircular shape as marked in Fig. 10.1.4b. The surface length of both cracks is approximately  $600\ \mu\text{m}$ . The position of the linkage highlights the black rectangle, and it is imaged in detail in the bottom part of Fig. 10.1.4a. The linkage has been accompanied by the crack bifurcation.

The crack paths on the surface were studied on the specimens loaded with small and high total strain amplitudes to determine the prevailing mechanisms of the surface crack growth. Approximately 25 cracks of different surface crack length were studied in each of the

specimens subjected to low ( $\epsilon_a = 0.25\%$ ) and high ( $\epsilon_a = 0.6\%$ ) strain amplitude cycling. By comparison of EBSD micrographs with SE micrographs of the surface cracks, the fraction of the total surface crack length corresponding to 1 of 3 types of crack growth path (i.e. along the TB, very close to GB, and along the PSMs within the grain, i.e., transgranular crack (TC) were identified for each crack. Figure 10.1.5 shows semilogarithmic plot of the crack path fraction vs. the total surface crack length. The results manifest the dominance of the TC path in specimens cycled with both strain amplitudes. The fraction of TC path in the case of high strain amplitude loading slightly decreases with increasing crack length, but the scatter of the data is appreciable. To assess the character of the TC path, the grain orientation of the surrounding grains was determined using EBSD analysis. The fraction of the TC crack path along the equivalent  $\{111\}$  slip planes was determined as well. The traces of the crystallographic planes corresponding to  $\{111\}$  slip planes were derived from the grain orientation using Euler angles and are marked by white segments in Fig. 10.1.5. It is apparent that the crack paths along the  $\{111\}$  slip planes predominate. Nevertheless, crack propagating at high strain amplitude had the average fraction of the crack path along the  $\{111\}$  slip planes is lower (approximately 70%) compared with that at low strain amplitude loading (approx. 90%).

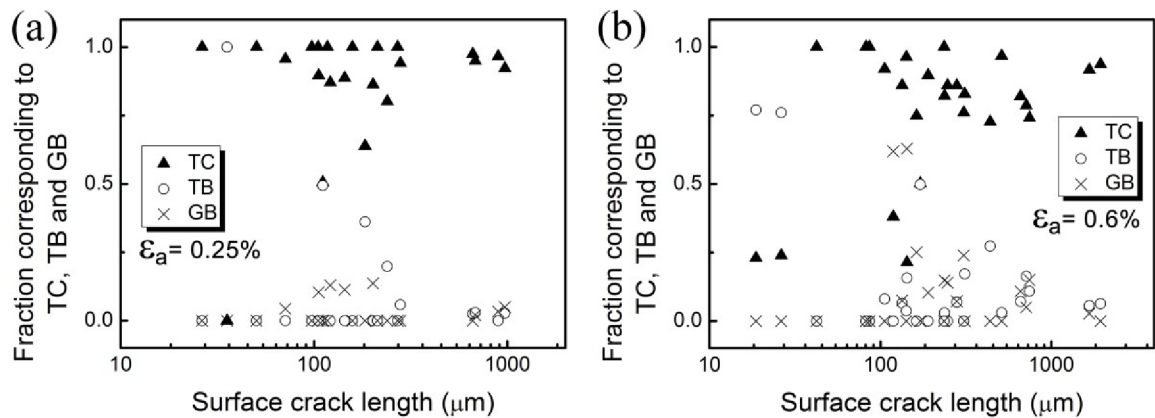


Figure 10.1.5: Fractions of 3 crack paths for low and high strain amplitude cycling. TC—Transgranular crack path (PSMs and secondary slip systems), TB—Twin boundary crack path (PSB along the TB plane), GB—Grain boundary crack path; (a) cycling with  $\epsilon_a = 2.5 \times 10^{-3}$ ; (b) cycling with  $\epsilon_a = 6 \times 10^{-3}$ .

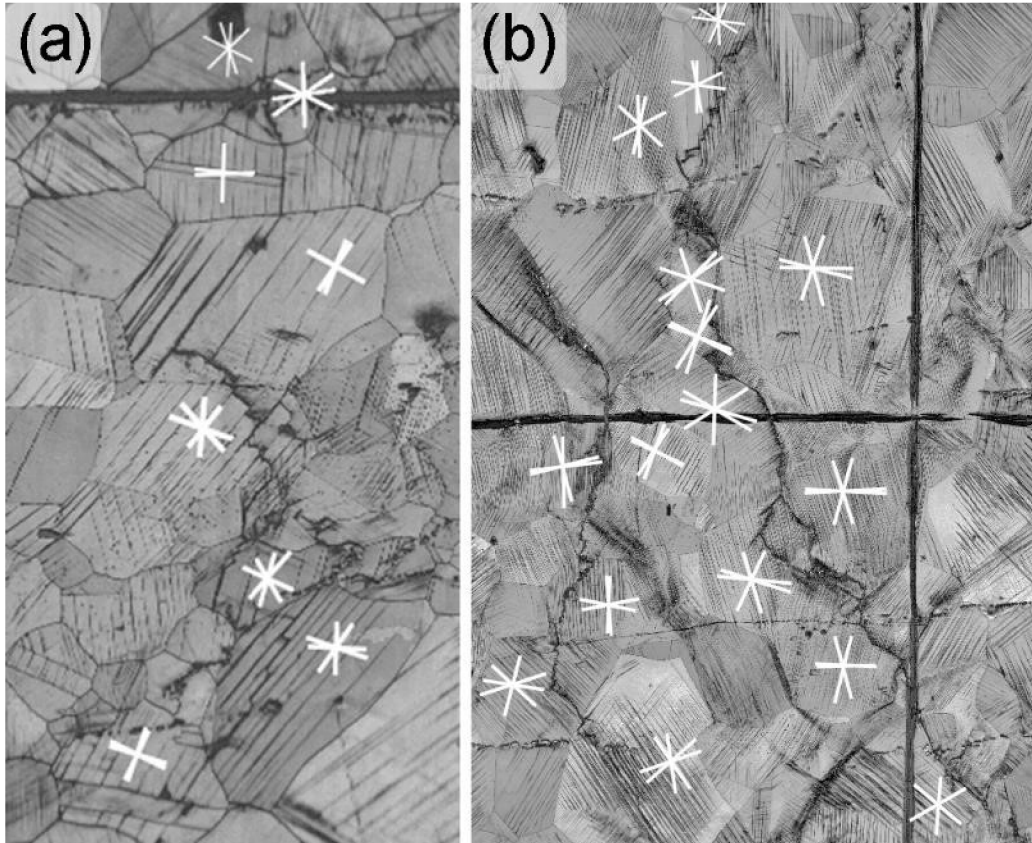


Figure 10.1.6: Typical crack paths in the specimen cycled with low and high strain amplitude; (a) cycling with  $\epsilon_a = 2.5 \times 10^{-3}$ ; (b) cycling with  $\epsilon_a = 5 \times 10^{-3}$ . The white segments indicate the traces of the equivalent  $\{111\}$  planes slip planes in all grains neighbor to the growing crack.

### 10.1.3. Crack growth in the bulk of the material

The crack growth mechanism in the bulk of the material was studied on the polished longitudinal section of the specimen gauge length. The specimen was cycled with total strain amplitude of 0.25 %. The example of the largest growing cracks as well as the early stage of crack growth is shown in BSE images in Fig. 10.1.7. The loading direction is horizontal. The individual grains and twins can be clearly recognized in image due to channeling effect of electrons. The microstructurally long crack (see Fig. 10.1.7a) grows preferentially in the trans-crystalline manner, however, some parts of the cracks path are parallel with the grain or twin boundaries. The results are very well in agreement with that observed at the specimen surface (see Fig. 10.1.5a). The crack has a tendency to propagate perpendicular to the loading axis, however, they often change their path direction (slip plane traces). The bifurcation of crack (white arrows) is apparent as well. The similar behaviour of the crack growth is found also in the case of microstructurally short crack (see Fig. 10.1.7b), which does not traverse the grain boundary. As discussed earlier the crack initiates along the PSM, which is parallel with the  $\{111\}$  slip plane trace. Nevertheless, it starts to deviate from its original direction (Stage I) and the crack grows in the Stage II crack growth along several slip planes.

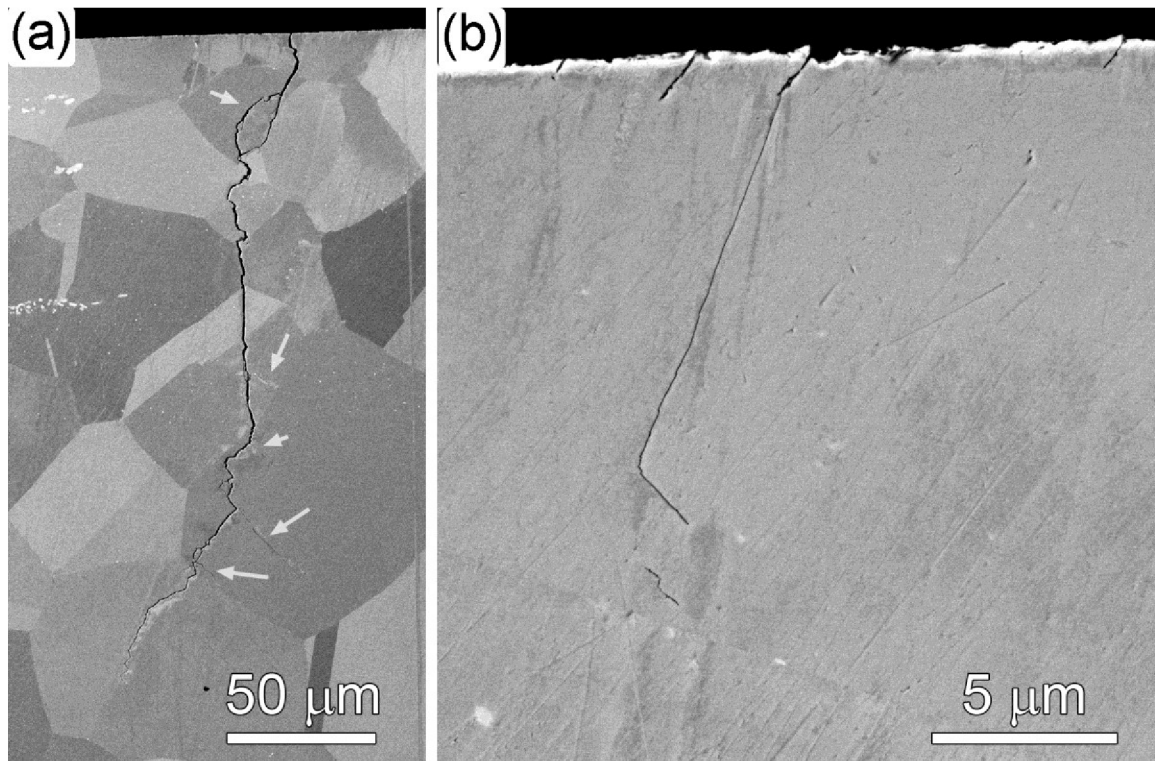


Figure 10.1.7: BSE micrographs showing typical growing cracks in the bulk of the sample cycled with  $\varepsilon_a = 0.25\%$ . Loading direction is horizontal. (a) Microstructurally long crack. The crack coalescence and the crack branching are marked by white arrows. (b) Microstructurally short crack.

The crack path analysed using the EBSD is shown in Fig. 10.1.8. The crack initiated at the TB. Later it slightly deviated from its original direction. In the grain 3 the crack path follows the  $\{111\}$  slip plane. No evident plastic deformation along the crack length is found in this grain. As the crack continues growing through the grain 4 it follows the  $\{011\}$  slip plane. In the grain 5 the crack has a tendency to grow along the  $\{011\}$  slip plane trace, however, it slightly deviated from this direction and grows along the  $\{111\}$  direction. The mixed mode of growing is apparent also in the grain 6. Here, some branching along the  $\{011\}$  slip plane trace is found. In the grain 7 the crack grows along the  $\{011\}$  plane trace and its growth is accompanied by the plastic deformation along the crack length. Contrary to that, the crack path changes in the grains 8, 9 and 10. The cracks follow other possible crystallographic planes.

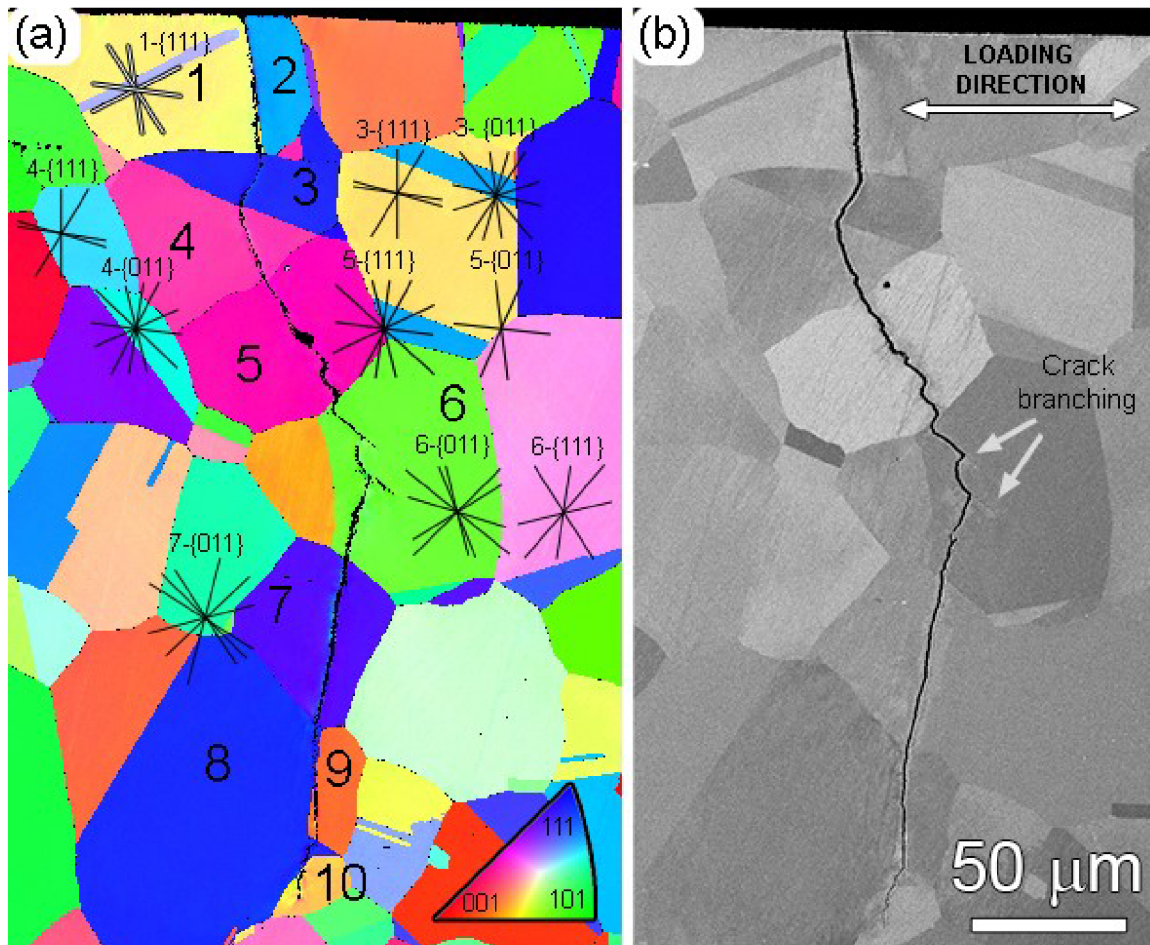
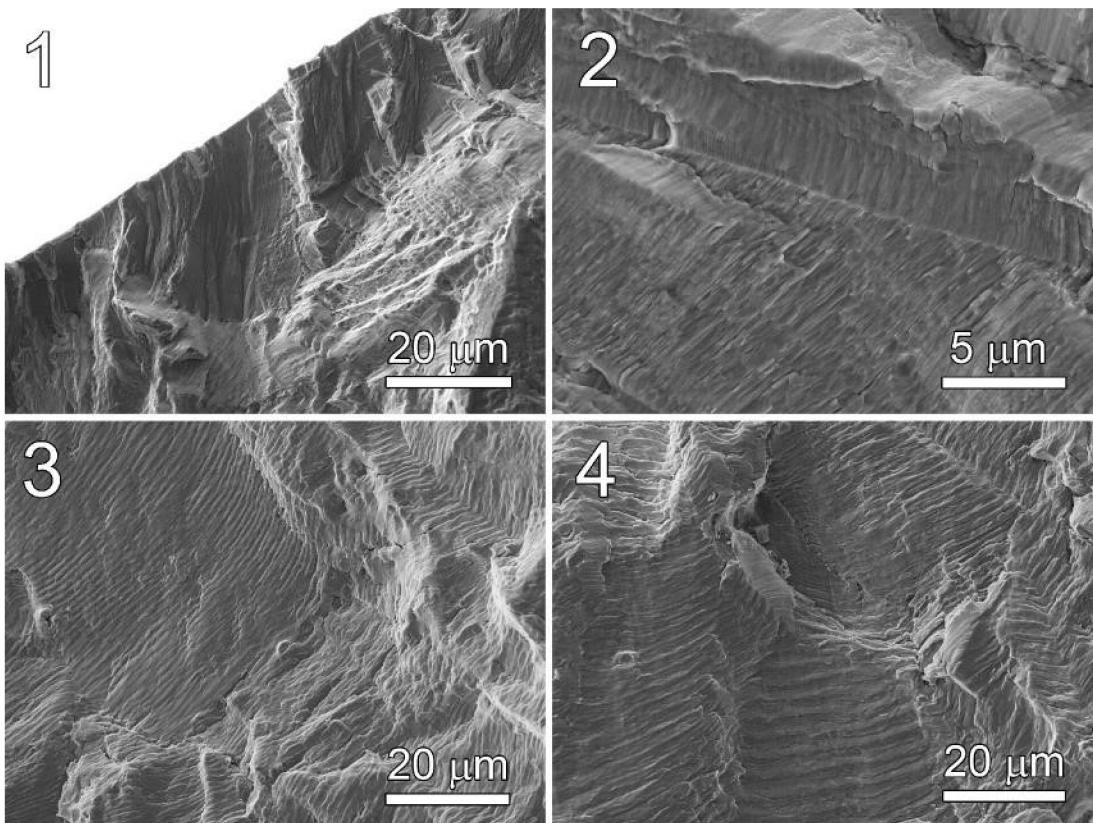
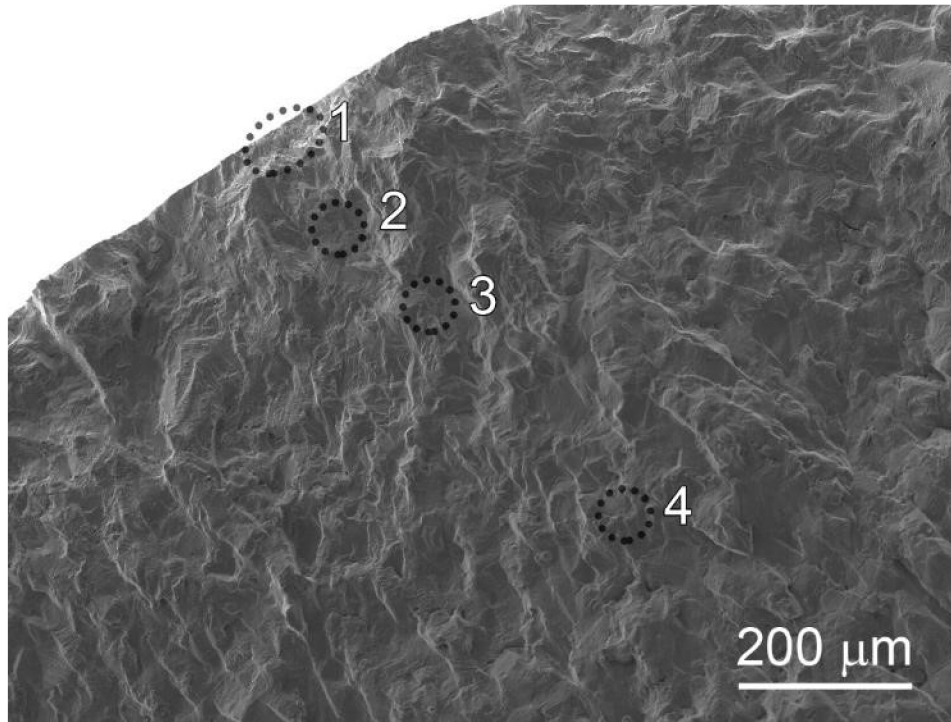


Figure 10.1.8: Crack path in the bulk of the material. Loading direction is horizontal. (a) EBSD analysis showing the grains orientation with individual  $\{111\}$  and  $\{011\}$  slip plane traces. The corresponding IPF map is included. (b) ECCI image of the studied crack.

Figure 10.1.9 shows the fractographic observations of the crack surface on the sample cycled with total strain amplitude 0.6%. Four areas at different distances from the crack initiation site are studied as marked in upper section of the image. However, the crack initiation site (number 1) exhibits cleavage fracture character in terms of facets. The striations are typical for the rest of the surface. They were found in about 100  $\mu\text{m}$  from the specimen surface, which is the distance equal to two grain sizes. The facets at the specimen surface correspond to the trans-granular crack initiation presented in Chapter 9.1. The directions of the rivers indicate the local crack direction. Multiple crack initiation plays an important role in the case of early crack growth. The spacing between the striations is small only of several nanometers. The coalescence of several cracks leads to the formation of macroscopic crack. The crack creates cyclic plastic zone ahead of the crack front and the growth due to crack tip plastic blunting leads to the formation of striations. With increasing crack length increases the crack growth rate and thus the spacing between striations (number 3 and 4). No facet-character of the crack growth was observed away from the specimen surface.



*Figure 10.1.9: SE micrographs show the fractographical observation of one of the longest cracks present in the specimen cycled by total strain amplitude 0.7 %. The details of the areas marked by dashed circles are present below.*

## 10.2. Crack growth rates of short natural cracks

Natural cracks initiate predominantly in PSMs as the shallow surface cracks. Usually, the crack is initiated in 1, 2, or up to 3 neighbor grains simultaneously. The depth of the initiated crack varies considerably but generally is lower than the half of the surface length. As the surface crack length increases, the shape of the crack gets closer to the shape of a semicircle. Blochwitz and Richter [118] evaluated the ratio of the projected crack depth to the projected surface crack length approximately to 0.44. Because the deviation from the semicircle is low, we have characterized the size of the crack by the half of the surface crack length projected to the plane perpendicular to the loading axis. It is approximately equal to the radius  $a$  of a semicircle projected to this plane.

During the fatigue life the surface of the shallow notch was documented in situ using optical microscope. When the first surface markings appeared within the notch area, the test was interrupted and the area of the notch was systematically inspected and documented using the optical microscope. That was repeated at selected number of cycles. The testing was finished when the largest crack achieved approximately 2 mm of surface length or the major crack was growing out of the notch area. The growth of the largest cracks could be followed backward to their initiation. Figure 10.2.1 shows the semilogarithmic plot of the crack length  $a$  of the longest cracks vs the number of cycles in specimens cycled with 6 applied strain amplitudes. In the case of cyclic straining with strain amplitude 0.7%, only 1 secondary crack was studied because others cracks were growing out of the observed notch area. The cracks in all specimens initiated during the early stage of cycling, i.e., in less than 5% of the fatigue life  $N_f$ . Figure 10.2.1 demonstrates that the effect of linkage of the growing cracks with smaller cracks present in its path affects strongly the growth rate of the cracks. The effect is most pronounced in the case of the total strain amplitude 0.25%. Crack C initiated as a small crack much later than other cracks; nevertheless, due to several linkages with other cracks, its length became at the end of cycling the same or larger as the length of remaining cracks. The average crack growth rate of the crack C was higher than the growth rate of other cracks. Similar behavior can be seen in the case of the specimen cyclically strained with other strain amplitudes. Sudden increase of the crack length due to the linkage is always followed by a period of apparent crack arrest. The crack does not grow on the surface, but it extends in the bulk reaching again semi-circular form (see Figs. 10.1.3 and 10.1.4). In specimens cycled with high strain amplitudes, the crack growth rate of one crack dominated over the others whose growth was even stopped. This was the case of cycling with strain amplitudes higher than 0.35% when only 2 or 1 crack reached appreciable length and other cracks stopped growing.



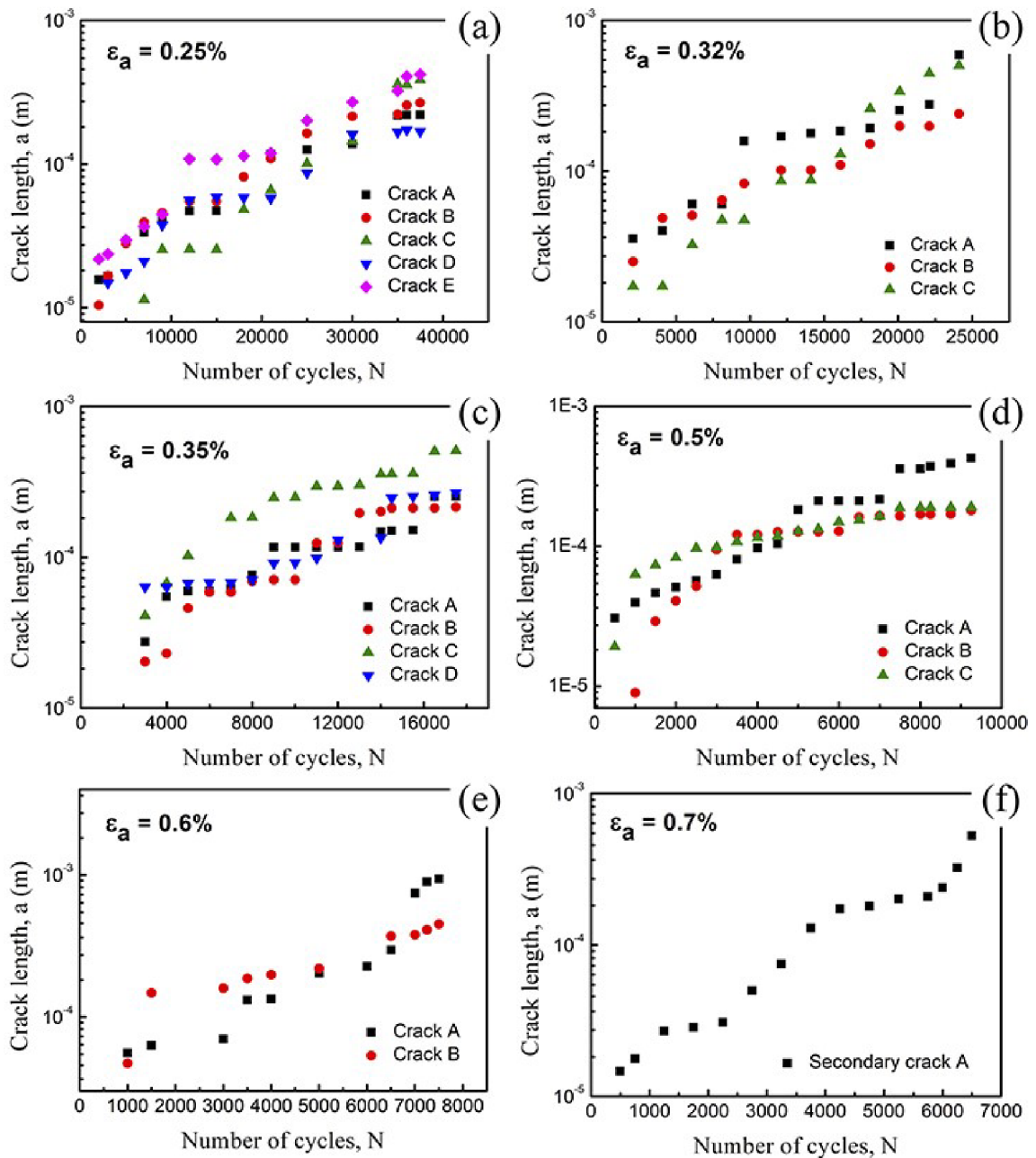


Figure 10.2.1: Semi-logarithmic plot of crack length  $a$  vs number of cycles  $N$  for different total strain amplitudes  $\epsilon_a$ . (a)  $\epsilon_a = 0.25\%$ , (b)  $0.32\%$ , (c)  $0.35\%$ , (d)  $0.5\%$ , (e)  $0.6\%$ , (f)  $0.7\%$ .

## 11. Fatigue at temperature of 700°C

### 11.1. Grain boundary oxidation and crack initiation

The study is focused on the effect of high temperature on the fatigue crack initiation and growth mechanism in detail. The results were obtained on the specimens cycled with constant total strain amplitude of  $5 \times 10^{-3}$  to the different stages of the fatigue life. First, the specimen cycled to the fracture ( $N_f = 852$  cycles) was investigated. The criterion  $\sigma_m/\sigma_a = -0.1$  was used to determine the fatigue life and failure. The cyclic hardening/softening curves of the specimen cycled at temperature of 700 °C are shown in Fig. 11.1.1. Stress amplitude  $\sigma_a$ , plastic strain amplitude  $\varepsilon_{ap}$ , and mean stress  $\sigma_m$  are plotted as a function of the number of cycles  $N$ . Second specimen used for the investigation of the crack initiation was cycled to approx. 10 % of  $N_f$  (90 cycles, see the dashed line in Fig. 11.1.1).

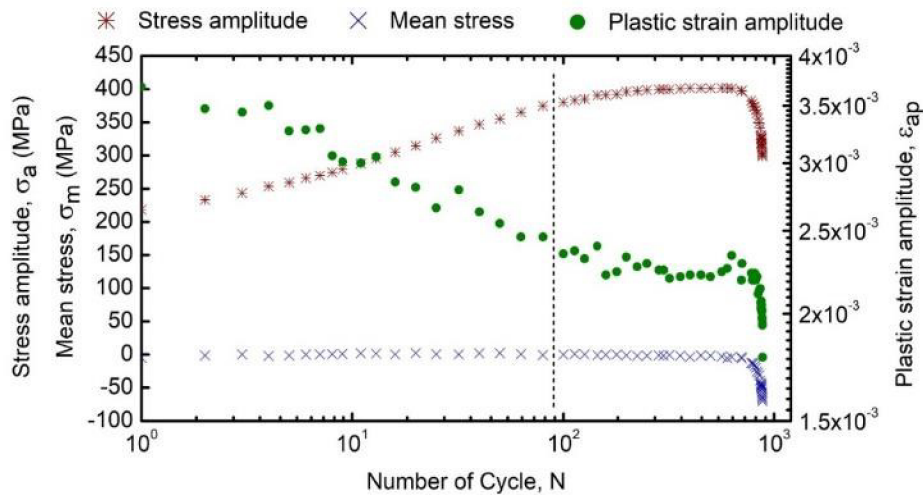


Figure 11.1.1: Cyclic hardening/softening curves of the specimen cycled with constant total strain amplitude  $5 \times 10^{-3}$  at temperature of 700°C to fracture ( $N_f = 852$  cycles). The dashed line (90 cycles  $\sim 10\%$   $N_f$ ) marks the number of cycles applied to the specimen subjected to the study of the fatigue crack initiation.

#### 11.1.1. Environmentally assisted crack initiation

The evolution of the surface relief was observed in SEM by using both SE and BSE imaging modes. In Fig. 11.1.2, BSE images of the surface of the specimen cycled to 10% of the fatigue life are shown. Thermal exposure of the specimen to the temperature 700°C during the test was about 5 hours. Being sensitive to the atomic number and scattering power of the elements, the BSE micrographs can effectively reveal grain-to-grain variations of the surface oxide layer thickness. This also correlates well with the change of the variation of the oxide nodules size. The thickness of the rough darker appearing oxides is up to 1  $\mu\text{m}$  while the thickness of the thin brighter appearing oxides varies around 0.2  $\mu\text{m}$ . The largest nodules are often observed accumulated at the grain boundaries (see Fig. 11.1.2a) implying that the oxidation at the grain boundaries is more pronounced. BSE imaging also reveals a network-like pattern of the oxides along the GBs. Appearing with brighter contrast the oxide layer along the GB is thinner relative to the surrounding surface relief. SEM-EDS

analysis (not shown here) confirmed that the rough oxides are enriched in Fe, while the area of the thin oxides is enriched in Cr and Ni.

BSE image in Fig. 11.1.2b shows the initiated crack as a result of the cracked rough oxide extrusion (see the detail in magnified inset). In general, no cracking of the oxide layer within the grain or along the twin boundaries was observed. Preferentially, the boundaries of the grains having the size of about 100  $\mu\text{m}$  and being oriented approximately perpendicular to the loading axis were cracked.

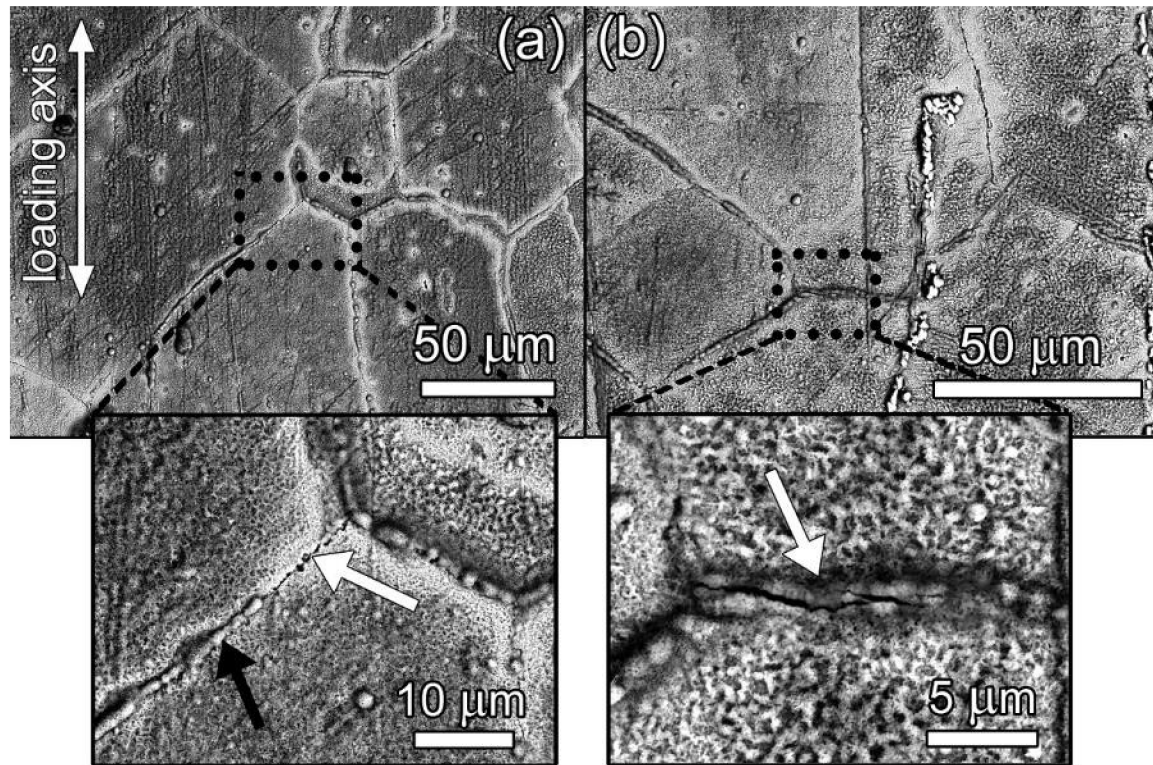


*Figure 11.1.2: BSE micrographs of the oxidized surface of the specimen cycled to 10% of  $N_f$ . The changes in the contrast suggest non-uniform distribution and different thickness of the oxides. (a) Areas close to the grain boundary (white arrow in magnified inset) appear as brighter indicating thin oxide layer. Early growth of the oxide at the grain boundary (black arrow in magnified inset) is shown in the detail. (b) Fatigue crack initiation from the cracked oxide extrusion at the grain boundary. Detail is highlighted by a white arrow in magnified inset.*

To reveal the growth mechanisms of the oxide layers not only on the surface but also inside of the material FIB-SEM dual-beam electron microscope was used to make cross sections perpendicular to the cracked oxide extrusions at GB. An example of the cracked GB is shown in Fig. 11.1.3. The positions of the future FIB cuts are marked by the platinum layers in the image denoted by the numbers 1, 2 and 3. FIB cut in the position 1 demonstrates the GB exhibiting no significant oxide extrusion, while the position 3 illustrates the GB with the cracked oxide extrusion.

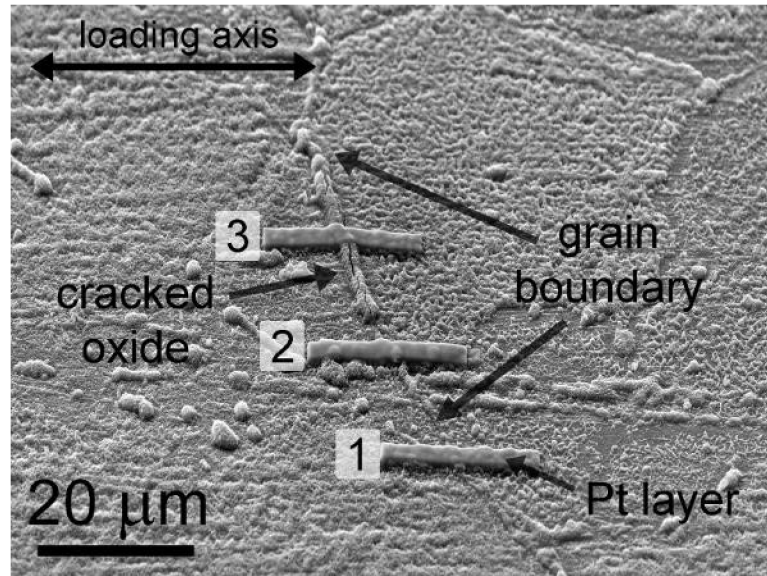


*Figure 11.1.3: Cracked oxide extrusion at the grain boundary subjected to the SEM/FIB study inside of the material. Positions of the future FIB cuts are marked by the Pt layers and are denoted by the numbers 1, 2 and 3.*

In Fig. 11.1.4 the shape of the oxide intrusion is correlated with the surface oxide layer. Three different FIB cross sections were obtained to demonstrate the process of the oxide intrusion growth. To obtain real dimensions, the images were acquired with the 35 degrees tilt correction. In FIB cross section 1 the thickness of the surface oxide above the oxidized intrusion is only slightly higher than that of the oxide layer in surrounding grains. The shape of the oxide intrusion is irregular and its depth is about 1.8  $\mu\text{m}$ . It is apparent that the oxide intrusion contains number of voids. Oxide growth follows grain boundary decorated with the secondary phases, presumably precipitates. From the FIB cross section 2 it is evident that the deeper intrusion is accompanied by the thicker oxide extrusion on the surface. Here, the depth of the oxide intrusion was 3  $\mu\text{m}$ . The oxide intrusion is not homogeneous. Moreover, the variations in the SE imaging contrast indicate that the oxide is full of voids, which appear darker than the surrounding oxide. At the tip of the oxide intrusion a cavity was found. FIB cross section 3 shows the oxide intrusion with the cracked oxide extrusion on the surface. Its depth is notably higher when compared to the previous cross sections and also the oxide thickness is approx. four times larger. The oxide intrusion grows in the direction perpendicular to the loading axis, presumably also along the grain boundary.

To reveal the 3D-profile of the initiated crack at the GB FIB-cut technique was used. Progressive FIB-cutting along the cracked oxide is marked in the insert in Fig. 11.1.5. Only six FIB-cuts were done perpendicular to both the GB and the specimen surface, respectively. Profiles of some cracks are shown in the image as well. The initial cracking is accompanied by the intensive oxidation of the grain boundary. Later, when the crack grows under elasto-plastic conditions the oxidation is not so notable and crack grows by mechanism of repeated oxidation of cracking of the oxide at the crack tip.

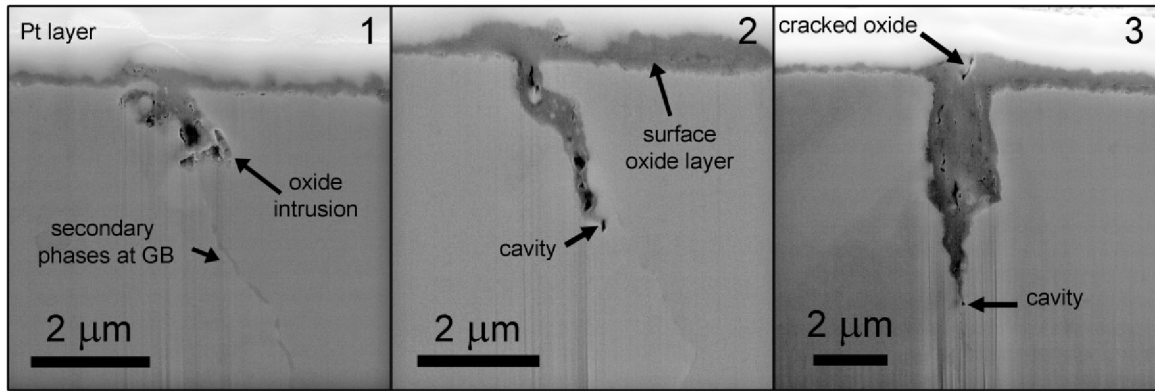


Figure 11.1.4: SE images of the FIB cross sections marked in Fig. 11.1.3. The oxide expands into the material along the GB. The deeper the oxide intrusion is extended in the material the higher the oxide extrusion is grown above the surface.

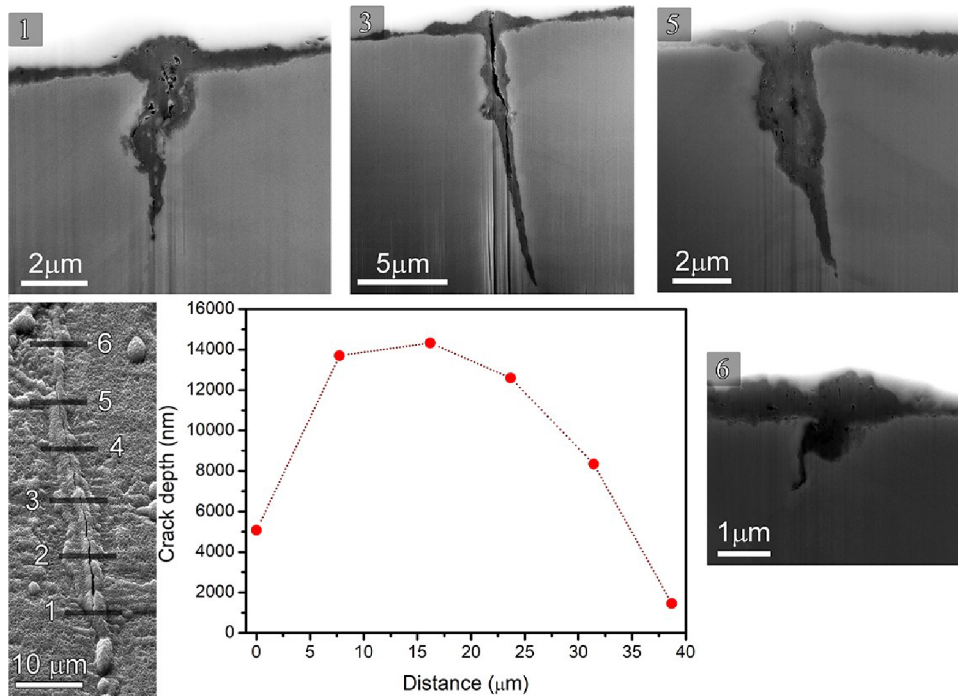


Figure 11.1.5: Depth profile of the initiated crack at grain boundary. Corresponding SE micrographs in selected positions are shown as well.

The depth of each crack was measured from the image after tilt correction of  $35^\circ$ . The plot of the crack length in the bulk vs. surface distance is plotted in Fig. 11.1.5. However, the number of FIB-cuts is not so high it is obvious that the crack has a tendency to grow in the bulk of the material approximately in the semi-elliptical shape. Nevertheless, the inhomogeneous oxidation of the grain boundary and its cracking effects the shape of the crack.

### 11.1.2. STEM characterization of the oxides at GB

The high-resolution characterization of the oxide layer at the grain boundary was carried out on the TEM lamella site-specifically extracted by the FIB nanofabrication. In Fig. 11.1.6a SEM micrograph shows grain boundary covered by rough oxide extrusions. The position of the lamella is denoted by the deposited platinum layer. Extracted TEM lamella after the final polishing is shown in Fig. 11.1.6b in bright field (BF) STEM imaging mode. The morphology of the surface oxides was investigated along with their local arrangement at the oxide intrusion tip and at the grain boundary. The profiles of the oxide extrusion at the surface as well as the oxide intrusion grown into the material are clearly recognized. It is apparent that the oxide intrusion continues along the grain boundary deep into the material. The cavity located in front of the oxide intrusion tip is evident. We can identify a duplex oxide layer. The outer layer is typical by large oxide nodules and a small density of voids while the inner layer is characteristic by small nodules and a high density of voids. Furthermore, in the austenitic matrix close to the oxide/matrix interface small voids were found (not shown here).

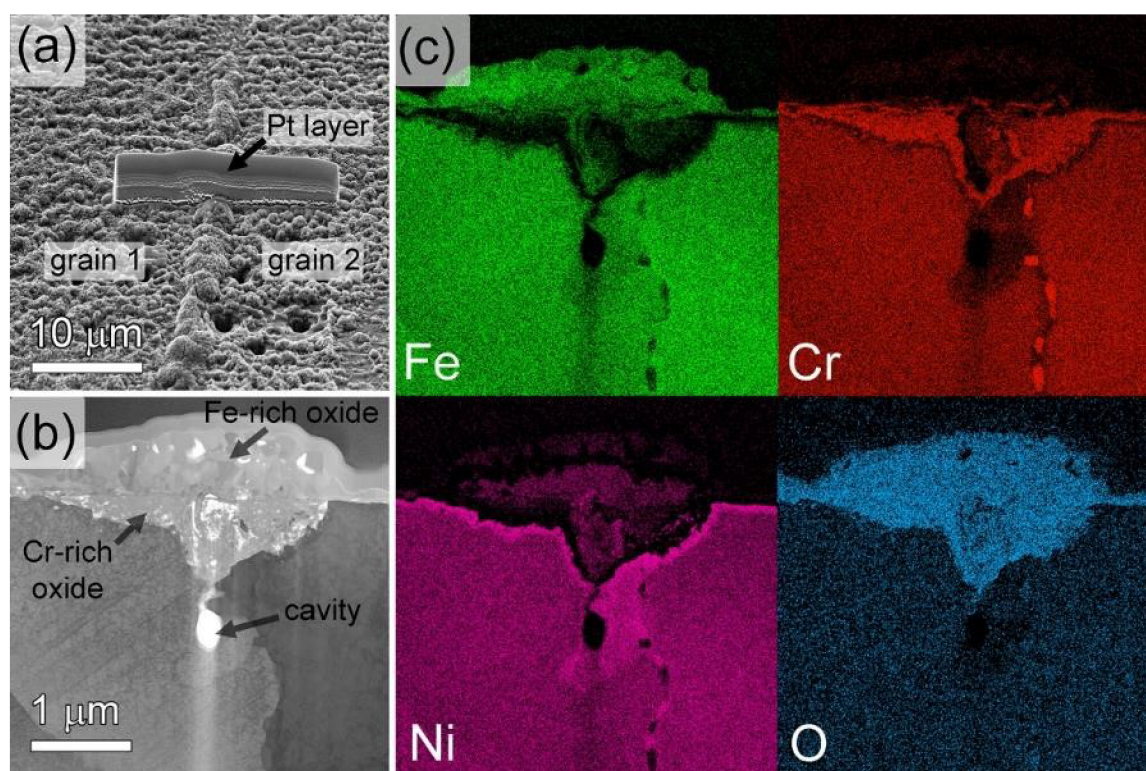


Figure 11.1.6: (a) SEM micrograph of the surface with the oxide nodules grown at the GB. Deposited platinum layer marks the position of the TEM lamella extraction. (b) BF STEM image of extracted TEM lamella. Oxide intrusion grew along the GB. Cavity was found at the tip of the oxide intrusion. (c) STEM-EDS map analysis of the oxide and surrounding matrix. Oxide layer is formed of the outer layer enriched in Fe and inner layer enriched in Cr. Layer heavily enriched in Ni is clearly distinctive in the austenitic matrix close to the oxides. Notably Ni-enriched area is observed also below the oxide intrusion (around the cavity).

Chemical composition of the oxides is revealed by the EDS-STEM map analysis as shown in Fig. 11.1.6c. Outer oxide is heavily enriched in Fe, even though small amount of Ni is found there as well. Below Fe-rich oxide, a thin Cr-rich oxide layer is located covering inner oxide layer enriched in Cr. In the centre, close to the former GB, Cr-rich oxide is depleted at the expense of Fe-rich oxide. At the interface of the oxide layers and austenitic matrix, significantly Ni-enriched layer is found demarking the boundary between the oxides and material surface. Interestingly, in the area of the intrusion and close to the cavity, Ni-enriched volume is observed as well. Below this feature, Cr-rich particles are found along the grain boundary decorating it. These precipitates are separated by substantially Ni-enriched and Cr-depleted areas as discussed further below.

### 11.1.3. Analysis of $M_{23}C_6$ Cr-rich carbides nucleated at the grain boundaries

The presence of carbon in steels with high Cr content is known to lead to rapid nucleation of numerous  $M_{23}C_6$  Cr-rich carbides [12]. At high temperatures, they nucleate very rapidly and can be found even in stabilized steels after very short aging times. Preferential nucleation sites are grain boundaries. However, they can be found also at twin boundaries and dislocations or stacking faults.

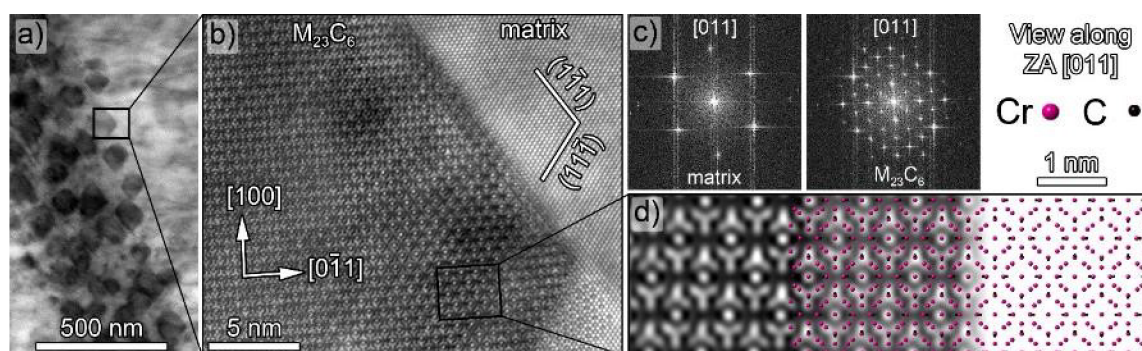
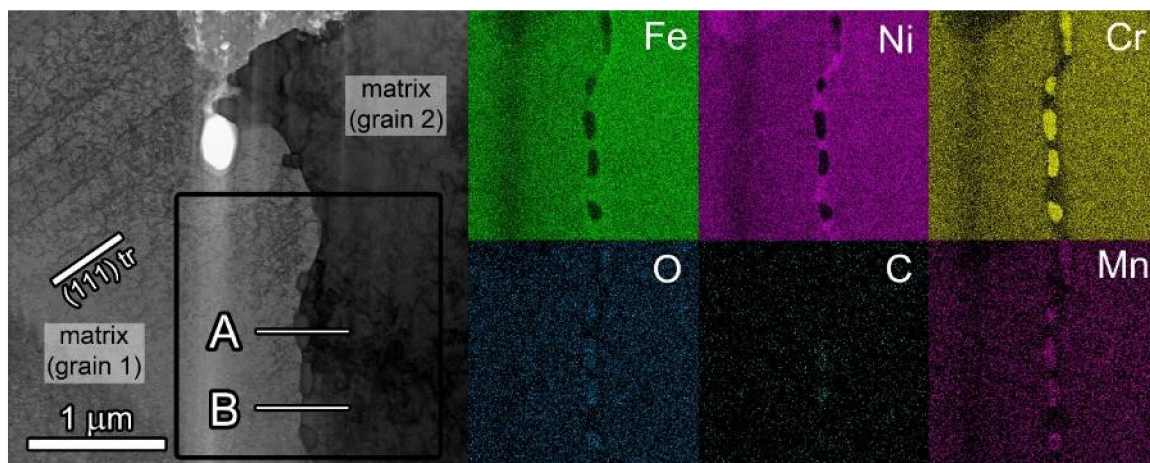


Figure 11.1.7: (a) An array of  $M_{23}C_6$  Cr-rich carbides nucleated at the low angle grain boundary. (b) HAADF-STEM image showing atomic structure of carbide viewed along [011] zone axis. (c) FFT diffraction patterns demonstrate cube-on-cube orientation of carbide relative to the FCC matrix. The shorter distance to the carbide diffraction spots by a factor of 3 relative to that of the matrix document that the carbide has lattice parameter almost exactly three times that of austenitic matrix. Small lattice misfit suggests interface of almost coherent or semi-coherent nature, where misfit dislocations can be present to relieve elastic strain at the interface. (d) Experimentally obtained and FFT filtered image of the carbide structure is compared with the model of structure made in Crystal Maker software.

An example of cuboidal  $M_{23}C_6$  Cr-rich carbide nucleated at the low angle grain boundary (approx.  $4^\circ$ ) is shown in the atomic resolution HAADF-STEM micrograph in Figs. 11.1.7a and 11.1.7b. The structure is viewed along the [011] zone axis. Fast Fourier transformation (FFT) filtering (frequencies corresponding to the noise and the transmitted beam spot were excluded) of the image was used to emphasize the carbide structure and also the {111}-type interface with the matrix, which suggests a cube-on-cube orientation. That is confirmed also by FFT diffraction patterns determined from the matrix, and  $M_{23}C_6$  areas as

shown in Fig. 11.1.7c. In the reciprocal space, the shorter distance to the carbide diffraction spots (by a factor of 3) relative to that of the FCC matrix corresponds well to the reported lattice parameter of  $M_{23}C_6$ , which is approximately three times larger than the lattice parameter of the austenitic FCC matrix [12]. Small lattice misfit of carbide and austenitic matrix suggests the coherent, and later, when particle coarsens, semi-coherent interface with misfit dislocations accommodating lattice mismatch and relieving coherency strains. According to Howe [152] such an interface can have rather small energy ranging from 50 to 300  $mJm^{-2}$ . In Fig. 8d, the experimentally obtained atomic structure was compared to a  $Cr_{23}C_6$  model [153] created in the Crystal Maker software. In the model, carbon atoms are coloured in black and chromium atoms in pink.

An array of  $M_{23}C_6$  carbides precipitated at the GB (misoriented by approx.  $7^\circ$ ) shown in Fig. 11.1.6 was studied in detail. Selected area electron diffraction based structural analysis has confirmed that the precipitates nucleated with cube-on-cube orientation relative to the matrix of grain 2 (right hand side of the image in Fig. 11.1.8). With grain 2, the precipitates share semi-coherent interface. On the other hand, they have random orientation and fully incoherent interface with grain 1 (left hand side of the image in Fig. 11.1.8). These structural facts play an important role in the characteristics of Cr-depleted and Ni-enriched zones observed in the vicinity of particles in the austenite matrix.



*Figure 11.1.8: BF-STEM image of grain boundary close to the surface shown in Fig. 11.1.6b. Dislocations lying on (111) slip plane in grain 1 are visible. Black inset highlights the area from which compositional EDS analysis was done. It shows  $M_{23}C_6$  Cr-rich carbides of average size 100 nm nucleated at the grain boundary. In the vicinity of carbides, matrix is significantly enriched in Ni at the expense of heavily depleted Cr.*

EDS linescans were performed across the precipitate (linescan A) and the grain boundary in between of precipitates (linescan B) as highlighted in black inset in Fig. 11.1.8. The raw data obtained from the spectral scans were quantified using Oxford Aztec software and are plotted in Fig. 11.1.9. Both scans show Cr-depleted/Ni-enriched zones at the grain boundary. In linescan A at the fully incoherent interface of “grain-1 /carbide” the affected zone is 37 nm with Cr depleted by 7 wt% and Ni enriched by 4 wt. %. On the other side, at the semi-coherent interface “carbide/grain 2” the affected zone is 87 nm, i.e. more than two times larger with both Cr content depleted and Ni content enriched by 10 wt. % in



maximum. This fact along with the orientation relationship suggests that the precipitates nucleated preferentially from the grain 2.

The size of the compositionally affected zone is even larger when a scan is performed across the grain boundary in between the nucleated precipitates. It seems that Cr needed for nucleation and coarsening of  $M_{23}C_6$  precipitates is consumed mostly from these areas since the diffusion along the grain boundaries can be easier than diffusion from the bulk of material. At the grain boundaries in between of particles, the Cr content is heavily depleted to minimum value of 4 wt. %, and fully replaced by Ni, which can reach up to 42 wt% in solid solution. The Cr-depleted/Ni-enriched zone in the grain 2 is again larger (here more than three times) than the zone in the grain 1, suggesting that the randomly oriented GB would present effective barrier for elemental diffusion compared to coherent interface.

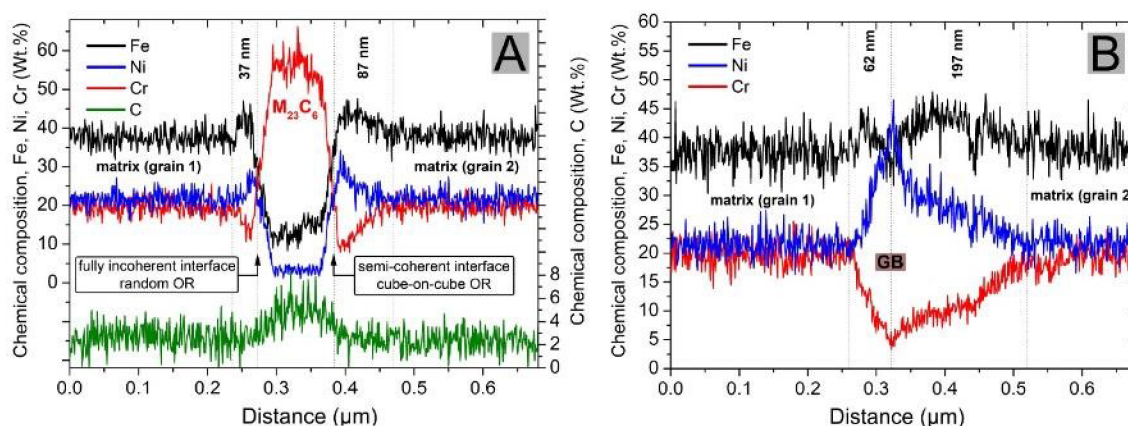


Figure 11.1.9: Quantified EDS linescans from the inset in Fig. 9 across the carbide (A) and across the grain boundary in between the carbides (B). Selected area electron diffraction confirmed that the carbides are semi-coherent, oriented as cube-on-cube with the grain 2, while with grain 1 they have random orientation with fully incoherent interface. EDS linescans demonstrate significant Cr-depleted/Ni-enriched zones in the vicinity of  $M_{23}C_6$  carbides. Since the particles nucleated from grain 2 the Cr-depleted/Ni-enriched zone is much larger on the semi-coherent side. Presumably, most of the Cr consumed for nucleation and coarsening of the precipitates came from the areas close to the grain boundary in between the carbides, as they are the most heavily Cr-depleted/Ni-enriched.

## 11.2. Crack growth under environmental conditions

### 11.2.1. Crack growth at the surface

Crack growth paths and respective crack growth mechanisms were studied using specimen cycled with the strain amplitude  $5 \times 10^{-3}$  to fracture. During initial temperature stabilization and following cyclic testing the specimen was held at temperature of 700 °C for 7 hours. The specimen surface was covered by the oxide scale of approximately the same thickness as the specimen cycled to 10 % of  $N_f$  except for grain boundaries and oxidized slip bands. In these locations more intensive oxidization was found when compared to the specimen cycled to 10 %  $N_f$ .

The crack growth paths were inspected by means of SEM techniques such as SE, EBSD and EDS, and were correlated with the structure of the material. To reveal the path of the

inner cracks longitudinal section of the specimen parallel with the direction of the loading axis was prepared. Both the crack paths on the surface and the paths of the cracks growing in the bulk were studied.

SE micrograph in Fig. 11.2.1 reveals that the growth of the cracks at the surface was strongly influenced by the cracking of the oxide extrusions at grain boundaries. Multiple crack initiation in GBs causes that the cracks close to the surface follow predominantly the grain boundaries. Further growth of the longer cracks on the surface is often transgranular in the direction approx. perpendicular to the loading axis (Fig. 11.2.1). Nevertheless, in the case of the surface cracks the intergranular crack path prevails as shown in Fig. 11.2.2.

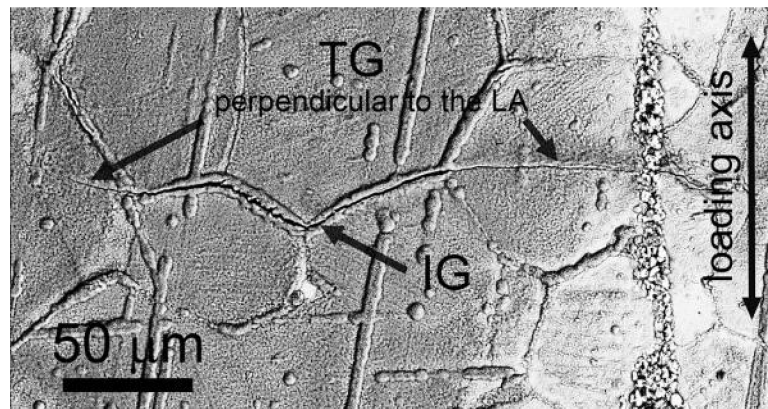


*Figure 11.2.1: Surface crack growing preferentially along the oxidized and cracked grain boundaries (IG – intergranular crack). Small part of the crack length corresponds to the transgranular crack path (TG) growing approximately perpendicular to the loading axis (LA).*

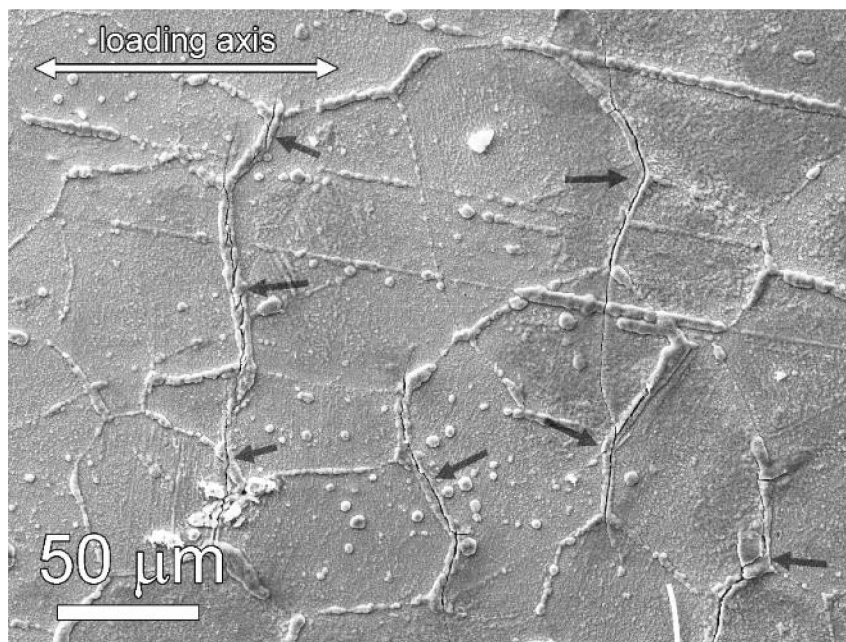


*Figure 11.2.2: Surface cracks growing predominantly in the intergranular manner in the direction approximately perpendicular to the loading axis (marked by black arrows). Cracks often bifurcate along the grain boundaries or within the grains.*

### 11.2.2. Crack growth in the bulk of the material

Figure 11.2.3 shows the crack growing deep into the bulk of the material. Grain boundaries can be easily recognized by means of the EBSD technique. It is apparent that crack initiated at the grain boundary on the specimen surface and grows approximately perpendicular to the loading axis. Later, the crack grows along the GBs only occasionally. Closer inspection of the trans-crystalline path of the crack reveals the change in contrast along both sides of the crack (grain with orange colour). This indicates the presence of the cyclic plastic zone along both sides of the crack. Its size is only a few micrometers and enlarges as the crack bifurcates (marked by white arrows). The plastic zone is observed also in front of the crack tip. However, in the case of the intergranular crack, the plastic zone absents.

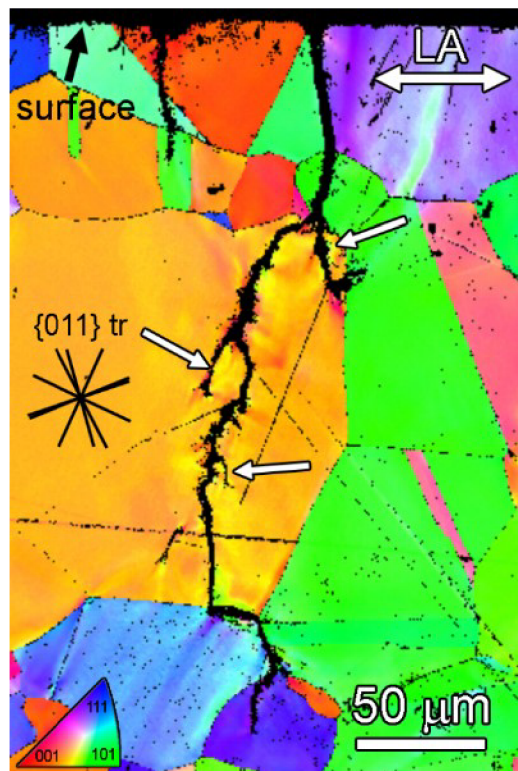


Figure 11.2.3: EBSD analysis of the grain orientation in correlation to the direction of the loading axis. The branching of the crack along the  $\{011\}$  slip plane traces is marked by white arrows.

The typical crack path of the growing crack is analysed in Fig. 11.2.4. Based on the crystallographic orientation information of each of the grains obtained by EBSD, the projections of all individual  $\{111\}$  and  $\{011\}$  slip planes traces at the surface were calculated. The crack initiated at the oxidized grain boundary. Later the path follows one of the primary slip planes of the type  $\{111\}$ . Nevertheless, as the crack length increases the crack starts to follow the other slip planes. Preferentially the crack grows along the traces corresponding to one of the  $\{011\}$  slip planes. Occasionally, the crack takes advantage of the grain boundary for its further extent. In grain 4 it is apparent that with the increasing crack length the crack follows less preferred crystallographic planes.

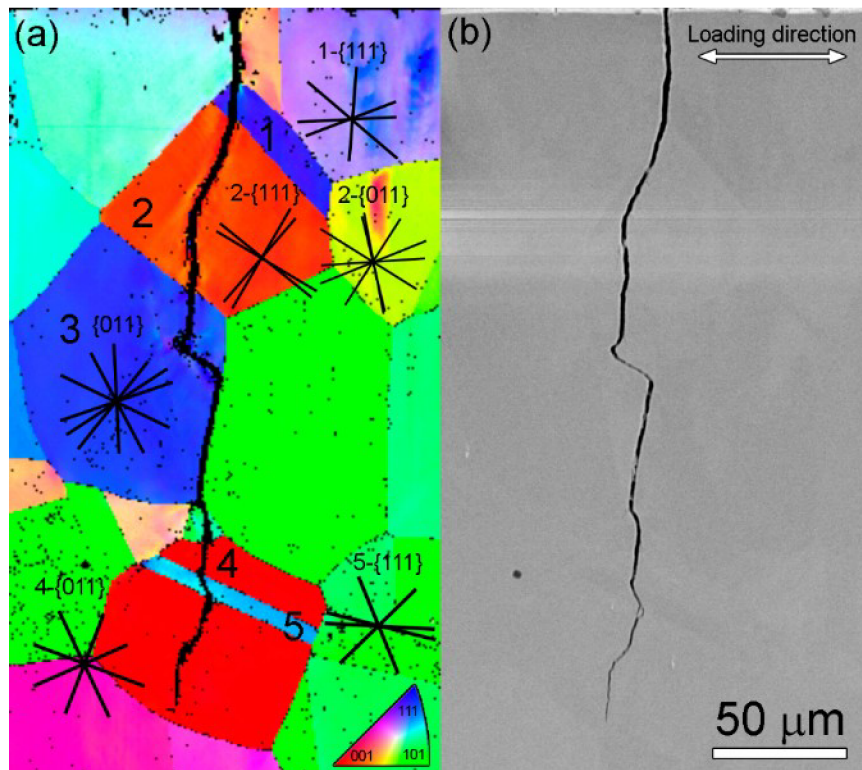


Figure 11.2.4: EBSD analysis of the crack path in the bulk of the material. The corresponding slip plane traces are included for each of the grains. (a) EBSD map. (b) Secondary electron image.

The growth of the cracks in the bulk is accompanied by the oxidation of the newly formed crack surface. Both the structure and the chemical composition of the oxides along the transgranular part of the crack path are shown in Fig. 11.2.5. In the lower part of Fig. 11.2.5 an opened crack is imaged and in the upper part the EDS-SEM line scan across the growing crack is shown. The chemical composition is shown here by directly measured counts per second of individual elements as a function of the distance across the crack. The oxide layer is about one micrometer thick on both sides of the crack. The duplex character of the oxide structure is apparent. The oxide layer close to the crack is enriched in Fe with a small amount of Cr. Further away in the direction deeper into the matrix the amount of Fe rapidly decreases while the amount of Cr increases, forming the inner oxide layer. At the metal/oxide interface, the sudden increase of Ni is notable.

The closer details of the tips of the growing cracks are shown in Fig. 11.2.6. It documents the role of the oxidation in terms of the crack growth in the harsh environment at high temperatures. As shown earlier the oxidation takes place during all the growth of the crack. The Fig. 11.2.6a shows the microstructurally long crack and its crack tip in the inset. The vast oxidation ahead of the crack tip, probably in the crystallographic direction (see Fig. 11.2.4), is notable. The inset shows the oxide layer extending of about 1  $\mu\text{m}$  ahead of the free surface of the crack. This oxide layer is not cracked. Contrary to that, the Fig. 11.2.6b documents the highly oxidized crack tip. The fracturing of the oxide at the crack tip is apparent. Two fine cracks in the oxide may be recognized. One of them extends into the deepest point of the interface oxide/matrix.

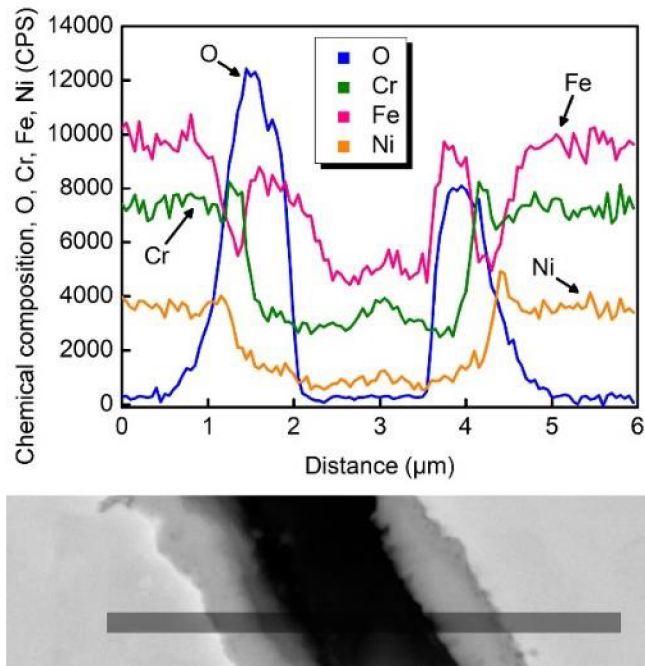


Figure 11.2.5: SEM-EDS line scan of the principal elements across the opened crack shown below. Both sides of the crack are oxidized. The chemical composition reveals that outer oxide is enriched in Fe while the inner oxide is enriched in Cr. Ni-rich area is found at the oxide/metal interface.

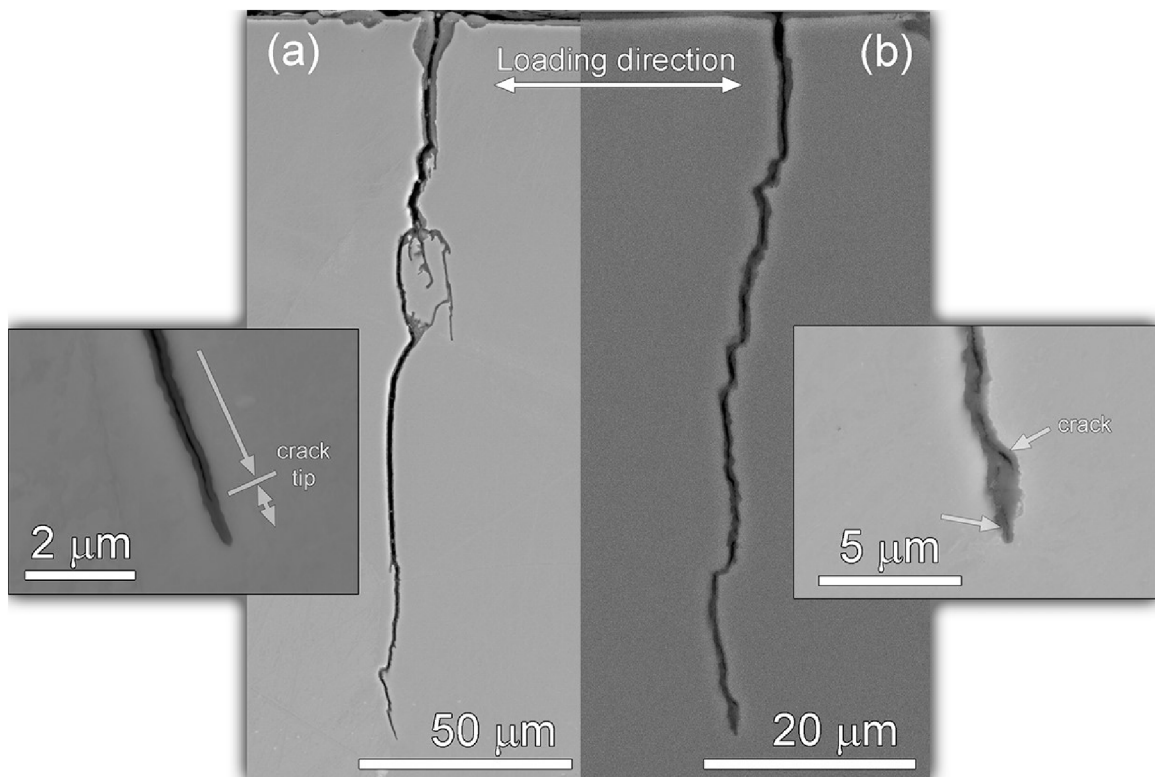


Figure 11.2.6: BSE images of the crack growth accompanied by the oxidation. The oxidation and fracture of the oxide at the crack tip are shown in the details.

### 11.2.3. Crack growth path statistics

Surface cracks and cracks growing in the bulk were inspected and the fractions of the crack path corresponding to trans- and intergranular growth were evaluated (Fig. 11.2.7). Since GB oxidation causes multiple crack initiation due to the cracked oxides later leading to the crack coalescence the intergranular growth on the surface prevails. The average fractions of the total length of the surface cracks growing intergranularly and transgranularly were about 66 % and 34 %, respectively.

More than 10 inner cracks having the depth higher than 100  $\mu\text{m}$  were studied and fractions of the crack path corresponding to trans- and intergranular growth were evaluated. Fig. 11.2.7 documents the high predominance of the transgranular growth over the intergranular growth. The average fraction of the total length of the cracks in the bulk of the material growing trans- and intergranularly was about 80 % and 20 %, respectively.

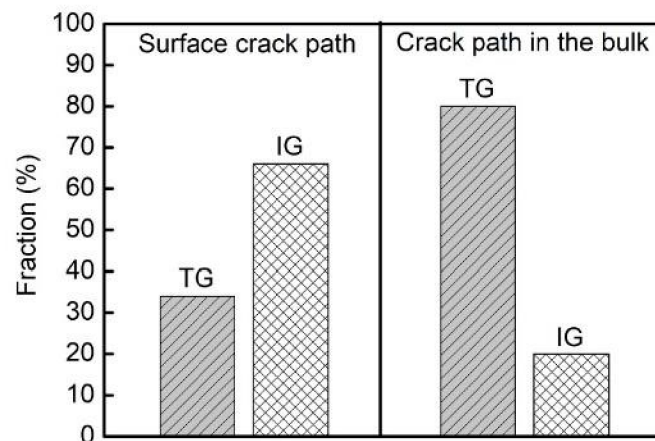


Figure 11.2.5: Fractions of the crack paths corresponding to the transgranular (TG) and intergranular (IG) growth at the surface and in the bulk of the material.

## VI. DISCUSSION

### 12. PSM assisted crack initiation at room temperature

Fatigue crack initiation is mainly related to the basic properties of the material such as chemical composition, crystalline structure, degree of strain localization, and others but also to more specific characteristics like grain size and cyclic straining amplitude. The impact of the fatigue-induced surface relief on crack initiation was found in the early 19<sup>th</sup> century [3]. Later, in the 60s of the 20<sup>th</sup> century, both extrusions and intrusions were accepted as the essential feature of the surface relief. Cottrell and Hull [40] used a shadow replica technique to reveal extrusions and intrusions on the surface of fatigued polycrystalline copper. Further evidence is given in reviews by Thompson et al. [57; 154] who showed that ‘intrusions’ could clearly grow into cracks. Furthermore, direct evidence of the role of intrusions in fatigued copper single crystals was given by Basinski and Basinski [155-157] and clearly by Hunsche and Neumann [158]. In recent years, AFM [159-164] has been applied to study the surface relief in fatigued polycrystals. AFM can detect extrusions, intrusions and Stage I cracks but cannot unequivocally distinguish between intrusions and short Stage I cracks. This differentiation is also impossible using SEM observation of the surface even if high resolution is used. This is due to the fact that extrusions emerge from the material at an angle approximately 45°, thus covering the neighbour intrusion and also due to the fact that intrusions are very thin.

#### 12.1. Cyclic strain localization and PSM formation

Later in the 70s and 80s of the 20<sup>th</sup> century the role of the internal dislocation structure in the form of persistent slip bands was found to be the essential feature leading to the formation of the surface relief [39; 74; 165; 166]. Material structure changes during the cyclic loading and after a few cycles the matrix is not able to absorb all the cumulative cyclic plastic strain anymore. The plastic deformation is represented by the motion, multiplication and mutual interaction of dislocations. At the beginning of cycling the dislocation density increases and very early the material reaches the saturated state. In the case of pure materials with high SFE such as Cu or Ni the clusters of edge dislocations in the form of veins and tangles are formed. In further cyclic loading the cyclic plastic strain is localized into the narrow persistent slip bands with dislocation rich walls and dislocation free channels [167-169] as shown in Fig. 12.1.1a. The ladder-like structures follow exactly the trace of the primary slip plane. The average distance between the rungs of the ladder-like dislocation structure of PSBs at room temperature was found to be more than 1  $\mu\text{m}$ . The number of cycles in which the localization of the cyclic plastic strain into the PSBs is significant can be determined from the change of the hysteresis loop shape. The characteristic loop shape parameter  $V_H$  increases when cyclic plastic strain starts to be localized into the PSBs [4]. As soon as the plastic strain is localized into the PSBs the fatigue-induced surface relief evolves. The PSMs originate on the surface where PSBs emerge.

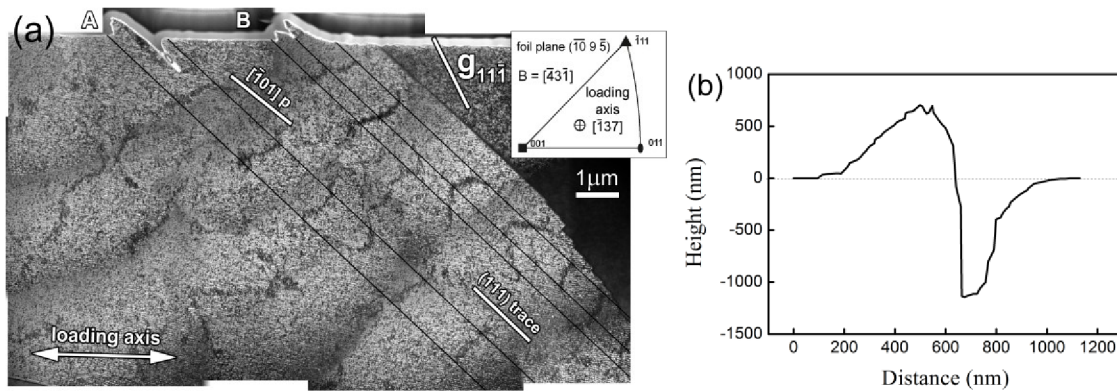


Figure 12.1.1: (a) BF-STEM image of dislocation structure of pure copper after cycling at room temperature. (b) Profile of the PSM A in the direction of the primary slip plane.

The situation is more complicated in structural materials such as austenitic steels. The presence of Ni [54] as one of three basic elements forming the face-centered cubic matrix as well as of the N [51] leads to the decrease of the SFE of the steels. The lower the SFE the more cross slip of dislocations is suppressed. Then the low stacking fault energy results in higher tendency to planar character of the dislocation structure. Furthermore, the short range ordering of Fe, Ni, Cr and other alloying elements may locally change the slip character of dislocations. The resulting critical shear stress needed for dislocation motion can be high enough to immobilize the dislocations or to change the character of their motion.

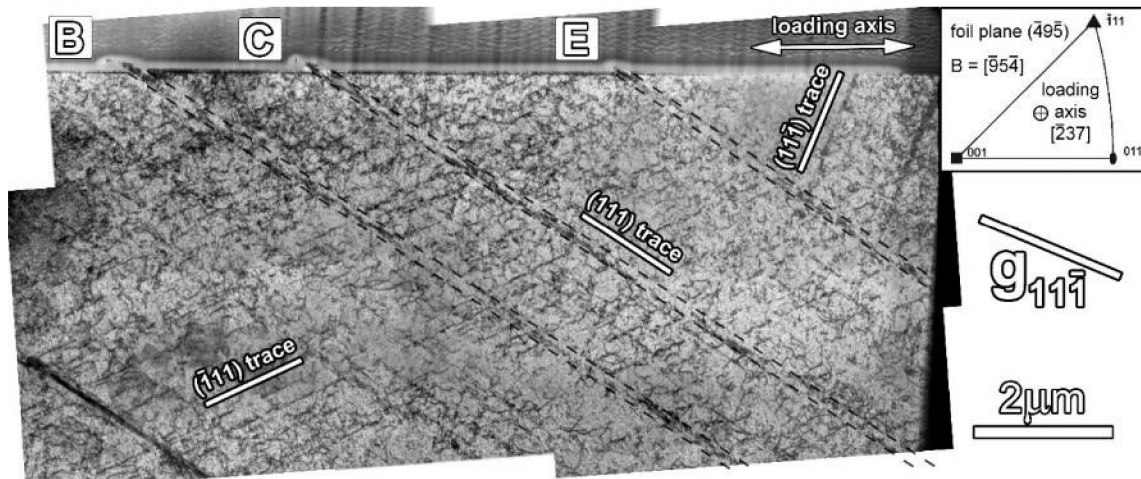


Figure 12.1.2: BF-STEM image of 316L steel subjected to cyclic straining at room temperature.

The localization of the cyclic plastic strain in the case of austenitic steels was thoroughly studied in well-known 316L steel [38; 46; 47; 170; 171]. Recently, the direct observation of the surface relief with surrounding dislocation structure using surface lamellae [172] revealed that dislocation structure of PSBs corresponding to surface PSMs differs significantly from that of pure materials (see Fig. 12.1.2). The dislocation structure of the PSBs does not clearly differ from the dislocation structure of the matrix. We have done



similar observations in the case of Sanicro 25 steel (see Fig. 9.2.7). Close inspection of the foils produced from the surface grains of Sanicro 25 steel, however, revealed generally lower dislocation density in PSBs than in the matrix, and definitely, dislocations from secondary slip systems running through the matrix were absent in the PSBs. We can suppose that in the initial stage of fatigue, dislocation structure of the matrix is formed and only later localization of the cyclic plastic strain into PSBs results in the formation of PSMs. The absence of the secondary dislocations in the PSBs in austenitic Sanicro 25 steel also points to the active movement of primary dislocations in the PSBs, their interaction and subsequent formation of point defects. The migration of point defects and their arrival to the dislocations of secondary slip system would result in a climb of these dislocations and their disappearance from PSBs. In several PSBs, the dislocation poor and dislocation rich areas are visible although ladder-like structure was recognized only in PSB B (see Fig. 9.2.8) close to the surface. In summary, two important differences of PSB structure from the matrix structure are apparent: (i) absence of dislocations from secondary slip systems, and (ii) low dislocation density in some areas of PSBs. We can thus characterize the dislocation structure as irregular alternations of the volumes rich and poor in dislocations.

Contrary to 316L steels, Sanicro 25 has higher tendency to the formation of planar dislocation structures during fatigue at ambient temperature mainly as a result of its chemical composition [21]. The thickness of the PSBs is about 250 nm, what is about 2 times less when compared to the thickness of PSBs in 316L steel (about 500 nm) [4; 172] and about 4 times less when compared to the thickness of PSBs of copper (about 1  $\mu\text{m}$ ) [173]. The strain localization into the narrow bands implies the primary role of PSMs in initiation of Stage I fatigue cracks. The fraction of the cracks initiated in PSMs highly prevails over the other mechanisms of the fatigue crack initiation (see Fig. 9.1.12).

In the early stages of the cycling the surface relief has a form of the protruded material in the direction of the primary Burgers vector (see Fig. 9.2.4). The early localization of the cyclic strain into the PSBs, even when the PSB dislocation structure is not fully developed, increases the internal tensile stresses within the PSB as predicted by Essmann et al. [78] and Polák et al. [85]. These tensile stresses decrease by the mutual dislocation movements leading to extrusion of the material. These observations agree with the observations of Man et al. [4] performed on 316L steel. They found that the extrusion develops first and later one or two intrusions are created along the extrusion at the PSB/matrix interface.

The shape of the well-developed PSMs of Sanicro 25 steel is similar to that observed in 316L steel [4], but is more complicated than in copper (see Fig. 12.1.1b). The volume of extrusions is higher than the volume of intrusions in all PSMs. The topography of the large extrusions is very rugged. In addition to large extrusions (see in Fig. 9.2.3), we can see small extrusions alternating with intrusions, whose average height is 50 nm and thickness of only 10 nm. It indicates high planarity of the slip on the primary slip plane.

Number of PSMs contains not only extrusions and intrusions but also already Stage I cracks (see Figs. 9.1.2, 9.1.3 and the detail of PSM C in Fig. 9.2.3). As reported earlier in austenitic stainless steels [96; 145; 174; 175] the cracks prefer to grow in the grains with the highest Schmid factor along one of the  $\{111\}$  slip planes. The cracks were found to initiate as the result of the stress concentration at the tip of the intrusions or intrusion-like valleys. According to Neumann [158] the crack can be distinguished from the intrusion by the vortex angle. Whereas the vortex angle of crack is zero, the intrusion has a non-zero vortex angle. The number of the initiated cracks was found to be dependent on the plastic strain amplitude as also observed previously in 316L steel [66; 118].

## 12.2. PSM profile/Crack initiation in relation to the theoretical models

All the Stage I cracks were found to nucleate at the surface of the samples. No cracks were observed to initiate in the bulk of the material as a consequence of the internal defects. As shown in Chapter 9.1, the surface crack nucleation was mostly preceded by the formation of the PSMs. The majority of the cracks initiated along the PSMs at the sites of stress concentration. Such sites were found to be intruded volumes, i.e. “intrusions” accompanying the extrusions, or valleys between two extrusions.

The shape of extrusion/intrusion pairs shows very steep steps between the extrusion and the intrusion (see Fig. 9.1.2 and PSM C in Fig. 9.2.3). These findings are more evident from the observations on pure copper tested at room temperature as shown in the PSM A in Fig. 12.1.1b where the shape of the PSMs is smoother compared to the PSMs in Sanicro 25. The finding indicates very large stress and strain gradient in the direction of the primary Burgers vector close to the plane which separates PSB and the matrix. Brown and co-workers [76; 77] took into consideration the dipolar structure of the dislocation rich walls of PSB and predicted the high tensile stresses at the interface PSB/matrix resulting from the small tensile strain within PSB. They predicted the elevated tension at a point where the interface PSB/matrix meets the surface leading to the crack opening. Although they predicted the preferential crack initiation site at an acute angle between the extrusion and the surface (what is in partial agreement with our observations), the mechanism of the crack initiation differs from that observed in Sanicro 25 steel. The crack initiation was found to be the consequence of the previously formed intrusion (see Fig. 9.1.3) and not due to the decohesion between the PSB and the matrix at an acute angle of the extrusion. The high stresses within the PSB and at the interface PSB/matrix lead to the appearance of the volumes contributing to the production of the extrusion and the production of the intrusion. Then, the crack can start on both sides of the extrusion near the interface PSB/matrix nucleating at the tip of the intrusion. Using AFM, it was shown earlier in 316L steel that due to lower yield stress of the PSB than the yield stress of the matrix [4] static extrusion arises first and the intrusions start growing with some delay. Later both extrusions and intrusions grow steadily until the crack nucleation. Then the plastic strain is concentrated into the front of the Stage I crack and both the extrusions and the intrusions stop growing. These statements agree with our experimental observations (see Fig. 9.1.3).

The pair of extrusion and intrusion is under consideration in the model based on dislocation pile-ups within the PSB near the surface proposed by Tanaka and Mura [89]. However, this model cannot explain the gradual growth of extrusions and intrusions during the cycling when the saturated state of the dislocation arrangement within the PSB is reached. Therefore, only the models taking into account the mass transfer due to vacancy migration between the PSB and matrix are discussed further.

The EGM model predicts formation of vacancies in the walls of PSBs. Vacancy production in the channels is neglected. Vacancies arise because of dislocation interactions in the dislocation-rich walls. In the case vacancies cannot migrate, they accumulate in the walls and the volume of PSB increases. Extra volume results in internal compressive stress and plastic relaxation of this stress in the direction of the Burgers vector produces extrusions where PSBs egress on the surface. These extrusions are called ‘static extrusions’ in reference to their origin. Static extrusions presumably produce stress concentration which is larger at the side of the extrusion where the emerging active slip plane is inclined to the surface at an acute angle. This is not in a complete agreement with our observations. According to Mughrabi [78; 176; 177] ‘intrusions’ develop as a consequence of the previously formed extrusions and are in fact embryonic Stage I shear cracks. This

contention does not agree with the present experimental finding (Figs. 9.1.3a and 12.1.1, PSMs B and C in Fig.9.2.3), because intrusions without crack running parallel to extrusions were observed. The production of intrusions prior to initiation of fatigue cracks has been proved. Moreover, as discussed earlier, the vortex angle of intrusion differs from that of a crack [158]. Then the initiated crack can be clearly distinguished from the intrusion.

The existence of static extrusions based on the EGM model is questionable because static extrusion can be produced only at temperatures where point defects are not mobile. The annealing spectrum of copper fatigued at low temperature have been measured using resistivity in copper single crystals [178; 179]. The main annealing stage in which point defects migrate to dislocations and disappear is at a temperature of about 40 °C. At room temperature, the migration rate of point defects is so high that vacancies produced in cyclic straining disappear continuously and cannot contribute to the formation of the static extrusion.

Polák's model [85] is based on the EGM assumption of the continuous production of point defects due to dislocation interactions in locations of cyclic plastic strain localization. Contrary to the EGM model, only point defects produced in the channels of the PSB can escape from PSB to the matrix and are systematically annihilated at edge dislocations in the matrix. Majority of them are absorbed at dislocations close to the PSB/matrix boundary. It results in systematic transfer of matter from the matrix to the PSB. The plastic relaxation of the internal stresses within the PSB in the direction of Burgers vector leads to the formation of extrusion and intrusion pairs at the surface. This situation has been treated quantitatively [180] and the shapes of extrusion and parallel intrusions have been predicted. It was shown that extrusions arise first because PSBs are softer than the neighbouring matrix. In SEM and AFM observations, the extrusions seem to be more numerous than intrusions because intrusions are often covered by parallel extrusions. Present observations of their true profiles show that majority of extrusions are during the fatigue life accompanied by one or two parallel intrusions. In the general formulation of the model [84; 85; 180] the ladder-like dislocation structure is not a necessary condition for the formation of PSMs. The only essential condition for the formation of PSMs is the localization of the cyclic plastic strain in the bands of cyclic slip (PSBs) with alternating dislocation rich and dislocation poor volumes. Because of the frequent interactions of dislocations in PSBs, point defects are produced and migrate to sinks. Local transport of matter results in formation of local internal tensile and compressive stresses. These stresses could relax plastically under the effect of cyclic stress and lead either to extrusions or intrusions. The structure of extrusions and intrusions depends thus on the internal dislocation arrangement which serves as the source and also as sinks for point defects. The distribution of dislocations in the matrix close to the PSB/matrix boundary and the ladder-like structure of PSB determines the position and the shape of the extrusion and intrusion. Provided the dislocation structure of the PSB is irregular like as observed in Sanicro 25 steel (Figs. 9.2.2 and 9.2.7), the shape of the PSM should consist of alternating extrusions and intrusion with preference of extrusions in the center and intrusions on the PSM/matrix interface. The surface relief in fatigued Sanicro 25 steel consisting of alternating extrusions and intrusions correspond to this prediction. Dislocation structure in the bands corresponding to PSMs is not markedly different from that of the matrix except the absence of dislocations belonging to secondary slip systems. The presence of the dislocation free areas facilitates the migration of point defects over longer distances and thus supports a more pronounced redistribution of matter. All this contributes to complicated structure of PSMs observed experimentally.

According to Polák's model the crack initiation could appear on both sides of the extrusion since the intrusions can form at both interfaces PSB/matrix what agrees with our experimental results. However, based on the conclusions done on fatigued 316L steel at room temperature by Man et al. [4] the intrusions start more frequently on the extrusion side where the active slip plane inclines to the surface at an acute angle.

### 12.3. PSM assisted TB and GB cracking

Not only the localization of the cyclic plastic strain leads to the crack initiation along the PSMs since also the intercrystalline crack initiation was found to be related to the PSMs. The transition from trans- to intercrystalline crack initiation increases with increasing applied total strain amplitude i.e. with increased plastic strain amplitude. The evidence is found in Figure 9.1.12 where the results from two samples subjected to loading with strain amplitudes of 0.25% and 0.6% are compared. The initiation along the PSMs in the case of high strain amplitude decreased from 90% to 70% while in the low strain amplitude cycling the initiation along the TBs increased from about 10% to nearly 30% and also some crack initiation along the GBs appeared. Presented results are in good agreement with the previous works carried out on the pure copper [61; 63] and the Waspaloy [181].

The cracking mechanism of the GBs due to the impingement of the PSBs at a GB was proposed by Christ et al. [63]. The mechanism is based on the emerging of the PSBs at the surface and formation of the fatigue induced relief according to the EGM model [78]. They consider the role of the interface edge dislocations located at the interface between PSB and matrix. In a grain where the component of Burgers vector of interface dislocation is parallel to the surface, the pile-up of these dislocations acts against the grain boundary. Then the locally increased stresses cause decohesion of the GB under the external tensile loading.

Contrary to that, our results show the significant role of the PSBs having the Burgers vector almost parallel to the surface (favourably oriented) and producing the fatigue induced relief at GB (see Fig. 9.1.8). The slip systems playing a role in the GB cracking are highly misoriented so that the PSM in one grain cannot continue in the neighbouring grain thus being stopped at GB. The GB is oriented to be perpendicular to the tensile loading where the GB is subjected to opening Mode I crack growth [61]. It was found that the impingement of PSBs with the favourably oriented Burgers vector forms PSMs at GB and cause the plastic incompatibility along the grain boundary. The increased plastic deformation along the grain boundary in a grain with well-developed surface PSMs (not favourably oriented Burgers vector) is notable due to the change of the image contrast in Fig. 9.1.7.

The existence of extrusions at GB similar to that as discussed in previous Chapters is well documented in Figs. 9.1.7 and 9.1.8. They grow during cycling and exert normal stress on the neighbour grain so high that extrusions are highly bent (see Fig. 9.1.9). Several parallel extrusions along the GB continuously push away the neighbouring grain. Moreover, if we consider the formation of the PSM in the form of the extrusion and intrusion pair as proposed by Polák [85] the intrusions are present at GB as well. The simultaneous growth of extrusions pushing away the GB and presence of the intrusions at GB lead to the grain boundary cracking. The intrusions act as the local discontinuities at grain boundary leading to partial decohesion and weakening of the GB. Only a few fatigue cracks initiated at GBs were observed. The initiated grain boundary crack grows later along the slip planes inclined at about 45 degrees to the loading direction (see Fig. 9.1.8).

No GB cracking was observed in the case of low strain amplitude cycling. It corresponds to low density of the PSBs/PSMs inducing the GB decohesion along the grain boundaries. With high applied strain amplitude the high plastic strain amplitude results in high volume fraction of PSBs [42] and appearance of grain boundary cracks.

Although some TBs have been cracked as a result of the impingement of PSMs at the TB, most of the TB cracking was observed to be related to the appearance of PSB emerging at the surface along the TB. The role of TBs in fatigue crack initiation have been studied in various simple metals [65; 66; 182] as well as in structural materials [118; 183]. The characteristic bands of the localized cyclic plastic deformation (PSBs) running parallel to the TBs were often reported for copper [42; 184]. Our observations reveal the characteristic PSBs inducing the surface relief in the form of extrusions and intrusion (see Chapter 9.2). Since we have observed the extrusions along the surface cracks running along TBs (see Fig. 9.1.4) we can conclude that the cracking of TBs was pronounced by the appearance of parallel PSBs.

The TBs were observed to be the second preferential site of fatigue crack initiation since they promote early cyclic slip localization and PSB formation [65; 184]. Consequently, it was demonstrated several times that the cracking of TBs plays an important role in specimens fatigued with low strain amplitudes [118]. However, their important role was found in 316L steel also at intermediate and high strain amplitudes [118; 183; 185]. Based on our observations the relative frequency of TB cracking increases with increasing strain amplitude (see Fig. 9.1.12). The results clearly show the increasing role of the TBs in the crack initiation of the dominant cracks during high strain amplitude cyclic loading while in the case of low strain amplitudes the initiation is preferentially transcrystalline along the narrow PSMs.

The most relevant theoretical model of crack nucleation along the TB was proposed by Neumann et al. [66; 186]. They analysed the elastic anisotropy of the TB pair and stress concentration near the emerging TBs. They concluded that the effective resolved shear stresses near the TB due to the elastic anisotropy of surrounding twins locally enhances the plasticity along the TB and intensify the formation of PSB/PSM since the TB is parallel with  $\{111\}$  slip plane. The model was slightly modified by Blochwitz et al. [118; 183; 187] for intermediate and high strain amplitudes considering the elasto-plastic solution. Their results are consistent with the observations of Neumann. This is in agreement with our observations which confirmed the role of TB both in low and high strain amplitude cycling. The probability that the nucleated crack along the TB would develop into the dominant crack is enhanced in the case of high strain amplitudes (see Fig. 9.1.12).

Our results on the crack growth along the TBs show the deflection of the crack paths in the direction perpendicular to the loading axis. The results correspond to the early crack initiation and growth of fatigue cracks initiated along the PSMs within the grains (see Fig. 10.1.7b). Similar observations were performed recently by Blochwitz et al. [120; 183] and Man et al. [94] who found that the crack leaves the TB plane after a few micrometers and follows the low-indexed slip planes as  $\{001\}$  or  $\{011\}$  (see Fig. 10.1.8).

## 13. Crack growth of short natural cracks

### 13.1. Crack growth mechanisms

The natural short fatigue cracks propagate in two stages of the crack growth. The first period is the crack initiation and early crack growth along PSM denoted as Stage I and the second is the crack growth approximately perpendicular to the loading axis denoted as Stage II (see Fig. 4.1.1). Fatigue crack initiation plays an important role in the fatigue life of the cyclically strained bodies since without the crack initiation there is no crack growth and no fracture. Nevertheless, in the low cycle fatigue domain the period of the crack initiation is usually not life determining. Early and easy crack initiation can however shorten the fatigue life.

Numerous studies on f.c.c. and b.c.c. materials show that the location of the crack initiation strongly depends on the applied strain and stress amplitude. Among variety of materials and alloys the austenitic stainless 316L steel has been subjected most frequently to the study of the crack initiation and short crack growth [4; 91; 118; 183; 188; 189]. Sanicro 25 steel also belongs to the family of austenitic steels with the high content of alloying elements as Ni, Cr and N. It is expected that the mechanisms of the crack initiation and growth will be similar to e.g. the 316 grade of steels [96; 133; 183; 188].

Stage I fatigue crack growth follows, similar to the 316L [4] steel, the highest shear stress planes oriented approximately 45 degrees in relation to the applied load (see Fig. 10.1.1) as shown in previous Chapter 12. As expected Stage I crack growth has a crystallographic character affected by the structure of the material (grain size, grain disorientation...) and by the fatigue induced dislocation microstructure (see Chapter 13.2.8). The Stage I crack grows under the shear loading during the tensile part of the cycle as shown in Chapter 3.3 (see Fig. 3.3.2). The early growth of the Stage I crack is characterized by the mutual interlinking of small semi-elliptical shallow cracks developed along the PSMs as observed in 316L steel [172]. Later, when the microstructurally small crack has reached the depth of several micrometers the parallel cracks within one grain link together typically along the {111} slip planes. Those are frequently associated with the emerging slip markings on the grain surface (see Fig. 10.1.2). The surface length of the Stage I cracks is of the structural unit length. Since the average grain size is sufficiently large (about 60  $\mu\text{m}$ ), the straight surface crack path was observed only occasionally. Similar observations were performed by Lindstedt [133] and Zhixue [190] on 316 austenitic steel. The zig-zag path of the Stage I cracks leads to the decrease of the crack growth rates as a result of the roughness-induced crack closure. On the other hand, the early crack linkage within one grain might increase the crack growth rate of the Stage I crack.

As discussed in the previous Chapter 12, the higher is the applied cyclic strain amplitude, the higher is the surface fraction of the PSMs within the grains. Hence, the probability of the crack initiation increases and the period of the early Stage I crack growth decreases. Moreover, the high number of the initiated cracks increases the probability of further crack extension over the grain boundary since grain boundaries represent the effective obstacles for the short crack growth. The high number of PSMs on the surface and subsequently the more frequent crack initiation was found in the materials with high nitrogen content [133] what is in agreement with our observations. The high activity of the slip systems also increases the initiation probability along the GBs and TBs. The early growth of Stage I cracks along TBs had the same shear character as observed for the cracks initiated along

the PSMs within the surface grains. These cracks grow along the  $\{111\}$  slip plane having the highest shear stress (see Figs. 9.1.4 and 9.1.5). Nevertheless, it has been observed, that the Stage I crack growth often does not exceed the length of the grain size. More commonly, the crack growing in Stage I deflects from its original crack path and continues to propagate perpendicular to the loading direction which is denoted as the Stage II crack growth (see Figs. 10.1.1 and 10.1.7b).

The number of the initiated cracks was observed to increase during the cycling for all cycled specimens. It is in agreement with the observations performed on the cycled 316 stainless steel [133; 134; 190] that the fraction of the surface cracks increases till the half of the lifetime. Later the fraction of the surface cracks decreases. This implies that initiated cracks link together and the linking of the cracks contributes to the growth of the cracks. This is more pronounced in the case of high strain amplitude cycling as shown in Fig. 13.1.1.

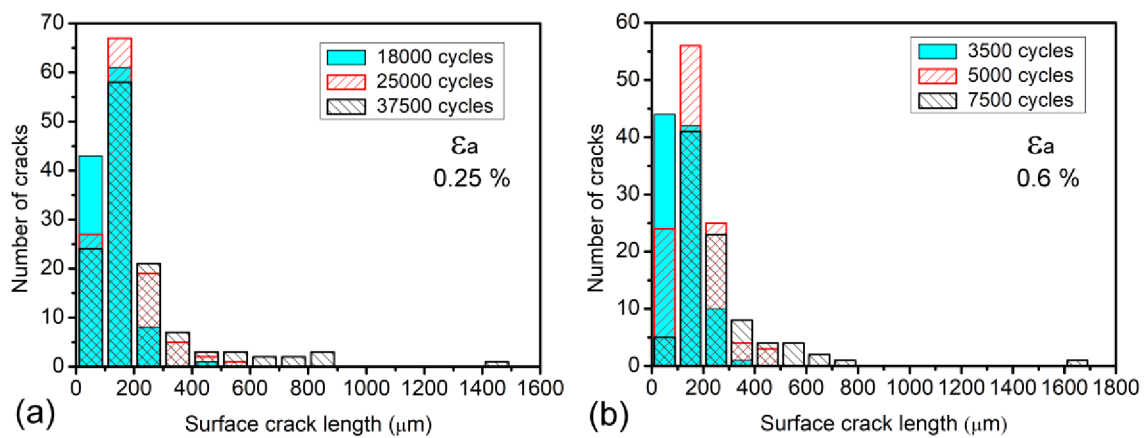


Figure 13.1.1: The evolution of the surface cracks during the cycling. The surface crack length vs. the number of cracks is evaluated for three stages of the fatigue life ( $\sim 50\%$ ,  $\sim 70\%$ ,  $100\%$ ). The samples were subjected to the cyclic loading with low ( $0.25\%$ ) and high ( $0.6\%$ ) strain amplitudes.

In high strain amplitude loading usually one crack becomes dominant crack (see Fig. 13.1.1b) and plastic strain is concentrated to its crack tip plastic zone. Moreover, the stress-shielding effect coming from the stress-free crack surfaces of the dominant crack causes the shielding of other cracks and only dominant crack propagates.

Other important feature affecting the crack growth rate is the roughness-induced crack closure. Comparing of Figs. 10.1.6, 10.1.8 and 10.1.9 we can see that the crack path character depends significantly on the applied strain amplitude. According to Blochwitz et al. [118] the fraction of PSMs, which corresponds to the slip systems with the highest SF (i.e.  $\{111\}$  slip planes), decreases with increasing applied strain amplitude. His findings are in a good agreement with our observations (see Figs. 10.1.6, 10.1.8 and 10.1.9). The crack path in the case of low strain amplitudes has a jagged character while in the case of high strain amplitudes the crack path is much smoother with the striations beginning early in the crack growth. The zig-zag crack path induces additional Mode II crack growth during the cycling causing the roughness-induced crack closure. As a result, the effective stress intensity factor of the crack reduces during cyclic straining and subsequently the crack propagation rate is reduced. Moreover, according to Lindstedt [133] the opening of the

Stage I cracks and also crack branching during the cycling consume energy leading to the decreasing of the energy release rate of the dominant crack for all strain amplitudes.

## 13.2. Crack growth kinetics

### 13.2.1. Equivalent crack length concept

The inspection of the short fatigue crack growth shows that for all strain amplitudes several cracks are initiated in most cases within the shallow notch. The growth of the individual cracks at the beginning of the cycling for all strain amplitudes is influenced by the microstructure of the material (i.e. grain orientation). The high angle grain boundaries represent the effective barriers for the further crack growth [191; 192]. As the crack length increases the increment of the crack rate becomes more stable and can be described by the exponential law (see Eq. 4.2.6). Though several cracks grow simultaneously at approximately the same rate (see Fig. 10.2.1), different physical crack can become instantaneously the longest crack in the notch. Based on the study by Polák et al. [92; 193] these two facts allow approximating the growth of all cracks growing under the cycling with constant strain amplitude by one representative crack. The same fatigue life is reached if the aggregate of growing short cracks in the specimen subjected to constant plastic strain amplitude loading is replaced by the growth of the instantaneously longest crack. This crack is called the equivalent crack [133; 134]. Since the plastic strain amplitude does not change significantly during the most of the fatigue life at a room temperature [194], we can consider that the cracks grow under “constant” plastic strain amplitude.

According to Polák et al. [131; 132; 195] the equivalent crack is the crack whose length is approximately equal to the length of the longest crack present in the investigated area. If only one crack is growing the equivalent crack is identical with this physical crack. The concept of equivalent crack allows to substitute the crack growth rates of all growing cracks by the growth rate of the equivalent crack resulting in the same fatigue life.

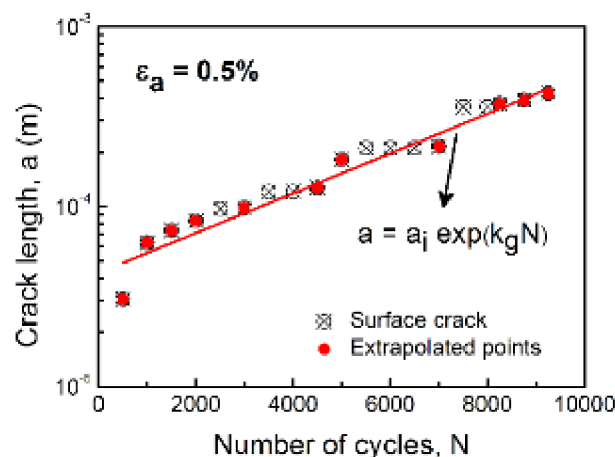


Figure 13.2.1: Evaluation of the data corresponding to the growth of the equivalent crack with semicircular shape (red full symbols). See the text for explanation.

Obrtlík et al. [111] and Blochwitz and Ritchie [118] found out that the difference between the semi-circular crack shape and the real semi-elliptical shape is negligible. Since it is



difficult to measure the depth of the crack in the cylindrical specimens, the crack length in the bulk has been described by the half of the surface crack length. When two cracks link together, the resulting crack stops growing on the surface (see Fig. 10.1.4) and the crack grows only into the bulk of the material. To evaluate properly the growth of the equivalent crack only the points in which the crack has approximately semi-circular shape should be considered. According to the mathematical analysis of the fatigue crack shape based on the fracture mechanics approach in the infinite space [196; 197], the crack tends to reach semi-circular shape. Since we cannot follow the growth of the crack in the bulk in the case of linkage of two semi-circular cracks we can only omit the points which do not correspond to the growth of the cracks having the semi-circular shape (see Fig. 13.2.1). Open symbols in the plot are derived from the measured surface crack length. If the crack length suddenly increased and stopped its further growth at the surface for some time it indicates the cracks linkage and the growth of the interlinked cracks in the bulk. Therefore, the last point before the sudden increase of the crack length determines the length of the equivalent crack. After the cracks linkage the first point, which shows the continual growth of the equivalent crack is considered. The relevant extrapolated points in Fig. 13.2.1 are represented by full (red) symbols. Other symbols (open circles) are excluded from the data characterizing the growth of the equivalent semi-circular crack. By considering the previously mentioned points the equivalent crack characterizes the growth of all cracks including their mutual interactions as the crack coalescence [133; 134] and the crack shielding effects as well.

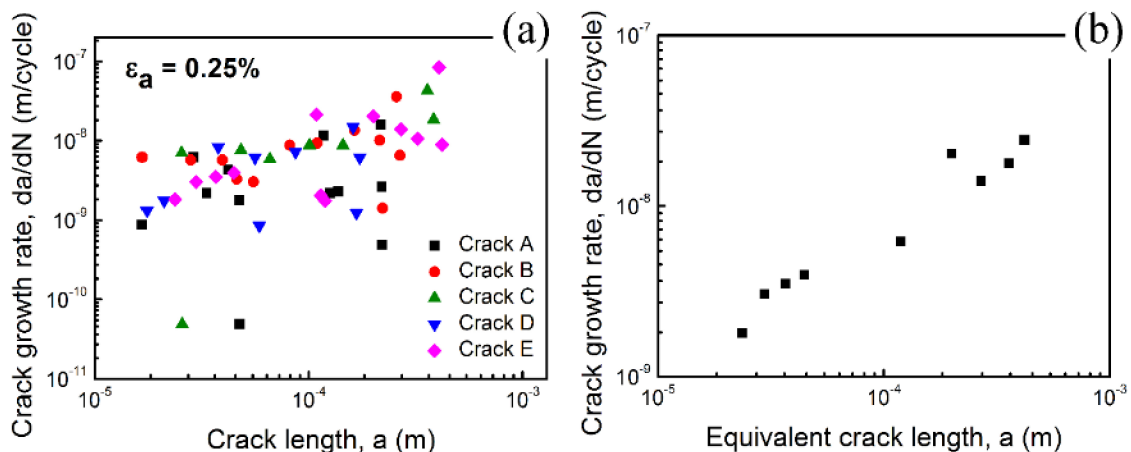


Figure 13.2.2: Crack growth rates vs. crack length in specimen cyclically strained with total strain amplitude 0.25%; (a) crack growth rates were evaluated from all measured data; (b) crack growth rates were evaluated from the data corresponding to equivalent semi-circular crack.

The method of the selection of the points corresponding to the growing equivalent semi-circular crack is shown in Fig. 13.2.2. Figure 13.2.2a shows the plot of crack growth rates evaluated using difference method vs. the crack lengths measured for the sample cycled with  $\epsilon_a = 0.25\%$  when all data points of measured cracks were considered. The points exhibit significant scatter in crack growth rates in the case of all cracks. This could bring some imperfection in the extrapolation of the data. Nevertheless, the cracks, in general, show approximately the same crack growth rates for the same crack length. If only data corresponding to the equivalent growing crack (data showing the growth of the largest crack observed at that moment within the area) are considered the scatter of the crack

growth rates is significantly lower. No important variations in the crack growth rates are present and the data can be fitted by the power law (see Fig. 13.2.2b).

### 13.2.2. Fracture mechanics approach

Short fatigue crack growth rates can be described using fracture mechanics approaches. Since the stress intensity factor is often chosen as the parameter characterizing the propagation of cracks the crack growth rate of the equivalent crack is plotted versus stress intensity amplitude  $K_a$ .  $K_a$  is calculated according to the model optimizing the crack front shape as described by Trávníček et al. [198] and Hutař et al. [141]. The crack front shape was found to be semi-ellipse. The crack length  $a$  in the bulk of the material was derived from the surface crack length. The stress intensity factor was calculated for physically short cracks, which have the length in the range 0.05 mm ÷ 2 mm.

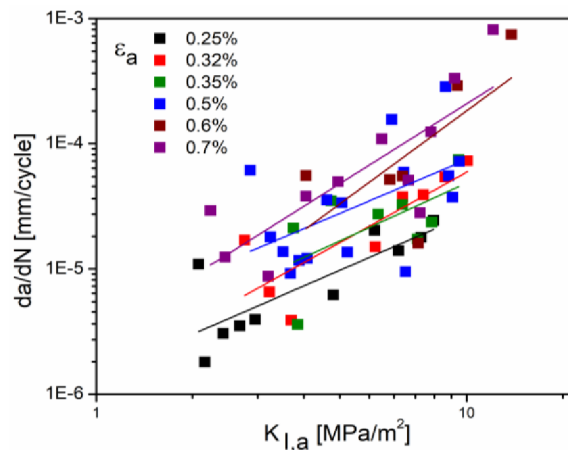


Figure 13.2.3: Short crack growth rate vs. stress intensity factor,  $K_{I,a}$  for Sanicro 25 steel for individual equivalent cracks growing under cycling with  $\epsilon_a$  in the range from 0.25% to 0.7%.

The crack growth rates in Fig. 13.2.3 show significant scatter. Crack growth rates of all equivalent cracks cannot be described by one master curve. With increasing applied strain amplitude propagation rates increases. According to Ritchie [199] the loading with strain amplitude resulting in appreciable plastic strain amplitude enhances the cyclic plastic zone ahead of the crack front. Since the stress intensity factor is applicable for small scale yielding when the plastic zone is much smaller than the crack length the description of the stress field around the crack tip based on the stress intensity factor is not appropriate. This is called the physically short crack effect [199].

Therefore, the parameter describing the intensity of elastic-plastic stress field ahead of the crack front has to be used as proposed by Rice [109]. The crack propagation rate can be characterized by  $J$ -integral.  $J$ -integral is composed of two components (see Chapter 4.2.2), the elastic and plastic component, and can be estimated for loading Mode I.

Since the  $J$ -integral approach considers nonlinear material behavior it is more applicable for description of the short crack growth rates. Crack growth rates plotted vs.  $J$ -integral amplitude,  $J_a$ , (Fig. 13.2.4) exhibit smaller scatter compared to that in Fig. 13.2.3. Although

the curves corresponding to individual equivalent cracks lie close to each other the scatter still indicates the dependence on the applied strain amplitude.

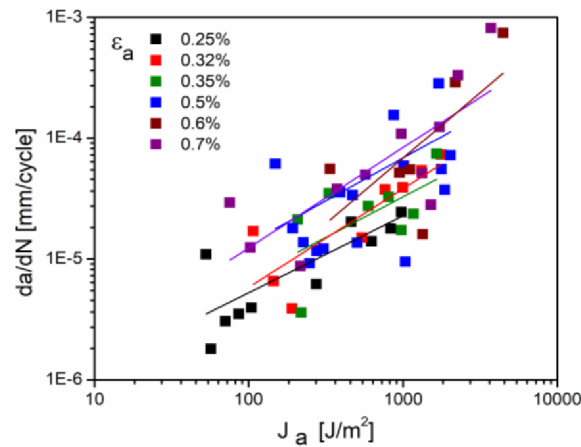


Figure 13.2.4: Short crack growth rate vs.  $J$ -integral amplitude for Sanicro 25 steel for individual equivalent cracks growing under the cycling with  $\epsilon_a$  in the range from 0.25% to 0.7%.

It was reported earlier [200; 201] that during the low cycle fatigue the fraction of the plastic part of  $J$ -integral increases with increasing applied total strain amplitude. It is shown by Trávníček et al. [198] that the fraction of plastic component increases from 66% of total  $J$ -integral for the lowest strain amplitude of  $2.5 \times 10^{-3}$  up to 82% of total  $J$ -integral for the highest strain amplitude of  $7 \times 10^{-3}$ . It was concluded that the plastic component of  $J$ -integral plays the main role in the short crack growth.

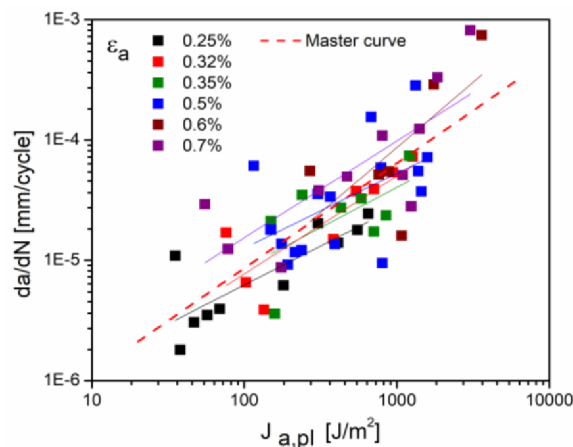


Figure 13.2.5: Short crack growth rate vs. plastic component of  $J$ -integral for Sanicro 25 steel for individual equivalent cracks growing under cycling with  $\epsilon_a$  in the range from 0.25% to 0.7%.

Nevertheless, the plot of crack growth rates of equivalent cracks vs. the plastic component of  $J$ -integral (see Fig. 13.2.5) still shows appreciable scatter. The dependence on the applied

strain amplitude remains. The high scatter in the values of crack growth rates may be caused by the mutual linkage of the initiated short cracks. During the coalescence of two cracks the plastic zone ahead of the crack front varies and this can also affect the crack growth rate. Nevertheless, even in the case of scatter the dependence of the crack growth rate on the  $J_{ap}$  can be extrapolated by the master curve (Eq. 4.2.5) with the parameters  $C_{Jp} = 1.522 \times 10^{-7}$  and  $m_{Jp} = 0.874$  characterizing the crack propagation in Sanicro 25.

The crack growth rates of the Sanicro 25 are compared with the crack growth rates of the 316L steel [139] in Fig. 13.2.6. In the case of 316L steel the short crack growth was measured on the samples cycled with constant strain amplitudes in the range of  $3.2 \cdot 10^{-3}$ . Fractographic analysis has revealed that the crack front shape of 316L steel slightly differs from that observed in the Sanicro25 steel. While, semi-circular crack front shape was found for the 316L steel, in the case of Sanicro 25 the semi-elliptical crack front shape was observed. Fig. 13.2.6 shows that the 316L steel exhibits higher crack growth rates for the same plastic component of the  $J$ -integral when compared to those of the Sanicro25 steel. The parameters of the Eq. 4.2.5 for 316L steel are  $C_{Jp} = 2.341 \times 10^{-8}$  and  $m_{Jp} = 1.342$ . The differences appear mainly in the domain of high applied strain amplitudes i.e. for high plastic strain amplitudes. The CSS curve of 316L steel [198] shows that there has to be higher stress amplitude for 316L steel to reach the same plastic strain amplitude as the Sanicro 25 steel. It means that the cyclic plastic deformation in the case of Sanicro25 steel is enhanced. The cyclic plastic deformation is localized into the narrow PSBs (see Chapter 9.2) leading to the smaller plastic zone ahead of the crack tip than in the 316L steel. Therefore, the crack tip blunting may be smaller than that in the case of 316L steel leading to the smaller crack increment in one cycle. The effective value of the  $K_a$  can be also decreased due to the high planar character of dislocation slip.

Later in Chapter 13.2.4, the measured fatigue lives will be compared with the predicted ones based on parameters characterizing the crack growth rate propagation. The residual fatigue lives (in the range of crack length from 0.1 mm to 0.5 mm) will be compared also with the ones calculated based on the parameters of the Master curve plotted in Fig. 13.2.6 which characterizes both materials. The parameters of the Master curve are listed as follows  $C_{Jp} = 3.970 \times 10^{-8}$  and  $m_{Jp} = 1.212$ .

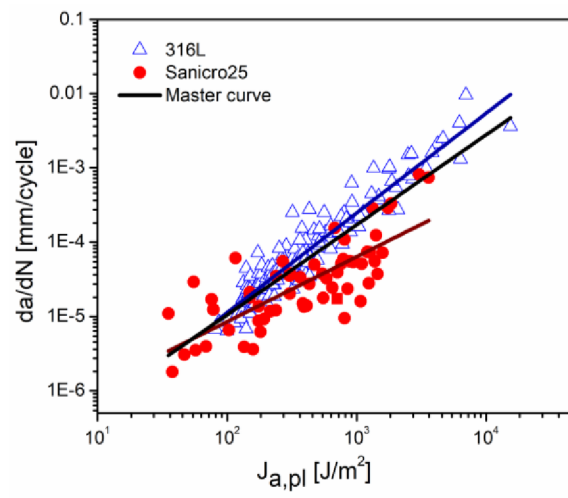


Figure 13.2.6: Short crack growth rate vs. plastic component of  $J$ -integral for Sanicro 25 steel and 316L steel.

### 13.2.3. Crack growth under plastic strain amplitude

Alternative approach to the fracture mechanics on the characterization of the short crack growth is presented by Polák [144]. We will analyze the same data by this approach described in Chapter 4.2.3.

Since the information about the crack shape in the bulk of the material is missing during cyclic straining the crack length  $a$  was evaluated under assumption that the crack shape was semi-circular as discussed in Chapter 13.2.1. The equivalent crack length has been evaluated from the experimental data according to the procedure described in previous Chapter 13.2.1 for all strain amplitudes. Fig. 13.2.7 shows the semi-logarithmic plots of the lengths of all equivalent cracks vs. the number of cycles. The data show a good linear dependence in the semi-logarithmic plot. The data were thus fitted by the exponential law corresponding to Eq. 4.2.6.

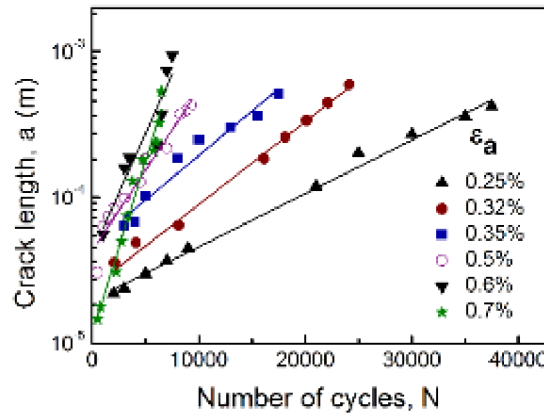


Figure 13.2.7: Length of equivalent semi-circular cracks vs. number of cycles in cycling with constant total strain amplitude in the range of  $(2.5-7.0) \times 10^{-3}$ .

Both parameters  $a_i$  and  $k_g$  of the Eq. 4.2.6 were evaluated using least-square regression analysis procedure, and the results for all strain amplitudes are shown in Table 13.2.1. The extrapolated initial crack length does not show a systematic dependence on the strain amplitude. The average value was 27  $\mu\text{m}$ , which is approximately the half of the average grain size of the material. In contrast to that, the crack growth coefficient increases systematically with the increasing applied strain amplitude. It means the crack length increment in one cycle increases with the increasing applied strain amplitude as was also shown previously in several materials [139]. Since the fatigue life in the regime of low cycle fatigue is dependent on the plastic strain amplitude as observed by Manson and Coffin [28; 29] we shall correlate  $k_g$  coefficient with the plastic strain amplitude.

$\varepsilon_a$ nominal	$2.5 \times 10^{-3}$	$3.2 \times 10^{-3}$	$3.5 \times 10^{-3}$	$5.0 \times 10^{-3}$	$6.0 \times 10^{-3}$	$7.0 \times 10^{-3}$
$a_i$ (m)	$1.98 \times 10^{-5}$	$2.40 \times 10^{-5}$	$4.74 \times 10^{-5}$	$4.28 \times 10^{-5}$	$4.20 \times 10^{-5}$	$1.15 \times 10^{-5}$
$k_g$	$8.51 \times 10^{-5}$	$1.31 \times 10^{-4}$	$1.40 \times 10^{-4}$	$2.55 \times 10^{-4}$	$3.75 \times 10^{-4}$	$5.48 \times 10^{-4}$

Table 13.2.1: Parameters of the exponential dependence of the equivalent crack length vs. number of cycles.

Since the cyclic plastic strain is considered to be the principal factor contributing to the growth of the fatigue cracks the rate of the short crack growth has been proposed to be the function of the plastic strain amplitude (see Eq. 4.2.8). Unfortunately, only the nominal values of the stress and the strain are known from the directly measured hysteresis loop. Since the shallow notch acts as the stress and the strain concentrator leading to the increase of the plastic strain in the area of the notch, it has to be analyzed before the further characterization.

Since the applied stress and strain amplitudes in the material are known, it is possible to estimate the plastic strain amplitude in the notch numerically using the finite element analysis with software ANSYS. Due to the geometrical symmetry, it was sufficient to use only one quarter of the specimen gauge section (see Fig. 6.1.2b). Previously measured experimental data [194] of cyclic stress-strain curve for Sanicro 25 steel lead to the stress-strain relation characterized by the power law function

$$\varepsilon_a = \frac{\sigma_a}{E} + \left(\frac{\sigma_a}{K'}\right)^{1/n} \quad (13.2.1)$$

where  $E$  is Young's modulus,  $K'$  and  $n'$  are the fatigue hardening coefficient and the fatigue hardening exponent. Based on the Fig. 13.2.8 the stress-strain response can be also described by the linear dependence between the stress and strain amplitudes. Therefore, the bilinear model can be considered to reasonably describe the elastic-plastic behavior of the material during the cycling. Plastic strain amplitudes in the notch root for different applied strain amplitudes evaluated using the ANSYS software are listed in Table 13.2.2.

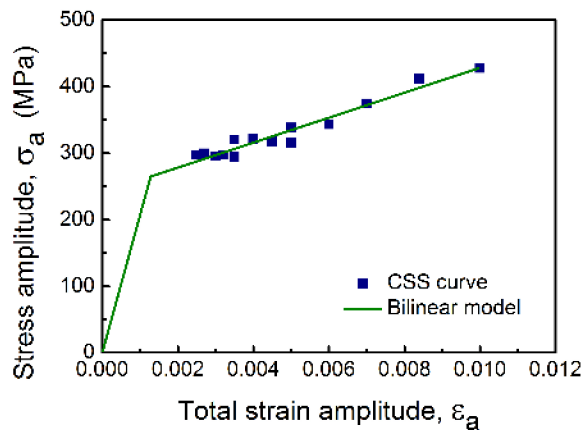


Figure 13.2.8: Bilinear model used for the evaluation of  $\varepsilon_{ap}$  in the notch. Stress amplitude is plotted vs. total strain amplitude.

Applied	$\varepsilon_a$ nominal	$2.5 \times 10^{-3}$	$3.2 \times 10^{-3}$	$3.5 \times 10^{-3}$	$5.0 \times 10^{-3}$	$6.0 \times 10^{-3}$	$7.0 \times 10^{-3}$
ANSYS	$\varepsilon_a$ in notch	$3.21 \times 10^{-3}$	$4.0 \times 10^{-3}$	$4.4 \times 10^{-3}$	$6.1 \times 10^{-3}$	$7.3 \times 10^{-3}$	$8.4 \times 10^{-3}$
	$\varepsilon_{ap}$ in notch	$1.75 \times 10^{-3}$	$2.50 \times 10^{-3}$	$2.82 \times 10^{-3}$	$4.40 \times 10^{-3}$	$5.44 \times 10^{-3}$	$6.48 \times 10^{-3}$

Table 13.2.2: Total and plastic strain amplitudes estimated by ANSYS.

Figure 13.2.9a shows the effect of the shallow notch on the amplitude of the plastic strain. Both the plastic strain amplitude in the notch evaluated using the ANSYS and the plastic strain amplitude derived from the measured hysteresis loop are plotted vs. the crack growth coefficient. As expected, the highest increase is found for the smaller strain amplitudes close to the elastic section of the cyclic stress-strain curve. Later, as the applied strain increases the increase in the plastic strain amplitude does not change significantly. The data can be very well approximated in the bilogarithmic plot by the straight line. The higher the plastic strain amplitude the higher the increase of the crack length during one cycle.

The parameters of Sanicro 25 describing the crack growth rates according to the Eq. 4.2.8 depend whether we use the measured plastic strain amplitude or the one calculated in the notch. By comparing Figs. 13.2.9a and 13.2.9b it is notable, that the crack growth law corresponding to the plastic strain amplitude calculated in the notch is in good agreement with the results shown in Fig. 13.2.9b. The lower crack growth rates of Sanicro 25 steel leads to the longer fatigue lives compared to 316L steel [48]. The plastic strain amplitude increased by the notch effect plays an important role in crack growth. Then the parameters representing the crack growth law derived for Sanicro 25 steel in Eq. 4.2.8 are as follows: the parameter  $k_{g0}$  is equal to 0.544 and the parameter  $d$  is equal to 1.393.

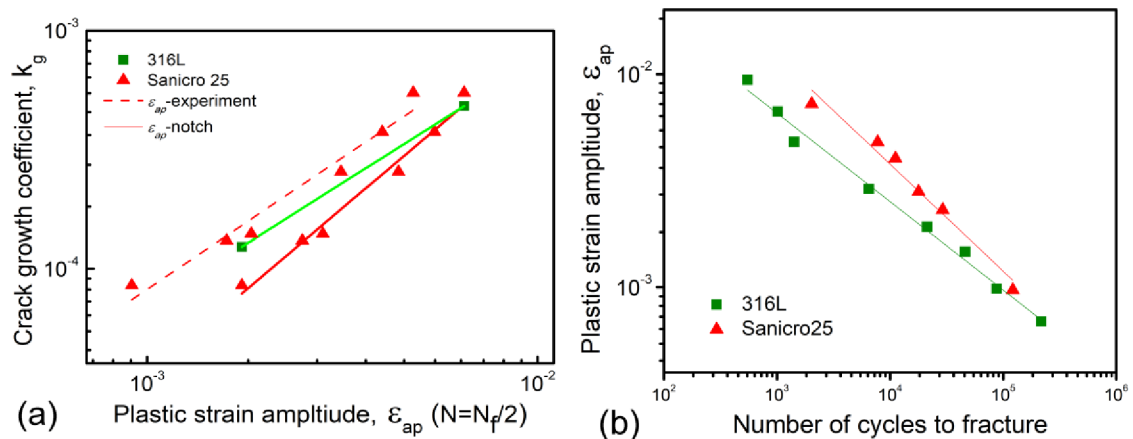


Figure 13.2.9: (a) Crack growth coefficient evaluated for two austenitic stainless steels 316L and Sanicro25. (b) Fatigue life curves of 316L steel [46] and Sanicro 25 steel [194] derived from the smooth cylindrical specimens.

By comparing the crack growth parameters (see Eq. 4.2.8) evaluated for the 316L steel [142]  $k_{g0} = 0.091$  and  $d = 1.04$  and the Sanicro 25 steel in the Fig. 13.2.9a the relation between the crack growth rate and the plastic amplitude shows different results when compared to Fig. 13.2.6. Contrary to the dependence on the  $J_{a,pl}$ , here the crack growth rates are getting closer for high cyclic plastic strain amplitudes and the rates differ for the decreasing cyclic plastic strain amplitude. Nevertheless, it is apparent that the short crack growth of both materials are different and cannot be characterized by the same parameters.

### 13.2.4. Fatigue life

The number of cycles needed to extend the crack length from the initial crack length  $a_0$  to the final crack length  $a_f$  can be estimated integrating equations 4.2.5, 4.2.6 and 4.2.7. To compare the estimated number of cycles using crack growth law or using  $J_{a,pl}$  with the experimental ones, the interval of the physically short crack length 0.1-0.5 mm, in which the crack lengths were measured, was chosen.

The predicted number of cycles estimated using both the fracture mechanics approach ( $J_{a,pl}$ ) and the cyclic plastic strain amplitude approach are plotted along with the experimental data in Fig. 13.2.10. Here, the cyclic plastic strain amplitude is plotted vs. the number of cycles corresponding to the number of cycles spent on the crack extend from 0.1 mm to 0.5 mm. The number of cycles calculated using parameters  $k_{g0}$  and  $d$  of the Polák's model give very good agreement with the experimental data. Contrary to that the number of cycles calculated analytically using  $J_{a,pl}$  with parameters derived for the Sanicro25 steel shows higher slope of the linear fit. The highest deviation from the experimental data shows plot using the Master curve derived for both steels 316L and Sanicro 25. The reason is that the Master curve in Fig. 13.2.6 is well above the data of Sanicro 25. It indicates that one Master curve cannot characterize several materials with different material properties.

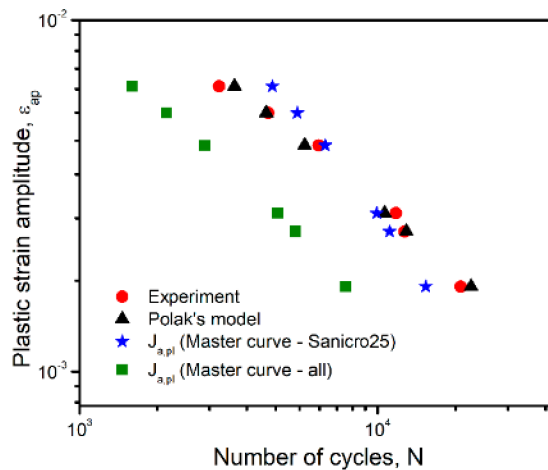


Figure 13.2.10: Dependency of the plastic strain amplitude  $\varepsilon_{ap}$  and the number of cycles  $N$ , which corresponds to the number of cycles spent on the crack extend from 0.1 mm to 0.5 mm in the Sanicro25 steel.

Provided that the initiation and growth of all fatigue cracks can be substituted by the growth of an equivalent crack from the initial crack length,  $a_i$ , up to final crack length,  $a_f$ , which follows the crack growth law (see Eq. 4.2.6) and the crack growth coefficient,  $k_g$ , depends on the plastic strain amplitude according to the relation 4.2.8 the crack growth law can be integrated and fatigue life is obtained using parameters of the crack growth law. Additionally, it was shown earlier by Polák [144] and Polák and Zezulka [143] that the parameters of the short crack growth law and the parameters of the Manson-Coffin law are related as follows:

$$d = -\frac{1}{c} \quad k_{g0} = 2(\varepsilon_f')^{1/c} \ln\left(\frac{a_f}{a_i}\right) \quad (13.2.2)$$



The parameters of the short crack growth law can be thus evaluated from the parameters  $c$  and  $\varepsilon_f'$  determined from the Manson-Coffin curve (Eq. 2.1.) provided the ratio of the final to the initial crack length is estimated. Similar to that, the parameters of the Manson-Coffin law can be inversely evaluated using the parameters of the crack growth law  $k_{g0}$  and  $d$  (see Eq. 13.2.2).

The fatigue life curves of previously measured smooth cylindrical specimens [194] and currently measured notched cylindrical specimens are compared in Fig. 13.2.11. Along with the experimentally measured data, the derived fatigue life curve estimated using the parameters of the Manson-Coffin law evaluated from the crack growth law parameters of notched specimens (using the Eq. 13.2.2) is plotted as well. The number of cycles to fracture was estimated by integrating derived Manson-Coffin law. Since the parameter  $\varepsilon_f'$  depends on the ratio of the initial crack length and final crack length, the initial crack length for Sanicro 25 steel was put equal to half of the grain size  $27 \mu\text{m}$  and  $1 \text{ mm}$  was considered as the final crack length.

The parameters of the crack growth law of smooth specimens are also evaluated using Eq. 13.2.2, from the measured parameters of Manson-Coffin law for smooth specimens. All parameters of the experimentally measured and derived Manson-Coffin laws and crack growth laws for smooth specimens as well as for notched specimens are listed in Table 13.2.3.

In the case of smooth specimens the number of cycles is plotted vs. plastic strain amplitude derived from the measured hysteresis loop. In the case of notched specimens, the number of cycles is plotted vs. plastic strain amplitudes calculated in the notch (see Tab. 13.2.2 and Fig. 13.2.9). All the plastic strain amplitudes are considered in the half of the fatigue life. However, the plastic strain amplitude does not change significantly during the cycling of Sanicro 25 [194] (see Chapter 1.1).

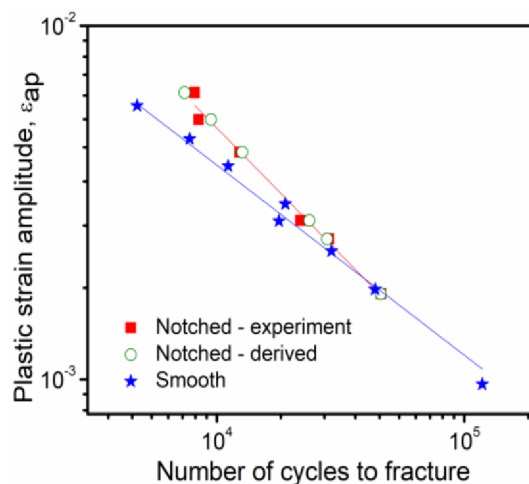


Figure 13.2.11. Manson-Coffin fatigue life curves of Sanicro25 steel (smooth [194] and notched specimens) compared with the Polák's crack growth law.

Both derived and experimentally measured Manson-Coffin laws of notched specimens lie very close. It indicates that the crack growth under the cyclic plastic strain determines the fatigue life of the specimen under low cycle fatigue conditions. Then the parameters of the

short crack growth law can be reasonably well used to evaluate the parameters of the Manson-Coffin law and to determine the residual fatigue life of the sample.

Samples	Manson-Coffin curve				Crack growth law			
	$\varepsilon_f'$		$c$		$k_{g0}$		$d$	
	exp.	der.	exp.	der.	exp.	der.	exp.	der.
Smooth	<b>7.22</b>		<b>-0.718</b>			0.754		1.393
Notched		6.404		-0.718	<b>0.544</b>		<b>1.393</b>	

Table 13.2.3: Parameters of the *experimentally measured* and calculated crack growth law and Manson-Coffin law for both smooth and notched specimens according to Eq. 13.2.2.

The small difference between the Manson-Coffin law measured on smooth specimens and the derived curve for notched specimens can be explained by the effect of the different surface preparation and also the effect of plastic strain gradient in the notch. The smooth samples were finally ground while the surface of notched specimen was electrolytically polished. The gradient of plastic strain can have different effect on crack growth rates for small and high plastic strain amplitudes.

## 14. The role of oxidation in damage mechanisms during high temperature loading

### 14.1. Oxidation assisted grain boundary cracking

High temperature fatigue damage mechanisms in austenitic stainless steels differ appreciably from that at room temperature [6]. Room temperature cyclic straining of Sanicro 25 is characterized by the strong localization of the cyclic plastic strain into the narrow persistent slip bands [21] and the crack initiation starting from the PSMs, especially from the tip of the intrusions (see Fig. 9.1.2). Contrary to that, the high temperature enhances temperature activated cross slip of dislocations and thus the localization of the cyclic plastic strain is more difficult as observed previously in 316L steel [55]. Furthermore, in the case of Sanicro 25 steel, the motion of dislocations is limited by their pinning by the NbN nanoprecipitates, which nucleated during the fatigue [202; 203]. Therefore, the localization of the cyclic plastic strain into the PSBs is very difficult. Due to that, the appearance of the extrusions along the PSBs within the grains at the surface is very sporadic and no cracks were observed to initiate from extrusions.

Material resistance to the near-surface high temperature degradation in terms of the oxide formation, especially along the interfaces, is closely connected with the chemical composition and the initial microstructural state. As mentioned earlier in Chapter 8 only Nb-rich Z-phase complex nitrides are present in the initial state of the material. Other particles, which may significantly influence the oxidation resistance at the GB, such as Cr-rich  $M_{23}C_6$  carbides, are absent in the initial state.  $M_{23}C_6$  carbides were observed within the grains as well as in the grain boundaries only after the high temperature cyclic loading. According to work of Trillo and Murr [202], an incoherent grain boundary might present

the primary nucleation site for the Cr-rich  $M_{23}C_6$  carbide precipitation at high temperature [6; 7; 19]. Structural analysis of Sanicro25 steel has revealed that the predominant fraction of the grain boundaries are randomly oriented HAGBs, as exemplified in Fig. 8.2. Boundaries of this type are characteristic by a high amount of lattice defects (such as dislocations and vacancy type defects) introducing an interface with high interfacial energy. The higher the interfacial energy of the boundary the more probable is the nucleation of carbides. In steels with high content of Cr and interstitial C dissolved in the matrix these particles start to nucleate and coarsen very rapidly [12] and shortly can be present at LAGBs. As a result, heavily Cr-depleted zones are formed at the GBs [202; 203] as well as at the carbide/matrix interfaces as shown in Figs. 11.1.6 and 11.1.8. As mentioned earlier in Chapter 3.4, if the Cr content in the grain boundary has dropped below 12 wt. % the material loses the ability to create a protective  $Cr_2O_3$  oxide layer and undergoes intergranular oxidation and cracking as shown in Figs. 11.1.9 and 11.1.6.

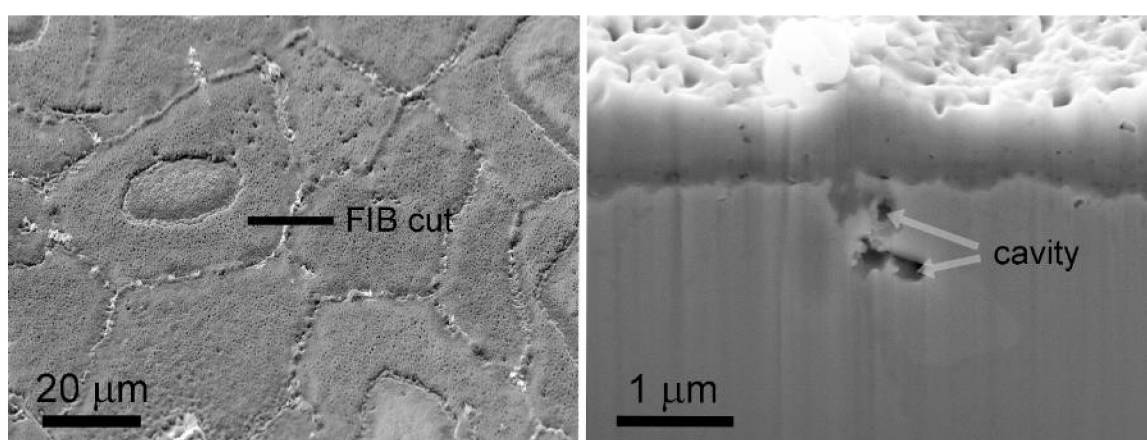


*Fig. 14.1.1: Surface of the polished specimen after high temperature exposure at 700 °C for 5 hours. FIB cross section reveals the preferred oxidation of the material along the grain boundaries as well as the preferential growth of the oxide extrusions and intrusions at these sites.*

The oxidation of the GBs is due to the easier penetration of the oxygen into the material by means of the motion of vacancies under the external loading or by high temperature activation of diffusion according to the Eq. 3.4.2, preferentially in HAGBs and also in grain boundaries with no specific orientation such as LAGBs (see Fig. 8.2) [9]. The early GB oxidation (see Figs. 11.1.2 and 11.1.4) is characterized by the growth of the internal oxide intrusion in the form of the Cr-rich layer as shown also by the sample exposed to a high temperature for 5 hours in Fig. 14.1.1. Such an oxide layer should create the protective layer against further penetration of the oxygen into the material and diffusion of the metallic elements to the surface. Nevertheless, as is shown in Fig. 14.1.2 oxide layer consists of outer scales enriched in Fe further from the matrix and Cr-rich scales close to the oxide/matrix interface. The Cr-rich layer is found to be porous which probably promotes further oxidation of the material. Below these oxide layers, thick oxidation-affected zone is formed in the matrix. This zone is heavily enriched in Ni and depleted in Cr and Fe as a result of Cr- and Fe-rich oxides growth on the surface. The Ni-rich zone represents the barrier for the further inward diffusion of the oxygen and outward diffusion of the metal elements. The results are in a good agreement with the experimental work of Rothman et

al. [204], who measured that the diffusion rate of Ni in the Fe-Cr-Ni based alloy system is notably lower when compared to that of Cr and Fe. These conclusions are also in accordance with the observations of Intiso et al. [18]. They have observed similar double-layered oxide structure after static oxidation tests at 600 °C in dry and wet O<sub>2</sub> environments performed on Sanicro 25 steel. Furthermore, cavities are formed at the tip of the oxide intrusions (see Figs. 14.1.1, 11.1.4 and 11.1.6). This can be related to the Kirkendall-type of diffusion [205] due to the significant difference between the diffusion rates of Cr, Fe and Ni. It is assumed that the diffusion of Cr, Fe and Ni in solid solution is due to vacancy mechanism in such a way that the flow of matter is matched by an equal and opposite flow of vacancies. Considering the fact that the diffusion rate of Ni is several times lower than that of Cr and Fe [204], it is natural that vacancies bound to Fe and Cr atoms flowing to the interface condense forming a cavity. Cavities were found also below the surface oxides and even also within the internal oxides as shown in Figs. 14.1.1 and 11.1.6.

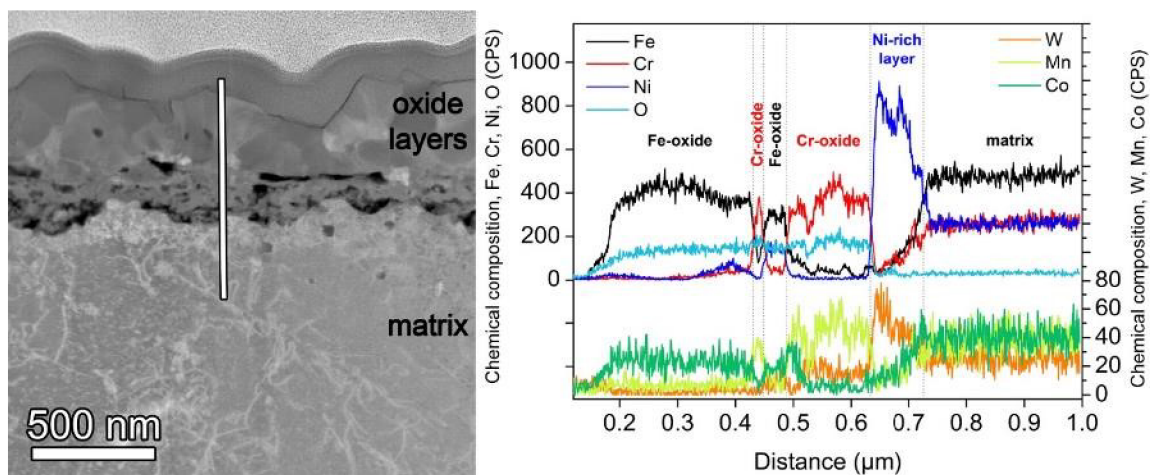


*Fig. 14.1.2: HAADF-STEM image showing oxidized surface of the material. Objects appearing black are holes in the oxidized layer corresponding to relatively high porosity. White line marks the position where EDS-linescan analysis was done. Raw data were plotted in terms of spectral intensity corresponding to each element as a function of distance. Oxide layer is composed of thick outer Fe-rich oxide, which is on the top of two thin overlapping Cr-rich and Fe-rich oxides. These are on the top of inner thick Cr-oxide layer, which is in contact with the surface of the material. Close to the interface in between the inner Cr-oxide and the matrix, layers heavily enriched in Ni and W arise.*

As discussed above, high temperature notably decreases fatigue endurance of Sanicro 25 steel not only by the change of slip character and the microstructure [21], but also by acceleration of the oxygen penetration along the grain boundaries leading subsequently to the modification of the fatigue crack initiation process. Instead of transgranular initiation observed at room temperature, the fatigue cracks initiate in the intergranular manner (see Figs. 11.1.2 and 11.1.4). The early stage of damage is in the form of wedge-shaped oxide intrusions and surface roughening (see Figs. 11.1.2 and 11.1.6) along the grain boundaries as a result of the environmental effects [22]. Since, the grain boundaries are the preferential sites for the oxidation, the crack nucleation appears as the rupturing of the brittle GB-oxide under tensile load. Therefore, preferentially GBs oriented approximately perpendicular to the loading axis have been cracked (see Figs. 11.1.5 and 11.2.2). Moreover, the resistance

of the GB-oxides to the rupturing is decreased by the presence of the cavities acting as the stress concentrators under the repeated external loading in the high temperature low cycle fatigue. After the rupture of the GB-oxide the freshly exposed metal is subjected to further oxidation. In addition to the diffusion of the oxygen and solute atoms by means of vacancy mechanisms the absence of protective Cr-rich oxide layer at the crack tip evokes increased internal oxidation of the material along the grain boundaries (see Figs. 11.1.6, 11.1.5 and 11.2.3). These findings specify the general model based on the repeated rupture of oxidized film proposed for Ni-based superalloys [9; 10] for austenitic stainless steel. Since the intergranular cracks predominate close to the surface (see Fig. 11.2.5), the grain boundary cracking due to the oxidation may be considered as the Stage I fatigue crack growth where the crack growth rate is sufficiently low under these loading conditions.

Moreover, it is worthy to note that despite the loading rate at high temperatures in LCF conditions can be considered as relatively low, no damage mechanisms as diffusion induced creep damage was observed. It is known that the creep damage in the form of cavitation at the interfaces accelerates the crack growth rate leading to short fatigue life. In the case of Sanicro 25 steel, the damage of the material in the form of cavitation was reported only in the presence of dwell period in a cycle [22].

#### **14.2. Crack growth under the environmental conditions**

The growth of the cracks under isothermal LCF conditions has been followed both on the surface and in the bulk of the specimen. As shown in the Chapter 11.2 the growth paths of the cracks are highly affected by the multiple grain boundary oxidation and cracking at the surface. Preferentially the grain boundaries oriented approximately perpendicular to the loading direction on the surface as well as in the bulk cracked as shown in Figs. 11.2.2, 11.2.3 and 11.2.4. It means that the oxidized GBs loaded by the highest tensile stress component rupture under the tensile part of the loading cycle and a new metal surface arises. Later during the cycling, the fresh metal surface is exposed to further heavy oxidation of the GB (see Fig. 11.1.4) resulting in the easier oxidation due to the high energy of the GB compared to the matrix. This mechanism of the GB-oxide cracking and oxidizing of the new metal surface at the crack tip periodically repeats during the cycling [10]. The lengths of these initiated cracks are mostly shorter than the size of the surface GB. Analogously to the crack growth at room temperature, this period of the crack growth can be referred to the Stage I crack growth under these loading conditions. Nevertheless, contrary to the room temperature loading (see Chapters 9.1.1 and 9.2) this Stage I crack grows under the opening Mode I. The crack initiation appears early during the cycling in less than 10% of the fatigue life ( $N_f = 688$  cycles) which is still lower number of cycles compared to the crack initiation at room temperature. The period of the crack initiation can be slightly enhanced due to the sufficient oxidation of the GB compared to the loading at a room temperature where the crack initiation was found to appear in less than 5% of  $N_f$  ( $N_f = 18394$  cycles) shown in Figure 9.1.3.

It is apparent that the multiple crack initiation along the oxidized GBs significantly affects the growth behavior of the cracks close to the surface. Cracks grow preferentially in the intergranular manner as shown in the statistical analysis in Fig. 11.2.5. Later, with further cycling, initiated cracks link together (see Fig. 11.2.2). As a result, the crack growth rates of the surface cracks rapidly increase.

The growth paths of the surface cracks are in contrast with the crack paths in the bulk of the material, where the transgranular character of the crack growth prevails (see Fig.

11.2.5). This crack growth stage can be referred to as the Stage II crack growth. The crack grows under the action of the cyclic plastic deformation ahead of the crack tip similarly as in the case of the crack growth at room temperature. This is in accordance with the appearance of the plastic zone localized along the crack path and in front of the crack tip as revealed by the EBSD (see Fig. 11.2.3). The observations of the transgranular crack growth are in a good agreement with the works of Pavinich et al. [7] and Yamaguchi et al. [8]. Pavinich et al. [7] studied the effect of the grain size, temperature, and the strain rate on the character of the crack path in polycrystalline copper containing a silica particles. They found that the transgranular crack path notably predominates over the intergranular path even at high temperatures. This tendency is stronger at higher strain rates. Similar observations were presented by Yamaguchi et al. [8], who studied the effect of the strain wave shape on the high temperature fatigue behavior of a 316 type steel at 600 °C and 700 °C. Fractographic observations revealed that in the testing with the slow triangular wave shape the fracture surface was of the intergranular character, while in the fast triangular wave shape tests fracture surface was of the transgranular character and the fatigue life was longer.

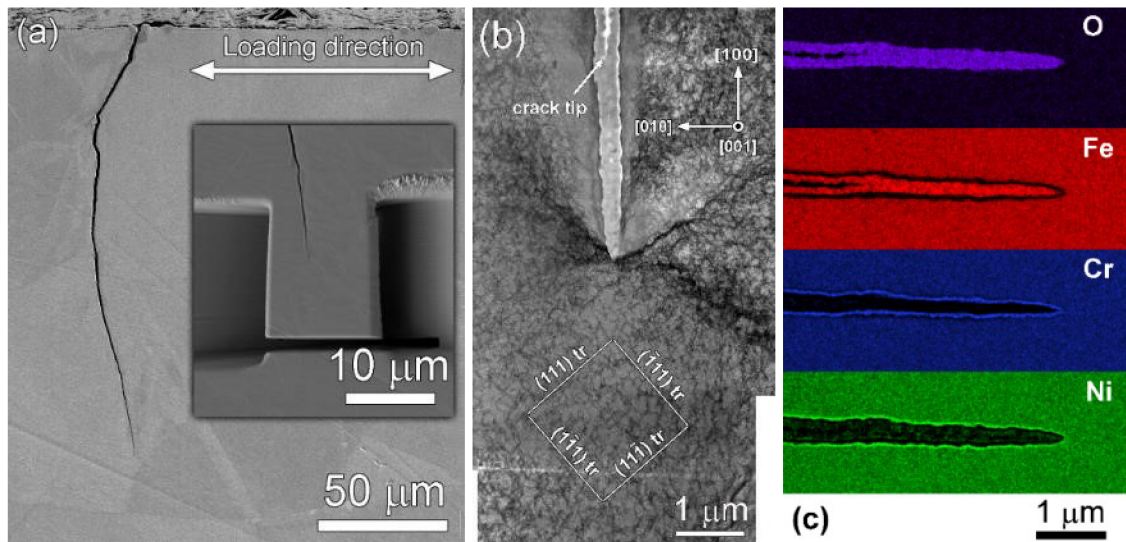


Figure 14.2.1: a) SE micrograph of the crack. Inset shows the position of the lamella. b) BF-STEM of the oxidized crack tip with the surrounding dislocation microstructure. c) EDS maps showing the chemical composition of the oxide at the crack tip and surrounding matrix.

The role of the plastic deformation in the crack growth is notable also from the Figs. 11.2.3 and 11.2.4. The cracks propagate approximately perpendicular to the loading axis preferentially following the low indexed crystallographic planes of type  $\{011\}$  and  $\{001\}$ . As shown in Fig. 14.2.1 the crack propagates under the coactive action of several slip systems of type  $\{111\}\langle 011\rangle$  as was earlier proposed by Neumann [122; 123] for the crack propagation at room temperature. The plastic zone ahead of the crack tip can be recognized due to the high lattice distortion and subsequently the loss of the diffraction contrast. Compared to the crack growth at a room temperature, here the crack growth is accompanied by the crack tip oxidation (see Figs. 11.2.5, 11.2.6 and 14.2.1). The oxidation in the matrix is not extensive and is localized only to a sheet of micron thickness along the crack sides. The similar mechanism as discussed earlier in the rupturing and further oxidation of the

freshly exposed metal surface takes place also during the crack propagation. In Fig. 11.2.6 two crack tips indicating the oxidation in the direction of the crack propagation and multiple rupturing of the brittle oxide at the crack tip are shown. Only occasionally the crack path follows the GB. It indicates that the loading rate and the crack growth rate are sufficient high to suppress the embrittlement of the grain boundaries [146; 147]. The growth of the crack under the cyclic plastic deformation along with the oxidation and rupturing of the brittle oxides can increase the crack growth rate and decrease the fatigue life compared to the cycling at a room temperature.

The crack growth rate of the principal crack leading to the fracture is determined by the range of the stress intensity factor  $\Delta K$  or by the range of  $J$ -integral  $\Delta J$ . In the early stages of the fatigue life the Stage I crack has approximately the semi-circular shape (see Fig. 11.1.5) leading to the use of the  $\Delta K$  for the description of the crack growth. By the coalescence of the initiated surface cracks a shallow semi-elliptical surface crack of depth  $a$  arise. Wormsen et al. [196] have shown that the stress intensity factor of the approximately half-elliptical surface crack at the deepest point of the crack is proportional to  $\sqrt{c}$ , where  $c$  is the half of the surface crack. The stress intensity factor at the surface is proportional to the square root of the crack depth  $\sqrt{a}$ . Therefore, the crack growth rates of the shallow cracks will be highest in the depth of the material and fatigue crack will have a tendency to reach rapidly the semi-circular shape. The period of slow crack growth can be thus overcome due to the initiation of cracks with the long surface length. This leads to the substantially shorter fatigue life compared to the specimens tested at room temperature (see Fig. 1.1.2) [12]. Multiple cracks are initiated at GBs during high temperature cyclic loading and generally the longest initiated surface crack (after linkage) becomes the principal crack and leads to the final fatigue fracture.

## VII. CONCLUSIONS

The experimental study of low cycle fatigue damage of advanced alloy based on Fe-Ni-Cr matrix tested both at room temperature and at a temperature of 700°C led to the following conclusions:

- The high planar character of the dislocation slip in the material leads to the cyclic plastic strain localization into the narrow persistent slip bands of about 200 nm in thickness during the cyclic loading at room temperature. Owing to the absence of the dislocations from secondary slip systems within the PSBs, the PSBs can be clearly distinguished in the matrix.
- Dislocation structure of well-developed persistent slip bands producing persistent slip markings does not need to be ladder-like. Nevertheless, it must accommodate the local intensive cyclic slip. Dislocation-rich and dislocation-poor regions are present in the persistent slip bands. The complicated shape of the persistent slip markings consisting of extrusions and intrusions is compatible with the internal dislocation structure of PSBs.
- Three specific types of crack initiation leading to the growth of the major cracks were found on the samples cyclically strained at room temperature: (i) along the fatigue induced surface relief in the form of persistent slip markings, (ii) twin boundaries and (iii) grain boundaries. Although the role of TBs and GBs was observed to increase with the increase of the applied total strain amplitude the role of PSMs prevails in cycling with all strain amplitudes.
- The cracks were observed to start along the PSMs from the tip of the intrusions or intrusion-like defects. The intrusion can be easily distinguished from the Stage I crack since its vortex angle is of about 10 degrees. The vortex angle of the crack is equal to zero degree.
- In the case of high angle GBs cracking the role of primary slip systems of the neighbor grains was found. The PSBs developed along the primary slip system emerge in the GB and produce PSMs. The PSMs arising in the GB are oriented almost parallel to the surface. The profile of the PSM causes local incompatibilities in the GB. The orientation of the GB approximately perpendicular to the loading direction and to the surface leads to the final decohesion of GB under the tensile loading.
- Cracks initiated in PSMs grow predominantly along the {111} slip planes due to high plastic strain localization in PSBs. Grain boundaries, secondary phases etc. locally slow down the crack growth rate of microstructurally short cracks. The mutual coalescence of the cracks increases the surface crack length and thus contributes to crack growth acceleration of natural short cracks. The equivalent crack length can reasonably well describe the damage evolution in cyclic straining with constant strain amplitudes.



- The crack growth rate was found to be proportional to the crack length. It corresponds to the exponential increase of the crack length. The crack growth coefficient characterizes the dependence of the growth rate on the applied plastic strain amplitude. The power law dependence of the crack growth coefficient corresponds to the Manson-Coffin law. The parameters of the crack growth law can be thus derived from the parameters of the Manson-Coffin law. The correlation of the crack growth rate with the plastic component to the  $J$ -integral gives a high scatter.
- The crack initiation during the cyclic loading at elevated temperature was found to be along the oxidized GBs. High interfacial energy and the presence of numerous lattice defects such as vacancy-type defects at the grain boundaries significantly facilitate oxygen diffusion and lead to notably enhanced oxidation. Cavities are formed at the tip of the oxide intrusions presumably as a result of different diffusion rates of elements.
- The cracking of the oxides at the grain boundaries is the main cause of very early fatigue crack initiation in these sites. Highly porous brittle oxides located at the grain boundaries perpendicular to the loading axis fracture as a result of external tensile stress. Fracture of oxides facilitates further diffusion of oxygen from the air to the crack tip. The growth of the oxide intrusion and its rupture contribute to the rapid crack growth.
- There is a difference between the mechanisms of fatigue crack propagation on the surface and in the bulk of the material. Rapid increase of crack density on the surface as a result of the fracture of oxidized grain boundaries leads to their linkage. Long surface cracks have high driving force for the growth in the bulk and both intergranular as well as transgranular crack paths are observed. Transgranular path is due to the localization of plastic deformation and formation of the cyclic plastic zone ahead of the crack tip. Rapid crack initiation due to the oxide cracking and rapid growth of the long surface cracks leads to substantial decrease of the fatigue life in comparison with the room temperature cyclic loading.

## VIII. REFERENCES

- [1] CHAI, G. C., T. SAND, J. HERNBLOM, U. FORSBERG AND T. PELTOLA. Development of Advanced Heat Resistant Materials for IGCC and AUSC Power Plants. In *Energy Materials 2014*, Springer, Cham, 2014, 227-234. DOI: 10.1007/978-3-319-48765-6\_25
- [2] POLÁK, J. *Cyclic plasticity and low cycle fatigue life of metals*. Edition ed. Amsterdam: Elsevier, 1991. ISBN 978-80-200-0008-8.
- [3] EWING, J. A. AND J. C. W. HUMFREY. The fracture of metals under repeated alternations of stress. *Philosophical Transactions of the Royal Society A*, 1903, **200**, 241-250. DOI: 10.1098/rsta.1903.0006
- [4] MAN, J., P. Klapetek, O. MAN, A. WEIDNER, K. OBRTLÍK AND J. POLÁK. Extrusions and intrusions in fatigued metals. Part 2. AFM and EBSD study of the early growth of extrusions and intrusions in 316L steel fatigued at room temperature. *Philosophical Magazine*, 2009, **89**(16), 1337-1372. DOI: 10.1080/14786430902917624
- [5] MAN, J., K. OBRTLÍK AND J. POLÁK. Extrusions and intrusions in fatigued metals. Part 1. State of the art and history. *Philosophical Magazine*, 2009, **89**(16), 1295-1336. DOI: 10.1080/14786430902917616
- [6] PINEAU, A. AND S. D. ANTOLOVICH. High temperature fatigue: behaviour of three typical classes of structural materials. *Materials at High Temperatures*, 2015, **32**(3), 298-317. DOI: 10.1179/0960340914Z.00000000072
- [7] PAVINICH, W. AND R. RAJ. Fracture at elevated temperature. *Metallurgical Transactions A*, 1977, **8**(12), 1917-1933. DOI: 10.1007/BF02646566
- [8] YAMAGUCHI, K. AND K. KANAZAWA. Effect of Strain Wave Shape on High-Temperature Fatigue Life of a Type-316 Steel and Application of the Strain Range Partitioning Method. *Metallurgical Transactions A*, 1980, **11**(12), 2019-2027. DOI: 10.1007/BF02655121
- [9] COFFIN, L. F. The effect of frequency on the cyclic strain and fatigue behavior of cast René at 1600° F. *Metallurgical Transactions A*, 1974, **5**(5), 1053-1060. DOI: 10.1007/BF02644317
- [10] MCMAHON, C. J. AND L. F. COFFIN. Mechanisms of damage and fracture in high-temperature, low-cycle fatigue of a cast nickel-based superalloy. *Metallurgical Transactions*, 1970, **1**(12), 3443-3450. DOI: 10.1007/BF03037877
- [11] CHAI, G. AND U. FORSBERG. Sanicro 25: an advanced high-strength, heat resistant austenitic stainless steel. In A. DIGIANFRANCESCO ed. *Materials for Ultra-Supercritical and Advanced Ultra-Supercritical Power Plants*. Amsterdam: Elsevier, 2017, p. 391-421. DOI: 10.1016/B978-0-08-100552-1.00012-9
- [12] SOURMAIL, T. Precipitation in creep resistant austenitic stainless steels. *Materials Science and Technology*, 2001, **17**(1), 1-14. DOI: 10.1179/026708301101508972
- [13] BARNARD, P. Austenitic steel grades for boilers in ultra-supercritical power plants. In A. DIGIANFRANCESCO ed. *Materials for Ultra-Supercritical and Advanced Ultra-Supercritical Power Plants*. Amsterdam: Elsevier, 2017, p. 99-119. DOI: 10.1016/B978-0-08-100552-1.00004-X
- [14] KORZHAVYI, P. A. AND R. SANDSTROM. First-principles evaluation of the effect of alloying elements on the lattice parameter of a 23Cr25NiWCuCo austenitic stainless steel to model solid solution hardening contribution to the creep strength. *Materials Science and Engineering A*, 2015, **626**, 213-219. DOI: 10.1016/j.msea.2014.12.057
- [15] POLÁK, J., R. PETRÁŠ, M. HECZKO, I. KUBĚNA, T. KRUML AND G. CHAI. Low cycle fatigue behavior of Sanicro25 steel at room and at elevated temperature. *Materials Science and Engineering A*, 2014, **615**, 175-182. DOI: 10.1016/j.msea.2014.07.075
- [16] HECZKO, M., B. D. ESSER, T. M. SMITH, P. BERAN, V. MAZANOVA, T. KRUML, J. POLAK AND M. J. MILLS. On the origin of extraordinary cyclic strengthening of the austenitic stainless

- steel Sanicro 25 during fatigue at 700 °C. *Journal of Materials Research*, 2017, **32**(23), 4342-4353. DOI: 10.1557/jmr.2017.311
- [17] HECZKO, M., B. D. ESSER, T. M. SMITH, P. BERAN, V. MAZÁNOVÁ, D. W. MCCOMB, T. KRUML, J. POLÁK AND M. J. MILLS. Atomic resolution characterization of strengthening nanoparticles in a new high-temperature-capable 43Fe-25Ni-22.5Cr austenitic stainless steel. *Materials Science and Engineering A*, 2018, **719**, 49-60. DOI: 10.1016/j.msea.2018.02.004
- [18] INTISO, L., L. G. JOHANSSON, S. CANOVIC, S. BELLINI, J. E. SVENSSON AND M. HALVARSSON. Oxidation Behaviour of Sanicro 25 (42Fe22Cr25NiWCuNbN) in O-2/H<sub>2</sub>O Mixture at 600 degrees C. *Oxidation of Metals*, 2012, **77**(5-6), 209-235. DOI :10.1007/s11085-011-9281-3
- [19] ZUREK, J., S. M. YANG, D. Y. LIN, T. HUTTEL, L. SINGHEISER AND W. J. QUADAKKERS. Microstructural stability and oxidation behavior of Sanicro 25 during long-term steam exposure in the temperature range 600-750 degrees C. *Materials and Corrosion*, 2015, **66**(4), 315-327. DOI: 10.1002/maco.201407901
- [20] PETRÁŠ, R., V. ŠKORÍK AND J. POLÁK. Thermomechanical fatigue and damage mechanisms in Sanicro 25 steel. *Materials Science and Engineering A*, 2016, **650**, 52-62. DOI: 10.1016/j.msea.2015.10.030
- [21] HECZKO, M., J. POLAK AND T. KRUML. Microstructure and dislocation arrangements in Sanicro 25 steel fatigued at ambient and elevated temperatures. *Materials Science and Engineering A*, 2017, **680**, 168-181. DOI: 10.1016/j.msea.2016.10.076
- [22] PETRÁŠ, R. AND J. POLÁK. Damage mechanism in austenitic steel during high temperature cyclic loading with dwells. *International Journal of Fatigue*, 2018, **113**, 335-344. DOI: 10.1016/j.ijfatigue.2018.02.017
- [23] CHAI, G. Damage mechanism of low cycle fatigue in an advanced heat resistant austenitic stainless steel at high temperature. *Procedia Materials Science*, 2014, **3**, 1754-1759. DOI: 10.1016/j.mspro.2014.06.283
- [24] POLÁK, J. AND M. KLESNIL. Cyclic Plasticity and Low Cycle Fatigue Life in Variable Amplitude Loading. *Fatigue Fracture and Engineering Materials and Structures*, 1979 1979, **1**(1), 123-133. DOI: 10.1111/j.1460-2695.1979.tb00371.x
- [25] SURESH, S. *Fatigue of Materials*. 2nd rev. ed., Cambridge: University Press, 1998, ISBN 9780511806575, DOI: 10.1017/CBO9780511806575
- [26] WÖHLER, A. Versuche über die Festigkeit der Eisenbahnachsen. *Zeitschrift Bauwesen*, 1860, **10**, 583-591.
- [27] BAUSCHINGER, J. Über die Veränderung der Elasticitätsgrenze und der Festigkeit des Eisens und Stahls durch Strecken und Quetschen, durch Erwärmen und Abkühlen, und durch oftmal wiederholte Beanspruchung. *Mitteilungen aus dem Mechanisch-technischen Laboratorium der königlichen Technischen Hochschule in Munchen*, 1886, **13**, 1-116.
- [28] COFFIN, L. F. A study of the effects of cyclic thermal stresses on a ductile metal. *Transactions of the ASME*, 1954, **76**, 931-950.
- [29] MANSON, S. S. Behavior of Materials Under Conditions of Thermal Stress. *National Advisory Committee for Aeronautics: Report no. 1170*, Cleveland, 1954.
- [30] KLESNIL, M. *Fatigue of Metallic Materials*. 2nd rev. ed. Amsterdam ; New York: Elsevier, 1992. Materials science monographs, 71. ISBN 978-0-444-98723-5.
- [31] POLÁK, J. Cyclic deformation, crack initiation, and low-cycle fatigue. In I.R. MILNE, R.O.; KARIHALOO, B. ed. *Comprehensive Structural Integrity*. Amsterdam: Elsevier, 2003, vol. **4**, p. 1-39. DOI: 10.1016/B978-0-12-803581-8.00890-0
- [32] POLÁK, J. AND M. KLESNIL. Cyclic stress-strain response and dislocation structures in polycrystalline copper. *Materials Science and Engineering*, 1984, **63**(2), 189-196. DOI: 10.1016/0025-5416(84)90120-4
- [33] CHARLESLEY, P. AND L. J. HARRIS. Condensed dislocation structures in polycrystalline aluminium fatigued at 77K. *Scripta Metallurgica*, 1987, **21**(3), 341-344. DOI: 10.1016/0036-9748(87)90225-0

- [34] BLOCHWITZ, C., K. MECKE AND R. STEPHAN. Der Einfluß der Stapelfehlerenergie und der Atomgröße-Schubmodul-Differenzen auf Versetzungsstruktur und ZSD ermüdeter kfz-Metallegierungen. *Kristall und Technik*, 1978, **13**(7), 851-861. DOI: 10.1002/crat.19780130720
- [35] LAIRD, C., P. CHARLESLEY AND H. MUGHRABI. Low-Energy Dislocation-Structures Produced by Cyclic Deformation. *Materials Science and Engineering*, 1986, **81**, 433-450. DOI: 10.1016/0025-5416(86)90281-8
- [36] VOGT, J. B., S. DEGALLAIX AND J. FOCT. Low-Cycle Fatigue Life Enhancement of 316-L Stainless-Steel by Nitrogen Alloying. *International Journal of Fatigue*, 1984, **6**(4), 211-215. DOI: 10.1016/0142-1123(84)90051-3
- [37] PHAM, M. S., C. SOLENTHALER, K. G. F. JANSSENS AND S. R. HOLDSWORTH. Dislocation structure evolution and its effects on cyclic deformation response of AISI 316L stainless steel. *Materials Science and Engineering A*, 2011, **528**(7-8), 3261-3269 .DOI: 10.1016/j.msea.2011.01.015
- [38] OBRTLÍK, K., T. KRUML AND J. POLÁK. Dislocation structures in 316L stainless steel cycled with plastic strain amplitudes over a wide interval. *Materials Science and Engineering A*, 1994, **187**(1), 1-9. DOI: 10.1016/0921-5093(94)90325-5
- [39] MUGHRABI, H., F. ACKERMANN AND K. HERZ. Persistent Slipbands in Fatigued Face-Centered and Body-Centered Cubic Metals. In J. FONG. *Fatigue Mechanisms*. West Conshohocken: ASTM International, 1979, p. 69-105. DOI: 10.1520/STP35885S
- [40] COTTRELL, A. H. AND D. HULL. Extrusion and intrusion by cyclic slip in copper. *Proceedings of the Royal Society A*, 1957, **242** (1229), 211-213. DOI: 10.1098/rspa.1957.0170
- [41] LAUFER, E. E. AND W. N. ROBERTS. Dislocations and Persistent Slip Bands in Fatigued Copper. *Philosophical Magazine A*, 1966, **14**(127), 65-78. DOI: 10.1080/14786436608218989
- [42] WINTER, A. T. Etching Studies of Dislocation Microstructures in Crystals of Copper Fatigued at Low Constant Plastic Strain Amplitude. *Philosophical Magazine*, 1973, **28**(1), 57-64. DOI: 10.1080/14786437308217433
- [43] LI, P., S. X. LI, Z. G. WANG AND Z. F. ZHANG. Fundamental factors on formation mechanism of dislocation arrangements in cyclically deformed fcc single crystals. *Progress in Materials Science*, 2011, **56**(3), 328-377. DOI: 10.1016/j.pmatsci.2010.12.001
- [44] POLÁK, J. Fatigue of steels. In S. HASHMI ed. *Reference Module in Materials Science and Materials Engineering*. Oxford: Elsevier, 2016, p. 1-46.
- [45] LI, Y. F. AND C. LAIRD. Cyclic Response and Dislocation-Structures of AISI 316L Stainless-Steel .2. Polycrystals Fatigued at Intermediate Strain Amplitude. *Materials Science and Engineering A*, 1994, **186**(1-2), 87-103. DOI: 10.1016/0921-5093(94)90307-7
- [46] POLÁK, J., K. OBRTLÍK AND M. HÁJEK. Cyclic plasticity in type 316L austenitic stainless steel. *Fatigue and Fracture of Engineering Materials and Structures*, 1994, **17**(7), 773-782. DOI: 10.1111/j.1460-2695.1994.tb00808.x
- [47] GERLAND, M., J. MENDEZ, P. VIOLAN AND B. A. SAADI. Evolution of Dislocation-Structures and Cyclic Behavior of a 316L-type Austenitic Stainless-Steel Cycled in Vacuo at Room-Temperature. *Materials Science and Engineering A*, 1989, **118**, 83-95. DOI: 10.1016/0921-5093(89)90060-9
- [48] POLÁK, J. Cyclic plastic response and fatigue life of duplex and superduplex stainless steels. *Kovove Materialy*, 2005, **43**(4), 280-289.
- [49] KRUML, T., J. POLÁK, K. OBRTLÍK AND S. DEGALLAIX. Dislocation structures in the bands of localised cyclic plastic strain in austenitic 316L and austenitic-ferritic duplex stainless steels. *Acta Materialia*, 1997, **45**(12), 5145-5151. DOI: 10.1016/S1359-6454(97)00178-X
- [50] PHAM, M. S., S. R. HOLDSWORTH, K. G. F. JANSSENS AND E. MAZZA. Cyclic deformation response of AISI 316L at room temperature: Mechanical behaviour, microstructural

- evolution, physically-based evolutionary constitutive modelling. *International Journal of Plasticity*, 2013, **47**, 143-164. DOI: 10.1016/j.ijplas.2013.01.017
- [51] VOGT, J. B., J. FOCT AND J. O. NILSSON. Low-Temperature Fatigue of a High Nitrogen Austenitic Steel. *Scandinavian Journal of Metallurgy*, 1990, **19**, 273-277.
- [52] VOGT, J. B., T. MAGNIN AND J. FOCT. Effective Stresses and Microstructure in Cyclically Deformed 316L Austenitic Stainless-Steel - Effect of Temperature and Nitrogen-Content. *Fatigue & Fracture of Engineering Materials & Structures*, 1993, **16**(5), 555-564. DOI: 10.1111/j.1460-2695.1993.tb00766.x
- [53] HONG, S. I. AND C. LAIRD. Mechanisms of slip mode modification in F.C.C. solid solutions. *Acta Metallurgica et Materialia*, 1990, **38**, 1581-1594. DOI: 10.1016/0956-7151(90)90126-2
- [54] LU, J., L. HULTMAN, E. HOLMSTROM, K. H. ANTONSSON, M. GREHK, W. LI, L. VITOS AND A. GOLPAYEGANI. Stacking fault energies in austenitic stainless steels. *Acta Materialia*, 2016, **111**, 39-46. DOI: 10.1016/j.actamat.2016.03.042
- [55] GERLAND, M., R. ALAIN, B. A. SAADI AND J. MENDEZ. Low cycle fatigue behaviour in vacuum of a 316L-type austenitic stainless steel between 20 and 600 degrees C. Part II: Dislocation structure evolution and correlation with cyclic behaviour. *Materials Science and Engineering A*, 1997, **229**(1-2), 68-86. DOI: 10.1016/S0921-5093(96)10560-8
- [56] KLESNIL, M. AND P. LUKÁŠ. *Fatigue of Metallic Materials*. Edition ed. Amsterdam: Elsevier Science Publishing Company, Inc., 1992, 270 p, ISBN 0-444-98723-1.
- [57] THOMPSON, N., N. WADSWORTH AND N. LOUAT. The Origin of Fatigue Fracture in Copper. *Philosophical Magazine*, 1956, **1**(2), 113-126. DOI: 10.1080/14786435608238086
- [58] BASINSKI, Z. S., R. PASCUAL AND S. J. BASINSKI. Low Amplitude Fatigue of Copper Single Crystals - 1. The Role of the Surface in Fatigue Failure. *Acta Metallurgica*, 1983, **31**(4), 591-602. DOI: 10.1016/0001-6160(83)90049-4
- [59] LAIRD, C., DUQUETTE, D. J. Mechanisms of fatigue crack nucleation. In A.J. MCEVILY, O. DEVEREUX AND R.J. STAEHLE eds. *Corrosion Fatigue: chemistry, mechanics and microstructure*, Houston: National Association of Corrosion Engineers, 1972, vol. **2**, p. 88-117
- [60] KIM, W. H. AND C. LAIRD. Crack Nucleation and Stage-I Propagation in High Strain Fatigue - I. Microscopic and Interferometric Observations. *Acta Metallurgica*, 1978, **26**(5), 777-787. DOI: 10.1016/0001-6160(78)90028-7
- [61] KIM, W. H. AND C. LAIRD. Crack Nucleation and Stage-I Propagation in High Strain Fatigue - II. Mechanism. *Acta Metallurgica*, 1978, **26**(5), 789-799. DOI: 10.1016/0001-6160(78)90029-9
- [62] MUGHRABI, H., R. WANG, K. DIFFERT AND U. ESSMANN. Fatigue crack initiation by cyclic slip irreversibilities in high-cycle fatigue. In J. LANKFORD, D.L. DAVIDSON, W.L. MORRIS AND R.P. WEI eds. *Advances in Quantitative Measurement of Physical Damage*. Philadelphia: American Society for Testing and Materials, 1983, p. 5-45. DOI: 10.1520/STP30551S
- [63] CHRIST, H. J. On the orientation of cyclic-slip-induced intergranular fatigue cracks in face-centred cubic metals. *Materials Science and Engineering A*, 1989, **117**, L25-L29. DOI: 10.1016/0921-5093(89)90115-9
- [64] MUGHRABI, H. Microstructural mechanisms of cyclic deformation, fatigue crack initiation and early crack growth. *Philosophical Transactions of the Royal Society A*, 2015, **373**(2038), 20140332. DOI: 10.1098/rsta.2014.0132
- [65] BOETTNER, R. C., A. J. MCEVILY AND Y. C. LIU. On the formation of fatigue cracks at twin boundaries. *Philosophical Magazine A*, 1964, **10**(103), 95-106. DOI: 10.1080/14786436408224210
- [66] NEUMANN, P. Analytical solution for the incompatibility stresses at twin boundaries in cubic crystals. *Fatigue '99: Proceedings of the Seventh International Fatigue Congress*, **1/4**, 1999, 107-114.

- [67] NEUMANN P. AND A. TÖNNESSEN. Crack initiation at grain boundaries in FCC materials. In L.T.K. KETTUNEN P.O., LEHTONEN M. E. ed. *Strength of Metals and Alloys (ICSMA 8)*. Oxford: Pergamon Press, 1989, vol. **2**, p. 743-748. DOI: 10.1016/B978-0-08-034804-9.50116-9
- [68] LANKFORD, J. AND F. N. KUSENBERGER. Initiation of fatigue cracks in 4340 steel. *Metallurgical Transactions A*, 1973, **4**(2), 553-559. DOI: 10.1007/BF02648709
- [69] MORRIS, W. L., O. BUCK AND H. L. MARCUS. Fatigue crack initiation and early propagation in Al 2219-T851. *Metallurgical Transactions A*, 1976, **7**(8), 1161-1165. DOI: 10.1007/BF02656599
- [70] ATRENS, A., W. HOFFELNER, T. W. DUERIG AND J. E. ALLISON. Subsurface crack initiation in high cycle fatigue in Ti6Al4V and in a typical martensitic stainless steel. *Scripta Metallurgica*, 1983, **17**(5), 601-606. DOI: 10.1016/0036-9748(83)90385-X
- [71] FORSYTH, P. J. E. Exudation of Material from Slip Bands at the Surface of Fatigued Crystals of an Aluminium Copper Alloy. *Nature*, 1953, **171**, 172-173. DOI: 10.1038/171172a0
- [72] FORSYTH, P. J. E. Slip-Band Damage and Extrusion. *Proceedings of the Royal Society of London Series A*, 1957, **242**(1229). DOI: 10.1098/rspa.1957.0168
- [73] LAUFER, E. E. AND W. N. ROBERTS. Dislocation Structures in Fatigued Copper Single Crystals. *Philosophical Magazine A*, 1964, **10**(107), 883-885. DOI: 10.1080/14786436408225391
- [74] LUKÁŠ, P., M. KLESNIL AND J. KREJČI. Dislocations and Persistent Slip Bands in Copper Single Crystals Fatigued at Low Stress Amplitude. *Physica Status Solidi B*, 1968, **27**(2), 545-558. DOI: 10.1002/pssb.19680270212
- [75] ATKINSON, J. D., L. M. BROWN, R. KWADJO, W. M. STOBBS, A. T. WINTER AND W. A. WOOD. The structure of persistent slip bands and the fatigue strength of metals. In *Proceedings The microstructure and Desing of Alloys (ICSMA 3)*. Cambridge, UK, 1973, vol. **1**, p. 402.
- [76] ANTONOPOULOS, J. G., L. M. BROWN AND A. T. WINTER. Vacancy Dipoles in Fatigued Copper. *Philosophical Magazine A*, 1976, **34**(4), 549-563. DOI : 10.1080/14786437608223793
- [77] BROWN L.M. AND S. L. OGIN. Role of internal stresses in the nucleation of fatigue cracks. In M.K.J. BILBY B.A., WILLIS J.R. ed. *Fundamentals of Deformation and Fracture*. Cambridge University Press, 1985, p. 501-528.
- [78] ESSMANN, U., U. GOSELE AND H. MUGHRABI. A Model of Extrusions and Intrusions in Fatigued Metals I. Point-Defect Production and the Growth of Extrusions. *Philosophical Magazine A*, 1981, **44**(2), 405-426. DOI: 10.1080/01418618108239541
- [79] MUGHRABI, H. Cyclic Hardening and Saturation Behavior of Copper Single-Crystals. *Materials Science and Engineering*, 1978, **33**(2), 207-223. DOI: 10.1016/0025-5416(78)90174-X
- [80] ESSMANN, U. AND H. MUGHRABI. Annihilation of Dislocations during Tensile and Cyclic Deformation and Limits of Dislocation Densities. *Philosophical Magazine A*, 1979, **40**(6), 731-756. DOI: 10.1080/01418617908234871
- [81] JOHNSON, E. W. AND H. H. JOHNSON. Imperfection Density of Fatigued and Annealed Copper Via Electrical-Resistivity Measurements. *Transactions of the Metallurgical Society A.I.M.E.*, 1965, **233**, 1333-1338.
- [82] POLÁK, J. Electrical resistivity of cyclically deformed copper. *Czechoslovak Journal of Physics B*, 1969, **19**(3), 315-322. DOI: 10.1007/BF01712868
- [83] POLÁK, J. The effect of intermediate annealing on the electrical resistivity and shear stress of fatigued copper. *Scripta Metallurgica*, 1970, **4**(10), 761-764. DOI: 10.1016/0036-9748(70)90056-6
- [84] POLÁK, J. On the role of point defects in fatigue crack initiation. *Materials Science and Engineering*, 1987, **92**, 71-80. DOI: 10.1016/0025-5416(87)90157-1
- [85] POLÁK, J. AND J. MAN. Fatigue crack initiation - The role of point defects. *International Journal of Fatigue*, 2014, **65**, 18-27. DOI: 10.1016/j.ijfatigue.2013.10.016

- [86] POLÁK, J. AND J. MAN. Mechanisms of extrusion and intrusion formation in fatigued crystalline materials. *Materials Science and Engineering A*, 2014, **596**, 15-24. DOI: 10.1016/j.msea.2013.12.005
- [87] POLÁK, J. Calculation of the electrical resistivity and the thermoelectric power of vacancies in copper and gold. *Czechoslovak Journal of Physics B*, 1967, **17**(2), 171-177. DOI: 10.1007/BF01696124
- [88] POLÁK, J. AND M. SAUZAY. Growth of extrusions in localized cyclic plastic straining. *Materials Science and Engineering A*, 2009, **500**(1-2), 122-129. DOI: 10.1016/j.msea.2008.09.022
- [89] TANAKA, K. AND T. MURA. A Dislocation Model for Fatigue Crack Initiation. *Journal of Applied Mechanics*, 1981, **48**(1), 97-103. DOI: 10.1115/1.3157599
- [90] KATAGIRI, K., A. OMURA, K. KOYANAGI, J. AWATANI, T. SHIRAISHI AND H. KANESHIRO. Early stage crack tip morphology in fatigued copper. *Metallurgical Transactions A*, 1977, **8**(11), 1769-1773. DOI: 10.1007/BF02646881
- [91] ROACH, M. D. AND S. I. WRIGHT. Investigations of twin boundary fatigue cracking in nickel and nitrogen-stabilized cold-worked austenitic stainless steels. *Materials Science and Engineering A*, 2014, **607**, 611-620. DOI: 10.1016/j.msea.2014.04.059
- [92] POLÁK, J. AND P. LIŠKUTÍN. Nucleation and short crack growth in fatigued polycrystalline copper. *Fatigue and Fracture of Engineering Materials and Structures*, 1990, **13**(2), 119-133. DOI: 10.1111/j.1460-2695.1990.tb00584.x
- [93] MAN, J., M. VALTR, M. PETRENEC, J. DLUHOS, I. KUBENA, K. OBRTLÍK AND J. POLÁK. AFM and SEM-FEG study on fundamental mechanisms leading to fatigue crack initiation. *International Journal of Fatigue*, 2015, **76**, 11-18. DOI: 10.1016/j.ijfatigue.2014.09.019
- [94] MAN, J., T. VYSTAVĚL, A. WEIDNER, I. KUBĚNA, M. PETRENEC, T. KRUML AND J. POLÁK. Study of cyclic strain localization and fatigue crack initiation using FIB technique. *International Journal of Fatigue*, 2012, **39**, 44-53. DOI: 10.1016/j.ijfatigue.2011.05.002
- [95] SEIDAMETOVA, G., J.-B. VOGT AND I. PRORIOL SERRE. The early stage of fatigue crack initiation in a 12%Cr martensitic steel. *International Journal of Fatigue*, 2018, **106**, 38-48. DOI: 10.1016/j.ijfatigue.2017.09.006
- [96] MU, P., V. AUBIN, I. ALVAREZ-ARMAS AND A. ARMAS. Influence of the crystalline orientations on microcrack initiation in low-cycle fatigue. *Materials Science and Engineering A*, 2013, **573**, 45-53. DOI: 10.1016/j.msea.2013.02.046
- [97] DÉPRÉS, C., C. F. ROBERTSON AND M. C. FIVEL. Crack initiation in fatigue: experiments and three-dimensional dislocation simulations. *Materials Science and Engineering A*, 2004, **387**, 288-291. DOI: 10.1016/j.msea.2003.12.084
- [98] BOSE, S. *High Temperature Coatings*. Edition ed. Oxford: Elsevier. ISBN 978-0-7506-8252-7.
- [99] MARSHALL, P. *Austenitic Stainless Steels: Microstructure and mechanical properties*. Edition ed.: Springer, 1984. ISBN 978-0853342779.
- [100] VISKARI, L., M. HÖRNQVIST, K. L. MOORE, Y. CAO AND K. STILLER. Intergranular crack tip oxidation in Ni-base superalloy. *Acta Materialia*, 2013, **61**, 3630-3639. DOI: 10.1016/j.actamat.2013.02.050
- [101] QIAN, J., C. F. CHEN, H. B. YU, F. LIU, H. YANG AND Z. H. ZHANG. The influence and the mechanism of the precipitate/austenite interfacial C-enrichment on the intergranular corrosion sensitivity in 310 S stainless steel. *Corrosion Science*, 2016, **111**, 352-361. DOI: 10.1016/j.corsci.2016.05.021
- [102] COFFIN, L. F. Environmental effect of high-temperature, low cycle fatigue. *Proceedings, Int. Symposium on Low Cycle Fatigue Strength and Elasto-Plastic Behavior of Materials*, 1979, 9-24.
- [103] TOMKINS, B. Role of mechanics in corrosion fatigue. *Metal Science*, 1979, **13**(7), 387-395. DOI: 10.1179/msc.1979.13.7.387

- [104] FORSYTH, P. J. A two stage process of fatigue crack growth. In *Symposium Crack Propagation*. College of Aeronautics: Cranfield, U.K., 1961, vol. II, p. 76.
- [105] FORSYTH, P. J. E. Fatigue damage and crack growth in aluminium alloys. *Acta Metallurgica*, 1963, **11**(7), 703-715. DOI: 10.1016/0001-6160(63)90008-7
- [106] SCHIJVE, J. *Fatigue of Structures and Materials*. Edition ed. New York: Springer, 2009, 623 p., ISBN 978-1-4020-6808-9
- [107] ANDERSON, T. L. *Fracture Mechanics: Fundamentals and Applications*. Edition ed.: CRC Press, 2005., 640 p., ISBN: 978-0849316562
- [108] SURESH, S. AND R. O. RITCHIE. The propagation of short fatigue cracks. *International Metals Reviews*, 1984, **29**, 445-475. DOI: 10.1179/imtr.1984.29.1.445
- [109] RICE, J. R. A path independent integral and the approximate analysis of strain concentrations by notches and cracks. *Journal of Applied Mechanics-Transactions of the ASME*, 1968, **35**, 379-386. DOI : 10.1115/1.3601206
- [110] HUTAŘ, P., L. NÁHLÍK, M. ŠEVČIK, S. SEITL, T. KRUML AND J. POLÁK. Fatigue crack propagation rate in EUROFER 97 estimated using small specimens. *Key Engineering Materials: Advances in Fracture and Damage Mechanics*, 2011, **452-453**, 325-328. DOI: 10.4028/www.scientific.net/KEM.452-453.325
- [111] OBRTLÍK, K. AND J. POLÁK. Fatigue Growth of Surface Cracks in the Elastic-Plastic Region. *Fatigue and Fracture of Engineering Materials and Structures*, 1985, **8**(1), 23-31. DOI: 10.1111/j.1460-2695.1985.tb00417.x
- [112] IRWIN, G. R. AND J. A. KIES. Critical energy rate analysis of fracture strength. *Welding Journal Research Supplement*, 1954, **33**, 193-198.
- [113] BLOM, A. F., A. HEDLUND, W. ZHAO, A. FATHULLA AND B. WEISS. Short Fatigue Crack Growth in Al 2024 and Al 7475. In *Proceedings of the Symposium on Behavior of Short Fatigue Cracks*, Sheffield England, 1986, 37-66.
- [114] SCHIJVE, J. Fatigue predictions and scatter. *Fatigue and Fracture of Engineering Materials and Structures*, 1994, **17**, 381-396. DOI: 10.1111/j.1460-2695.1994.tb00239.x
- [115] STOLARZ, J. Multicracking in low cycle fatigue - a surface phenomenon? *Materials Science and Engineering A*, 1997, **234-236**, 861-864. DOI: 10.1016/S0921-5093(97)00408-5
- [116] CHENG, A. S. AND C. LAIRD. The transition from stage I to stage II fatigue crack propagation in copper single crystals cycled at constant strain amplitudes. *Materials Science and Engineering*, 1983, **60**(2), 177-183. DOI: 10.1016/0025-5416(83)90188-X
- [117] FORSYTH, P. J. E. A two stage process of fatigue crack growth. In *Cranfield Symposium*. London: Her Majesty's Stationery Office, 1962, p. 76-94.
- [118] BLOCHWITZ, C. AND R. RICHTER. Plastic strain amplitude dependent surface path of microstructurally short fatigue cracks in face-centred cubic metals. *Materials Science and Engineering A*, 1999, **267**(1), 120-129. DOI: 10.1016/S0921-5093(99)00060-X
- [119] BLOCHWITZ, C., W. TIRSCHLER AND A. WEIDNER. Crack opening displacement and propagation rate of micro structurally short cracks. *Materials Science and Engineering A*, 2003, **357**(1-2), 264-269. DOI: 10.1016/S0921-5093(03)00212-0
- [120] BLOCHWITZ, C., S. JACOB AND W. TIRSCHLER. Grain orientation effects on the growth of short fatigue cracks in austenitic stainless steel. *Materials Science and Engineering A*, 2008, **496**(1-2), 59-66. DOI: 10.1016/j.msea.2008.04.050
- [121] FORSYTH, P. J. E. AND D. A. RYDER. Fatigue fracture. *Aircraft Engineering*, 1960, **32**, 96-99.
- [122] NEUMANN, P. The geometry of slip processes at a propagating fatigue crack - II. *Acta Metallurgica*, 1974, **22**(9), 1167-1178. DOI: 10.1016/0001-6160(74)90072-8
- [123] NEUMANN, P. New experiments concerning the slip processes at propagating fatigue cracks—I. *Acta Metallurgica*, 1974, **22**(9), 1155-1165. DOI: 10.1016/0001-6160(74)90071-6
- [124] MEYN, D. A. Observations of micromechanisms of fatigue crack propagation in 2024 aluminum. *Transactions of the American Society for Metals*, 1968, **61**, 42-51.



- [125] PELLOUX, R. M. N. Mechanisms of formation of ductile fatigue striations. *Transactions of the American Society for Metals*, 1970, **62**, 281-285.
- [126] NOWACK, H. AND R. MARISSSEN. Fatigue crack propagation of short and long cracks: physical basis, prediction methods and engineering significance. In *Proceedings of the EMAS*, Warley, UK, R.O. RICHTIE AND E.A. STARKE eds. Proc. Fatigue, 1987, 207-230.
- [127] BOWLE, C. AND J. SCHIJVE. Crack Tip Geometry for Fatigue Cracks Grown in Air and Vacuum. In J. LANKFORD, D. DAVIDSON, W. MORRIS AND R. WEI eds. *Fatigue Mechanisms: Advances in Quantitative Measurement of Physical Damage*. Philadelphia: ASTM, 1983, STP 811, p. 400-425. DOI: 10.1520/STP30566S
- [128] HUDAK, S. J., D. L. DAVIDSON, K. S. CHAN, A. C. HOWLAND AND M. J. WALSCH. Growth of small fatigue cracks in aeroengine disc materials. *Report no. AFWAL-TR-88-4090 in D.A.F.W.A. LABORATORIES*, 1988.
- [129] GAO, N., M. W. BROWN AND K. J. MILLER. Crack growth morphology and microstructural changes in 316 stainless steel under creep-fatigue cycling. *Fatigue & Fracture of Engineering Materials & Structures*, 1995, **18**(12), 1407-1422. DOI: 10.1111/j.1460-2695.1995.tb00865.x
- [130] VAŠEK, A., J. POLÁK AND K. OBRTLÍK. Fatigue damage in two-step loading of 316L steel II. Short crack growth. *Fatigue and Fracture of Engineering Materials and Structures*, 1996, **19**(2-3), 157-163. DOI: 10.1111/j.1460-2695.1996.tb00955.x
- [131] OBRTLÍK, K., J. POLÁK, M. HÁJEK AND A. VAŠEK. Short fatigue crack behaviour in 316L stainless steel. *International Journal of Fatigue*, 1997, **19**(6), 471-475. DOI: 10.1016/S0142-1123(97)00005-4
- [132] POLÁK, J., K. OBRTLÍK AND A. VAŠEK. Short crack growth kinetics and fatigue life of materials. *Materials Science and Engineering A*, 1997, **234-236**, 970-973. DOI: 10.1016/S0921-5093(97)00308-0
- [133] LINDSTEDT, U., B. KARLSSON AND M. NYSTR. Small Fatigue Cracks in an Austenitic Stainless Steel. *Fatigue & Fracture of Engineering Materials & Structures*, 1998, **21**(1), 85-98. DOI: 10.1046/j.1460-2695.1998.00476.x
- [134] ZHAO, GAO AND WANG. Interaction and evolution of short fatigue cracks. *Fatigue & Fracture of Engineering Materials & Structures*, 1999, **22**(6), 459-467. DOI: 10.1046/j.1460-2695.1999.00195.x
- [135] IRWIN, G. R. Plastic zone near a crack and fracture toughness. In *Seventh Sagamore Ordnance Material Conference*. Syracuse University, New York, 1961, vol. **4**, p. 63-78.
- [136] IRWIN, G. R. Analysis of stresses and strains near the end of a crack traversing a plate. *Journal of Applied Mechanics-Transactions of the ASME*, 1957, **24**, 361-364.
- [137] PARIS, P. C. AND F. ERDOGAN. A critical analysis of crack propagation laws. *Journal of Basic Engineering -Transactions of the ASME*, 1963, **85**, 528-533. DOI: 10.1115/1.3656900
- [138] SHIH, C. F. AND J. W. HUTCHINSON. Fully plastic solutions and large-scale yielding estimates for plane stress crack problems. *Journal of Engineering Materials and Technology - Transaction of the ASME*, 1976, **98**, 289-295. DOI: 10.1115/1.3443380
- [139] HUTAŘ, P., J. PODUŠKA, M. ŠMÍD, I. KUBĚNA, A. CHLUPOVÁ, L. NÁHLÍK, J. POLÁK AND T. KRUML. Short fatigue crack behaviour under low cycle fatigue regime. *International Journal of Fatigue*, 2017, **103**, 207-215. DOI: 10.1016/j.ijfatigue.2017.06.002
- [140] DOWLING, N. AND E. BEGLEY. Fatigue crack growth during gross plasticity and the J-integral. *Special Technical Publication 590*, pp. 82-103. PHILADELPHIA: American Society For Testing And Materials., 1976. DOI: 10.1520/STP33940S
- [141] HUTAŘ, P., I. KUBĚNA, M. ŠEVČÍK, M. ŠMÍD, T. KRUML AND L. NÁHLÍK. Small fatigue crack propagation in Y2O3 strengthened steels. *Journal of Nuclear Materials*, 2014, **452**(1-3), 370-377. DOI: 10.1016/j.jnucmat.2014.05.071
- [142] POLÁK, J., T. KRUML, K. OBRTLÍK, J. MAN AND M. PETRENEC. Short crack growth in polycrystalline materials. *Procedia Engineering*, 2010, **2**(1), 883-892. DOI: 10.1016/j.proeng.2010.03.095

- [143] POLÁK, J. AND P. ZEŽULKA. Short crack growth and fatigue life in austenitic-ferritic duplex stainless steel. *Fatigue & Fracture of Engineering Materials & Structures*, 2005, **28**(10), 923-935. DOI: 10.1111/j.1460-2695.2005.00936.x
- [144] POLÁK, J. Plastic strain-controlled short crack growth and fatigue life. *International Journal of Fatigue*, 2005, **27**(10-12), 1192-1201. DOI: 10.1016/j.ijfatigue.2005.06.028
- [145] MINEUR, M., P. VILLECHAISE AND J. MENDEZ. Influence of the crystalline texture on the fatigue behavior of a 316L austenitic stainless steel. *Materials Science and Engineering A*, 2000, **286**(2), 257-268. DOI: 10.1016/S0921-5093(00)00804-2
- [146] CARPENTER, W., B. S. J. KANG AND K. M. CHANG. SAGBO mechanism on high temperature cracking behavior of Ni-base superalloys. In *Superalloys 718 625 706*, 1997, 679-688. ISBN: 0873393767
- [147] KRUPP, U. Dynamic Embrittlement — Time-dependent Quasi-brittle Intergranular Fracture at High Temperatures. *International Materials Reviews*, 2005, **50**(2), 83-97. DOI: 10.1179/174328005X14320
- [148] NISHINO, S. AND K. YAMADA. Surface And In-Depth Crack Propagation in High Temperature Low-Cycle Fatigue of SUS 316 Stainless Steel. *Fatigue and Fracture of Engineering Materials and Structures*, 1994, **17**(11), 1327-1334. DOI: 10.1111/j.1460-2695.1994.tb00220.x
- [149] BRESSERS, J., U. SCHUSSER AND B. ILSCHNER. Environmental Effects on the Fatigue Behaviour of Alloy 800H. In K.-T. RIE ed. *Low Cycle Fatigue Elasto-Plast. Behav. Mater.* Dordrecht: Springer Netherlands, 1987, p. 365–370. DOI: 10.1007/978-94-009-3459-7\_55
- [150] SKELTON, R. P. The treatment of very short crack growth in low cycle fatigue and creep fatigue. *Materials at High Temperatures*, 2015, **32**(3), 323-339. DOI: 10.1179/0960340914Z.00000000074
- [151] REUCHET, J. AND L. REMYN. High temperature low cycle fatigue of MAR-M 509 superalloy II: The influence of oxidation at high temperatures. *Material Science and Engineering*, 1983, **58**, 33-42. DOI: 10.1016/0025-5416(83)90135-0
- [152] HOWE, J. M. *Interfaces in Materials: Atomic Structure, Thermodynamics and Kinetics of Solid-Vapor, Solid-Liquid and Solid-Solid Interfaces*. Edition ed.: Wiley-Interscience, 1997. ISBN 978-0-471-13830-3.
- [153] BOWMAN, A. L., G. P. ARNOLD, E. K. STORMS AND N. G. NERESON. The crystal structure of Cr<sub>23</sub>C<sub>6</sub>. *Acta Crystallographica Section B*, 1972, **28**(10), 3102-3103. DOI: 10.1107/S0567740872007526
- [154] THOMPSON, N. AND N. J. WADSWORTH. Metal Fatigue. *Advances in Physics*, 1958, **7**(25), 72-169.
- [155] BASINSKI, S. J., Z. S. BASINSKI AND A. HOWIE. Early Stages of Fatigue in Copper Single Crystals. *Philosophical Magazine*, 1969, **19**(161), 899-924. DOI: 10.1080/14786436908225856
- [156] BASINSKI, Z. S. AND S. J. BASINSKI. Low Amplitude Fatigue of Copper Single-Crystals .2. Surface Observations. *Acta Metallurgica*, 1985, **33**(7), 1307-1317. DOI: 10.1016/0001-6160(85)90241-X
- [157] BASINSKI, Z. S. AND S. J. BASINSKI. Low Amplitude Fatigue of Copper Single-Crystals .3. PSB Sections. *Acta Metallurgica*, 1985, **33**(7), 1319-1327. DOI: 10.1016/0001-6160(85)90242-1
- [158] HUNSCHE, A. AND P. NEUMANN. Quantitative Measurement of Persistent Slip Band Profiles and Crack Initiation. *Acta Metallurgica*, 1986, **34**(2), 207-217. DOI: 10.1016/0001-6160(86)90192-6
- [159] HARVEY, S. E., P. G. MARSH AND W. W. GERBERICH. Atomic-Force Microscopy and Modeling of Fatigue-Crack Initiation in Metals. *Acta Metallurgica et Materialia*, 1994, **42**(10), 3493-3502. DOI: 10.1016/0956-7151(94)90481-2
- [160] CRETEGNY, L. AND A. SAXENA. AFM characterization of the evolution of surface deformation during fatigue in polycrystalline copper. *Acta Materialia*, 2001, **49**(18), 3755-3765. DOI: 10.1016/S1359-6454(01)00271-3

- [161] RISBET, M., X. FEAUGAS, C. GUILLEMER-NEEL AND M. CLAVEL. Use of atomic force microscopy to quantify slip irreversibility in a nickel-base superalloy. *Scripta Materialia*, 2003, **49**(6), 533-538. DOI: 10.1016/S1359-6462(03)00357-9
- [162] MAN, J., M. PETRENEC, K. OBRTLÍK AND J. POLÁK. AFM and TEM study of cyclic slip localization in fatigued ferritic X10CrAl24 stainless steel. *Acta Materialia*, 2004, **52**(19), 5551-5561. DOI: 10.1016/j.actamat.2004.08.014
- [163] WANG, Y., H. KIMURA, Y. AKINIWA AND K. TANAKA. EBSD-AFM hybrid analysis of crack initiation in stainless steel under fatigue loading. *Key Engineering Materials*, 2007, **340-341**, 531-536. DOI: 10.4028/www.scientific.net/KEM.340-341.531
- [164] MAN, J., M. VALTR, A. WEIDNER, M. PETRENEC, K. OBRTLÍK AND J. POLÁK. AFM study of surface relief evolution in 316L steel fatigued at low and high temperatures. *Procedia Engineering*, 2010, **2**, 1625-1633. DOI: 10.1016/j.proeng.2010.03.175
- [165] LAIRD, C., Z. WANG, B. T. MA AND H. F. CHAI. Low-Energy Dislocation-Structures Produced by Cyclic Softening. *Materials Science and Engineering A*, 1989, **113**, 245-257. DOI: 10.1016/0921-5093(89)90313-4
- [166] MUGHRABI, H. Dislocation Wall and Cell Structures and Long-Range Internal-Stresses in Deformed Metal Crystals. *Acta Metallurgica*, 1983, **31**(9), 1367-1379. DOI: 10.1016/0001-6160(83)90007-X
- [167] POLÁK, J., S. DEGALLAIX AND G. DEGALLAIX. The Role of Cyclic Slip Localization in Fatigue Damage of Materials. *Journal De Physique IV France*, 1993, **3**(C7), 679-684. DOI: 10.1051/jp4:19937107
- [168] WEIDNER, A., R. BEYER, C. BLOCHWITZ, C. HOLSTE, A. SCHWAB AND W. TIRSCHLER. Slip activity of persistent slip bands in polycrystalline nickel. *Materials Science and Engineering A*, 2006, **435-436**, 540-546. DOI: 10.1016/j.msea.2006.07.039
- [169] WEIDNER, A., C. BLOCHWITZ, W. SKROTZKI AND W. TIRSCHLER. Formation of slip steps and growth of extrusions within persistent slip bands in cyclically deformed polycrystals. *Materials Science and Engineering A*, 2008, **479**(1-2), 181-190. DOI: 10.1016/j.msea.2007.06.044
- [170] VOGT, J. B., J. FOCT, C. REGNARD, G. ROBERT AND J. DHERS. Low-Temperature Fatigue of 316L and 316LN Austenitic Stainless-Steels. *Metallurgical Transactions A*, 1991, **22**(10), 2385-2392. DOI: 10.1007/BF02665004
- [171] KRUMML, T., K. OBRTLÍK AND J. POLÁK. Dislocation Structures in Cyclically Deformed Steel AISI 316L. *Kovove Materialy-Metallic Materials*, 1993, **31**(6), 529-540.
- [172] POLÁK, J., V. MAZÁNOVÁ, M. HECZKO, R. PETRÁŠ, I. KUBĚNA, L. CASALENA AND J. MAN. The role of extrusions and intrusions in fatigue crack initiation. *Engineering Fracture Mechanics*, 2017, **185**, 46-60. DOI: 10.1016/j.engfracmech.2017.03.006
- [173] POLÁK, J., V. MAZÁNOVÁ, M. HECZKO, I. KUBĚNA AND J. MAN. Profiles of persistent slip markings and internal structure of underlying persistent slip bands. *Fatigue & Fracture of Engineering Materials & Structures*, 2017, **40**(7), 1101-1116. DOI: 10.1111/ffe.12567
- [174] VILLECHAISE, P., M. MINEUR AND J. MENDEZ. Analysis of texture effects on fatigue behaviour of 316L stainless steel. *Journal De Physique IV France*, 2001, **11**(PR4), 311-319. DOI: 10.1051/jp4:2001438
- [175] SIGNOR, L., P. VILLECHAISE, T. GHIDOSSI, E. LACOSTE, M. GUEGUEN AND S. COURTIN. Influence of local crystallographic configuration on microcrack initiation in fatigued 316LN stainless steel: Experiments and crystal plasticity finite elements simulations. *Materials Science and Engineering A*, 2016, **649**, 239-249. DOI: 10.1016/j.msea.2015.09.119
- [176] MUGHRABI, H. Cyclic slip irreversibilities and the evolution of fatigue damage. *Metallurgical and Materials Transaction A*, 2009, **40**, 1257-1279. DOI: 10.1007/s11661-009-9839-8
- [177] MUGHRABI, H. Microstructural fatigue mechanisms: Cyclic slip irreversibility, crack initiation, non-linear elastic damage analysis. *International Journal of Fatigue*, 2013, **57**, 2-8. DOI: 10.1016/j.ijfatigue.2012.06.007

- [178] POLÁK, J. Resistivity of fatigued copper single crystals. *Materials Science and Engineering*, 1987, **89**, 35-43. DOI: 10.1016/0025-5416(87)90247-3
- [179] BASINSKI, Z. S. AND S. J. BASINSKI. Electrical-Resistivity of Fatigued Copper-Crystals. *Acta Metallurgica*, 1989, **37**(12), 3275-3281. DOI: 10.1016/0001-6160(89)90200-9
- [180] POLÁK, J. AND J. MAN. Quantitative Model of the Surface Relief Formation in Cyclic Straining. *Acta Physica Polonica A*, 2015, **128**(4), 675-680. DOI: 10.12693/APhysPolA.128.675
- [181] DAVIDSON, D. L., R. TRYON, M. OJA, R. MATTEWS AND K. S. R. CHANDRAN. Fatigue crack initiation in WASPALOY at 20 °C. *Metallurgical and Materials Transactions A*, 2007, **38**(13), 2214-2225. DOI: 10.1007/s11661-007-9178-6
- [182] WINTER, A. T., O. B. PEDERSEN AND K. V. RASMUSSEN. Dislocation Microstructures in Fatigued Copper Polycrystals. *Acta Metallurgica*, 1981, **29**(5), 735-748. DOI: 10.1016/0001-6160(81)90117-6
- [183] BLOCHWITZ, C. AND W. TIRSCHLER. Influence of texture on twin boundary cracks in fatigued austenitic stainless steel. *Materials Science and Engineering A*, 2003, **339**(1-2), 318-327. DOI: 10.1016/S0921-5093(02)00126-0
- [184] LLANES, L. AND C. LAIRD. The Role of Annealing Twin Boundaries in the Cyclic Deformation of FCC Materials. *Materials Science and Engineering A*, 1992, **157**(1), 21-27. DOI: 10.1016/0921-5093(92)90094-H
- [185] KAMAYA, M. Influence of bulk damage on crack initiation in low-cycle fatigue of 316 stainless steel. *Fatigue & Fracture of Engineering Materials & Structures*, 2010, **33**(2), 94-104. DOI: 10.1111/j.1460-2695.2009.01420.x
- [186] HEINZ, A. AND P. NEUMANN. Crack Initiation during High Cycle Fatigue of an Austenitic Steel. *Acta Metallurgica et Materialia*, 1990, **38**(10), 1933-1940. DOI: 10.1016/0956-7151(90)90305-Z
- [187] BLOCHWITZ, C., R. RICHTER, W. TIRSCHLER AND K. OBRTLICK The effect of local textures on microcrack propagation in fatigued f.c.c. metals. *Materials Science and Engineering A*, 1997, **234-236**, 563-566. DOI: 10.1016/S0921-5093(97)00320-1
- [188] ROACH, M. D., S. I. WRIGHT, J. E. LEMONS AND L. D. ZARDIACKAS An EBSD based comparison of the fatigue crack initiation mechanisms of nickel and nitrogen-stabilized cold-worked austenitic stainless steels. *Materials Science and Engineering A*, 2013, **586**, 382-391. DOI: 10.1016/j.msea.2013.08.027
- [189] VAŠEK, A. AND J. POLÁK. Initiation and propagation of fatigue cracks in Arema iron in elastoplastic cyclic loading. *Metallic Materials (English translation of Kovove Materialy)*, 1991, **29**(2), 80-86.
- [190] ZHIXUE, W. Short fatigue crack parameters describing the lifetime of unnotched steel specimens. *International Journal of Fatigue*, 2001, **23**(4), 363-369. DOI: 10.1016/S0142-1123(00)00101-8
- [191] KRUPP, U., O. DUBER, H. J. CHRIST, B. KUNKLER, P. KOSTER AND C. P. FRITZEN. Propagation mechanisms of micro structurally short cracks - Factors governing the transition from short-to long-crack behavior. *Materials Science and Engineering A*, 2007, **462**(1-2), 174-177. DOI: 10.1016/j.msea.2006.03.159
- [192] KRUPP, U., H. KNOBBE, H. J. CHRIST, P. KOSTER AND C. P. FRITZEN. The significance of microstructural barriers during fatigue of a duplex steel in the high- and very-high-cycle-fatigue (HCF/VHCF) regime. *International Journal of Fatigue*, 2010, **32**(6), 914-920. DOI: 10.1016/j.ijfatigue.2009.09.010
- [193] POLÁK, J., P. LISKUTIN AND A. VASEK. Short crack growth and fatigue life evaluation. In K.-T. RIE, H.W. GRÜNLING, G. KÖNIG, P. NEUMANN, H. NOWACK, K.-H. SCHWALBE AND T. SEEGER eds. *Low Cycle Fatigue and Elasto-Plastic Behaviour of Materials - 3*. Dordrecht: Springer, 1992, p. 502-507. DOI: 10.1007/978-94-011-2860-5\_81

- [194] POLÁK, J., R. PETRÁŠ, M. HECZKO, I. KUBĚNA, T. KRUML AND G. C. CHAI. Low cycle fatigue behavior of Sanicro25 steel at room and at elevated temperature. *Materials Science and Engineering A*, 2014, **615**, 175-182. DOI: 10.1016/j.msea.2014.07.075
- [195] POLAK, J. Plastic strain-controlled short crack growth and fatigue life. *International Journal of Fatigue*, 2005, **27**(10-12), 1192-1201. DOI: 10.1016/j.ijfatigue.2005.06.028
- [196] WORMSEN, A., A. FJELDSTAD AND G. HÄRKEGÅRD. The application of asymptotic solutions to a semi-elliptical crack at the root of a notch. *Engineering Fracture Mechanics*, 2006, **73**, 1899-1912. DOI: 10.1016/j.engfracmech.2006.02.006
- [197] FINDLEY, K., S. W. KOH AND A. SAXENA. J-integral expressions for semi-elliptical cracks in round bars. *International Journal of Fatigue*, 2007, **29**(5), 822-828. DOI: 10.1016/j.ijfatigue.2006.09.001
- [198] TRÁVNÍČEK, L., V. MAZÁNOVÁ, J. POLÁK, J. PODUŠKA, L. NÁHLÍK AND P. HUTAŘ. Estimation of short fatigue crack growth rate and residual fatigue life prediction of austenitic Sanicro 25 stainless steel. *Submitted for publication*.
- [199] RITCHIE, R. O. AND J. O. PETERS. Small Fatigue Cracks: Mechanics, Mechanisms and Engineering Applications. *Materials Transactions*, 2001, **42**(1), 58-67. DOI: 10.2320/matertrans.42.58
- [200] KRUML, T., P. HUTAŘ, L. NÁHLÍK, S. SEITL AND J. POLÁK. Fatigue cracks in Eurofer 97 steel: Part II. Comparison of small and long fatigue crack growth. *Journal of Nuclear Materials*, May 1 2011, **412**(1), 7-12. DOI: 10.1016/j.jnucmat.2011.01.018
- [201] HUTAŘ, P., I. KUBĚNA, M. ŠMÍD, M. ŠEVČÍK, T. KRUML AND L. NÁHLÍK. Description of small fatigue crack propagation in ODS steel. *Advanced Material Research*, 2014, **891-892**, 911-916. DOI: 10.4028/www.scientific.net/AMR.891-892.911
- [202] TRILLO, E. A. AND L. E. MURR. A TEM investigation of M23C6 carbide precipitation behaviour on varying grain boundary misorientations in 304 stainless steels. *Journal of Materials Science*, 1998, **33**(5), 1263-1271. DOI: 10.1023/A:1004390029071
- [203] ASHBY, M. F. AND D. R. H. JONES. *Engineering materials 1. An introduction to their properties and applications* Edtion ed.: Butterworth-Heinemann, 1996. ISBN 0750630817.
- [204] ROTHMAN, S. J., L. J. NOWICKI AND G. E. MURCH. Self-diffusion in austenitic Fe-Cr-Ni alloys. *Journal of Physics F: Metal Physics*, 1980, **10**, 383-398. DOI: 10.1088/0305-4608/10/3/009
- [205] FAN, H. J., U. GÖSELE AND M. ZACHARIAS. Formation of Nanotubes and Hollow Nanoparticles Based on Kirkendall and Diffusion Processes: A Review. *Small*, 2007, **3**(10), 1660-1671. DOI: 10.1002/sml.200700382

## IX. LIST OF ABBREVIATIONS / SYMBOLS

### Abbreviations

ADF – annular dark field  
AFM – atomic force microscopy  
BCC/b.c.c. – body-centered cubic  
BF – bright field  
BSE – backscattered electrons  
CSL – coincidence site lattice  
CSSC – cyclic stress-strain curve  
EBSD – electron back-scatter diffraction  
EBSP – electron backscattered diffraction pattern  
ECCI – electron channeling contrast imaging  
EDS – energy dispersive X-ray spectroscopy  
EGM model – Essmann – Gösele – Mughrabi model  
FCC/f.c.c. – face-centered cubic  
FEM – finite element method  
FESEM – field emission gun operated scanning electron microscope  
FIB – focused ion beam  
GB – grain boundary  
HAADF – high-angle annular dark-field  
HAGB – high angle grain boundaries  
IG – intergranular crack  
LA – loading axis  
LAGB – low angle grain boundaries  
LCF – low cycle fatigue  
LEFM – linear elastic fracture mechanics  
LM – light microscope  
PSB – persistent slip band  
PSM – persistent slip marking  
SE – secondary electrons  
SEM – scanning electron microscopy  
SFE – stacking fault energy  
STEM – scanning transmission electron microscopy  
TB – twin boundary  
TC – transcrystalline crack path  
TEM – transmission electron microscopy  
TG – transgranular crack path

### Symbols

$y_e$  – annihilation distance of two edge dislocations with opposite sign  
 $\gamma_M$  – constant plastic shear strain amplitude in the matrix  
 $\gamma_{PSB}$  – constant plastic shear strain amplitude in the PSB  
 $C^{sat}$  – saturated concentration of point defects

$\gamma_{pl}$  – shear plastic strain  
 $\Delta\gamma$  – shear strain range  
 $f_{ij,l}(\Theta)$  – trigonometric functions which depend on the  $ij$  components of stress tensor  
 $A$  – the annihilation coefficient expressed as the fraction of vacancies swept by mobile dislocations during one cycle  
 $a$  – the crack length; length of a crack growing under the tensile mode with tensile stress  $\sigma$   
 $a_i$  – the crack length extrapolated back to zero number of cycles  
 $b$  – fatigue strength exponent  
 $b$  – modulus of Burgers vector  
 $c$  – fatigue ductility exponent  
 $C, m$  – experimentally determined material constants  
 $c_j$  – the vacancy concentration  
 $d$  – crack growth exponent  
 $d$  – structural diameter  
 $D_v$  – the diffusion coefficient of vacancies  
 $e$  – elongation of PSB/PSM in the direction of the active slip vector  
 $E$  – Young modulus of elasticity  
 $f$  – fraction of persistent slip bands  
 $F(a, w)$  – function depending on the crack length  $a$  and characteristic dimension  $w$  of a body in the direction of the crack  
 $h$  – the height of the surface in the direction of the Burgers vector  
 $J$  – path-independent  $J$ -integral  
 $J_a$  – amplitude of  $J$   
 $J_{a,el}$  – elastic amplitude of  $J$   
 $J_{a,pl}$  – plastic amplitude of  $J$   
 $J_v$  – vacancy flux  
 $k$  – parabolic constant  
 $k$  – rate constant  
 $K'$  – fatigue hardening coefficient  
 $k_l$  – constant  
 $Ka$  – stress intensity amplitude  
 $k_g$  – crack growth coefficient  
 $K_I$  – stress intensity factor  
 $K_t$  – theoretical stress concentration factor of the notch  
 $l$  – the length of PSB below the surface  
 $m$  – thickness of the oxide scale  
 $N$  – number of cycles  
 $N$  – the number of cycles.  
 $n'$  – fatigue hardening exponent  
 $N_f$  – number of cycles to fracture  
 $P_{pj}$  – the probability of production of a dipole of vacancies of unit height responsible for mass transfer and internal mean stresses in a channel within a half-cycle  
 $p_v$  – the production rate of point defect of vacancy type in a cycle  
 $R$  – gas constant  
 $R$  – the asymmetry parameter of the cyclic loading  
 $r, \Theta$  – polar coordinates  
 $R_{p0.2}, R_{p0.02}$  – yield stress defined at engineering strain equal to 0.2% and 0.02% respectively

$t$  – exposure time  
 $T$  – temperature  
 $V_H$  – loop shape parameter  
 $W$  – hysteresis loop area, specific energy dissipated in a material within one cycle  
 $\Delta G_{activ.}$  – free energy of activation  
 $\Delta K$  – range of stress intensity factor  
 $\varepsilon'_f$  – fatigue ductility coefficient  
 $\varepsilon_a$  – total strain amplitude  
 $\varepsilon_{a,el}$  – elastic strain amplitude  
 $\varepsilon_{ap}$  – plastic strain amplitude  
 $\sigma'_f$  – fatigue strength coefficient  
 $\sigma_a$  – total stress amplitude  
 $\tau$  – the cycle period  
 $\beta$  – the angle between specimen axis and the normal to the active slip plane  
 $\gamma_p$  – average plastic shear strain amplitude within the PSB  
 $\rho$  – dislocation density  
 $\rho_{ch}$  – density of edge dislocations in the channels  
 $\rho_e$  – edge dislocation density responsible for vacancy concentration  
 $\rho_w$  – density of edge dislocations in the walls



# X. Curriculum Vitae

**Veronika Mazánová**

(\* December 10, 1989)

mazanova@ipm.cz

ORCID ID: 0000-0002-6804-2632

ResearcherID: B-1028-2017

Scopus Author ID: 57004902800

## EDUCATION

---

<b>Brno University of Technology</b> , Faculty of Mechanical Engineering <b>Republic &amp; Institute of Physics of Materials AS CR</b> PhD Physical and Materials Engineering ( <i>expected</i> )	<b>Brno, Czech</b> Sep 2014 – 2019
<b>Slovak University of Technology</b> , Faculty of Mechanical Engineering <b>Slovakia</b> MS Applied mechanics (Ing.) BS Mechanics (Bc.)	<b>Bratislava,</b> Sep 2012 – Jun 2014 Sep 2009 – Jun 2012

## RESEARCH EXPERIENCE

---

<b>Institute of Physics of Materials AS CR</b> <b>Republic</b> PhD Student <b>Advisor:</b> Prof. Jaroslav Polák, Prof. Tomáš Kruml	<b>Brno, Czech</b> Aug 2014 - Present
<b>Paul Scherrer Institute, Laboratory for Nuclear Materials</b> Visiting Researcher <b>Advisor:</b> Prof. Philippe Spätig	<b>Villigen, Switzerland</b> Feb 2018 – Jul 2018
<b>Slovak University of Technology, Faculty of Mechanical Engineering</b> MS Student <b>Advisor:</b> Ing. Vladimír Chmelko, Ph.D	<b>Bratislava, Slovakia</b> Sep 2012 – Jun 2014

## TEACHING EXPERIENCES

---

<b>Presenter and lecturer</b> Introduction to Materials Science and Engineering Structure and Properties of Materials Production Technologies	<b>Brno University of Technology</b> Nov 2014 – Jul 2017 Nov 2014 – Jul 2017 Nov 2014 – Jul 2017
--	---

## CONFERENCE SPEAKING ENGAGEMENTS

---

18th International Conference on the Strength of Materials	<i>Columbus, OH, USA</i> Jul 2018
Symposium on Multi-Scale Fatigue, Fracture and Damage in Materials in Harsh Environments	<i>Gabway, Ireland</i> Aug 2017
International Colloquium Mechanical Fatigue of Metals	<i>Gijon, Spain</i> Sep 2016
Microscopy & Microanalysis 2016	<i>Columbus, OH, USA</i> Jul 2016
International Conference on Multiaxial Fatigue and Fracture 11	<i>Seville, Spain</i> Jun 2016
Materials Structure & Micromechanics of Fracture 8	<i>Brno, Czech Republic</i> Jun 2016
27th Colloquium on Fatigue Mechanisms	<i>Vienna, Austria</i> Mar 2016
International Conference on Mechanical Behavior of Materials 12	<i>Karlsruhe, Germany</i> May 2015

## XI. Veronika Mazánová - List of publications

- [1] MAZÁNOVÁ, V., M. HECZKO, V. ŠKORÍK, A. CHLUPOVÁ, J. POLÁK and T. KRUML: Microstructure and martensitic transformation in 316L austenitic steel during multiaxial low cycle fatigue at room temperature, *Material Science and Engineering A*. 2019, **767**, 138407
- [2] MAZÁNOVÁ, V., M. HECZKO and J. POLÁK: Fatigue crack initiation and growth in 43Fe-25Ni-22.5Cr austenitic stainless steel at a temperature of 700°C, *International Journal of Fatigue*. 2018, **114**, 11-21.
- [3] MAZÁNOVÁ V. and J. POLÁK: Initiation and short crack growth in austenitic Sanicro 25 steel under the LCF conditions at room temperature. *Fatigue Fracture of Engineering Materials and Structures*. 2018, **41**(7), 1529-1545.
- [4] POLÁK, J., V. MAZÁNOVÁ, R. PETRÁŠ and M. HECZKO: Early damage and fatigue crack initiation at ambient and elevated temperatures in heat resistant austenitic steel, *MATEC Web of Conferences*. 2018, **165**, 04008.
- [5] HECZKO, M., B.D. ESSER, T.M. SMITH, P. BERAN, V. MAZÁNOVÁ, D.W. MCCOMB, T. KRUML, J. POLÁK and M.J. MILLS: Atomic resolution characterization of strengthening nanoparticles in a new high-temperature-capable 43Fe-25Ni-22.5Cr austenitic stainless steel, *Materials Science & Engineering A*. 2018, **719**, 49-60.
- [6] HECZKO, M., B.D. ESSER, T.M. SMITH, P. BERAN, V. MAZÁNOVÁ, T. KRUML, J. POLÁK and M.J. MILLS: On the origin of extraordinary cyclic strengthening of the austenitic stainless steel Sanicro 25 during fatigue at 700°C, *Journal of Materials Research*. 2017, **32**(23), 4342-4353.
- [7] POLÁK, J., V. MAZÁNOVÁ, M. HECZKO, R. PETRÁŠ, I. KUBĚNA, L. CASALENA and J. MAN: The role of extrusions and intrusions in fatigue crack initiation, *Engineering Fracture Mechanics*. 2017, **185**, 46-60.
- [8] MAZÁNOVÁ V., V. ŠKORÍK, T. KRUML and J. POLÁK, Cyclic response and early damage evolution in multiaxial cyclic loading of 316L austenitic steel, *International Journal of Fatigue*. 2017, **100**, 466-476.
- [9] POLÁK, J., V. MAZÁNOVÁ, M. HECZKO, I. KUBĚNA and J. MAN: Profiles of persistent slip markings and internal structure of underlying persistent slip bands, *Fatigue & Fracture of Engineering Materials & Structures*. 2017, **40**(7), 1101-1116.

- [10] POLÁK, J., R. PETRÁŠ and V. MAZÁNOVÁ: Mechanisms of fatigue damage at ambient and elevated temperatures in heat resistant stainless steel. *ICF 2017-14th International Conference on Fracture*. 2017, **1**, 237-238.
- [11] MAZÁNOVÁ V., J. POLÁK, V. ŠKORÍK and T. KRUML: Multiaxial elastoplastic cyclic loading of austenitic 316L steel, *Frattura ed Integrità Strutturale*. 2017, **11**(40), 162-169.
- [12] MAZÁNOVÁ, V., M. HECZKO, I. KUBĚNA and J. POLÁK: Surface Relief Formation in Relation to the Underlying Dislocation Arrangement, *Solid State Phenomena*. 2017, **258**, 526-529.
- [13] POLÁK, J., V. MAZÁNOVÁ, I. KUBĚNA, M. HECZKO and J. MAN: Surface relief and internal structure in fatigued stainless Sanicro 25 steel, *Metallurgical and Materials Transactions A*. 2016, **47**(5), 1907-1911.
- [14] POLÁK J., R. PETRÁŠ and V. MAZÁNOVÁ: Basic mechanisms leading to fatigue failure of structural materials, *Transactions of the Indian Institute of Metals*. 2016 **69**(2), 289-294.
- [15] KAROL M., A. CHLUPOVÁ, V. MAZÁNOVÁ and T. KRUML: Fatigue crack growth in 316L under uniaxial and torsional loading. *METAL 2016-25<sup>th</sup> Anniversary International Conference on Metallurgy and Materials, Conference Proceedings*, 2016, 568-573.
- [16] KAROL M., A. CHLUPOVÁ, V. MAZÁNOVÁ and T. KRUML, Fatigue crack initiation and growth in 316L steel in torsional cyclic loading. *ENGINEERING MECHANICS 2017, Svatka, Czech Republic, 15-18 May 2017*.